Biomechanical assessment of RTSA functional outcomes towards optimising the prosthesis configuration

Jonathan Daniel Glenday

Thesis presented for the degree of

Doctor of Philosophy

in the Department of Human Biology

University of Cape Town

November 2018

The financial assistance of the National Research Foundation (NRF) towards this research is hereby acknowledged. Opinions expressed, and conclusions arrived at, are those of author and are not necessarily to be attributed to the NRF.

Plagiarism Declaration

- I know that plagiarism is wrong. Plagiarism is to use another's work and pretend that it is one's own.
- I have used the Harvard convention for citation and referencing. Each contribution to, and quotation in, this report from the work(s) of other people has been attributed, and has been cited and referenced.
- This thesis has been submitted to the Turnitin module and I confirm that my supervisor has seen my report and any concerns revealed by such have been resolved with my supervisor.
- I confirm that I have been granted permission by the University of Cape Town's Doctoral Degrees Board to include the following publication in my PhD thesis, and where co-authorships are involved, my co-authors have agreed that I may include the publication:
  - Glenday, J., Kontaxis, A., Roche, S. and Sivarasu, S. "Effect of humeral tray placement on impingement-free range of motion and muscle moment arms in reverse shoulder arthroplasty". *Submitted to Clinical Biomechanics, under review*.

Signed by candidate

06/09/18

Jonathan Daniel Glenday (GLNJON001)

Date

Acknowledgements

Firstly, I would like to thank Sudesh Sivarasu for supervising this thesis. Your enthusiasm, support, and guidance throughout this process has been invaluable. Thank you for providing me with an environment that has allowed me to grow as an engineer and researcher.

To Stephen Roche, thank you for co-supervising this thesis and for your clinical insight. Thank you for willingness to delve into the "black box" that is biomechanics, and for always encouraging me to think of the clinical perspective. Your passion for the advancement of orthopaedics through the collaboration of clinicians and engineers is inspiring.

To all the members of the Motion Analysis Laboratory at the HSS, thank you for your support and friendship during my internship, and beyond. To Andreas Kontaxis and Xiang Chen, thank you for exemplifying the spirit of academia with your openness to impart knowledge and collaborate, and for your patience during the formative stages of this thesis.

To Bhushan Borotikar, thank you for your support and friendship during my internship at LaTIM, and beyond. Thank you for never hesitating to ask the tough questions in the pursuit of knowledge.

To Roopam, Leanne, Seth and Saadiq, thank you for making the Orthopaedic Biomechanics Laboratory a great place to work.

To Leith, Emma, Raquel, Michael, Caitlin and Royden thank you all for your friendship. Thank you for being there for me, and for helping to maintain my sanity during this process.

To my family in the USA. Nigel and Betsy, Ian and Kay, and Alex and Justine, thank you for giving me a home away from home during my internship at HSS.

Most importantly, to my parents. Carol and Craig, without your never-ending love and support, none of this would have been possible. Thank you.

Financial assistance for this thesis was provided by an NRF Innovation Doctoral Scholarship. Financial assistance for the internship to HSS was provided by the Max and Lillie Sonnenberg Scholarship. Financial assistance for the internship to LaTIM was provided by an NRF South Africa/France Science and Technology Research Collaboration.

Abstract

Reverse total shoulder arthroplasty (RTSA) alleviates pain and restores function to patients with cuff tear arthropathies or massive rotator cuff tears. The procedure uses a semi-constrained prosthesis to reverse the orientation of the glenohumeral joint, thereby altering the biomechanics of the deltoid and allowing it to restore shoulder function in the presence of an irreparably damaged rotator cuff. However, there are complications that can impact long-term success of RTSA. Adaptations to the design and placement of the prosthesis have been investigated to address these complications and this has led medical device manufacturers to develop divergent implants. This divergence, as well as previous literature regarding RTSA biomechanics, suggest that a configuration that optimises reverse shoulder functional outcomes has yet to be determined and that it can be obtained by combining multiple modifications.

A biomechanical assessment framework was established to characterise reverse shoulder function and the effect of modifying prosthesis configuration. It utilised the Newcastle Shoulder Model (NSM) and a custom-made impingement detection algorithm to simulate seven standardised motions that either elevated or rotated the humerus. Four outcome measures (deltoid elongation, deltoid moment arm, joint stability and impingement-free range of motion) were evaluated for each motion. The framework took anatomical variability into consideration by performing the simulations using a subject-specific reverse shoulder cohort. Further, 36 modified configurations of the prosthesis (based on offsets to the placement of glenosphere, humeral tray and greater tuberosity) were evaluated. The effect of each of these modifiable parameters on the outcome measures was characterised as beneficial, detrimental, or negligible, in comparison to a default prosthesis configuration.

Seven of the most beneficial parameters were then selected for combination and evaluated using the assessment framework. Due to an antagonistic relationship between the outcome measures, and differing functional requirements of the motions, none of the configurations were able to simultaneously maximise all outcome measures. Rather, the optimised configuration (which inferiorly translated the glenosphere and posteromedially translated the humeral tray) provided balanced, moderate improvements to majority of the outcome measures. Overall, the deltoid did not excessively elongate, and deltoid moment arms, joint stability, and impingement-free range of motion improved by 17.9%, 57.1%, and 32.1%, respectively compared to the default configuration.

Subsequently, comparisons between the effect of the default and optimised configurations on muscle fatigue and micromotion at the bone-implant interface were made. Muscle fatigue was assessed by adapting the NSM, and micromotion was assessed through a finite element analysis of a subset of the reverse shoulder cohort. The optimised configuration had a beneficial impact on

the time to initiate muscle fatigue by decreasing the force required by the middle deltoid to initially elevate the humerus, and it had no appreciable effect on micromotion.

In summary, an optimised RTSA configuration has been presented in this thesis. For a rotator cuff deficient reverse shoulder, the proposed configuration provided balanced, moderate improvements to majority of the functional outcomes. Additionally, the configuration was able to mitigate the effect of muscle fatigue and did not affect micromotion. Future studies should look to experimentally validate these findings, determine their clinical significance, and enhance both the assessment techniques and framework.

Contents

List of Figures

List of Tables

List of Abbreviations

2D	Two-Dimensional
3D	Three-Dimensional
% CI	% Confidence Interval
AA	Acromial Angle
ABD(h)	(Held) Abduction
AC	Acromioclavicular
AI	Inferior Angle
AP	Anteroposterior
API	Application Programming Interface
ASTM	American Society for Testing and Materials
BV	Bone Volume
BW	Bodyweight
CT	Computed Tomography
CTA	Cuff Tear Arthropathy
DE	Deltoid Elongation
DMA	Deltoid Moment Arm
DOF	Degrees of Freedom
DSEM	Delft Shoulder and Elbow Model
EMG	Electromyography
ER20	External Rotation at 20° of humeral abduction
ER90	External Rotation at 90° of humeral abduction
FDA	Food and Drug Administration
FE(A)	Finite Element (Analysis)
FF(h)	(Held) Forward Flexion
FM	Fatigable Muscles
FS	Fibre State
GH	Glenohumeral
GS_A	Glenosphere Anterior Translation
GS_AI	Glenosphere Anteroinferior Translation
GS_I	Glenosphere Inferior Translation
GS_IR	Glenosphere Inferior Rotation
GS_L	Glenosphere Lateralisation
GS_P	Glenosphere Posterior Translation
GS_PI	Glenosphere Posteroinferior Translation
GT_RI	Greater Tuberosity Radius Increase
HSS	Hospital for Special Surgery
HTD_D	Humeral Tray Depth Decrease

HTD_I	Humeral Tray Depth Increase
HTT_A	Humeral Tray Anterior Translation
HTT_AL	Humeral Tray Anterolateral Translation
HTT_AM	Humeral Tray Anteromedial Translation
HTT_L	Humeral Tray Lateral Translation
HTT_M	Humeral Tray Medial Translation
HTT_P	Humeral Tray Posterior Translation
HTT_PL	Humeral Tray Posterolateral Translation
HTT_PM	Humeral Tray Posteromedial Translation
HU	Hounsfield Unit
IFROM	Impingement Free Range of Motion
IR20	Internal Rotation at 20° of humeral abduction
IR90	Internal Rotation at 90° of humeral abduction
ISB	International Society of Biomechanics
ISG	International Shoulder Group
JCF	Joint Contact Force
JS	Joint Stability
LE	Lateral Epicondyle
MATLAB	MATrix LABoratory
ME	Medial Epicondyle
MF	Muscle Force
MM	Micromotion
NFM	Non-Fatgiable Muscles
NSM	Newcastle Shoulder Model
NYU	New York University
OHSU	Oregon Health and Science University
PC	Principal Component
PEW	Polyethylene Wear
RTSA	Reverse Total Shoulder Arthroplasty
SC	Sternoclavicular
SI	Superoinferior
SICAS	Swiss Institute for Computer Assisted Surgery
SPE(h)	(Held) Scapular Plane Elevation
SR	Stability Ratio
STGP	Scapulothoracic Gliding Plane
SUNY	State University of New York
TIF	Time to Initiate Fatigue
TS	Trigonum Spinae
TSA	Total Shoulder Arthroplasty
UCLA	University of California, Los Angeles

Chapter 1

Introduction

1.1 Background

The glenohumeral joint is a ball-and-socket type joint that connects the convex humeral head of the humerus with the concave glenoid fossa of the scapula. Due to a mismatch in size between the ball and socket, it is the most mobile joint in the human body and enables a wide range of motion during everyday activities. However, this high degree of mobility means that it is the least stable joint in the body and relies upon the rotator cuff (a group of four muscles that originate on the scapula, cross the glenohumeral joint and encapsulate the humeral head) to act as primary actuators and stabilisers.

Like the other joints in the body, the glenohumeral joint can suffer from age-related degenerative diseases, such as osteoarthritis or rheumatoid arthritis. Total shoulder arthroplasty (TSA) is a well-established surgical procedure that replaces the arthritic humeral head and glenoid fossa of the joint with a prosthesis that has a radial mismatch between its components (Neer 2011). While the unconstrained prosthesis provides good mobility and stability when the rotator cuff is intact, it has been found to fail when the rotator cuff is damaged (Franklin et al. 1988; Pollock et al. 1992). This damage can be due to either cuff tear arthropathies (a type of degenerative osteoarthritis caused by an untreated rotator cuff tear (Neer et al. 1983)) or a sudden, massive rotator cuff tear. In the case of cuff tear arthropathy, the tear propagates progressive joint instability and impingement between the scapula and humerus.

Adequate treatment of osteoarthritis in conjunction with an irreparably damaged rotator cuff remained unsuccessful until the 1980s. It was during this time that French surgeon, Paul Grammont, developed a semi-constrained, non-anatomic prosthesis that reversed the orientation of the gleno-humeral joint (Grammont and Baulot 1993). In doing so, reverse total shoulder arthroplasty (RTSA) altered the function of the deltoid muscle and allowed it to restore mobility and stability to a shoulder with an irreparably damaged rotator cuff (Boileau et al. 2005). Early follow-up studies reported good clinical outcomes (Sirveaux et al. 2004; Frankle et al. 2005; Boileau et al. 2006; Wall et al. 2007) and, consequently, usage of the prosthesis has grown in recent years, alongside its indications. The number of upper extremity arthroplasties performed in the United States has increased drastically

since the approval of RTSA by the Food and Drug Administration in 2003, and in 2015, RTSA was responsible for approximately 37% of the market share (Day et al. 2010; Kim et al. 2011; Ponce et al. 2015). While comparable data are not available for the South African orthopaedic market, a similar trend can be expected due to the global uptake of RTSA and a growing elderly population in the country (StatsSA 2017).

The uptake of RTSA has occurred despite several complications that can impact long-term success. Some of these include intra- and extra-articular impingement; joint dislocation; implant loosening; and abnormal muscle function, which can propagate muscle fatigue (Simovitch et al. 2007; Garberina and Williams 2008; Molé and Favard 2007; Walker et al. 2014). While these complications stem from different sources, they can all diminish the functional outcomes of the prosthesis and increase the likelihood of revision surgery, which place an increased burden on the patient and the health care system (Day et al. 2015).

Research groups (typically comprised of biomedical engineers and orthopaedic surgeons) have performed studies on the reverse shoulder using cadaveric shoulder models, mechanical testing rigs, and computer models (Petrillo et al. 2016). These studies have measured properties such as impingement-free range of motion, muscle moment arms, muscle forces, joint contact forces, implant micromotion, and implant stress-strain in order to understand the biomechanics of RTSA and evaluate the effect of modifying individual aspects of the implant design and placement. Medical device manufacturers have used this research to develop prostheses that diverge from Grammont's original design. Consequently, it is hypothesised that an optimised configuration of the prosthesis has yet to be determined and that it can be obtained by combining multiple modifications to the prosthesis configuration.

1.2 Aims and objectives

The aim of this thesis is to identify, and evaluate, an optimised configuration of RTSA. Aims 1 and 2 investigate the effect of modifying the prosthesis configuration on functional outcomes of the reverse shoulder in order to determine an optimised configuration. Subsequently, aim 3 evaluates the performance of this optimised configuration with respect to additional outcomes. The subsequent list provides details of these aims and their associated objectives.

Aim 1 Assess the effect of individual prosthesis configuration modifications on functional outcomes of the reverse shoulder.

Objectives:

1. Develop a biomechanical assessment framework to evaluate reverse shoulder function.
2. Establish a baseline of functional outcomes using a default configuration of the prosthesis.

3. Characterise the effect of each modified configuration on functional outcomes as beneficial, detrimental, or negligible, relative to the default configuration.[1]

Aim 2 Optimise functional outcomes of the reverse shoulder by combining prosthesis configuration modifications.

Objectives:

1. Establish a set of modified configurations through the systematic combination of the beneficial modifications identified in Aim 1.
2. Use the biomechanical assessment framework to characterise the effect of the modified configurations on reverse shoulder function as beneficial, detrimental, or negligible, relative to the default configuration.
3. Compare the effect of the modified configurations and identify a configuration that optimises functional outcomes.

Aim 3 Evaluate the performance of the optimised configuration by assessing additional outcomes.

Objectives:

1. Develop a protocol to predict muscle fatigue in the reverse shoulder. Use the protocol to compare the response of the default and optimised configurations to muscle fatigue.[2]
2. Use finite element analysis to compare the effect of the default and optimised configurations on micromotion at the bone-implant interface.

1.3 Layout

The layout of the thesis (Figure 1.1) is based on the aforementioned aims and objectives. Chapter 2 provides a review of the relevant literature. Chapter 3 describes the development of the biomechanical assessment framework and the establishment of baseline reverse shoulder function. Chapter 4 details the assessment of the individual modifications and the characterisation of the effect of each modification. This is followed by the assessment of systematically combined modifications, and the identification of an optimised prosthesis configuration in Chapter 5. Subsequently, the assessment of the performance of the optimised configuration with regards to muscle fatigue and micromotion at the bone-implant interface is provided in Chapters 6 and 7, respectively. Finally, Chapter 8 summarises the conclusions of the preceding chapters and provides recommendations for future studies.

[1] An aspect of this objective has been presented at the 2017 Orthopaedic Research Society Annual Meeting and is under review with the journal of Clinical Biomechanics.

[2] An aspect of this objective has been presented at the XXVI Congress of the International Society of Biomechanics.

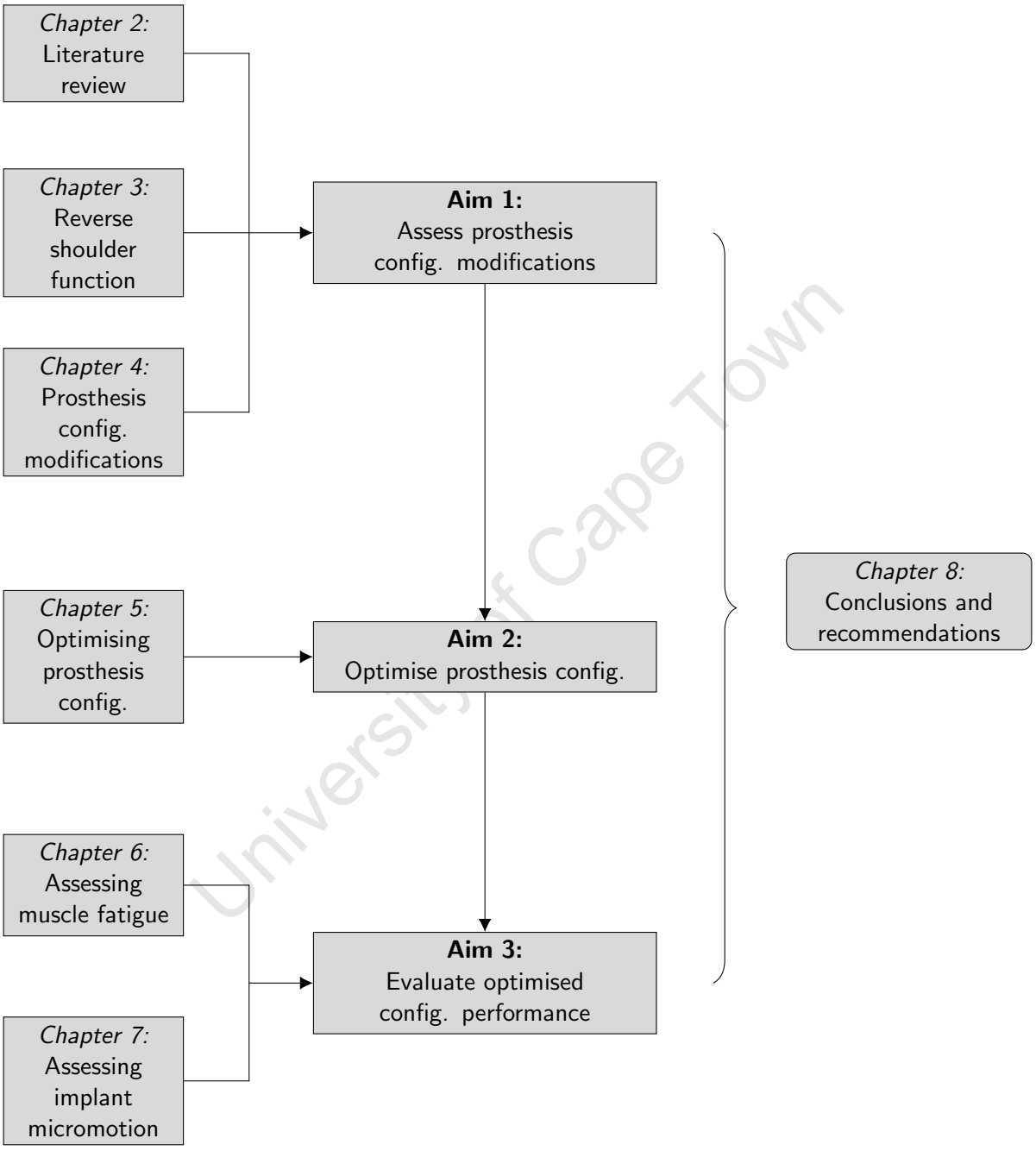

Figure 1.1 Thesis layout

Chapter 2

Literature Review

2.1 Introduction

The aim of this chapter is to provide an overview of shoulder anatomy, reverse total shoulder arthroplasty (RTSA), and the biomechanical research techniques that can be used to analyse prosthesis modifications. The review focuses on biomechanics as it is a technique that allows for an in-depth, *what-if* analysis of the effect of prosthesis modifications on a variety of functional outcomes, something that is not possible with other commonly used research methods (such as epidemiological and clinical cohort studies).

First, an explanation of the basic anatomical terminology used throughout the thesis is provided. Then, shoulder anatomy and function will summarised briefly (with detailed descriptions available in Appendix A). Subsequently, a description of the fundamentals of RTSA, the indications for the procedure, the complications that occur due to the procedure, and modifications to the original prosthesis design will be provided. Finally, a review of the physical and virtual research techniques that have been used to biomechanically evaluate the prosthesis will be presented.

2.2 Anatomical terminology

When discussing human anatomy, there are a number of general terms and reference geometries that are useful descriptors. These will be used extensively throughout this thesis, and Table 2.1 provides a list of commonly used directional terms.

Table 2.1 Directional terminology

Term	Definition
Superior/Inferior	Vertically towards/from the head of the body
Anterior/Posterior	Horizontally towards the front/back of the body
Medial/Lateral	Horizontally towards/from the midline of the body
Proximal/Distal	Towards/From a reference point

There are three mutually perpendicular planes of the human body (Figure 2.1). Firstly, the coronal plane is a vertical plane that divides the body into anterior and posterior portions. Secondly, the sagittal plane is a vertical plane that divides the body into left and right sides. Thirdly, the transverse plane is a horizontal plane that divides the body into upper and lower parts. From these body planes, three axes can be defined: the superioinferior axis (a vertical axis perpendicular to the transverse plane), the anteroposterior axis (a horizontal axis perpendicular to the coronal plane), and the mediolateral axis (a horizontal axis perpendicular to the sagittal plane).

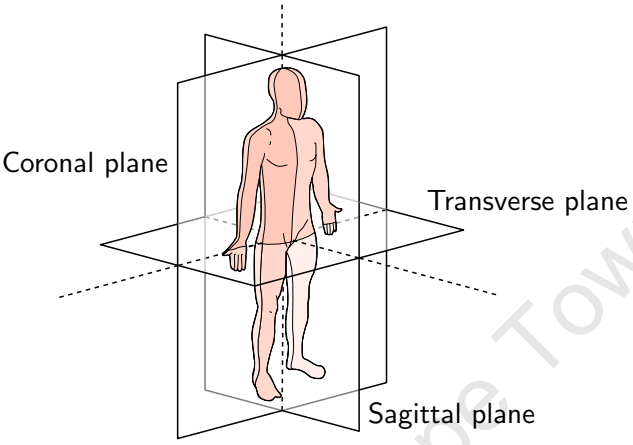

Figure 2.1 The anatomical planes of the human body

2.3 Shoulder anatomy and function

The shoulder consists of the clavicle, scapula, and humerus bones; which are connected via a series of joints that enable movement of the upper arm. This movement is driven by the articulation of the glenohumeral joint and the activation of the surrounding muscles and ligaments. The standardised motions of the upper arm (Figure 2.2) are abduction-adduction, flexion-extension, and internal-external rotation, and combinations of these motions can produce activities of daily living. A more detailed description of shoulder anatomy and function can be found in Appendix A.

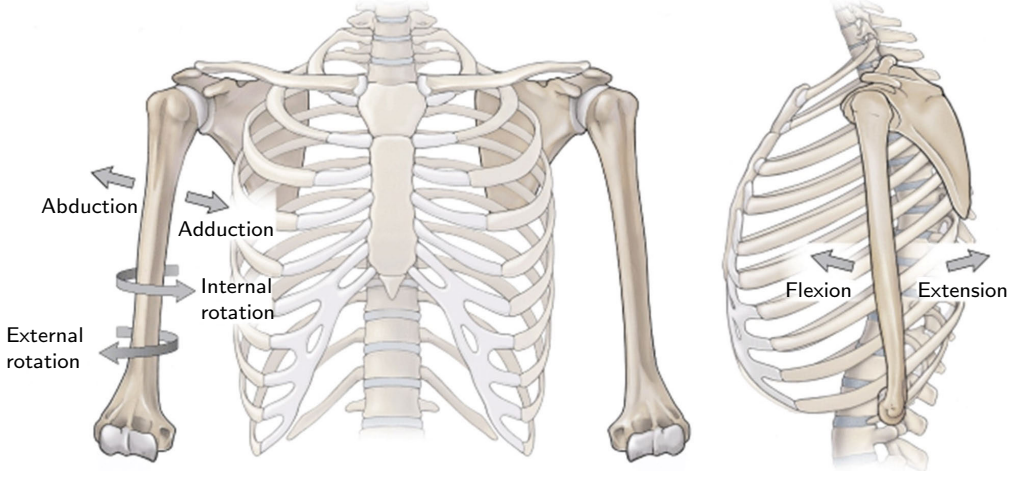

Figure 2.2 The shoulder joint and its standardised humeral motions (Morton et al. 2011)

2.4 Reverse total shoulder arthroplasty

The first successful RTSA design was devised by French surgeon Paul Grammont in the 1980s (Grammont and Baulot 1993). The prosthesis addressed the failings of both the unconstrained total shoulder arthroplasty and constrained ball-and-socket arthroplasty to treat cuff tear arthropathy (CTA), or a massive rotator cuff tear in the presence of osteoarthritis (Sirveaux et al. 2004; Frankle et al. 2005; Boileau et al. 2006). Unconstrained prostheses were unable to elevate the limb due to an unstable centre of rotation caused by the lack of a rotator cuff, and constrained prostheses were unable to provide satisfactory function and experienced excessive stress at the interface between the bone and the prosthesis (Post et al. 1980; Lettin et al. 1982; Broström et al. 1992; Edwards et al. 2002). A Grammont-style, semi-constrained ball-and-socket prosthesis (Figure 2.3) uses prosthetic components to reverse the orientation of the glenohumeral joint. The head of the humerus is resected (using a non-anatomic resection angle of 155°) and replaced by a polyethylene humeral cup. The cup is anchored to the humerus using a metallic stem that is inserted into the medullary cavity. The glenoid fossa of the scapula is reamed to subchondral bone and a metallic hemisphere (commonly referred to as a glenosphere) is fixed to the glenoid. The hemispherical glenosphere, with no neck, is anchored to the scapula using a baseplate with a metallic central peg and a series of screws. The baseplate is commonly referred to as the metaglene.

Figure 2.3 The Delta III prosthesis and its constitutive components (Boileau et al. 2005)

These changes to the glenohumeral joint lower the position of the humerus relative to the acromion and medialise the centre of rotation (Figure 2.4). In doing so, the moment arms of the deltoid are altered, allowing it to restore shoulder function (Boileau et al. 2005). Additionally, as the glenosphere has no neck, the centre of rotation is located at the bone-implant interface. Consequently, any torque which could be produced by the glenohumeral joint contact force is mitigated as

there is no moment arm between the centre of rotation and the reamed glenoid surface (Grammont and Baulot 1993; Boileau et al. 2005).

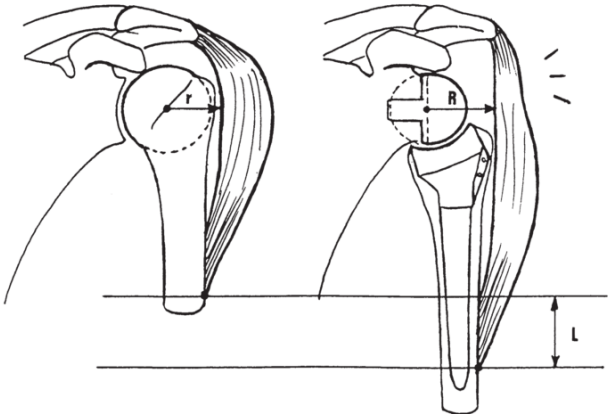

Figure 2.4 A comparison between the normal and reverse shoulders (Boileau et al. 2005). Note the medialised centre of rotation and lowered humerus

As a non-anatomic angle is used to resect the humeral head, the origin of the long head of the biceps and the insertion of the supraspinatus (if present) are removed and these muscles are typically not reattached. Additionally, due to CTA and the massive cuff tear, it is common for the infraspinatus and subscapularis to be irreparably damaged and are resected. Therefore, in worst-case scenarios, the teres minor is the only intact rotator cuff muscle after the surgery. However, most surgeons will attempt to preserve and repair any remnants these muscles if possible.

2.4.1 Indications

As mentioned previously, RTSA was first prescribed for patients with CTA or a massive rotator cuff tear in the presence of osteoarthritis. CTA is a type of degenerative osteoarthritis (Figure 2.5) that develops after a tear to the rotator cuff occurs and goes untreated (Neer et al. 1983). RTSA showed good clinical outcomes for these patients (Sirveaux et al. 2004; Frankle et al. 2005; Boileau et al. 2006; Wall et al. 2007) and received approval for use in the USA by the Food and Drug Administration (FDA) in 2003. Consequently, the number of indications for RTSA has grown in recent years; it is being used to treat rotator cuff tears with pseudo-paralysis (with or without osteoarthritis), proximal humeral head fractures or non-unions, reconstructive surgery after tumour removal, and reimplantation after the removal of an infected shoulder arthroplasty (Werner et al. 2005; Wall et al. 2007; Cuff et al. 2008; Sanchez-Sotelo 2009). In addition, it is being used for the revision of failed total shoulder arthroplasty if the rotator cuff is deficient or if the components are unstable (Werner et al. 2005; Boileau et al. 2006; Levy et al. 2007). Due to these broadened indications, the patient demographic has expanded from elderly patients to patients younger than 65 years old (Ek et al. 2013). These patients would require decades of shoulder function and potentially may need to undergo multiple revision surgeries.

Figure 2.5 Superior migration of the humeral head due to CTA (Craig 2013)

2.4.2 Complications

Despite the early good clinical outcomes of RTSA, a number of mechanical and non-mechanical complications have been reported. The mechanical complications include impingement, dislocation, metaglene loosening, acromial stress fractures, abnormal muscle function, and osteolysis (Boileau et al. 2005; Simovitch et al. 2007; Garberina and Williams 2008; Molé and Favard 2007; Levy et al. 2013; Walker et al. 2014). The non-mechanical complications include intra- and post-operative infection and intra-operative fractures (Sanchez-Sotelo 2009). All these complications are a concern as they reduce the functional outcomes of the prosthesis and increase the likelihood of revision surgery (which is concerning for younger patients who may need multiple revision surgeries over time).

2.4.2.1 Impingement

Impingement is characterised by the abutment of the scapula with the humeral components or humerus due to the drastic changes made to the glenohumeral joint during the surgery. As can be seen in Figure 2.6(a), impingement is commonly identified between the infraglenoid tubercle of scapula and the medial portion of the polyethylene humeral cup when the arm is adducted (Sirveaux et al. 2004; Nyffeler et al. 2004; Simovitch et al. 2007).

This type of intra-articular impingement (often referred to as scapular notching) can cause erosion of the scapular neck and wear the polyethylene humeral cup (Figure 2.6(b)) thereby destabilising the glenoid components by exposing the screws used to anchor the glenosphere to the scapula (Nicholson et al. 2011). Farshad and Gerber (2010) have suggested that scapular notching is the most common RTSA complication due to its increasing incidence over the functional life of the prosthesis. In addition, a study by Melis et al. (2011) found that, in a cohort of 68 shoulders, 60 (88%) showed signs of a notch after an eight to 12-year follow-up period.

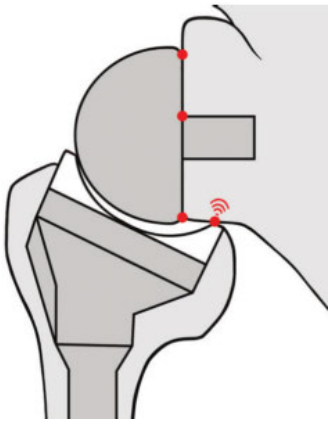

(a) Intra-articular impingement (Simovitch et al. 2007)

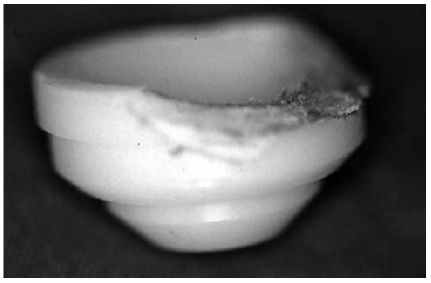

(b) Humeral cup wear (Boileau et al. 2005)

Figure 2.6 Intra-articular impingement and its effect on the humeral cup

In conjunction with scapular notching, the potential for extra-articular impingement has been identified recently (Kontaxis et al. 2017). This type of impingement is characterised by contact of the greater tuberosity of the humeral head with either the acromion or coracoid process when the arm is abducted (Figure 2.7).

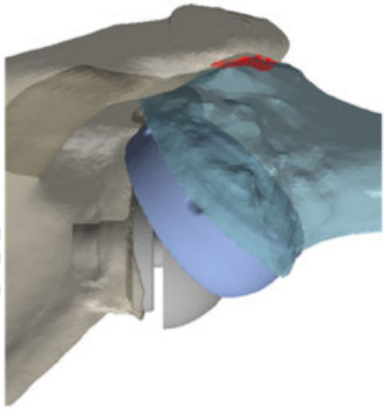

Figure 2.7 An example of extra-articular impingement between the greater tuberosity and the acromion (highlighted in red) when the arm is abducted (Kontaxis et al. 2017)

The impact of impingement on the patient is debated. Some authors believe that it does not impact shoulder function (Boileau et al. 2005; Lévigne et al. 2011), others have found a relationship between impingement (predominately due to progressive notch development) and a functional decline in the deltoid (Sirveaux et al. 2004; Simovitch et al. 2007). However, it is generally accepted that notching compromises the longevity of the prosthesis due to erosion of the tubercle (Nicholson et al. 2011) and humeral cup wear.

Complication source: Intra-articular contact between the humeral cup and the scapula (infraglenoid tubercle), or extra-articular contact between the greater tuberosity and the scapula (acromion or coracoid process).

2.4.2.2 Dislocation

Due to the semi-constrained nature of the prosthesis, dislocation of the joint is possible (Figure 2.8). This can occur due to joint instability as a result of incorrect placement of the prosthetic components and insufficient tensioning of the deltoid (Werner et al. 2005; Garberina and Williams 2008). Wall et al. (2007), at a 40-month mean follow-up, found that a 7.5% prevalence rate of dislocation, and Gallo et al. (2011) reported a 15.8% prevalence of joint instability within the first 6 months of the surgery. The treatment of joint dislocation requires revision surgery (Edwards et al. 2009).

Complication source: Insufficient deltoid tension.

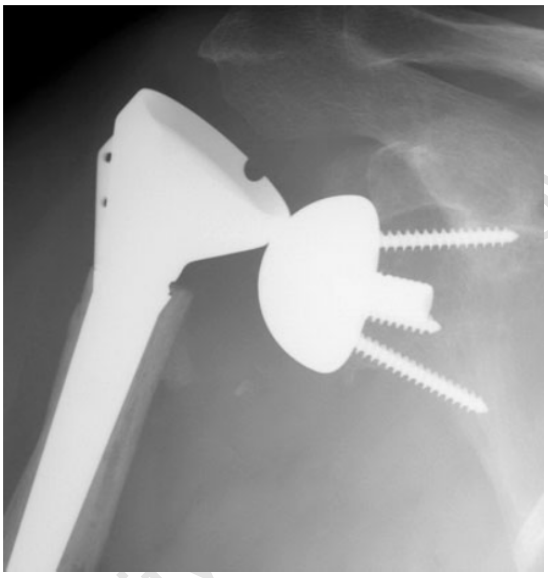

Figure 2.8 Radiograph of a dislocated prosthesis (Sanchez-Sotelo 2009)

2.4.2.3 Metaglene loosening

Poor fixation of the metaglene on the reamed glenoid surface can result in the loosening of the metaglene (Molé and Favard 2007; Gerber et al. 2009). If micromotion between the prosthetic components and the surrounding bone is in the range of 28 to 150 micrometres (μm), satisfactory osseointegration cannot be achieved (Favre et al. 2011). Molé and Favard (2007) found a 4.1% prevalence of metaglene loosening after a 2-year follow-up. The suggested treatment method for this complication involves multiple revision surgeries and the use of bone grafts to provide sufficient surface area for fixation (Gerber et al. 2009).

Complication source: Improper fixation of the implant components (either due to unsatisfactory placement of the components or due to scapular notching).

2.4.2.4 Acromial stress fractures

Acromial stress fractures have recently become recognised as an RTSA complication and is believed to be related to excessive deltoid stress (Hamid et al. 2011; Levy et al. 2013). Deltoid stress can cause acromial stress that exceeds the bone's capacity for repair thereby repeatedly damaging the bone (Pattin et al. 1996; Pepper et al. 2006). It has a prevalence rate of between 0.8% and 7.2% and typically occurs within 10 months of the surgery (Levy et al. 2013). The location of the stress fractures have been defined by Levy et al. (2013) and can extend from the acromion to the scapula spine. Both operative and non-operative treatment methods have been proposed, with the latter limiting functional outcomes.

Complication source: Excessive deltoid tension.

2.4.2.5 Abnormal deltoid function

Post-surgical abnormal deltoid function has been observed by Walker et al. (2014). In their electromyographic (EMG) analysis of reverse shoulders, they noted an increase in deltoid and upper trapezius activity during load-bearing abduction and forward flexion. In comparison to normal shoulders, the reverse shoulders required increased activity to perform a diminished range of motion. These observations may be attributed to incorrect placement of the prosthetic components, which can over- or under-tension the deltoid and may lead to the early onset of fatigue during prolonged or repeated activities.

Complication source: Incorrect deltoid tension (either insufficient or excessive).

2.4.2.6 Osteolysis

Osteolysis is characterised by the destruction of bone tissue and has been connected to the release of debris into the body due to progressive polyethylene component wear (Ingham and Fisher 2005). In RTSA, osteolysis can be predominately attributed to the wear of the humeral cup (Figure 2.6(b)) due to scapular notching (Boileau et al. 2005). However, debris released via long-term mechanical wear of the humeral cup socket by the glenosphere may also propagate osteolysis (Ribeiro et al. 2011; Vaupel et al. 2012).

Complication source: Progressive wear of the polyethylene humeral cup.

2.4.3 Prosthesis modifications

With RTSA seeing increased use due to good preliminary clinical outcomes and FDA approval, a number of modifications to the Grammont-style prosthesis have been proposed to address the associated complications in order to extend the functional life of the prosthesis and minimise the need for revision surgery. Modifications have been made to the design and configuration of the prosthesis. These have had varying degrees of success and have biomechanical trade-offs that need to be taken into consideration when deciding if they should be implemented.

2.4.3.1 Glenosphere lateralisation

Lateralisation of the glenosphere translates the centre of rotation of the joint away from the bone-implant interface (Figure 2.9). Lateralisation has been achieved by inserting a spacer between the metaglene and glenosphere or by increasing the arc of the sphere.

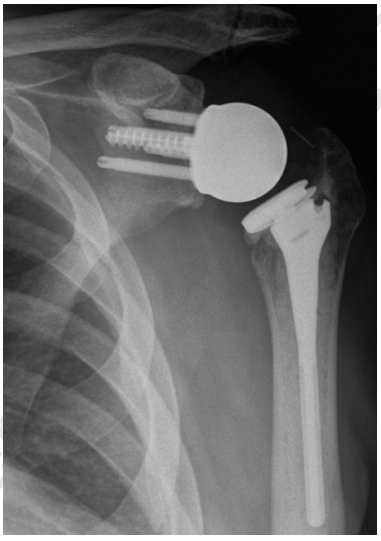

Figure 2.9 Radiograph of a lateralised prosthesis (Cuff et al. 2008). This prosthesis, the Reverse Shoulder Prosthesis (Encore Medical, TX, USA, (Encore-Medical 2008)) makes use of a two-thirds a sphere, rather than the standard Grammont-style hemisphere

Clinical studies by Frankle et al. (2005) and Cuff et al. (2008) found that lateralisation decreased scapular notching and improved functional outcome scores. Biomechanical studies have found a similar trend of results, with decreased impingement and increased joint stability (De Wilde et al. 2010; Costantini et al. 2015). However, these improvements were achieved at the expense of increased deltoid forces and increased glenoid component torque due to a lever arm created by translating the centre of rotation away from the bone-implant interface (Henninger et al. 2012b; Giles et al. 2015; Liou et al. 2017; Costantini et al. 2015).

In addition to these design modifications, lateralisation of the glenoid components can be obtained through bone grafts fixed to the reamed glenoid surface (Boileau et al. 2011). This has been implemented by the BIO-RSA prosthesis (Figure 2.10, Tornier, MN, USA,Tornier (2016)). In

this instance, the lateralisation improvements can be obtained without increasing glenoid component torque as the centre of rotation of the joint is located at the interface between the glenosphere and the bone graft.

Figure 2.10 BIO-RSA prosthesis (Tornier 2016). Note that the centre of rotation (red dot) is in contact with the lateral surface of the bone graft

2.4.3.2 Glenosphere diameter

The diameter of the glenosphere varies between manufacturers and ranges from 32 mm to 53 mm (Langohr et al. 2015). Manufacturers generally offer two options, a small and a large diameter; for example, the Delta XTEND prosthesis (DePuy Synthes, IN, USA (DePuy-Synthes 2013)) provides 38 and 42 mm diameter glenospheres. A larger diameter glenosphere has been shown to decrease impingement during abduction and rotation (Chou et al. 2009; De Wilde et al. 2010; Virani et al. 2013; Berhouet et al. 2014b). However, this occurs at the expense of increased joint and deltoid muscle forces (Langohr et al. 2015) and can be surgically challenging (Berhouet et al. 2014b).

2.4.3.3 Glenosphere eccentricity

RTSA manufacturers initially recommended placement of the baseplate at the centre of the reamed glenoid (Kelly et al. 2008). As can be seen in Figure **??**, this can result in impingement when the arm is adducted. An investigation by Kelly et al. (2008) found that placement of the baseplate 12 mm inferior to the centre of the glenoid led to decreased rates of impingement (provided there was sufficient bone stock to adequately secure the inferior fixation screw). Research conducted by other authors (Simovitch et al. 2007; Chou et al. 2009; De Wilde et al. 2010; Mizuno et al. 2012) has confirmed that inferior translation has a beneficial impact on impingement. As such, manufacturers are either recommending inferior placement of the glenoid-based prosthesis (Figure 2.11(a)), or the use of implant-based eccentricity (Figure 2.11(b)) to achieve inferior placement without shifting the metaglene. In addition to the improvements to range of motion, Clouthier et al. (2013) found that

inferior glenosphere placement can increase joint stability by up to 30%. It should also be noted that other eccentric placements of the glenosphere, such as posterior or anterior translations are possible, but have not been investigated yet.

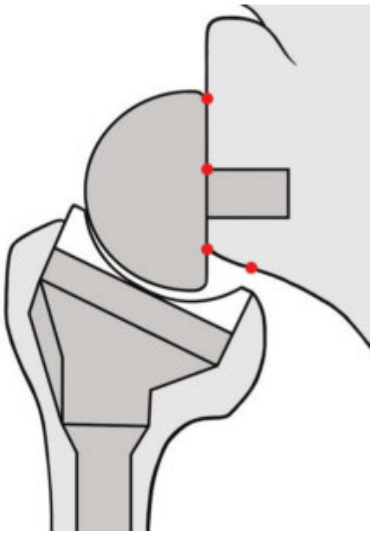

(a) Inferior glenosphere placement (Simovitch et al. 2007)

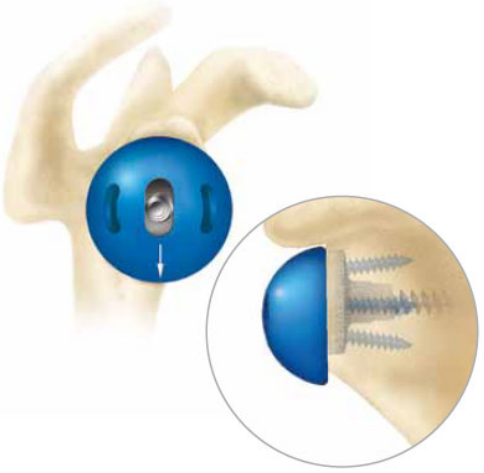

(b) Implant-based eccentricity (Zimmer-Biomet 2015)

Figure 2.11 The different techniques used to achieve glenosphere eccentricity: (a) inferior placement of the metaglene during the surgery and (b) implant-based inferior translation of the glenosphere which preserves typical metaglene placement

2.4.3.4 Glenosphere inclination angle

The inclination angle of the glenosphere can be modified by changing the angle at which the glenoid fossa is reamed. Superiorly tilting the glenosphere is commonly regarded as disadvantageous as it can induce a *rocking horse effect* due to an unbalanced load distribution between the superior and inferior fixation screws (Gutiérrez et al. 2011). Whereas, inferiorly tilting the glenosphere has the potential to decrease impingement and improve joint stability (Nyffeler et al. 2005; De Wilde et al. 2010; Gutiérrez et al. 2007). However, in a clincial follow-up by Edwards et al. (2012), inferior tilt did not reduce the radiographic incidence of scapular notching. In addition, recent cadaveric and finite element studies (Chae et al. 2015; Chae et al. 2016) have raised concerns regarding the increased likelihood of metaglene loosening when an inferior tilt is employed due to increased micromotion. Therefore, current recommendations suggest using a conservative neutral inclination angle (0 ° tilt) during the reaming process, especially when used in conjunction with glenosphere eccentricity (Gutiérrez et al. 2011; Chae et al. 2015; Chae et al. 2016).

2.4.3.5 Humeral stem neck-shaft angle

The Grammont-style prosthesis uses a neck-shaft angle of 155°. This non-anatomic angle helped to change deltoid biomechanics and restore shoulder function. However, this neck-shaft angle can

result in scapular notching and, consequently, the different neck-shaft angles have been employed by some manufacturers. For example, the Comprehensive Reverse Shoulder System (Biomet, IN, USA, Zimmer-Biomet (2015)) uses a 135° neck-shaft angle (Figure 2.12), and the Aequalis Ascend Flex (Tornier (2017)) uses a 145° angle. Studies have found that this angle can greatly decrease the incidence of intra-articular impingement and scapular notching when the arm is adducted. A systematic review by Erickson et al. (2015) found that the rate of scapular notching decreased from 16.8% (with the 155° neck-shaft angle) to 2.8%, and a biomechanical study by Lädermann et al. (2015) found that adduction angle increased by 28°.

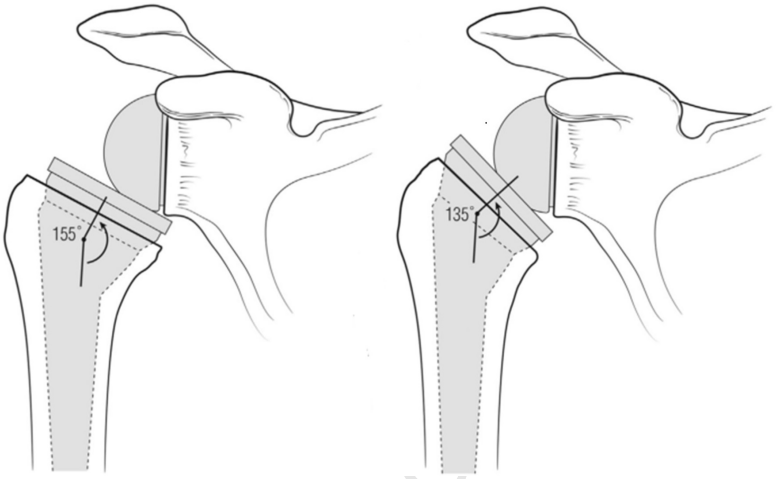

Figure 2.12 A comparison between 155° and 135° neck-shaft angles (Erickson et al. 2015)

However, this decrease in adduction impingement comes at a cost. Biomechanical studies found that a 135° neck-shaft angle increased impingement during abduction, decreased joint stability (especially during internal rotation), and increased joint contact stress. Lädermann et al. (2015) also reported an 18° decrease in abduction angle. Oh et al. (2014) reported that the force required for anterior dislocation significantly decreased, and Langohr et al. (2016) reported that peak contact stress increased from approximately 2.5 MPa (155° neck-shaft angle) to approximately 11 MPa.

2.4.3.6 Humeral head resection version

The version of the humeral head resection can be modified during the surgery. The humeral head can be resected using the native version of the humerus or using an anteverted or retroverted angle (Figure 2.13). A consensus regarding the correct version has not yet been obtained due to the effect of the modification on impingement, rotational capabilities, and joint stability. Some authors have suggested that a retroversion angle of 20° is an adequate compromise to improve range of motion and muscle function during standardised motions (Stephenson et al. 2011; Gulotta et al. 2012; Roche et al. 2013; Berton et al. 2015). Gulotta et al. (2012) found that this angle maximised internal rotation with the arm adducted, whilst limiting external rotation with the arm adducted and had no effect on external rotation with the arm abducted. Conversely, Favre et al. (2010) suggested

that retroversion had a negative effect on joint stability and that anterior stability can be improved when an anterversion angle of 20° is utilised. A recent study has postulated that the effect of the version angle on standardised motions might not correlate to a similar effect on activities of daily living, and that the native version angle can potentially maximise outcomes (Kontaxis et al. 2017).

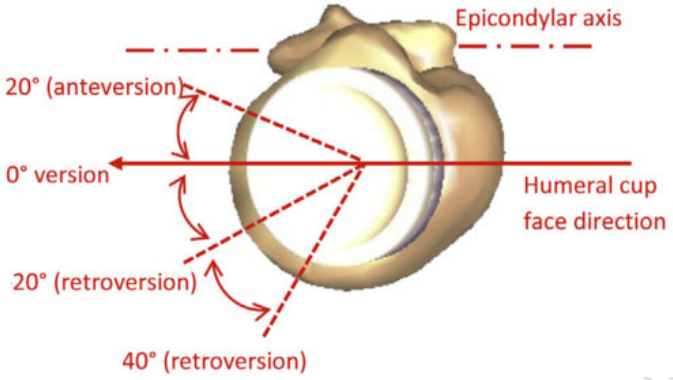

Figure 2.13 Different humeral head resection version angles (Berton et al. 2015). The 0° version is parallel with the epicondylar axis. Clockwise rotation of the humeral components results in anteversion and anti-clockwise rotation results in retroversion

2.4.3.7 Humeral tray type

The Grammont-style inlay tray utilises a single component for the stem and tray (Figure 2.3). Whereas, recent designs, like the Comprehensive Reverse Shoulder System (Zimmer-Biomet 2015), have opted to separate the tray from the stem thereby allowing the tray to placed onto the resected humeral head (Figure 2.14). The onlay design, when used in conjunction with a 135° neck-shaft angle, caters for conversion from TSA to RTSA without the need for removal of the humeral stem and further humeral head resection. In addition, the onlay design enables eccentric placement of the humeral tray, which is discussed the subsequent section.

Figure 2.14 Onlay humeral tray design (Zimmer-Biomet 2015). Note that the stem and tray are separate components

2.4.3.8 Humeral tray placement

The onlay humeral tray design, due to the separation of the tray from the humeral stem, enables eccentric placement of the tray on the resected humeral head. Giles et al. (2015) and Liou et al. (2017) have assessed the effect of tray medialisation, which resulted in lateralisation of the

humerus. These biomechanical studies found that deltoid muscle force decreased, and that joint compression increased thereby increasing joint stability. However, Lädermann et al. (2015), found that tray medialisation increased impingement when the arm was abducted. Berhouet et al. (2014a) investigated the effect of various humeral tray offsets on impingement and muscle moment arms. Like Lädermann et al. (2015), they found that tray placement had no affect on impingement with arm adducted but did effect range of motion with the arm abducted. They found that a laterally or posteriorly offset tray (which shifted the humerus medially and anteriorly, respectively) led to the best outcomes for range of motion during abduction, scapular plane elevation, and rotation. Additionally, they found that, if preserved during surgery, the subscapularis moment arms during rotation were improved using a posterior offset, and that the infraspinatus and teres minor moment arms were improved using an anterior offset. These results highlight the trade-off between improving impingement and improving muscle function due to this modification.

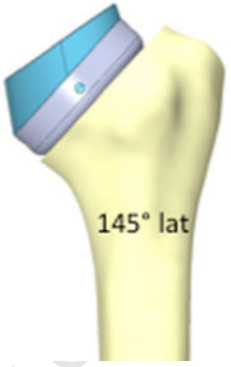

Figure 2.15 Humeral tray lateralisation using an onlay design (Lädermann et al. 2015). Note that the tray must be medialised to lateralise the humerus

2.4.3.9 Humeral tray depth

Modifying humeral tray depth changes the position of the humerus relative to the scapula by altering the extent to which the humeral components protrude from the resected humeral head. In doing so, impingement characteristics and deltoid function can be improved slightly. Henninger et al. (2012a) found that increasing humeral cup thickness increased deltoid tension and decreased impingement with the arm adducted. Giles et al. (2015) found that the force required to abduct the shoulder increased when a spacer was added to increase humeral cup thickness.

2.4.3.10 Humeral cup depth

Humeral cup depth has been found to effect joint stability, with Gutiérrez et al. (2008a) finding that cup depth was the second most important factor (behind joint compression) in providing joint stability. Increasing cup depth increases joint stability until a maximum stability is obtained when the depth is equal to the radius of the glenosphere thereby replicating the constrained prosthesis

(Kontaxis and Johnson 2009). However, an increase in depth is simultaneously associated with an increase in impingement (De Wilde et al. 2010). The opposite relationship has also been observed; a decrease in cup depth decreased both impingement and joint stability. Therefore, Kontaxis and Johnson (2009) proposed that the design of the cup should optimise stability whilst minimising impingement.

2.4.3.11 Prosthesis modifications summary

The effects of the prosthesis modifications on RTSA function that were documented throughout this section are summarised in Table 2.2. From this table it is evident that all the modifications have some form of biomechanical trade-off that must be taken into consideration.

Table 2.2 Summary of the documented effects of the prosthesis modifications on RTSA function. A $\wedge$ indicates a beneficial impact and a $\vee$ indicates a detrimental impact.
Imp: Impingement. DF: Deltoid function. JS: Joint stability

Location	Modification		Imp	DF	JS
Glenosphere	Lateralisation[1]		$\wedge$	$\vee$	$\wedge$
	Diameter	Increase (large)	$\wedge$	$\vee$	$\vee$
	Eccentricity	Inferior placement	$\wedge$		$\wedge$
	Inclination angle	Superior tilt			$\vee$
		Inferior tilt[2]	$\wedge$		
Humerus	Stem neck-shaft angle	135°	$\wedge$	$\vee$	$\vee$
	Head resection version	Anteversion	$\vee$		$\wedge$
		Retroversion	$\wedge$		
	Tray placement	Lateralisation	$\wedge$		
		Medialisation	$\vee$	$\wedge$	$\wedge$
	Tray depth	Increase	$\wedge$	$\vee$	
	Cup depth	Increase	$\vee$		$\wedge$

[1] Lateralisation via a spacer introduces a bending moment which increases glenosphere torque.

[2] Increased micromotion at the glenoid bone-implant interface.

The prosthesis designs identified during the literature review are summarised in Table 2.3. This table highlights the fundamental design parameters and some of the prosthesis modifications that can be implemented by an orthopaedic surgeon using one of these implants. For example, a surgeon using the Zimmer-Biomet prosthesis could opt to inferiorly translate the glenosphere using implant-based eccentricity. Conversely, a surgeon using the Delta XTEND prosthesis would have to inferiorly translate the glenosphere by inferiorly placing the metaglene. Note that, while this table is not a comprehensive list of prosthesis designs currently on the market, majority of prostheses are variations on these fundamental parameters.

Table 2.3 Summary of the prosthesis designs identified during the literature review.
GS: Glenosphere. Dia: Diameter (in mm). Lat: Lateralisation. Ecc: Eccentricity. NS: Neck-shaft

Manufacturer	GS Dia.	GS Lat.	GS Ecc.	Stem type	NS angle
Arthrex	36/39/42	Inc. arc[1]	Implant-based	Onlay	135°/155°
Encore Medical	32/36/40	Inc. arc		Inlay	150°
Delta XTEND	38/42			Inlay	155°
Tornier[2]	36/42	Inc. arc/bony		Onlay	145°
Zimmer-Biomet	36/41		Implant-based	Onlay	135°

[1] Inc. arc: lateralisation achieved by increasing the arc of the glenosphere.

[2] Aequalis Ascend Flex: increased arc. BIO-RSA: bony lateralisation.

2.5 Research techniques

The assessment of RTSA outcome measures can be performed retrospectively or prospectively. Retrospective studies take the form of clinical studies that investigate patient outcomes at some follow-up period. These studies typically use radiographs, shoulder scores (such as the American Shoulder and Elbow Surgeons score, the Constant-Murley score, and the disabilities of the arm, shoulder and hand score (Wylie 2014)) and electromyography to measure outcomes.

On the other hand, prospective studies take the form of biomechanical studies that evaluate outcome measures using either physical or virtual techniques. Physical techniques utilise cadaveric shoulders, surrogate bone specimens such as Sawbones (Pacific Research Laboratories, Vashon, WA), or mechanical testing rigs to approximate outcomes. Virtual techniques utilise musculoskeletal or finite element models to simulate the shoulder and predict outcomes. Given the nature of this thesis, an investigation into, and summary of, these biomechanical research techniques was performed. This was predominately based upon a systematic review of RTSA research models conducted by Petrillo et al. (2016). Note that any of the subsequently listed research techniques that were not covered by Petrillo et al. (2016) will be indicated as such.

2.5.1 Cadaveric shoulder models

2.5.1.1 Hospital for Special Surgery (HSS) model

The HSS model, which was not included in Petrillo et al. (2016), has been used to measure muscle forces during abduction (Gulotta et al. 2012). The model, as shown in Figure 2.16, clamped the scapula to the test rig and attached the humerus (which had its distal epiphysis removed) to a weighted guide rail. A pulley-cable system connected the muscles to motors that were actuated by a control system. A motion-capture system used marker triads on the humerus and overhead plate to track glenohumeral joint position. The control system regulated the motors based on a muscle loading profile that was estimated by a computational model of the shoulder. The load cells then

recorded the muscle forces and an optimisation algorithm determined the muscle forces required to maintain static equilibrium of the humerus at a given elevation angle.

Outcome measure: Muscle forces.

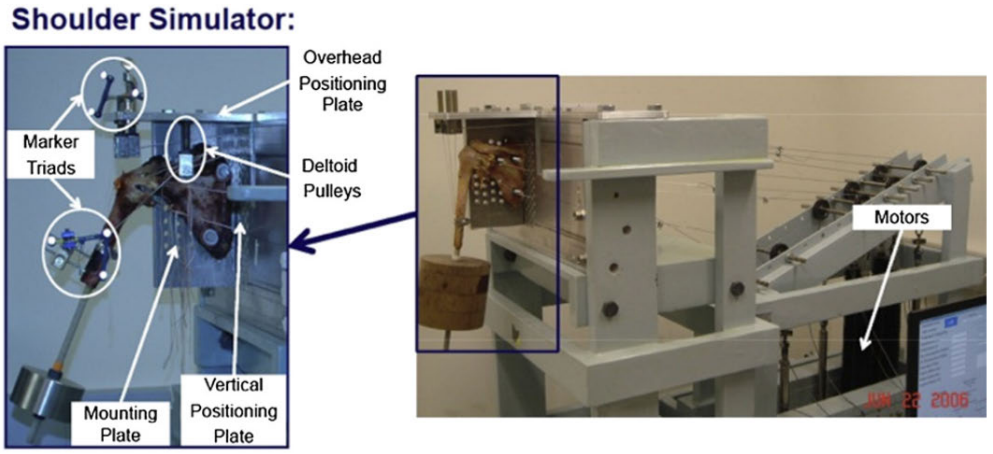

Figure 2.16 HSS cadaveric shoulder model (Gulotta et al. 2012)

2.5.1.2 New York University (NYU) model

The NYU model (Kwon et al. 2010) is divided into two components. The first component attached a fresh-frozen cadaveric shoulder (which had undergone an RTSA) to a rig that used two motors and a guidance rod to reproduce elevation of the shoulder from 10° to 120° (Figure 2.17(a)). A video recording of the shoulder elevation was made, and the compressive and shear joint contact forces were calculated from free body diagrams superimposed on top of the recorded images.

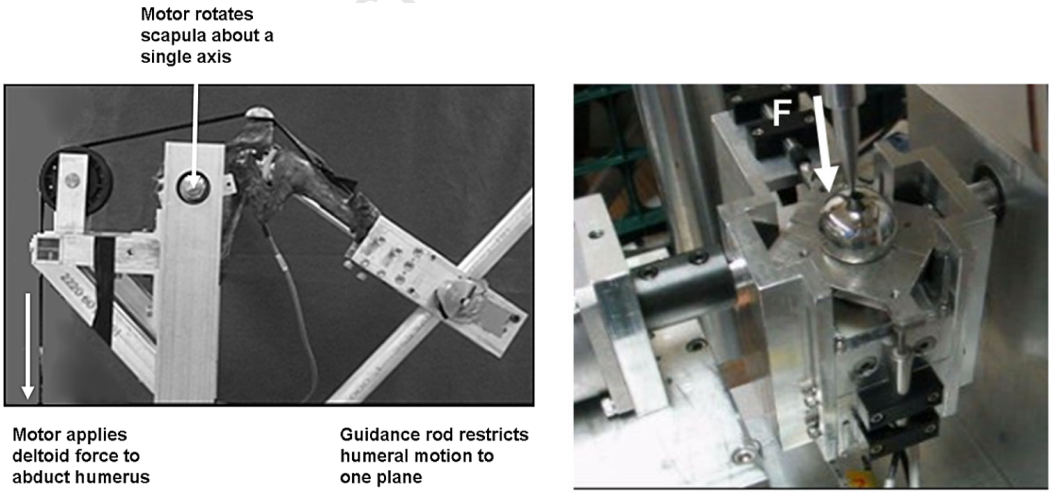

(a) Joint force rig (b) Micromotion rig

Figure 2.17 NYU cadaveric shoulder model (Kwon et al. 2010)

The second component of the model utilised the scapula and glenoid prostheses (which were extracted from the first component and separated from the humerus and surrounding soft tissue)

in a different rig (Figure 2.17(b)). This rig applied cyclical force (based on the forces calculated in the first component) to the glenosphere and used a series of sensors to measure micromotion. After 10,000 cycles the cumulative micromotion and micromotion of the final cycle were measured for 30°, 60°, 90°, and 120° of shoulder elevation.

Outcome measure: Joint contact forces and micromotion.

2.5.1.3 University of California, Los Angeles (UCLA) model

The UCLA model (Figure 2.18) has been used to measure the impingement during rotation (Stephenson et al. 2011). After the joint replacement, the medial border of the scapula (rotated to be perpendicular to the floor) was fixed to the rig and loads were applied to the muscles (deltoid, pectoralis major and teres major) using weights. Rotations were then applied at varying levels of abduction until impingement was visually observed and measured using a goniometer.

Outcome measure: Impingement.

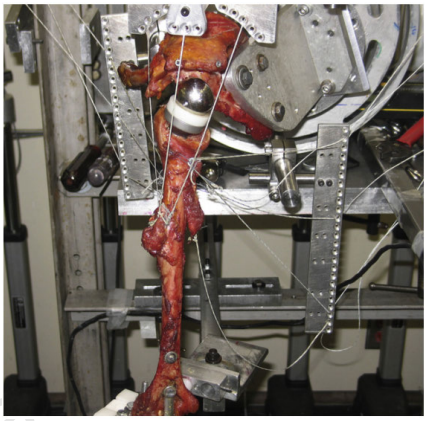

Figure 2.18 UCLA cadaveric shoulder model (Stephenson et al. 2011)

2.5.1.4 University of Melbourne model

The University of Melbourne model has been used to calculate muscle moment arms and muscle and joint contact forces (Ackland et al. 2010; Ackland et al. 2011; Ackland et al. 2012). The model replicated six DOF glenohumeral motion during abduction and flexion using a rotatory frame and a series of linear actuators connected to the muscles via cable-pulley systems (Figure 2.19). The cadaveric shoulder (which had undergone an RTSA) was attached to the frame using a potting block, and motion was tracked using a motion-capture system and retro-reflective marker triads attached to the scapula and humerus. Muscle tension was maintained during the motions by freely hanging weights that weighed 10 Newtons (N) and were passed through the pulleys.

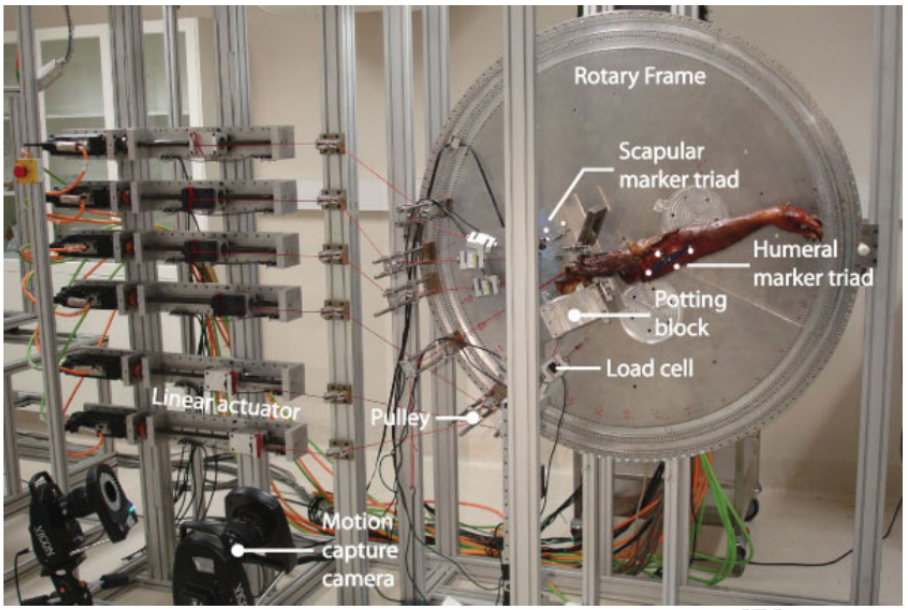

Figure 2.19 University of Melbourne cadaveric shoulder model (Ackland et al. 2011)

The vertical displacement of the 10 N weights (measured using the motion-capture system and markers placed on the weights) was used to calculate muscle moment arms. The load cells connected to each linear actuator system were used to measure the forces applied, and the resultant joint contact force was measured using a universal force-moment sensor attached to the potting block.

Outcome measure: Centre of rotation, moment arms, muscle forces, and joint contact forces.

2.5.1.5 University of Utah model

The University of Utah model has been used to measure abduction angle, deltoid force and joint dislocation force during scapular plane elevation (Henninger et al. 2012a; Henninger et al. 2012b). After joint replacement, each fresh-frozen scapula was mounted to the 6 DOF rig in its anatomic orientation, which was measured from computed tomography (CT) data. The deltoid muscle was connected to pneumatic cylinders via pulley-cable systems and the remnant rotator cuff muscles were tensioned by freely hanging weights (Figure 2.20). Sensors were used to track the position of the cylinders and a control system ensured that a constant force was maintained across all the cylinders. During the motion, the cylinders extended and retracted in response to the change in the lines of action of the deltoid. Load cells connected to the pulley-cable systems measured deltoid force and tracking diodes placed at the distal humerus and ulna were used to measure the minimum abduction angle (which is analogous to impingement). After these tests were conducted, the force required to dislocate the joint (which is analogous to joint stability) was manually applied via a cable wound around the metaphysis of the humerus and measured using a load cell.

Outcome measure: Centre of rotation, impingement, muscle forces, and joint stability.

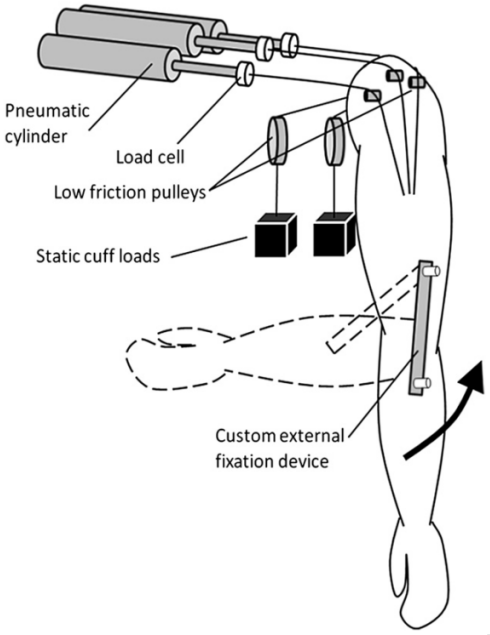

Figure 2.20 Schematic of the University of Utah cadaveric shoulder model (Henninger et al. 2012a)

2.5.2 Sawbones shoulder models

Sawbones shoulder models use a similar pulley-cable system as described previously. However, in this instance, the pulleys are attached directly to the bones at the muscle insertion site rather than the muscles themselves. An example of a Sawbones shoulder model given in Petrillo et al. (2016) is the Tampa model (Gutiérrez et al. 2007; Gutiérrez et al. 2008b). The model (Figure 2.21) was used to measure the location of the glenohumeral joint centre and estimate impingement characteristics during abduction. The scapula was clamped to the rig at its medial border and an electric goniometer was attached to the humerus via the rig, using a ring mounted to its distal end.

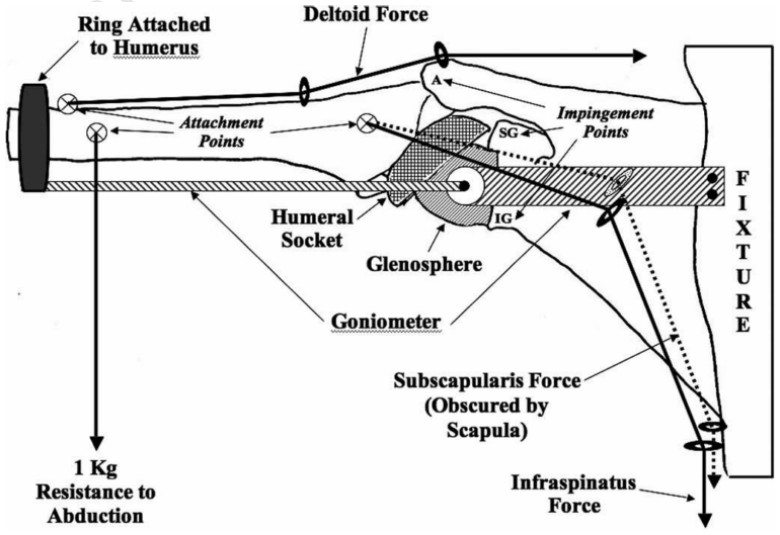

Figure 2.21 Tampa Sawbones shoulder model (Gutiérrez et al. 2007)

Cables were inserted at the muscle insert sites of the deltoid and the remnants of the infraspinatus and subscapularis. A 1 kg weight was attached at the end of the pulleys to maintain tension and an additional 1 kg weight was hung from the humerus to resist abduction. The goniometer was used to both control and measure the abduction range of motion and the glenohumeral joint centre and impingement were measured using video analysis.

Outcome measure: Centre of rotation and impingement.

2.5.3 Mechanical testing rigs

2.5.3.1 Royal Oak testing rig

The Royal Oak testing rig (Figure 2.22) was used to estimate wear of the polyethylene humeral cup using a converted hip simulator (Vaupel et al. 2012). The rig simulated physiologic conditions and produced sinusoidal loading profiles during simulated abduction and forward flexion. Every 250 000 cycles the rig switched from abduction to forward flexion loading profiles until 5 million cycles were obtained. Afterwards, gravimetric analysis of the humeral cup was used to characterise wear.

Outcome measure: Polyethylene wear.

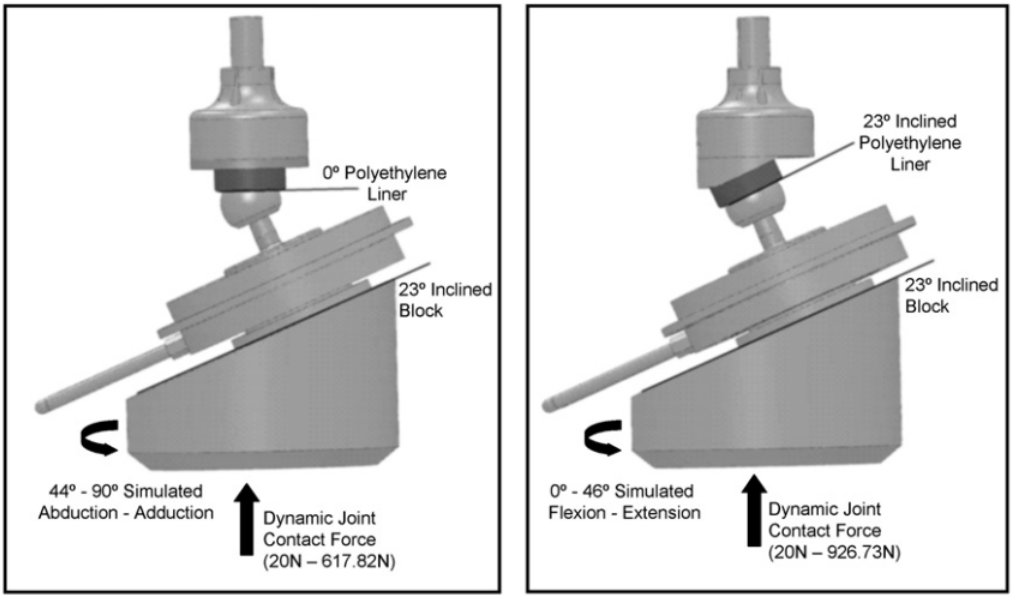

Figure 2.22 Royal Oak testing rig (Vaupel et al. 2012)

2.5.3.2 Tampa testing rig

The Tampa testing rig was used to assess joint stability by simulating dislocation and measuring the associated forces (Gutiérrez et al. 2008a). The glenoid and humeral components were attached to two separate movable platforms (Figure 2.23). The glenoid platform was free to translate along the Y-axis and weights were added to the platform to simulate joint compression. The horizontal platform was free to translate along the X-axis and was driven by a motor at a fixed rate. The

translation of the horizontal platform induced a shear force on the joint that progressively increased until the joint dislocated. The dislocation force was measured by a load cell and the platform translations were measured by displacement transducers.

Outcome measure: Joint stability.

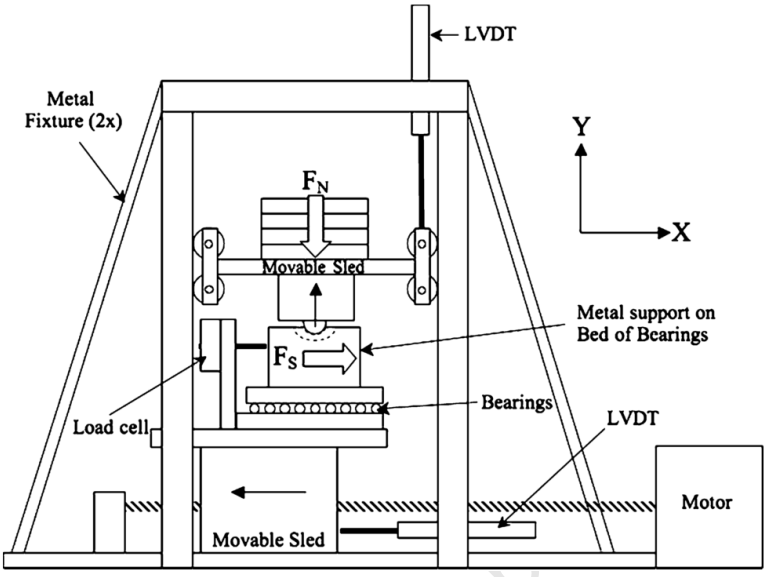

Figure 2.23 Tampa mechanical testing rig (Gutiérrez et al. 2008a)

2.5.3.3 University of Zurich testing rig

The University of Zurich testing rig was used to assess joint stability or implant micromotion (Favre et al. 2010; Favre et al. 2011). It functions in a similar manner to the Tampa testing rig, except for the addition of a third movable platform (Figure 2.24). In this instance, the rig uses two platforms to move the glenosphere in two orthogonal directions, thereby simulating medial to lateral and superior to inferior joint translations. A third platform is attached to the humeral components and allows for translation in the anterior to superior direction. Additionally, adjustable clamps were able to modify the version of the glenosphere and humeral tray. A freely hanging weight was attached to the medial to lateral platform to apply joint compression and the humeral platform was translated from a predefined resting position by a motor at a fixed rate. This translation induced a shear force and stability was estimated using a load-displacement curve recorded by the rig until dislocation occurred. On the other hand, implant micromotion was measured using displacement gauges and high resolution imaging.

Outcome measure: Joint stability and micromotion.

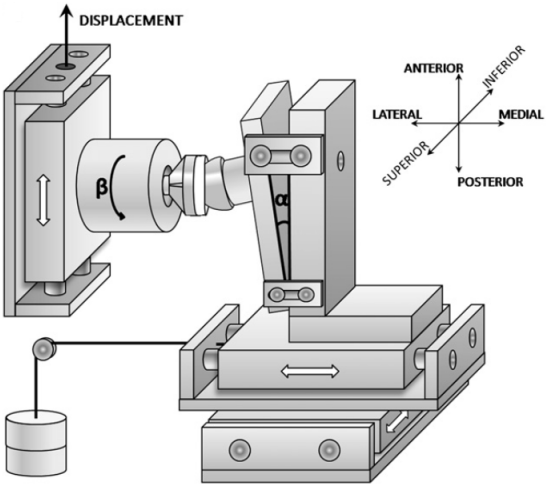

Figure 2.24 University of Zurich testing rig (Favre et al. 2010)

2.5.4 Musculoskeletal models

2.5.4.1 Berlin model

The Berlin 3D computer shoulder model has been used to measure the origin to insertion distance of the remnant rotator cuff muscles and estimate their associated moment arms (Herrmann et al. 2011). Fresh-frozen cadaveric shoulders underwent RTSA using a prosthesis replica constructed from polycarbonate resin. During the surgery the muscles surrounding the rotator cuff were removed to expose the rotator cuff. Radio-opaque markers were then placed at the origin and insertion of the muscles and CT scans of the shoulders were performed. As shown in Figure 2.25, the 3D geometries of the bones and prosthesis were reconstructed in AMIRA (Mercury Computer Systems, MA, USA) and aligned with the joint co-ordinate systems described by the International Society of Biomechanics (Wu et al. 2005). The location of the markers were digitised and used to evaluate the origin to insertion distance and muscle moment arms during simulated ranges of motion.

Outcome measure: Moment arms.

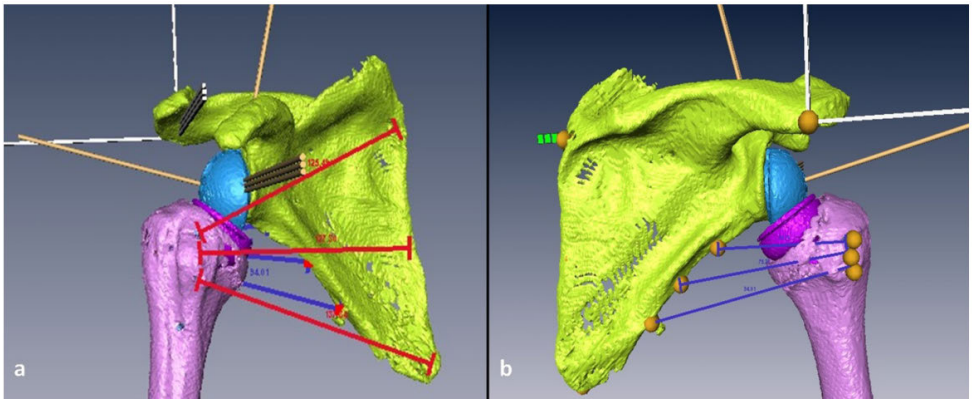

Figure 2.25 Berlin 3D computer shoulder model (Herrmann et al. 2011). The red and blue lines indicate the lines of action of the subscapularis and teres minor, respectively

2.5.4.2 Delft model

The Delft 3D computer shoulder and elbow model (DSEM), not included in Petrillo et al. (2016), has been used to measure the location of the glenohumeral joint centre, and estimate muscle and joint contact forces for different prosthesis configurations (Liou et al. 2017). The DSEM, which was originally developed to assess normal shoulder function (van der Helm 1994; Nikooyan et al. 2010), is a combination of a finite element model and an OpenSim musculoskeletal model (Stanford University, CA, USA, Delp et al. 2007). It models the bones of the upper extremity (thorax, clavicle, scapula, humerus, radius and ulna) as rigid elements, the muscles as force generating truss elements and the ligaments as passive truss elements. Virtual surgery was performed on the scapula and humerus, and, as shown in Figure 2.26, the prosthetic components were incorporated into the model. An inverse dynamics simulation, driven by motions applied to the bones and external loading profiles, calculates the muscle forces and a static optimisation process calculates joint contact forces.

Outcome measure: Centre of rotation, muscle forces, and joint contact forces.

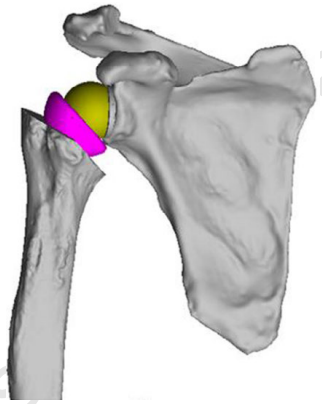

Figure 2.26 Delft 3D computer shoulder model (Liou et al. 2017). Note that the muscles and ligaments have been excluded from this representation of the model

2.5.4.3 Ghent model

The Ghent 2D computer shoulder model has been used to measure impingement during scapular plane elevation for different prosthesis configurations (De Wilde et al. 2010). The model utilises the data from 200 subjects to reconstruct the average shape (in the anteroposterior view) of the glenoid, infraglenoid tubercle and lateral scapular border (Figure 2.27). A virtual representation of the Delta III prosthesis was inserted into the model and, for various prosthesis configurations, the angle of impingement during arm adduction (notch angle) was measured.

Outcome measure: Impingement.

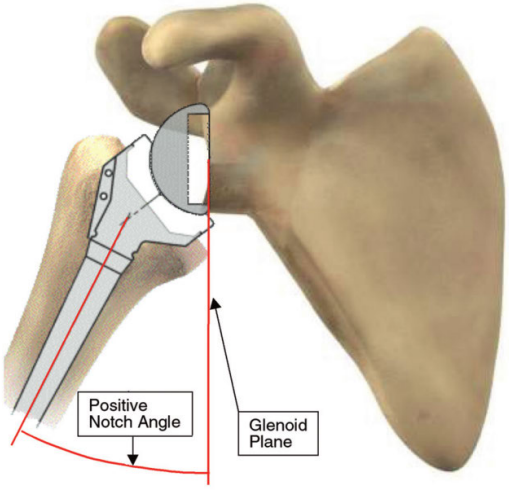

Figure 2.27 Ghent 2D computer shoulder model (De Wilde et al. 2010)

2.5.4.4 HSS computer model

The HSS 3D computer shoulder model has been used to measure impingement during rotation at various levels of scapular plane elevation (Gulotta et al. 2012). The model was developed from the 3D reconstructions of the scapula and humerus, which were sourced from CT scans. The bones were aligned with the ISB joint co-ordinate systems and underwent virtual RTSA (Figure 2.28). VisualNastran 4D software (MSC, CA, USA) was used to apply motion to the model and record incidences of prosthesis to bone, and bone to bone impingement.

Outcome measure: Impingement.

Figure 2.28 HSS 3D computer shoulder model (Gulotta et al. 2012)

2.5.4.5 Newcastle shoulder model

The Newcastle 3D computer shoulder model (NSM) has been used to predict muscle moment arms and forces, joint contact forces and impingement for different prosthesis configurations (Kontaxis and Johnson 2009; Berhouet et al. 2014a; Berton et al. 2015; Costantini et al. 2015). The NSM, originally

developed to assess normal shoulder function (Charlton and Johnson 2006), is a combination of SIMM (Motion Analysis Corporation, CA, USA) model and custom-made MATLAB (MathWorks, MA, USA) routines. It models the bones of the upper extremity and includes representations of 31 muscles and three ligaments. Virtual surgery was performed on the scapula and humerus and the prosthetic components were incorporated into the model (Figure 2.29). Motions can be applied to the SIMM component of the NSM to calculate muscle lengths and trajectories. These can then be used by an inverse dynamics protocol in MATLAB to minimise a physiological cost function and predict muscle and joint contact forces. Subsequently, joint stability can be estimated using a ratio between joint compression and shear. Additionally, components of the model have been used to establish a MATLAB-based algorithm that can predict incidences of prosthesis to bone, and bone to bone impingement.

Outcome measure: Centre of rotation, impingement, moment arms, muscle forces, joint contact forces, and joint stability.

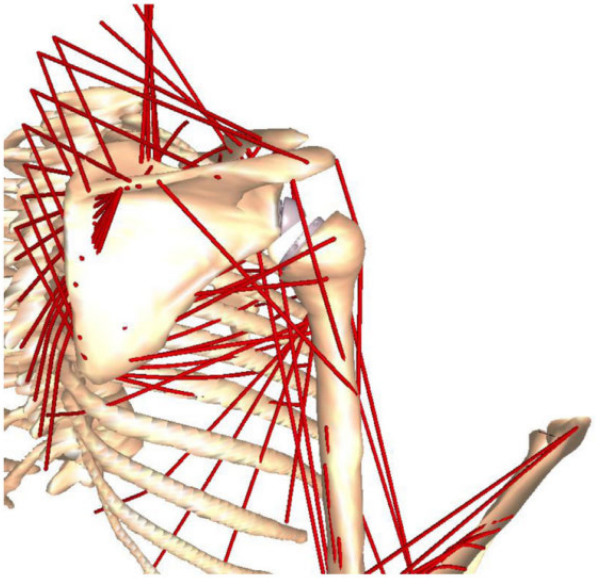

Figure 2.29 Newcastle 3D computer shoulder model (Berhouet et al. 2014a). Note that the red lines represent the muscles

2.5.4.6 State University of New York (SUNY) Upstate Medical University model

The SUNY 3D computer shoulder model has been used to assess optimal glenoid fixation (Sutton et al. 2010). The 3D geometry of the scapula from a cadaveric shoulder was reconstructed from a CT scan. A virtual RTSA was performed on the scapula and the changes in scapula bone volume and area at the reamed glenoid surface were measured for various reaming profiles using the SolidWorks (Dassault Systèmes, Velizy-Villacoublay, France) computer-aided design software.

Outcome measure: Bone volume.

2.5.4.7 Tampa computer model

The Tampa 3D computer shoulder model has been used to measure impingement and the location of glenohumeral joint centre of rotation for different prosthesis configurations (Gutiérrez et al. 2008b; Gutiérrez et al. 2009; Gutiérrez et al. 2011; Virani et al. 2013). The model uses a SolidWorks add-in, COSMOSMotion, to evaluate the 3D contact properties of a reverse shoulder during scapular plane elevation. The model consists of the prosthetic components, scapula (attached to a fixed frame) and humerus which were 3D reconstructed from the CT scans of Sawbones surrogates. COSMOSMotion applied the motion to the humerus and the simulation was stopped when contact was identified either inferiorly or superiorly. An example of superior impingement is shown in Figure 2.30.

Outcome measure: Centre of rotation and impingement.

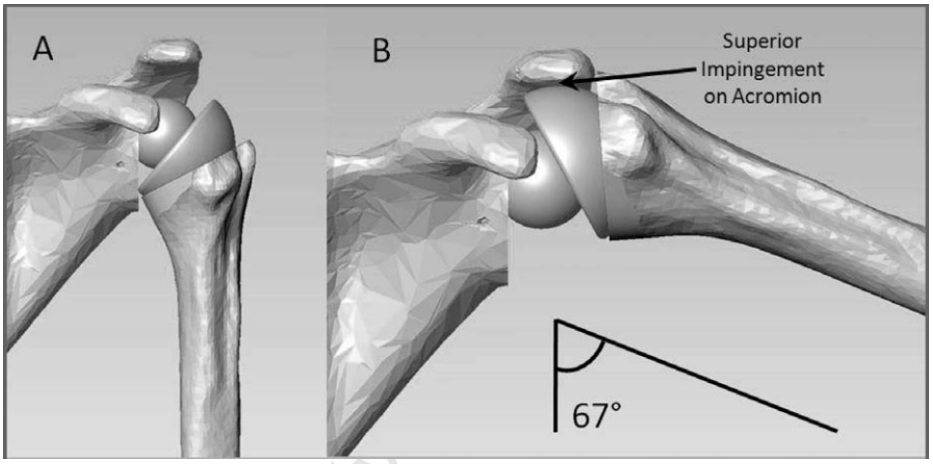

Figure 2.30 Tampa 3D computer shoulder model (Gutiérrez et al. 2009)

2.5.5 Finite element models

Studies that use finite element analysis (FEA) to assess RTSA outcomes were not included in Petrillo et al. (2016). FEA has become an establish research technique within the field, with an increased number of publications occurring in the past few years (Hettrich et al. 2015; Chae et al. 2016; Wong et al. 2016; Denard et al. 2017; Elwell et al. 2017; Permeswaran et al. 2017). FEA can be used as either a comparative tool or the next step in the assessment of prosthesis modifications, as the outputs from the other models (cadaveric, Sawbones, mechanical testing or musculoskeletal) can be used as the inputs to the analysis. These models have been used to evaluate outcome measures like implant micromotion and stress-strain distributions for the implant or bone. The subsequent sections will highlight some of these models and detail their methodology.

2.5.5.1 Oregon Health and Science University (OHSU) Model

The OHSU model has been used to evaluate stress and displacement for different prosthesis configurations (Denard et al. 2017). 3D representations of the glenoid components (glenosphere, baseplate and screws) were derived from the Universe Reverse (Arthrex, FL, USA) shoulder prosthesis and implanted into a fixed rigid foam block used to mimic the scapula (Figure 2.31(a)). All the material properties were assumed to be homogeneous, isotropic and linear elastic; the glenosphere was made from cobalt-chrome, the baseplate and screws (which were modelled as cylinders) were made out of a titanium alloy and the foam block was made out of Sawbones 1522-04 material. The components were meshed using 10-node linear tetrahedral elements and the interactions between them were said to mimic the real condition. Drawing from the American Society for Testing and Materials (ASTM[1]) standards, static 750 N compressive and shear forces were applied to the glenosphere surface and resultant the Von Mises stress (Figure 2.31(b)) and displacement were measured for all assessed configurations.

Outcome measure: Implant stress-strain.

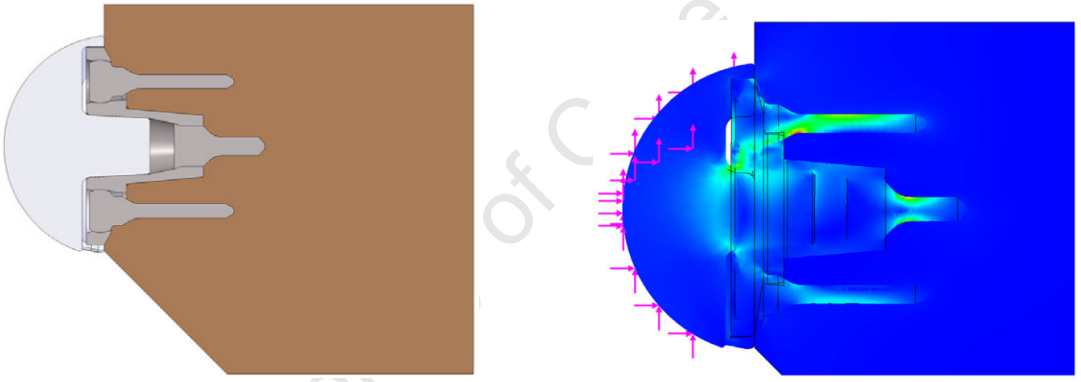

(a) Implanted prosthesis (b) Von Mises stress distribution

Figure 2.31 OHSU finite element model (Denard et al. 2017))

2.5.5.2 SUNY Binghamton model

The SUNY Binghamton model (Figure 2.32) has been used to measure metaglene micromotion for different prosthesis configurations (Elwell et al. 2017). The 3D model replicates the glenohumeral joint and consists of the metaglene, fixation screws (modelled as cylinders) and a series of scapula that were reconstructed from the CT scans of cadaveric shoulders. Each scapula was reamed, and the glenoid components implanted using two screw configurations. The material properties of the scapula were derived from an equation describing the relationship between Hounsfield units (HU) and bone density. The metaglene and fixation screws were assigned material properties for titanium,

[1]The ASTM F2028–14 standard provides a description of the test methodology required to measure glenoid component loosening or disassociation for anatomical and reverse total shoulder arthroplasties. It recommends the application of a 750 $\pm$ 15 N force in order to simulate the worst-case loading scenario for an assumed body weight of 86 kg (ASTM-International 2014).

with a modified elastic modulus used for the screws in an attempt to compensate for the cylindrical geometry. The medial border of the scapula was a fixed boundary condition and after preliminary analyses a 1.3 mm edge length was used for the meshing and a frictional coefficient of 0 and 0.8 were used for the interface between the scapula and the metaglene, and the scapula and the screws, respectively. 1 bodyweight (BW) compressive and superior shear loads were applied to the lateral surface of the metaglene for each prosthesis configuration.

Outcome measure: Micromotion.

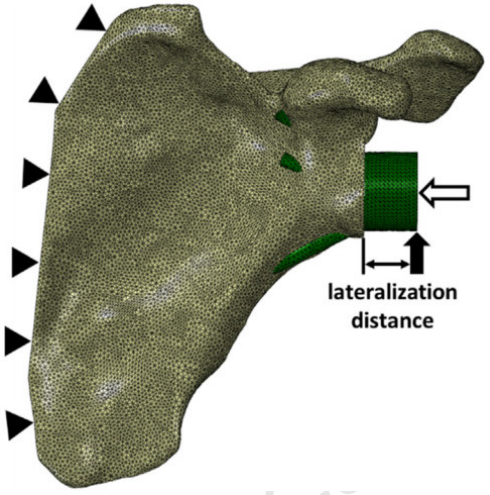

Figure 2.32 SUNY Binghamton finite element model (Elwell et al. 2017)

2.5.5.3 Tampa finite element model

The Tampa finite element model (Figure 2.33) has been used to evaluate micromotion of the metaglene for different prosthesis configurations (Virani et al. 2008).

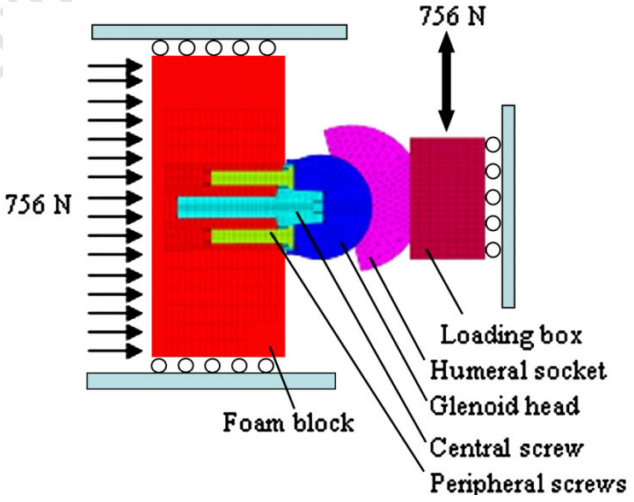

Figure 2.33 Tampa finite element model (Virani et al. 2008)

This 3D model is similar to the OHSU model in that the prosthetic components (based on the Reverse Shoulder Prosthesis and the Delta III) were implanted into a foam block that acted as a surrogate for the scapula and had similar material properties. However, in this instance, the humeral component was also modelled and attached to a loading box. The foam block and socket were meshed with quadratic tetrahedral elements and other components, due to their proportionally greater densities, were meshed with linear elements. The ASTM standard loading profile was also used here, with the compressive force applied to the foam block and the shear force applied to the loading box. The foam block was constrained such that it could only translate horizontally (in response to the compression) and the loading box was constrained such that it could only translate vertically (in response to the shear). Frictional interactions were modelled at the interface between the glenoid components and the foam block and at the joint contact surface. The simulated micro-motion of the metaglene varied based on the frictional co-efficient used and prosthesis configuration and was strongly correlated with the finding of an in-vitro test conducted during the same study.

Outcome measure: Micromotion.

2.5.5.4 University of Iowa model

The University of Iowa model has been used to evaluate impingement contact pressure for different prosthesis configurations (Hettrich et al. 2015; Permeswaran et al. 2017). The 3D model replicates the glenohumeral joint and consists of the glenosphere, metaglene, humeral cup and stem, which were based on Aequalis prosthesis, and the scapula and humerus which were reconstructed from the female cadaver of the Visible Human Project. The humerus and scapula were resected during a virtual surgery process and the prosthetic components implanted into the bones (Figure 2.34); material properties for the components were sourced from previous literature.

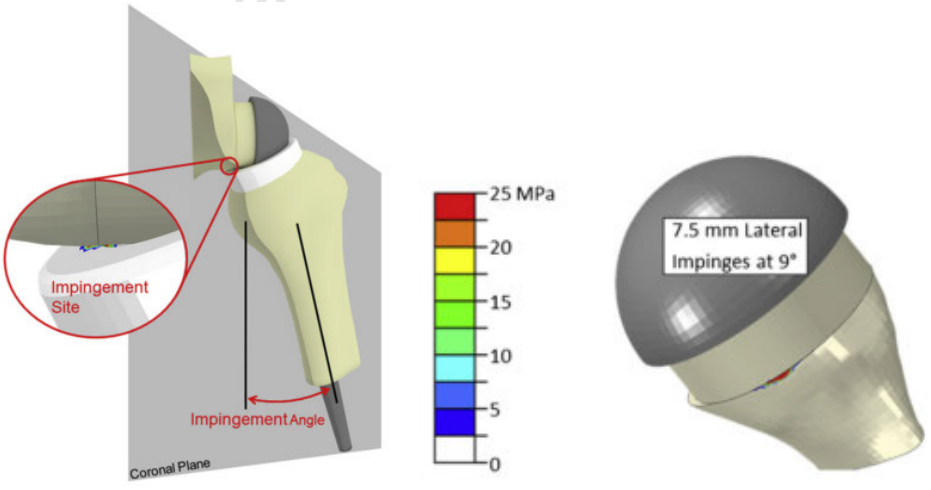

(a) Model configuration (b) Impingement and contact pressure

Figure 2.34 University of Iowa finite element model (Hettrich et al. 2015)

Due to the study investigating impingement between the scapula and humeral cup, these components were meshed with hexahedral elements; whereas, the other components were meshed as rigid bodies. During simulated scapular plane elevation and forward flexion, the humerus was elevated to 40° and a load was applied at the humerus. This resulted in adduction until impingement occurred, at which time the contact pressure between the scapula and humeral cup were measured. It should be noted that the boundary conditions of the model and the interaction properties between the components were not stated. However, in a different study by the same research group, they performed a cadaveric validation of their finite element model (Permeswaran et al. 2016).

Outcome measure: Impingement.

2.5.5.5 University of Korea model

The University of Korea model was used to evaluate metaglene micromotion and von Mises stress distribution around the reamed glenoid for different prosthesis configurations (Chae et al. 2016). As can be seen in Figure 2.35, the 3D model replicates the glenohumeral joint and consists of the glenosphere, metaglene and fixation screws (based on the Aequalis prosthesis) and scapula that were reconstructed from the CT scans of cadaveric shoulders. The scapula was reamed, and the glenoid components implanted using four screws, which were modelled as cylinders. The cancellous and cortical bone of the scapula were differentiated using the grey-value of the CT scans and were assigned their own material properties. As with the OHSU model, the glenosphere was assigned the material properties for cobalt-chrome and the metaglene and screws were assigned the material properties for titanium, and all the components were meshed using 10-node linear tetrahedral elements. A mesh refinement protocol was implemented for the scapula, a fine mesh was used around the reamed glenoid and a coarse mesh was used elsewhere. Frictional interactions (frictional co-efficient of 1.7) between the glenoid components and the scapula were modelled and the medial border of the scapula was a fixed boundary condition. 70% and 100% bodyweight (BW) loads were applied along the humeral stem long axis at 30°, 60° and 90° of simulated scapular plane elevation.

Outcome measure: Micromotion and implant stress-strain.

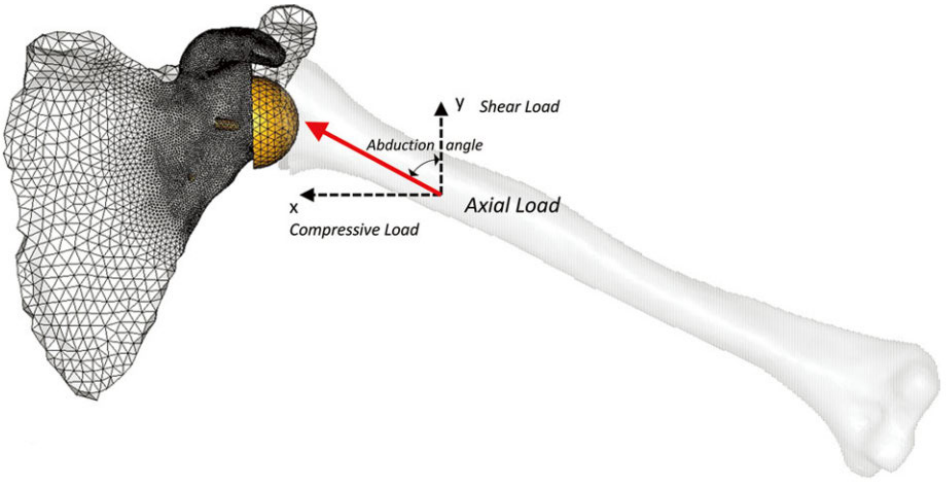

Figure 2.35 University of Korea finite element model (Chae et al. 2016)

2.5.5.6 University of Western Ontario model

The University of Western Ontario model was used to assess acromial stress distribution for different prosthesis configurations (Wong et al. 2016). The study calculated the deltoid muscle force required for scapular plane elevation using a custom-made musculoskeletal model. This model (Figure 2.36(a)) consisted of the 3D reconstructions of the scapula and humerus from CT scans of cadaveric shoulders, which were resected during virtual surgery, the implanted Delta XTEND prosthesis (DePuy Synthes, IN, USA (DePuy-Synthes 2013)) and seven lines of action replicating the deltoid muscle.

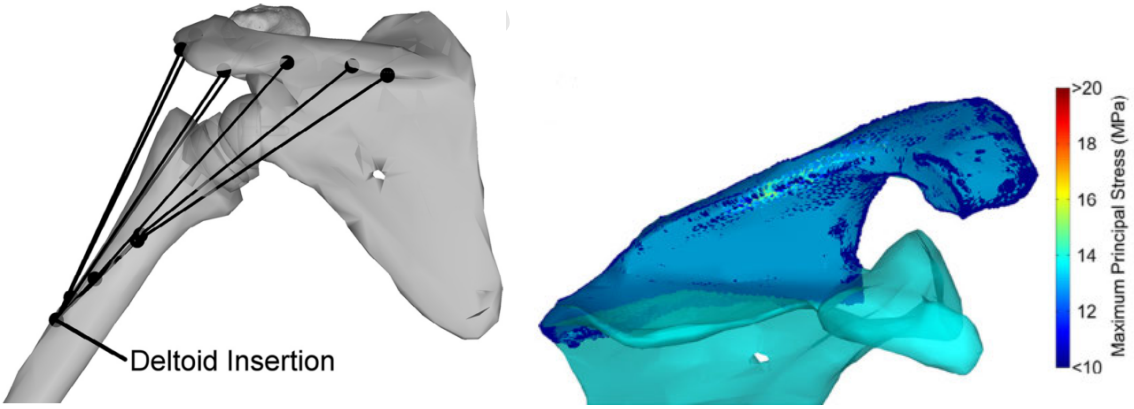

(a) Musculoskeletal model (b) Acriomal stress distribution

Figure 2.36 University of Western Ontario finite element model (Wong et al. 2016)

The finite element model consisted of the 3D reconstructed scapula, which was fixed along its inferior border. The material properties of the scapula were assigned using the grey-values of the CT scan and empirical relationship between Young's modulus and density. The muscle forces were applied at the origin of each line of action and the maximum principal stress distribution across the acromion was calculated during scapular plane elevation (Figure 2.36(b)). No details were provided about the mesh used for the scapula and, since there was only one component in the model, no interaction properties were required.

Outcome measure: Scapular stress-strain.

2.5.6 Research techniques summary

Table 2.4 provides a summary of the biomechanical research techniques that were investigated. This table illustrates the variety of outcome measures that can be assessed, ranging across geometric properties (impingement and glenohumeral joint centre of rotation), to kinetic properties (muscle forces and joint contact forces), to structural properties (implant micromotion and implant stress-strain). It also demonstrates the inability of a single research technique to evaluate all of these outcome measures. Therefore, in an ideal situation, these differing research techniques should be used in conjunction to assess RTSA and the effect of prosthesis modifications.

Table 2.4 Summary of the biomechanical research techniques investigated during the literature review.
BV: Bone Volume. COR: Centre of Rotation. FE: Finite Element. Imp: Impingement. JCF: Joint Contact Force. JS: Joint Stability. MA: Moment Arm. MF: Muscle Force. MM: Micromotion. MS: Musculoskeletal. PEW: Polyethylene Wear. σ: Stress. ϵ: Strain

		Outcome measures									
Type	**Name**	**COR**	**Imp**	**MA**	**MF**	**JCF**	**JS**	**MM**	σ/ϵ	**PEW**	**BV**
Cadaveric	HSS model				✓						
	NYU model					✓		✓			
	UCLA model		✓								
	U. Melbourne model	✓		✓	✓	✓					
	U. Utah model	✓	✓		✓		✓				
Sawbones	Tampa model	✓	✓								
Testing rigs	Royal Oak rig									✓	
	Tampa rig						✓				
	U. Zurich rig						✓	✓			
MS models	Berlin model			✓							
	Delft model	✓			✓	✓					
	Ghent model		✓								
	HSS computer model		✓								
	Newcastle shoulder model	✓	✓	✓	✓	✓	✓				
	SUNY Upstate model										✓
	Tampa computer model	✓	✓								
FE models	OHSU model								✓		
	SUNY Binghamton model							✓			
	Tampa FE model							✓			
	U. Iowa model		✓								
	U. Korea model							✓	✓		
	U. Western Ontario model								✓		

Chapter 3

Assessing reverse shoulder function

3.1 Introduction

As demonstrated in Chapter 2, there are several research techniques that can be implemented to predict and assess reverse total shoulder arthroplasty (RTSA) function. These techniques, and their research outputs, have helped to characterise reverse shoulder biomechanics and improve prosthesis design and surgical procedures. These studies are often directed, measuring only one or two outcome measures for a few motions, and utilise relatively small subject cohorts. Therefore, their conclusions are focused, typically suggesting that a prosthesis modification is beneficial under a set of circumstances. Consequently, the overarching aim of this chapter is to establish a baseline of RTSA function that takes into consideration a broader set of factors. This baseline will subsequently be as a frame of reference for an investigation into the effects of prosthesis configuration modifications (Chapter 4) and, ultimately, the determination of an optimised configuration by strategically combining a subset of beneficial modifications (Chapter 5).

This aim will be accomplished by assessing the functional outcomes of the normal and the reverse shoulder using musculoskeletal modelling techniques. Kinematic and kinetic properties are to be assessed using the Newcastle Shoulder Model[1] (NSM) and RTSA impingement is to be assessed using a custom-made impingement detection algorithm (IDA). These assessments will be conducted during a variety of standardised motions to comprehensively understand reverse shoulder function. Anatomical variability will also be taken into consideration through the development of a model-set of normal and reverse shoulders. Consequently, a secondary aim of this chapter is to provide a description of the NSM, IDA and the processes required to develop the normal and reverse shoulder model-sets.

[1]Based upon the capability of the NSM to evaluate a wide variety of reverse shoulder outcome measures (as highlighted in Section 2.5.6), it was selected for use during the thesis. Access to the NSM was gained through the establishment of a collaboration with Dr Kontaxis in the Leon Root Motion Analysis Laboratory at the Hospital for Special Surgery (New York, USA) during the initial stages of the doctoral candidacy.

3.2 Materials

3.2.1 Newcastle shoulder model

The NSM, in its original state, is representative of a healthy anatomical shoulder (Charlton and Johnson 2006). It contains a series of interconnected bone geometries, and the associated muscle and ligaments that form the upper extremity. The musculoskeletal component of the NSM is constructed and visualised using SIMM (Motion Analysis Corporation, CA, USA). This software can apply motion to the model and calculate the lengths, vectors and moment arms of the muscles over the duration of the motion. These outputs are then utilised by custom MATLAB-based (MathWorks, MA, USA) inverse dynamics and load-sharing protocols to calculate muscle and joint contact forces. The flowchart shown in Figure 3.1 provides an overview of the NSM, and a description of its processes are given in the subsequent section.

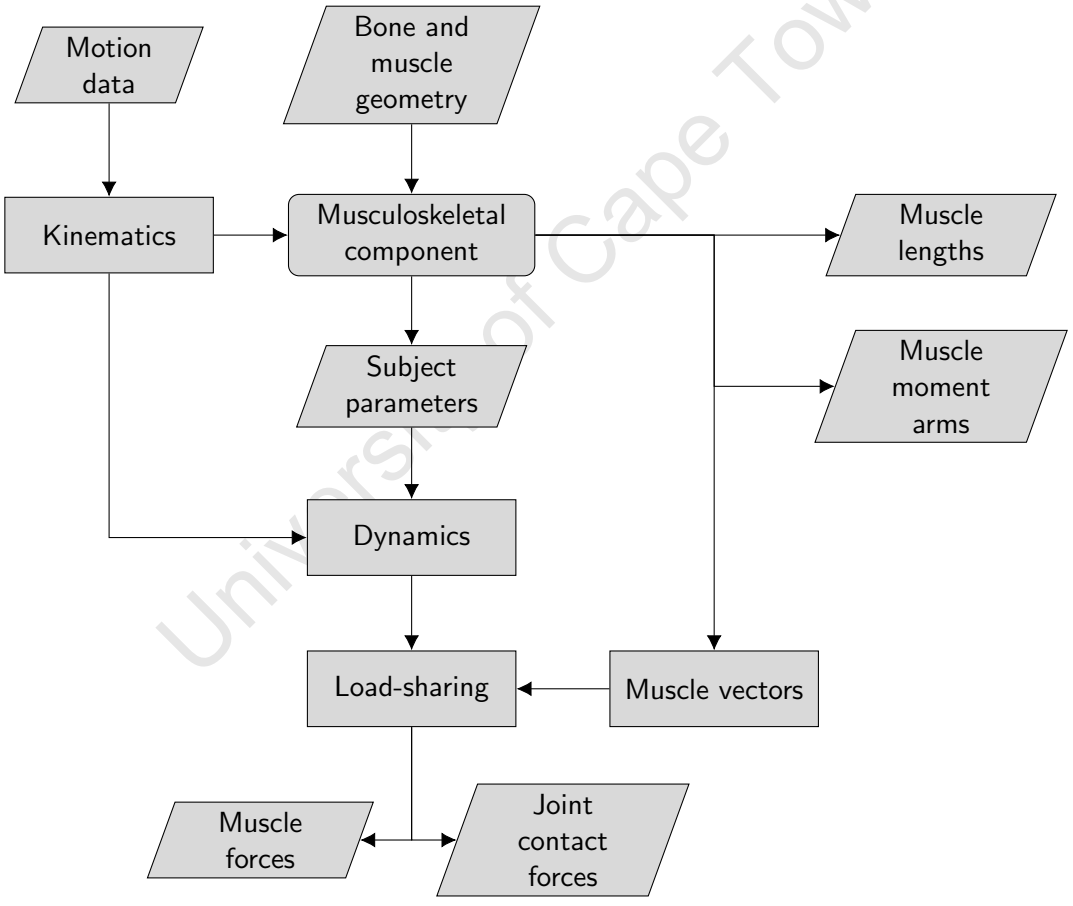

Figure 3.1 Newcastle Shoulder Model overview

3.2.1.1 Musculoskeletal component

The musculoskeletal component of the NSM (Figure 3.2) consists of 3D geometries of the thorax, clavicle, scapula, humerus, radius and ulna bones that were reconstructed from the Visible Human

data-set (National Library of Medicine, USA, Spitzer and Whitlock 1998). These geometries are orientated into their respective co-ordinate systems using anatomical landmarks (Wu et al. 2005) and, through these co-ordinate systems, are connected by a series of joints. The sternoclavicular (SC) joint (spherical, 3 degree of freedom, DOF) connects the thorax to the clavicle, the acromioclavicular (AC) joint (spherical, 3 DOF) connects the clavicle to the scapula, the glenohumeral (GH) joint (spherical, 3 DOF) connects the scapula to the humerus, and the elbow joints (two hinge joints, 1 DOF each) connects the humerus to the radius and ulna. In addition, the scapulothoracic gliding plane (STGP), is defined in the model. The STGP, constructed from prismatic joints that connect the inferior and superior scapular angles to an ellipsoid approximating the rib cage, acts as an articulation between the scapula and thorax that is inter-dependent with the SC and AC joints.

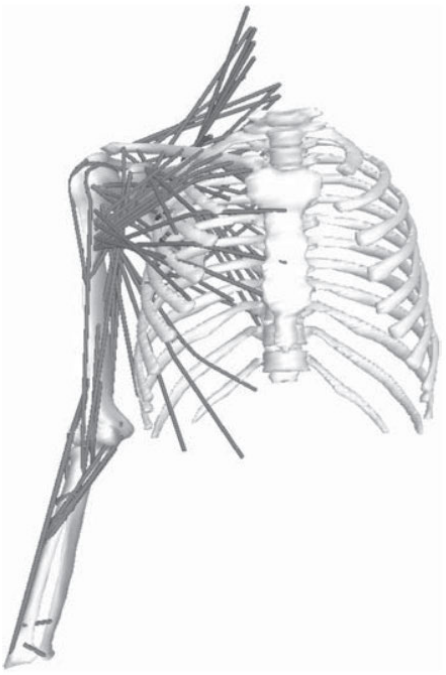

Figure 3.2 The musculoskeletal component of the NSM, visualised in SIMM (Charlton and Johnson 2006)

The musculoskeletal component also includes geometries for 31 muscles and 3 ligaments. Research conducted by van der Helm et al. (1992), Johnson et al. (1996) and Veeger et al. (1997) was used to construct the musculature of the NSM. They are modelled as elastic strings that have a line of action between its origin and insertion sites. Muscles with broad attachment sites, such as the latissimus dorsi or trapezius, are separated into numerous strings that are indicative of their anatomical division into fascicles. This resulted in 90 lines of action used to represent the musculature of the NSM (Table 3.1). The bone geometries also define frictionless wrapping objects that improve the accuracy of muscle trajectories during the analysis (Charlton and Johnson 2001). These are based on basic geometric shapes that approximate the bone geometries and the wrapping objects. Ellipsoids are used for the STGP and the anterolateral aspect of the rib cage; cylinders are used for the humeral column, radial column and the olecranon; and a sphere is used for the humeral head.

Table 3.1 NSM musculature

Muscle	**Origin**	**Insertion**	**Fascicles**	**Reference**
Clavicular trapezius	Thorax	Clavicle	3	van der Helm et al. (1992)
Scapular trapezius			13	
Levator scapulae			4	
Rhomboid minor			2	
Rhomboid major			5	
Serratus anterior			9	
Pectoralis minor			3	
Latissimus dorsi	Thorax	Humerus	5	Johnson et al. (1996)
Thoracic pectoralis major			5	
Clavicular pectoralis major			5	
Anterior deltoid	Clavicle	Humerus	2	van der Helm et al. (1992)
Middle deltoid	Scapula	Humerus	1	
Posterior deltoid			2	
Supraspinatus			1	
Infraspinatus			3	
Subscapularis			3	
Teres minor			1	
Teres major			1	
Coracobrachialis			2	
Biceps short head	Scapula	Radius	1	Veeger et al. (1997)
Biceps long head	Humerus	Radius	1	
Triceps long head	Scapula	Ulna	2	
Triceps medial head	Humerus	Ulna	2	
Triceps lateral head			1	
Brachialis			2	
Anconeus			1	
Brachioradialis	Humerus	Radius	2	
Humeral supinator			1	
Ulnar supinator	Ulna	Radius	1	
Humeral pronator teres	Humerus	Radius	1	
Ulnar pronator teres	Ulna	Radius	1	
Pronator quadratus	Radius	Ulna	1	
Ligaments	**Origin**	**Insertion**	**Fascicles**	**Reference**
Costoclavicular	Thorax	Clavicle	1	Johnson et al. (1996)
Conoid	Clavicle	Scapula	1	
Trapezoid			1	

3.2.1.2 Kinematics

Shoulder motion is reproduced by the model through the application of rigid body rotations about the joints connecting the bones (Table 3.2). The rotation sequences for the spherical AC, SC and GH joints are based on recommendations of the International Shoulder Group (ISG, van der Helm 1996). The GH joint uses Euler angles (where the first and last rotations share a common axis, Figure 3.3) and the AC and SC joints use Cardan angles (where the first and last rotations do not share a common axis). The rotation sequence for the elbow is based on the orientation of the two hinge joints.

Table 3.2 Rotation sequences used to describe shoulder motion

Bone	Rotation Sequence	Corresponding elemental rotation		
Clavicle	$Y_c - Z'_c - X''_c$	Protraction	Elevation	Rotation
Scapula	$Y_s - Z'_s - X''_s$	Protraction	Rotation	Backwards Tip
Humerus	$Y_h - Z'_h - Y''_h$	Azimuth	Elevation	Rotation
Radius	R_r	Forearm pronation	N/A	N/A
Ulna	R_u	Elbow flexion	N/A	N/A

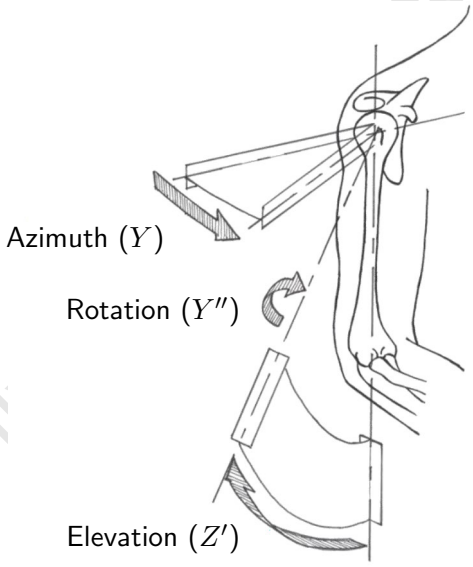

Figure 3.3 The Euler angle rotation sequence used to describe humeral motion (Charlton 2003)

The rigid body rotations applied to the joints to reproduce shoulder motion were derived from regression equations; in particular, the scapulothoracic and clavicular kinematics regression equations were derived from measurements of healthy subjects (Barnett et al. 1999; Marchese and Johnson 2000). Healthy kinematic data were used as a compromise as highly variable post-RTSA kinematics have been demonstrated in the literature (Kontaxis and Johnson 2009). Consequently, there are currently no regression equations available in the literature that generalise scapulothoracic and clavicular kinematics for the reverse shoulder.

3.2.1.3 Dynamics and load-sharing

The construction of the upper extremity as a series of connected joints that utilise rigid body rotations allowed for the modelling of the upper extremity as a robotic linkage, as illustrated in Figure 3.4, by (Murray 1999; Charlton 2003). Inverse dynamics, based on the recursive Newton-Euler method, is used to calculate the net forces and moments of each joint in the linkage for a given motion (Corke 1996). These joint forces and moments establish the equations of motions that must be balanced by some combination of muscle activity to ensure equilibrium is maintained during the motion. In order to negate the effect of inertia on the equilibrium, the given motion must be applied with a low constant speed. This results in quasi-static motion that has a 0.13 second increment (dt) between steps.

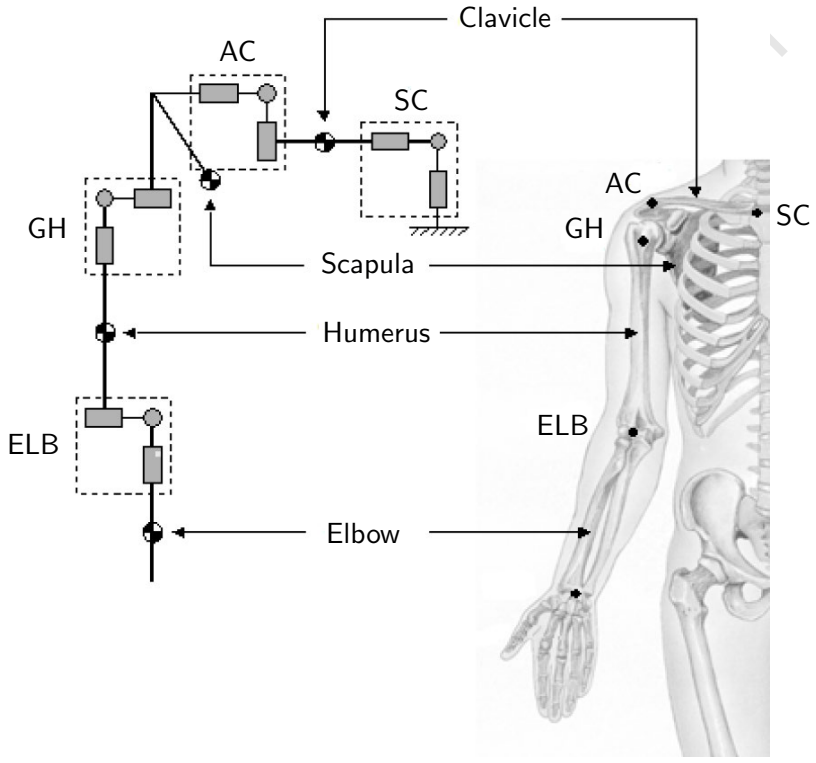

Figure 3.4 Robotic linkage model of the upper extremity (Charlton 2003). The equations of de Leva (1996) defined the subject specific bone parameters (mass, centre of mass and inertial properties). SC: Sternoclavicular. AC: Acromioclavicular. GH: Glenohumeral. ELB: Elbow

Due to the complex, inter-dependent nature of upper extremity musculature, the NSM makes use of a load-sharing protocol to calculate the contribution of each muscle to balance the equations of motion. The protocol, shown in Equation 3.1, minimises a physiological cost function that is based on the square of muscle stresses (Hogfors et al. 1995).

$$V(F_i) = \sum_i \left(\frac{F_i}{PCSA_i} \right)^2 \tag{3.1}$$

Where:

1. F_i is the force of a given muscle i

2. $PCSA_i$ is the physiological cross-sectional area of a given muscle i

The results of the protocol are constrained by the stability of the GH joint. Only solutions where the GH joint contact force vector is maintained within an ellipse approximating the glenoid fossa are deemed suitable (Charlton 2003). The method for calculating this constraint was initially developed by van der Helm and Pronk (1994) and an example of a stable and unstable solution is provided in Figure 3.5.

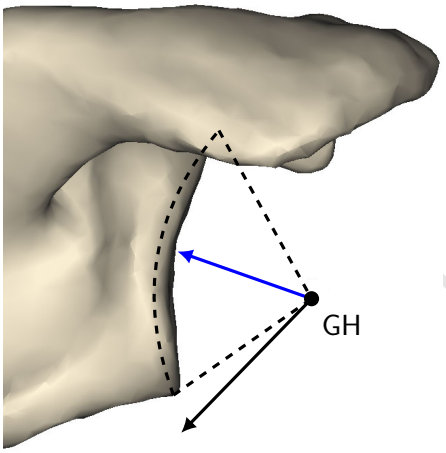

Figure 3.5 2D comparison between constrained (blue) and unconstrained (black) GH joint contact forces. The black GH joint force vector is not contained within the glenoid fossa (dashed lines) and, therefore, is rejected by the load-sharing protocol

Additionally, the force generating capabilities of the muscles are constrained by a Hill muscle model (Hill 1938). Based on the differences in scale between the Hill model, which is traditionally used to evaluate individual muscles, and the NSM, which performs large scale shoulder simulations, a simplified Hill model was implemented (Charlton 2003). As can be seen in Figure 3.6, only the contractile element (CE) and elastic series element (SE) are used to calculate the force generating capabilities of a given muscle (F_{cap}).

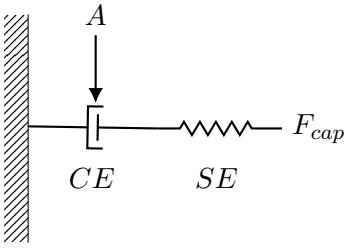

Figure 3.6 Simplified Hill muscle model

The differential equation constructed from the simplified Hill model is shown in Equation 3.2. The lower and upper limits of the force generating capabilities of a muscle are determined by A, muscle activity, which controls the CE. A is calculated in the Hill model using activation state

dynamics described by Winters (1995). The minimum value of A determines the lower limit of F_{cap} and the maximum value of A determines the upper limit of F_{cap}.

$$\frac{dF_{cap}}{dt} = \frac{K_{SE} \cdot V_{SE}(t)}{LM_{SE} \cdot (e^{K_{SE}} - 1)} \cdot \left(F_{cap}(t) \cdot (e^{K_{SE}} - 1) + F_{max} \right) \tag{3.2}$$

Where:

- K_{SE} is a shape parameter (Winters 1990).
- LM_{SE} is the maximum muscle elongation at F_{max}.
- $V_{SE}(t) = V(t) - V_{CE}(t)$. V is the resultant muscle velocity and V_{CE} is determined by A.
- $F_{max} = \sigma \cdot PCSA$. F_{max} is the theoretical maximal force a muscle can generate based on its $PCSA$ and maximal stress, which is limited to 100 N/mm^2 for all muscles (Crowninshield and Brand 1981; van der Helm 1994).
- $F_{cap}(t)$ is the resultant force generating capability of a muscle at any given step in the quasi-static motion.

3.2.1.4 Model outputs

The outputs of the NSM can be divided in two sections. Firstly, outputs from the musculoskeletal component and, secondly, outputs from the load-sharing component. The outputs from both these sections are given as a function of glenohumeral joint angle during a given motion. The kinematic outputs from the musculoskeletal component of the NSM include muscle lengths, vectors and moment arms. Figure 3.7 provides an example of these outputs using the middle deltoid muscle.

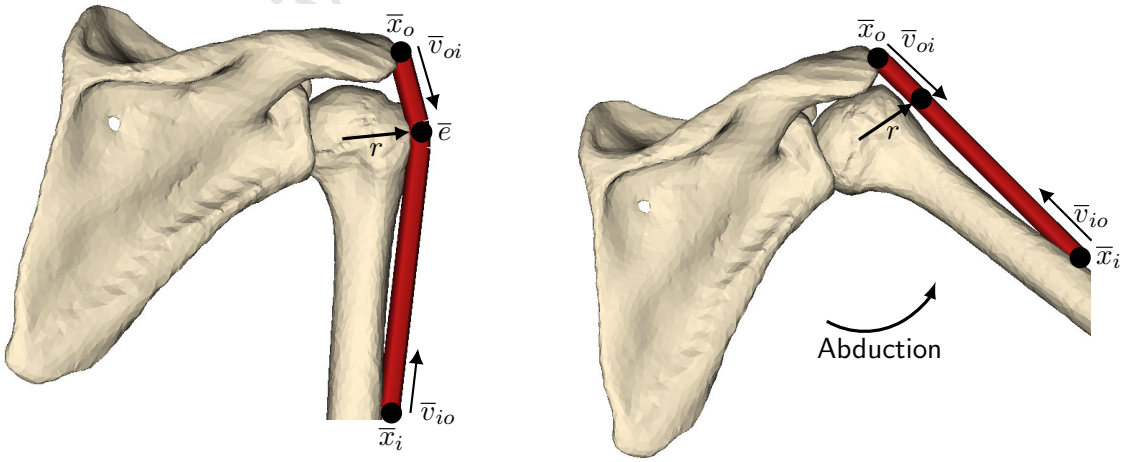

(a) Middle deltoid wrapping around the humeral head when the humerus is in the neutral position

(b) Middle deltoid unwrapping from humeral head as the humerus is abducted

Figure 3.7 Simplified representation of the outputs of the musculoskeletal component of the NSM during abduction of the arm

Muscle length (l_m) is a measure of the Euclidean distance between the origin ($\overline{x}_o$) and insertion ($\overline{x}_i$) of a muscle. Muscle vectors are a measure of the trajectory of a muscle between its origin and insertion ($\overline{v}_{oi}$) and vice-versa ($\overline{v}_{io}$). The vectors are measured relative to the co-ordinate system of the bone locating either its origin or insertion. They are unit vectors that are either divided by l_m or, in the case of the muscle wrapping, the distance between the effective muscle centre ($\overline{e}$) and the origin or insertion site, l_{oe} and l_{ie}, respectively. Muscle moment arm (r) is a measure of the torque generating effectiveness of a muscle and is calculated using the tendon-excursion method (An et al. 1983). Moment arms are measured with respect to a given joint and take into consideration any associated wrapping objects.

The kinetic outputs from the load-sharing component of the NSM primarily include muscle forces and joint contact forces (with the GH joint being of primary interest). The magnitude of the muscle force is a measure of the effort (in Newtons, N) required by a muscle to aid in performing a given motion whilst maintaining GH joint stability. Joint contact force is a measure (in N) of the contact mechanics between the articulating surfaces of a given joint, during a given motion. By definition, the joint contact forces pass through the joint centre of rotation and are decomposed into their constitutive joint axes. As can been seen in Figure 3.8, the resultant GH joint contact force has been projected into the glenoid co-ordinate system and decomposed into a compressive force (X-axis), a superoinferior shear force (Y-axis) and an anteroposterior shear force (Z-axis).

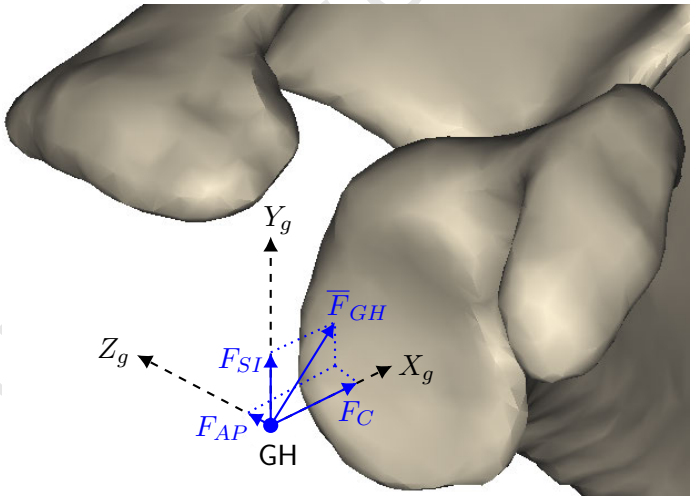

Figure 3.8 Decomposition of the GH joint contact force into the glenoid co-ordinate system

3.2.1.5 OpenSim conversion

Usage of the NSM can be restricted due to the use of SIMM for its musculoskeletal model. SIMM is relatively niche software and a limited number of institutions have the necessary licenses required to make use of it. Conversely, OpenSim (Stanford University, CA, USA, Delp et al. 2007) is the open-source counterpart to SIMM and sees widespread use in the field of biomechanics. Due to the

ease of access to OpenSim, a decision was made to convert the musculoskeletal component of the NSM from SIMM to OpenSim.

SIMM and OpenSim are both based on the SimTK infrastructure. This allows for SIMM models to be imported into OpenSim and converted to the OpenSim architecture. While this direct conversion is advantageous, it has a shortcoming due to a fundamental difference between the two software platforms. Joint rotation sequences in OpenSim use Cardan angles, and, therefore, the GH joint of the musculoskeletal model (which uses Euler angles) is unable to be converted during the importing process. To circumvent this problem, the rotation sequence of the GH joint was changed from Euler to Cardan angles prior to model import. The Cardanic representation of the GH joint was described by Wu and Cavanagh (1995) and uses a $X_h - Z'_h - Y''_h$ rotation sequence. The corresponding elemental rotations are flexion (X_h), elevation (Z_h) and rotation (Y_h). The primary difference between the use of Cardan and Euler angles for the GH joint is its ease of interpretation. The position of the humerus relative to the thorax can be directly inferred from the Euler angles; whereas, the Cardan angles describe the position of the humerus relative to the scapula, which is of little value to clinicians. However, this can be rectified using Equation 3.3, which allows for the description of the motion using clinically relevant Euler angles and the implementation of the motion in OpenSim using Cardan angles.

$$R_h^t = R_s^t \cdot R_h^s \tag{3.3}$$

Where:

- R_s^t is a rotation matrix describing the position of the scapula relative to the thorax. This is representative of the SC and AC joint rotations.
- R_h^s is a rotation matrix describing the position of the humerus relative to the scapula.
- R_h^t is a rotation matrix describing the position of the humerus relative to the thorax.

In addition to the change in GH joint rotation sequence, OpenSim is unable to directly calculate the muscle vectors in the same manner as SIMM. This necessitated the development of a custom protocol to extract the muscle vector data from the Application Programming Interface (API) of OpenSim. The protocol was developed in MATLAB and a flowchart of the generalised process is shown in Figure 3.9. The protocol loads the musculoskeletal model into MATLAB and, for every muscle during each step of a given motion, calculates the vectors between the attachment sites. The protocol takes into consideration muscle wrapping and performs the calculation going from origin to insertion (o2i) and from insertion to origin (i2o). The vectors calculated in both instances differ as the reference co-ordinate system is updated to the relevant bone. For example, the o2i vectors for the middle deltoid (Figure 3.7) use the scapula as the reference co-ordinate system; whereas, the i2o vectors use the humerus as the reference co-ordinate system.

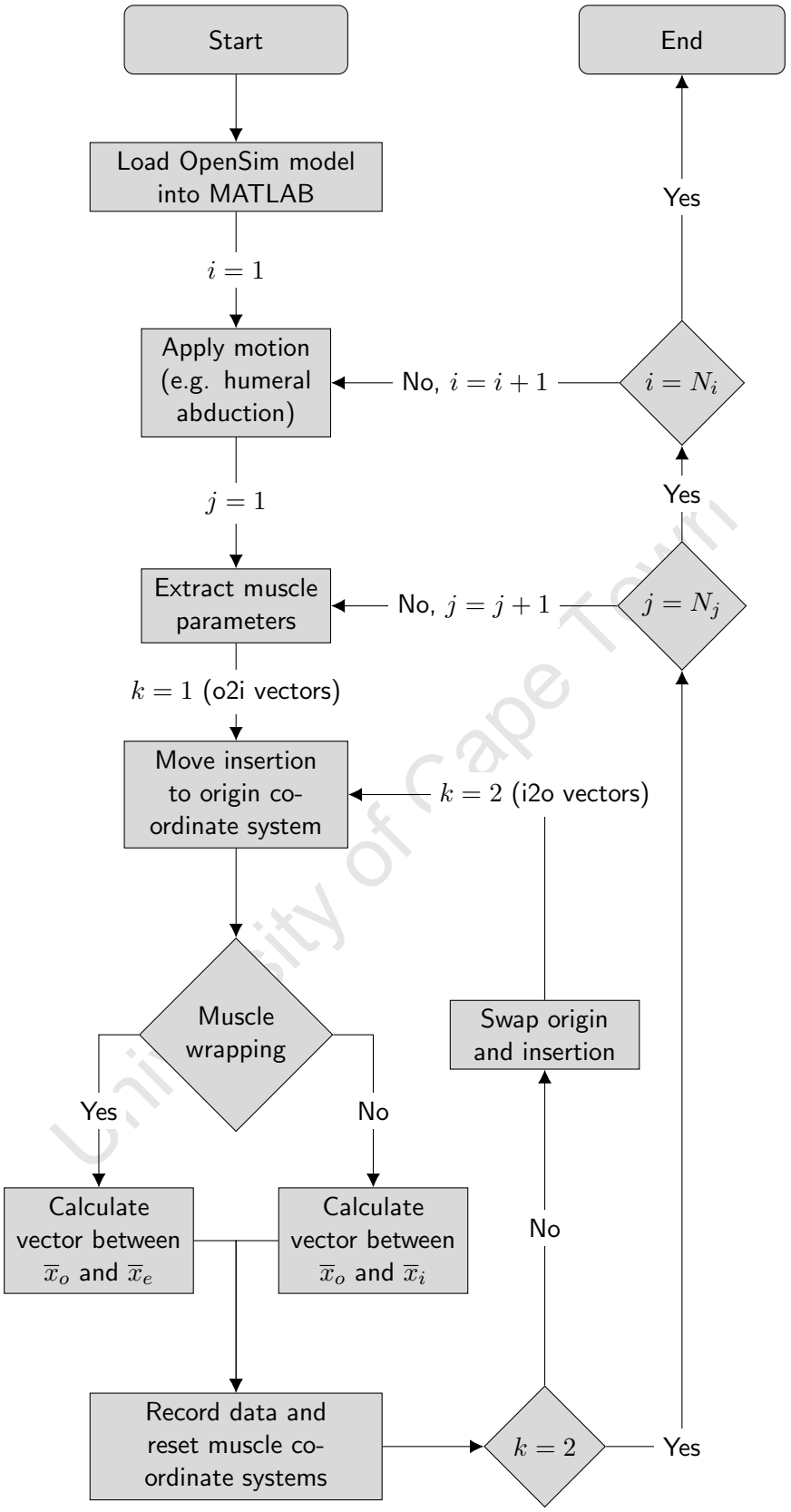

Figure 3.9 Flowchart of the generalised OpenSim muscle vector calculation protocol

For each step of humeral abduction (Figure 3.31), the vector between the attachment sites of all the muscles and ligaments was calculated using SIMM and the custom OpenSim protocol. These vectors were compared to inspect the accuracy of the protocol, and the range of differences for the entirety of these calculations was found to be -0.0056 $< \Delta <$ 0.0072. This range is likely attributed to minor differences in the definition of wrapping objects between the software platforms, and it was deemed small enough to not have a significant effect on the load-sharing protocol.

3.2.2 Reverse shoulder model-set

As mentioned in Section 3.2.1.1, the bone geometries of the NSM were derived from the Visible Human data-set (Spitzer and Whitlock 1998). Bone geometry plays a crucial role in the definition of muscle geometry; the locations of their attachment sites, and any associated wrapping objects. To account for this anatomical variability in the assessment of RTSA, a subject-specific reverse shoulder model-set was developed. The default NSM was individualised through the incorporation of subject-specific bone geometries for the scapula and humerus. Figure 3.10 highlights the steps followed during the development process of each model. To contextualise the outputs of this process, these models would replace the musculoskeletal component of the flowchart shown in Figure 3.1.

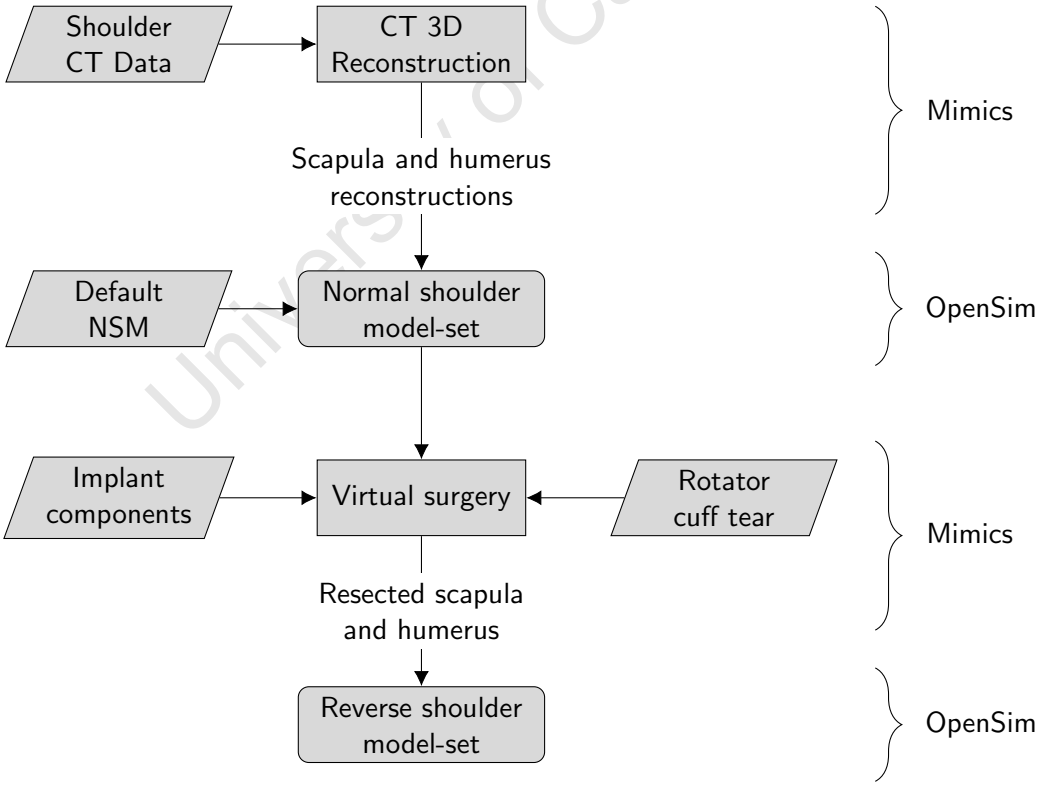

Figure 3.10 Subject-specific model development flowchart

3.2.2.1 Shoulder CT data

Whole-body computed tomography (CT) scans of 15 subjects were obtained from the SICAS (Swiss Institute for Computer Assisted Surgery) Medical Image Repository (Kistler et al. 2013). The anthropometric characteristics of the subjects can be found in Table 3.3 and, based on the observations of the clinical collaborators, none of the scans exhibited radiographic signs of osteoarthritis. The CT scans were imported into Mimics (Materalise, Leuven, Belgium) for the subsequent model-set development. The use of multiple subjects for musculoskeletal modelling is uncommon. Many studies use the geometry of a single subject (Gutiérrez et al. 2008b; Sutton et al. 2010; Berhouet et al. 2014a; Costantini et al. 2015; Liou et al. 2017) and this inherently negates the ability to take anatomical variability into consideration. Conversely, select studies, such as (Kontaxis et al. 2017), have utilised relatively large cohorts (in the range of approximately 20 to 30 shoulders). Based on the time-consuming nature of the model-set development, a cohort size of 15 shoulders was selected as a compromise between these two cases.

Table 3.3 Anthropometric characteristics of the subjects

Subject	Sex	Age	Height (m)	Weight (kg)
1	M	69	1.69	59
2	M	56	1.7	68
3	M	56	1.85	85
4	F	45	1.65	54
5	F	57	1.66	45
6	F	75	1.54	55
7	M	28	1.59	61
8	M	89	1.7	70
9	F	78	1.62	75
10	F	90	1.57	41
11	F	51	1.77	90
12	F	60	1.54	45
13	M	60	1.66	54
14	M	61	1.73	73
15	M	56	1.65	64
Mean ($\pm$ 1 SD):	8M/7F	62.1 $\pm$ 16	1.7 $\pm$ 0.10	62.6 $\pm$ 14.40

During the initial data collection process, the native version and tilt of the glenoid fossa were measured from the CT scans. Glenoid version was measured using a plane defined by the anatomical landmarks of the glenoid fossa centre, the medial border of scapular spine and the inferior angle (Friedman et al. 1992). When this plane is viewed from a top-down perspective, glenoid version is measured as the angle made by the bisection of the line between the anterior and posterior margins of the glenoid and the line between the centre of the fossa and the medial border (Figure 3.11(a)). When viewed from a side-on perspective, tilt can be measured in the same plane. It is the angle made by the bisection of the line between the superior and inferior margins of the glenoid and the line between the centre of the fossa and the medial border (Figure 3.11(b)).

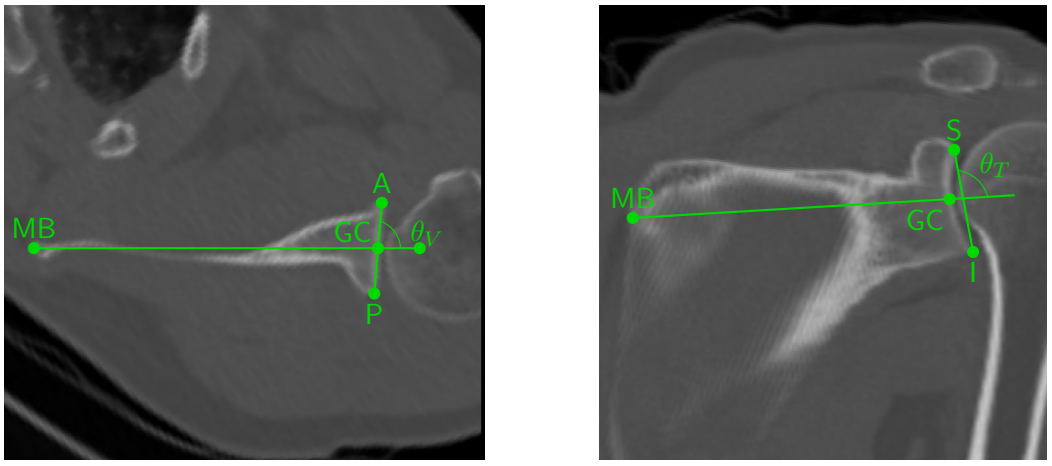

(a) Glenoid version (θ_V) measurement

(b) Glenoid tilt (θ_T) measurement

Figure 3.11 Glenoid version and tilt measurement (Friedman et al. 1992)

3.2.2.2 3D reconstruction

3D reconstruction of subject-specific bone geometries was carried out in Mimics from imported raw CT data. Grey-value thresholding was used to separate bone from the surrounding soft tissue and create a two-dimensional (2D) mask of the skeleton. The masks of the right-hand side scapula and humerus were then automatically separated from the skeleton through region growing. Manual editing of the masks corrected any errors made during the previous steps. Subsequently, 3D bone geometries were reconstructed from the 2D masks. The geometries were then simplified using triangle reduction and smoothing methods. These methods simplify bone geometry without negatively affecting downstream usability and overall quality. Figure 3.12 provides an example of the output from this procedure.

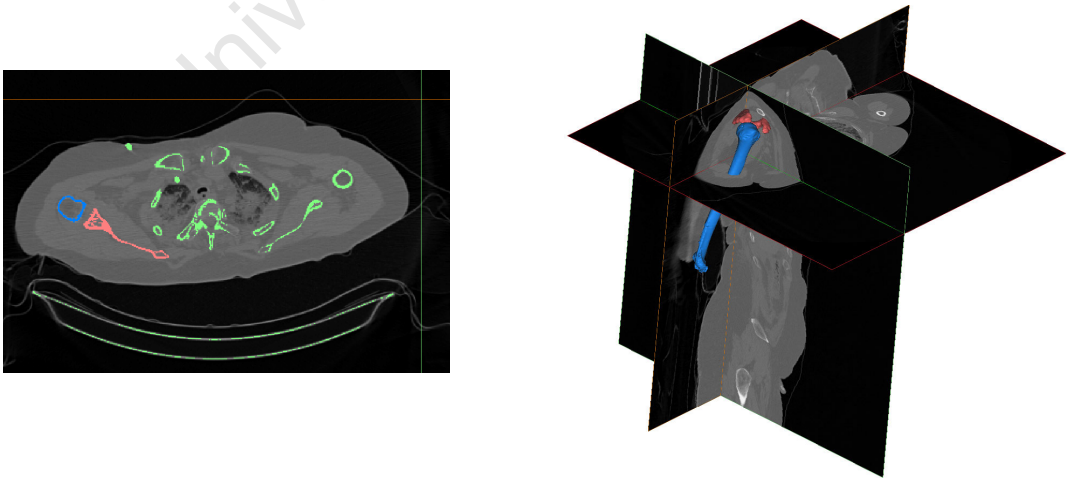

(a) 2D masks for the skeleton (green), scapula (red) and humerus (blue)

(b) 3D reconstructions of the scapula and humerus

Figure 3.12 3D reconstruction of the scapula and humerus

In order to incorporate the reconstructed scapula and humerus into the NSM, their bone geometries must be scaled to match the size of the default bone geometries. Equations 3.4 were used to calculate the necessary linear scaling factors, S_s and S_h for the scapula and humerus, respectively. The numbers in bold indicate the lengths of the original Visible Human bone geometries.

$$S_s = \frac{\mathbf{213.00}}{|\overline{AC} - \overline{AI}|}$$
$$S_h = \frac{\mathbf{292.70}}{\left|\overline{GH} - \frac{\overline{ME} + \overline{LE}}{2}\right|} \tag{3.4}$$

Equations 3.4 are based on the estimation of bone length from anatomical landmarks, namely the AC joint and inferior angle (AI) for the scapula, and the medial and lateral epicondyles (ME and LE, respectively) and the centre of rotation of the GH joint for the humerus. The location of GH can be approximated by fitting a sphere to the humeral head (van der Helm et al. 1989).

3.2.2.3 Co-ordinate system orientation

As mentioned in Section 3.2.1.1, the subject-specific scapula and humerus need to be orientated from the native CT scan reference frame into their respective co-ordinate systems to be used in the NSM. The technique for these transformations has been standardised by the ISB (Wu et al. 2005) and is largely adhered to by the NSM. This technique requires the identification of anatomical landmarks, the establishment of axes from these landmarks, and the alignment of the bone geometries with these axes. This process was conducted in Mimics.

The scapular co-ordinate system (Figure 3.13) is defined by the AI, acromial angle (AA) and trigonum spinae (TS, root of the scapular spine) landmarks using Equations 3.5.

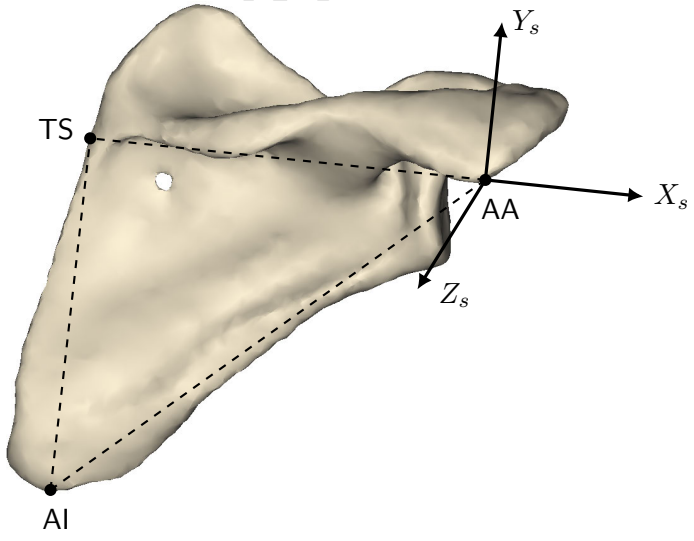

$$\overline{X_s} = \frac{\overline{AA} - \overline{TS}}{|\overline{AA} - \overline{TS}|}$$
$$\overline{Z_s} = \overline{X_s} \times \frac{\overline{AA} - \overline{AI}}{|\overline{AA} - \overline{AI}|}$$
$$\overline{Y_s} = \overline{Z_s} \times \overline{X_s} \tag{3.5}$$

Figure 3.13 Scapular co-ordinate system

The humeral co-ordinate system (Figure 3.14) is defined by Equations 3.6 and the same landmarks used to estimate its length, the medial and lateral epicondyles (ME and LE) and the GH joint centre of rotation (GH).

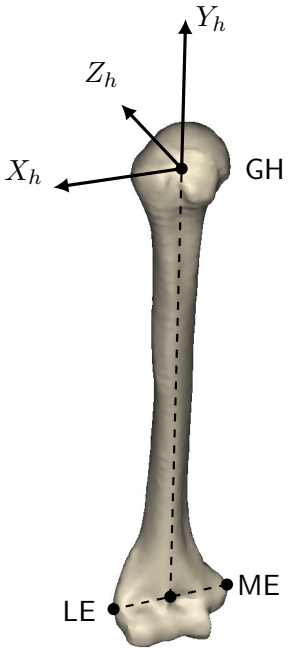

$$\overline{Y_h} = \frac{\overline{GH} - \frac{\overline{ME} + \overline{LE}}{2}}{\left|\overline{GH} - \frac{\overline{ME} + \overline{LE}}{2}\right|}$$
$$\overline{Z_h} = \overline{Y_h} \times \frac{\overline{ME} - \overline{LE}}{|\overline{ME} - \overline{LE}|}$$
$$\overline{X_h} = \overline{Y_h} \times \overline{Z_h} \quad (3.6)$$

Figure 3.14 Humeral co-ordinate system

The NSM co-ordinate system of the humerus differs from the ISB standardisation in two ways. Firstly, the Z axis is directed posteriorly (instead of anteriorly) and, secondly, the X and Z axes are swapped. These differences are attributed to the implementation of techniques described by the ISG (van der Helm 1996) during the initial development of the NSM that were established prior to ISB standardisation and do not fundamentally change the outputs of the model.

3.2.2.4 Normal shoulder model-set development

Once the scapula and humerus of each subject were orientated into the required co-ordinate systems, they were used to construct the normal shoulder model-set in OpenSim. The scapula and humerus in the original musculoskeletal component of the NSM were replaced by their respective bone geometries from each subject (which were exported from Mimics as *stl* files). Subsequently, the origin and insertion sites of the muscles affected by the change in bone geometries were modified. Here, the musculature of the original NSM (which compares well with literature (Charlton and Johnson 2006; Kontaxis and Johnson 2009)) was used a ground truth and the modified sties were matched to the corresponding locations via visual inspection. The size and location of the humeral wrapping objects were also modified to best fit the individualised geometries.

After completing this process, a set of 15 normal shoulder models with subject-specific bone geometries for the scapula and humerus and subject-specific musculature around the glenohumeral joint was established.

3.2.2.5 Virtual surgery

A virtual surgery was performed on each reconstructed scapula and humerus in Mimics using the Delta XTEND Reverse Shoulder System (DePuy Synthes, IN, USA, DePuy-Synthes (2013)). 3D models of the prosthesis components (Figure 3.15) were created from a retrieved implant that had been scanned using a NextEngine 3D Laser Scanner (NextEngine, CA, USA).

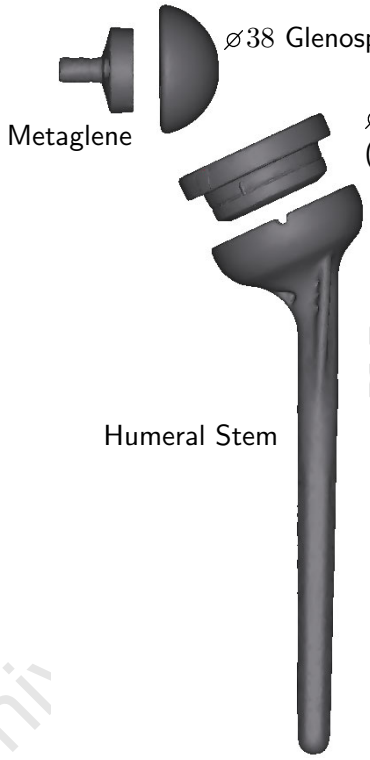

Figure 3.15 3D reconstruction of the retrieved Delta XTEND implant components

As can be seen in Figure 3.16(a), the centroid of the metaglene (glenoid baseplate) was positioned in line with the superior-inferior axis of the glenoid and placed 12 mm superior to the inferior glenoid rim (Kelly et al. 2008). To ensure that the metaglene was implanted in a neutral (0°) orientation, the previously measured native glenoid version and tilt were removed when the glenoid was reamed to subchondral bone (Figure 3.16(b)). Glenosphere implantation was simplified by omitting the screws used to secure the metaglene to the scapula, as these screws are not taken into consideration during the NSM simulations.

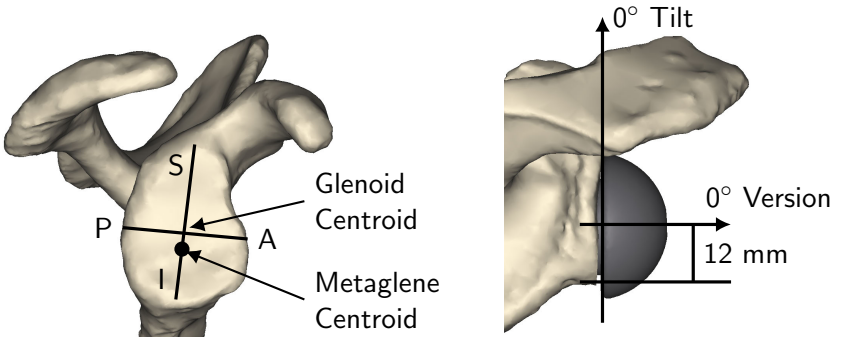

(a) Centroid locations on the glenoid

(b) Implanted glenosphere on the reamed glenoid

Figure 3.16 Virtual surgery of the scapula

The humeral head was resected proximally to the greater tuberiosity using a cutting angle of 155° (DePuy-Synthes 2013) and a retroversion angle of 20° (Gulotta et al. 2012; Berton et al. 2015). The retroversion angle was measured relative to the epicondylar axis, a line connecting the medial and lateral epicondyles of the distal humerus. After resection, the humeral stem was implanted in to the medullary cavity and the cup placed in the stem (Figure 3.17).

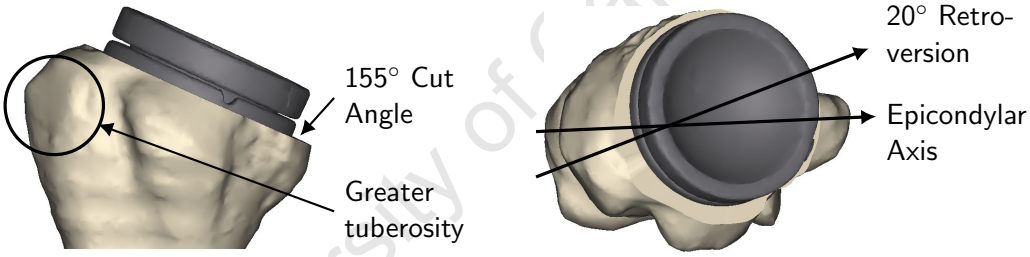

(a) Humeral head resection: cutting angle

(b) Humeral head resection: retroversion angle

Figure 3.17 Virtual surgery of the humerus

3.2.2.6 Implant co-ordinate system definition

As with the bone geometries, the implanted components required co-ordinate systems. For the purposes of representing the reverse shoulder in OpenSim, the scapular implants (metaglene and glenosphere) were combined and the humeral implants (stem and cup) were combined. Due to the rotational symmetry of the glenosphere, the co-ordinate system for the scapular component (Figure 3.18(a)) was defined by the centroid of the glenosphere and the normal of the plane placed on its rim. The humeral component co-ordinate system (Figure 3.18(b)) was defined by the centroid of the cup, the normal of a plane placed on its rim, and the long axis of the stem.

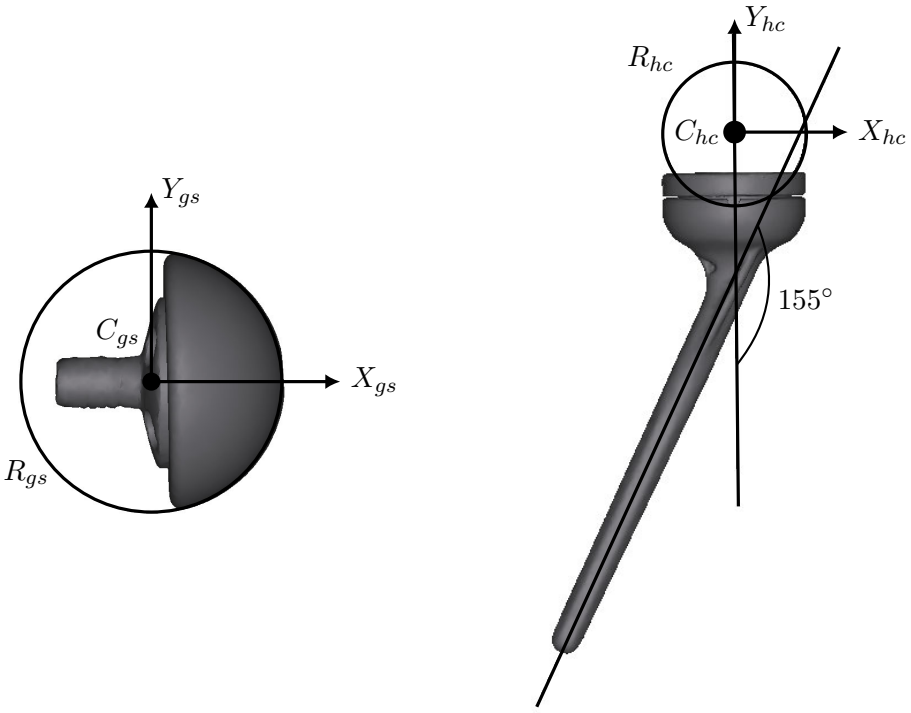

(a) Scapular component generic co-ordinate system. The Z_{gs} axis is directed out of the page

(b) Humeral component generic co-ordinate system. The Z_{hc} axis is directed out of the page

Figure 3.18 Default co-ordinate systems for the implant components

In order to orientate the components from their default co-ordinate systems into their subject-specific implanted positions, transformation matrices were constructed. The rotational component of the transformation matrix for the scapular implant was defined by equations 3.7. These equations make use of four points equally distributed on the rim of the implanted glenosphere (Figure 3.19). The translational component of the transformation was defined as the centre of the glenosphere in its implanted position relative to the origin of the co-ordinate system of the scapula (Figure 3.13).

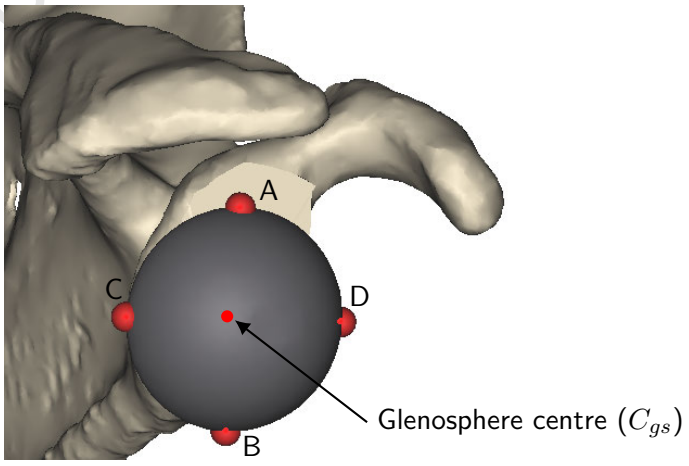

Figure 3.19 Scapular component implanted co-ordinate system

$$
\begin{aligned}
\overline{AB} &= \overline{A} - \overline{B} \qquad \overline{CD} = \overline{C} - \overline{D} \\
\overline{Y_{gs}} &= \frac{\overline{AB}}{|\overline{AB}|} \\
\overline{X_{gs}} &= \overline{Y_{gs}} \times \frac{\overline{CD}}{|\overline{CD}|} \\
\overline{Z_{gs}} &= \overline{X_{gs}} \times \overline{Y_{gs}} \\
T_{gs} &= \begin{bmatrix} X_x^{gs} & Y_x^{gs} & Z_x^{gs} & C_x^{gs} \\ X_y^{gs} & Y_y^{gs} & Z_y^{gs} & C_y^{gs} \\ X_z^{gs} & Y_z^{gs} & Z_z^{gs} & C_z^{gs} \\ 0 & 0 & 0 & 1 \end{bmatrix}
\end{aligned} \tag{3.7}
$$

The transformation matrix of the humeral implant was constructed in a similar manner. The rotational component was defined by equations 3.8 that make use of four points equally distributed on the inner rim of the implanted cup (Figure 3.20) and the translation component was defined as the centre of the cup in its implanted position relative to the origin of the humeral co-ordinate system.

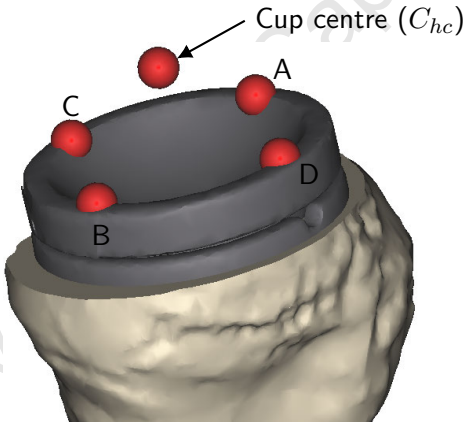

Figure 3.20 Humeral component implanted co-ordinate system

$$
\begin{aligned}
\overline{AB} &= \overline{A} - \overline{B} \qquad \overline{CD} = \overline{C} - \overline{D} \\
\overline{X_{hc}} &= \frac{\overline{AB}}{|\overline{AB}|} \\
\overline{Y_{hc}} &= \overline{X_{hc}} \times \frac{\overline{CD}}{|\overline{CD}|} \\
\overline{Z_{hc}} &= \overline{X_{hc}} \times \overline{Y_{hc}} \\
T_{hc} &= \begin{bmatrix} X_x^{hc} & Y_x^{hc} & Z_x^{hc} & C_x^{hc} \\ X_y^{hc} & Y_y^{hc} & Z_y^{hc} & C_y^{hc} \\ X_z^{hc} & Y_z^{hc} & Z_z^{hc} & C_z^{hc} \\ 0 & 0 & 0 & 1 \end{bmatrix}
\end{aligned} \tag{3.8}
$$

3.2.2.7 Reverse shoulder model-set development

The reverse shoulder model-set was developed from the normal shoulder model-set. For each model in the set, the corresponding anatomical scapula and humerus were replaced by their respective resected bone geometries (which were exported from Mimics as *stl* files after completing the virtual surgery process). The implant components (exported from Mimics in their generic co-ordinate systems) were positioned using their respective transformation matrices, thereby forming the reverse glenohumeral joint (Figure 3.21).

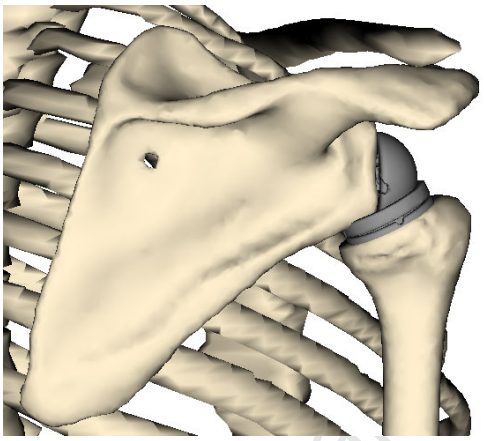

Figure 3.21 OpenSim implementation of a reverse shoulder model with subject-specific bone geometries for the scapula and humerus

Due to the nature of the surgery, and the preoperative condition of a shoulder with cuff tear arthropathy, some of the muscles were removed from the NSM (Figure 3.22). The long head of the biceps was removed as the origin of muscle is on the portion of the humeral head that is resected (DePuy-Synthes 2013). Additionally, the supraspinatus, infraspinatus and subscapularis were removed. This change mimics a massive rotator cuff tear that is present in patients with cuff tear arthropathy, the primary indication for RTSA (Grammont and Baulot 1993; Boileau et al. 2005).

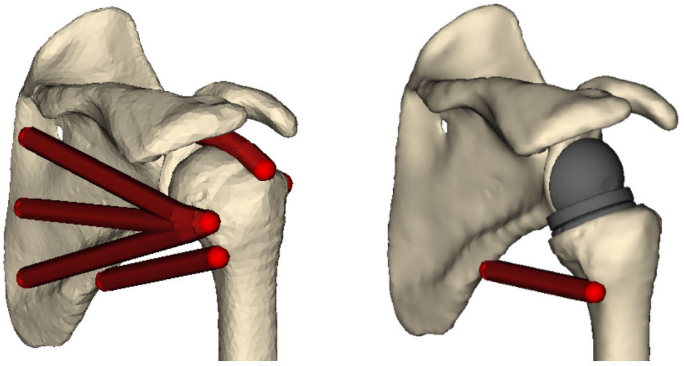

Normal Shoulder - Intact rotator cuff

Reverse Shoulder - Teres Minor only

Figure 3.22 Modified musculature of a subject-specific reverse shoulder. Note that only the teres minor of the rotator cuff is preserved

3.2.2.8 Prosthetic glenohumeral joint constraint

As the virtual surgery replaced the anatomical GH joint with a prosthetic joint, the stability constraint used in the load-sharing protocol (Section 3.2.1.3) was updated to be representative of the reversed joint. Stability in the reverse shoulder is achieved when the GH joint force vector is contained within the humeral cup. Figure 3.23 provides a description of the updated constraint parameters (Kontaxis 2009).

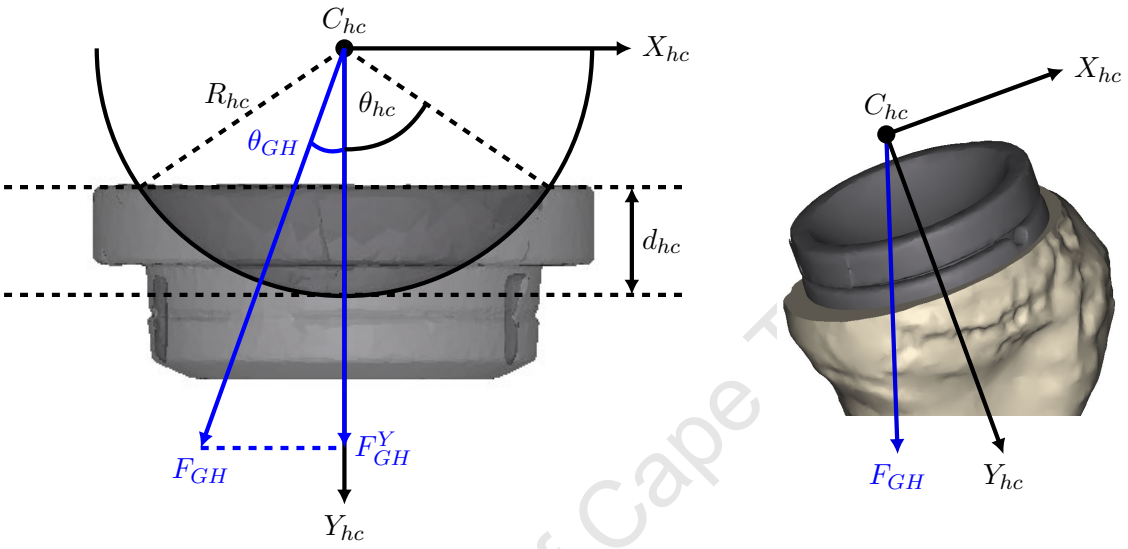

Figure 3.23 Reverse shoulder GH joint constraint parameters. Note that for these calculations, the Y-axis (Y_{hc}) is directed into the humeral cup, instead of away from it, and the Z_{hc} axis is directed into the page

In this instance, stability is maintained when the angle between the GH force vector (orientated into implanted co-ordinate system of the humeral component) and the Y-axis of the humeral cup (θ_{GH}) is less than the angle between the inner rim of the humeral cup and the Y-axis (θ_{hc}). Equations 3.9 and 3.10 are used to calculate θ_{GH} and θ_{hc}, respectively.

$$\theta_{GH} = arcsin\left(\frac{F^{Y}_{GH}}{|\overline{F}_{GH}|}\right) \tag{3.9}$$

Where:

- F^{Y}_{GH} is the compressive component of GH force vector
- $|\overline{F}_{GH}|$ is the magnitude of the GH force vector

$$\theta_{hc} = arccos\left(\frac{R_{hc} - d_{hc}}{R_{hc}}\right) \tag{3.10}$$

Where R_{hc} and d_{hc} are the radius and depth of the humeral cup, respectively.

3.2.3 Impingement detection algorithm

An IDA, developed using MATLAB, utilised subject-specific outputs from the virtual surgery process to detect graphical overlaps between the scapula and the humeral cup or humerus and estimate incidences of estimate incidences of intra- and extra-articular impingements for a given subject and motion. Overall impingement-free range of motion (IFROM) was then be defined as the extent during a motion where neither type of impingement is present.

3.2.3.1 Algorithm inputs

The inputs to the algorithm were derived from the virtual surgery process carried out in Mimics. These included the 3D geometries of the implant components and the subject-specific resected scapula and humerus. These geometries were exported from Mimics as *stl* files and imported into MATLAB. For each of the imported components, this function extracted matrices that defined the 3D vertices and faces (a vertex connectivity map) of their geometries. A visualisation of the imported components is shown in Figure 3.24. The components were orientated such that the co-ordinate system was located at the centre of rotation of the glenohumeral joint. To reduce computational time for the algorithm, the scapular and humeral geometries were modified to only include the areas in vicinity of the glenohumeral joint prior to being imported into MATLAB.

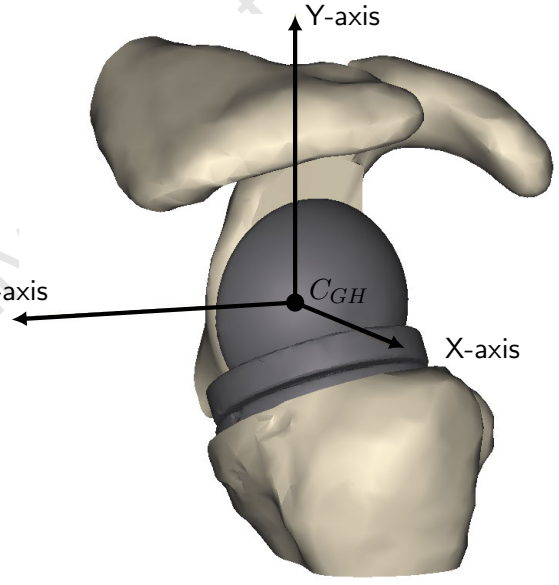

Figure 3.24 Visualisation of a reverse shoulder in the IDA

As the scapular components of the shoulder were aligned with the centre of rotation of the joint, they were fixed in space. This allowed for the application of motion using only the glenohumeral joint angles to move the humeral components of the shoulder (Figure 3.25).

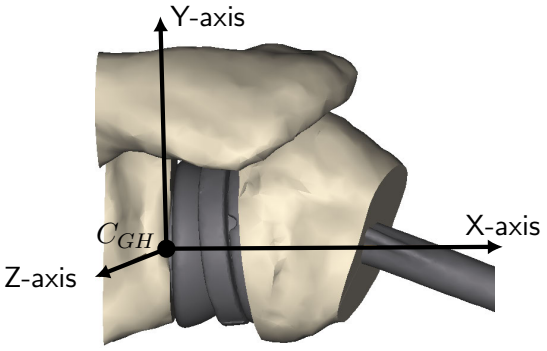

Figure 3.25 Visualisation of the reverse shoulder with the humerus abducted

In addition to the bone geometries, parameters required for the algorithm were initially defined in Mimics. These input parameters (Figure 3.26) included the humeral head resection plane, the humeral cup rim properties and lateral humeral head properties. Correct orientation of the parameters with respect to the humeral components was maintained by the algorithm during the application of motion.

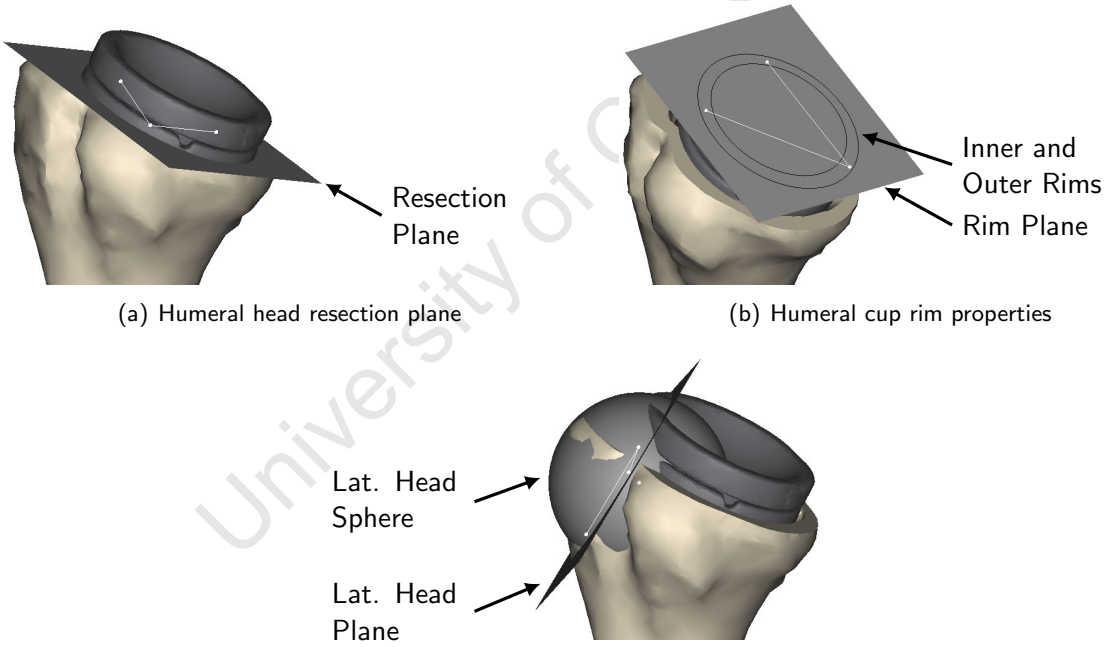

(a) Humeral head resection plane

(b) Humeral cup rim properties

(c) Humeral head lateral surface

Figure 3.26 Algorithm input parameters

3.2.3.2 Intra-articular impingement detection

Intra-articular impingement was calculated using a 3D triangle-plane bisection check. A flowchart illustrating the process is shown in Figure 3.28. For the i^{th} step of a motion, the vertices of the j^{th}

triangle in vertices matrix of the scapula were extracted. The dot product between the humeral cup rim plane and the vertices was calculated using equation 3.11.

$$V_{dot} = \overline{n}_{rim} \cdot (\overline{V} - \overline{c}_{rim}) \tag{3.11}$$

Where:

- $\overline{n}_{rim}$ is the normal of the rim plane
- $\overline{V}$ is a triangle vertex
- $\overline{c}_{rim}$ is the centre of the rim
- V_{dot} is the dot product resultant

If a uniform distribution of V_{dot} signs (three positives or three negatives) was found using equation 3.11, the triangle did not bisect the plane and algorithm moved on to the $(j+1)^{th}$ triangle. Conversely, if a non-uniform distribution was found, the triangle did bisect the plane and the algorithm moved on to its final loop. The purpose of this loop was to ensure that the bisection occurred within the rim of the humeral cup and not at an erroneous point on the plane, far away from the rim. During the loop, the distance (D_R) between the centre of the rim and the k^{th} vertex of the given triangle was calculated using equation 3.12.

$$D_R = \sqrt{\overline{V} - \overline{c}_{rim}} \tag{3.12}$$

If the distance of any vertex was within the inner and outer rim radii (R_i and R_o, respectively), intra-articular impingement was detected and the algorithm moved on to the $(j+1)^{th}$ triangle. Figure 3.27 provides a pictorial representation of this condition. The algorithm was executed until all triangles were assessed ($j = N_j$) for all the steps in a given motion ($i = N_i$).

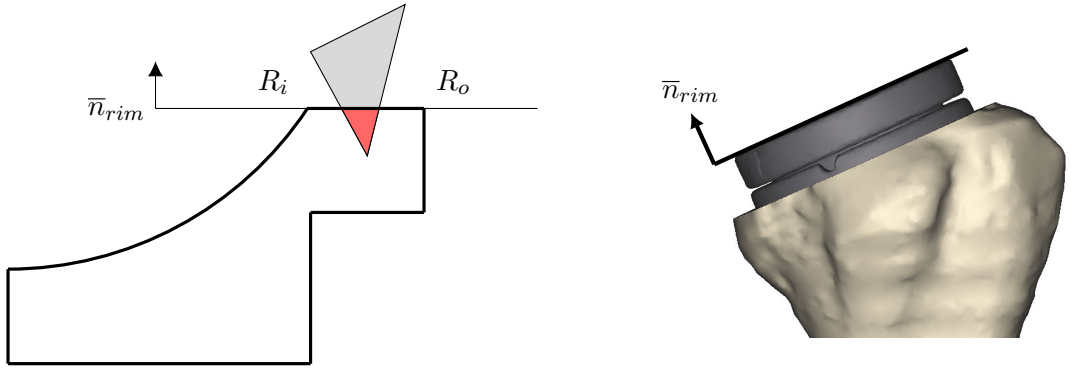

Figure 3.27 Left: pictorial representation of intra-articular impingement between a given triangle on the scapular geometry and the humeral cup rim. The red area denotes the region of impingement for this triangle. **Right:** context for the pictorial representation

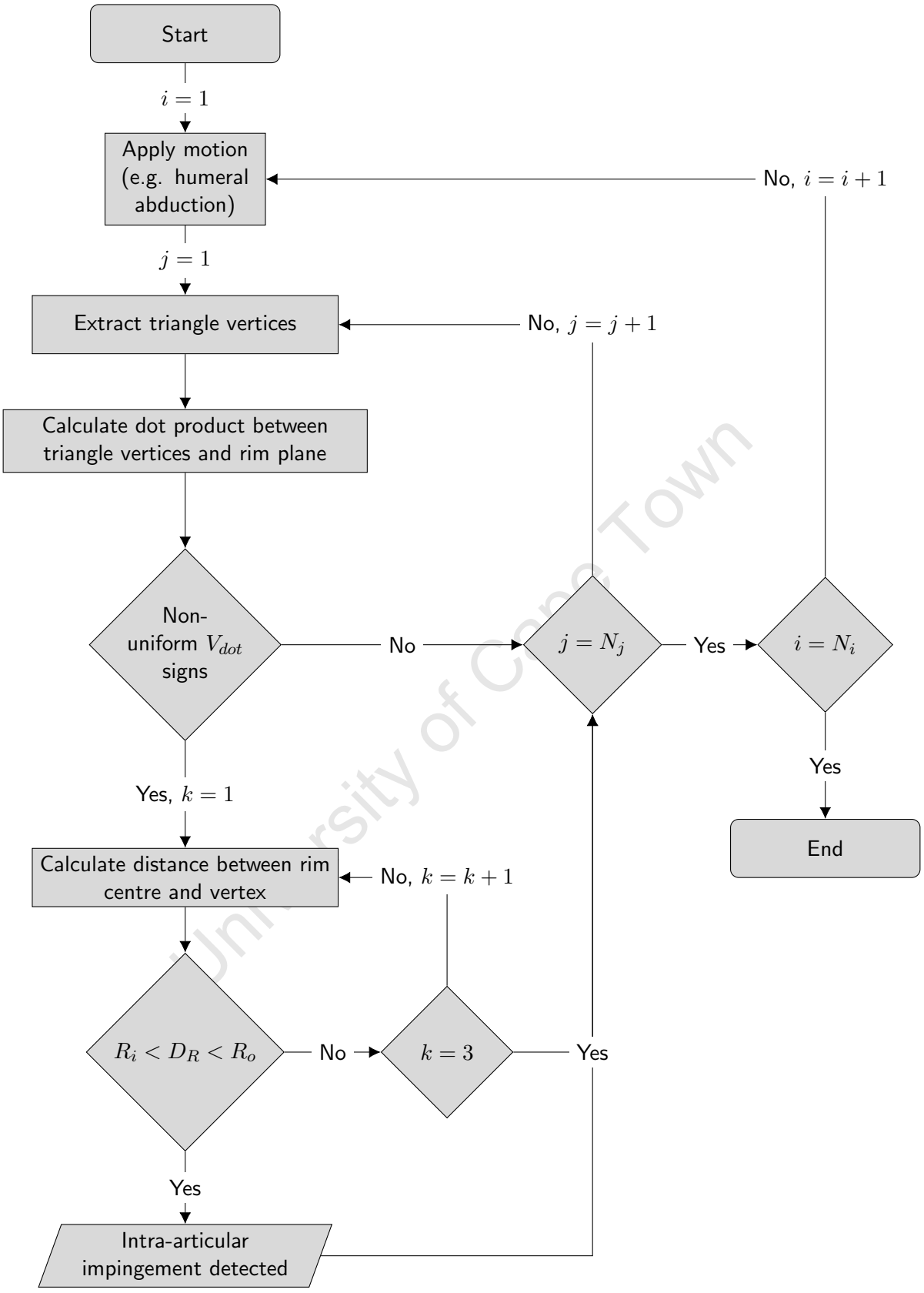

Figure 3.28 Flowchart of the intra-articular IDA

3.2.3.3 Extra-articular impingement detection

Extra-articular impingement was calculated in a similar manner to intra-articular impingement. The algorithm made use of a two triangle-plane bisection checks and a distance to sphere centre check (Figure 3.30). For the i^{th} step of a motion, the vertices of the j^{th} triangle in vertices matrix of the scapula were extracted. The dot product between the vertices and both the resection plane and lateral surface plane were calculated using equation 3.11 (where $\overline{c}_{rim}$ was replaced by $\overline{c}_{sphere}$, and the centre of the sphere and $\overline{n}_{rim}$ were replaced by the normal of the respective planes).

If uniformly positive distributions were found in both instances, the triangle is lateral to both planes, and the algorithm moved on to its final loop. This loop checked the location of the triangle and ensured that it was inside the lateral surface sphere. During the loop, the distance (D_S) between the centre of the lateral surface sphere and the k^{th} vertex of the given triangle was calculated using equation 3.12 (where $\overline{c}_{rim}$ was again replaced by $\overline{c}_{sphere}$). If the distance of any vertex was within the radius of the sphere (R_s), extra-articular impingement was detected and the algorithm moved on to the $(j+1)^{th}$ triangle. Figure 3.29 provides a pictorial representation of this condition. As with intra-articular impingement detection, the algorithm was executed until all triangles have been assessed ($j = N_j$) for all steps in a given motion ($i = N_i$).

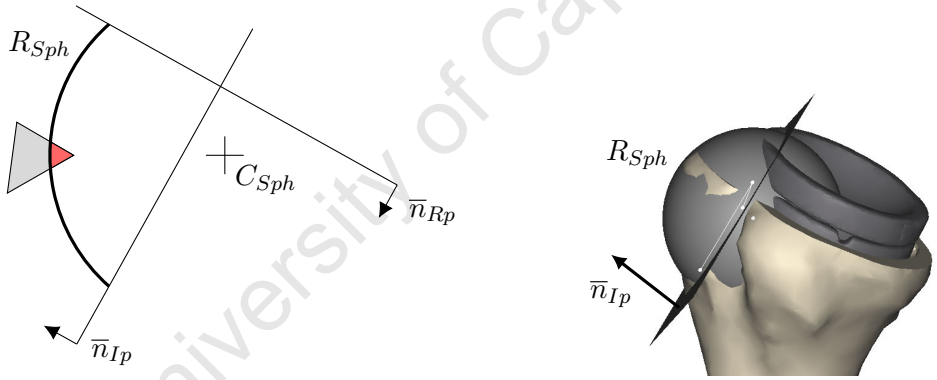

Figure 3.29 Left: pictorial representation of extra-articular impingement between a given triangle on the scapular geometry and the lateral surface of the humeral head. The red area denotes the region of impingement for this triangle. **Right:** context for the pictorial representation

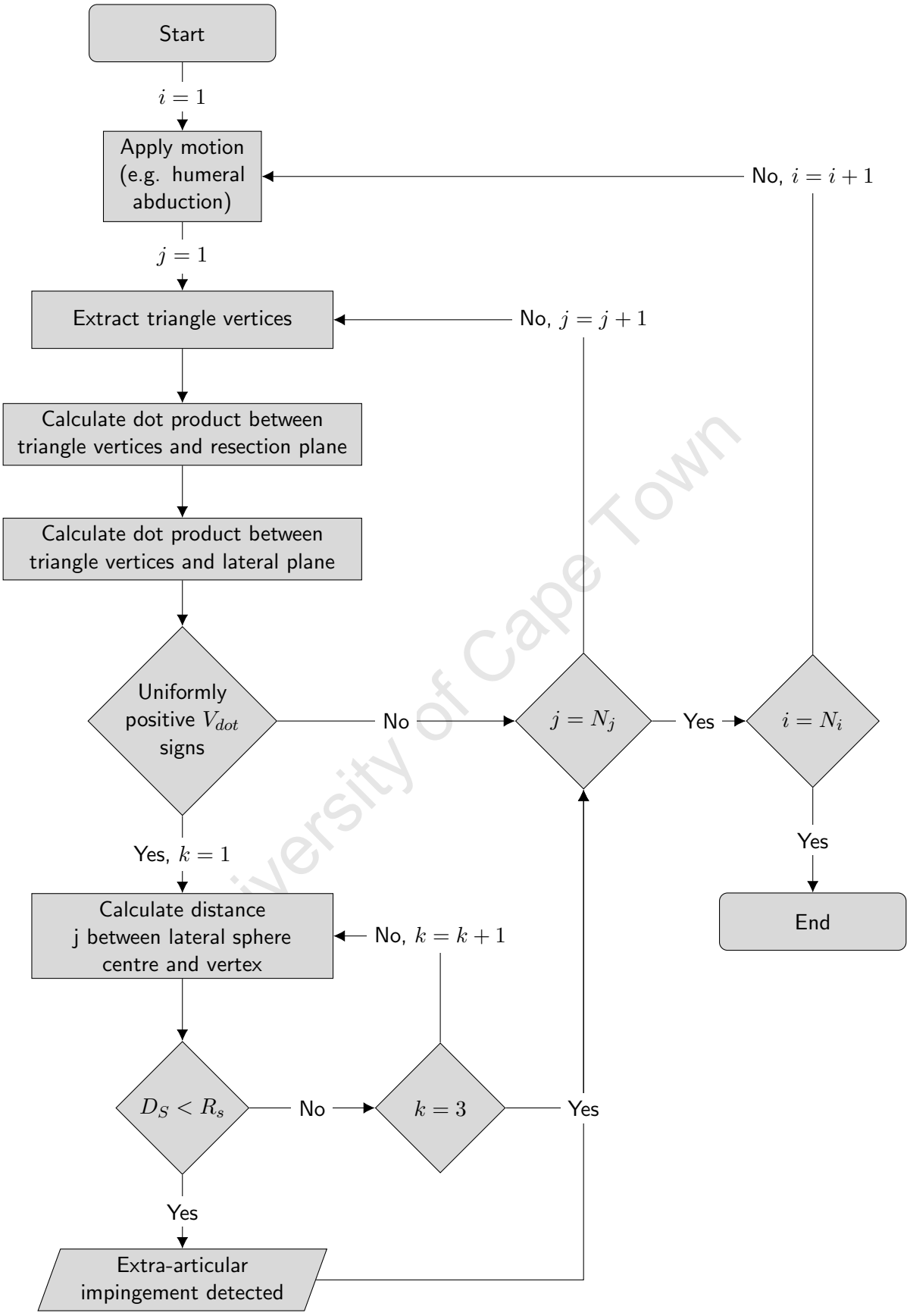

Figure 3.30 Flowchart of the extra-articular IDA

3.3 Methods

3.3.1 Motions

Seven standardised motions were simulated during the assessment of normal and reverse shoulder functional outcomes:

1. Abduction (ABD): humeral elevation in the frontal plane from 0° to 120°

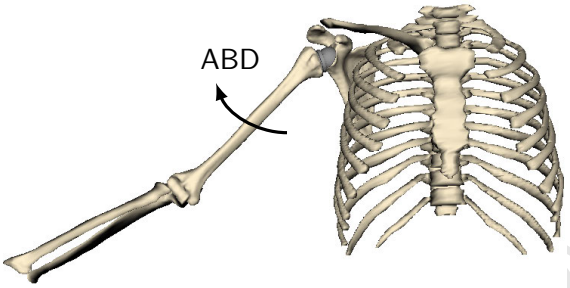

Figure 3.31 Abduction

2. Forward flexion (FF): humeral elevation in the sagittal plane from 0° to 120°

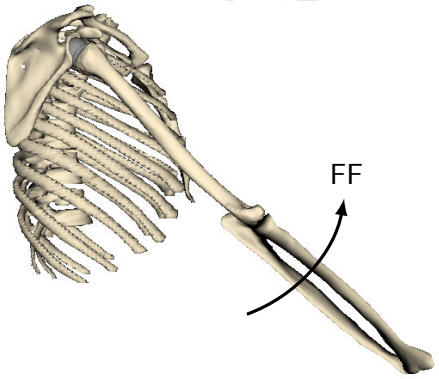

Figure 3.32 Forward flexion

3. Scapular plane elevation (SPE): humeral elevation in the scapular plane from 0° to 120°

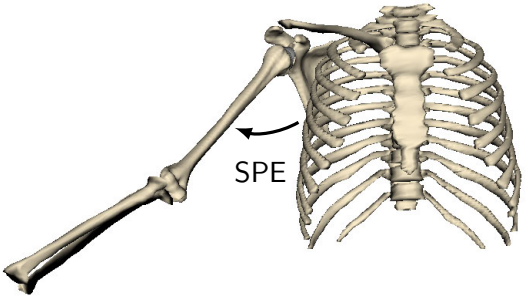

Figure 3.33 Scapular plane elevation

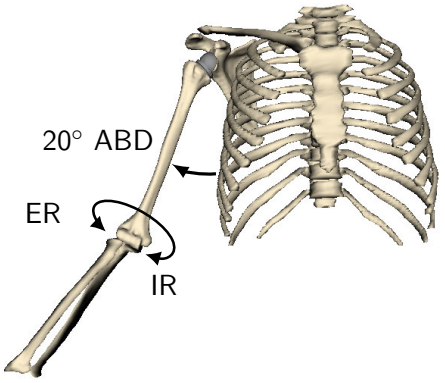

Figure 3.34 Rotation at 20° of humeral abduction

4. Rotation at 20° of humeral abduction:
   (a) Internal rotation (IR20): humeral rotation from 0° to 60°
   (b) External rotation (ER20): humeral rotation from -90° to 0°
5. Rotation at 90° of humeral abduction:

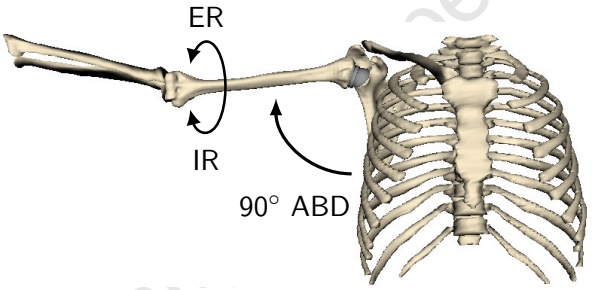

Figure 3.35 Rotation at 90° of humeral abduction

   (a) Internal rotation (IR90): humeral rotation from 0° to 60°
   (b) External rotation (ER90): humeral rotation from -90° to 0°

These motions, simulated in 5° increments, were characterised by humerothoracic angles (the position of the humerus relative to the thorax) and include clavicular and scapular kinematics (Section 3.2.1.2). For ABD, FF and SPE, the motions were limited to 120° based on the findings of Kwon et al. (2012), who reported a maximum elevation in RTSA recipients of 112°$\pm$ 12°. For the rotational motions, by convention, negative angles represent external rotation and positive angles represent internal rotation (Wu et al. 2005).

3.3.2 Outcome measures

Seven outcomes were measured during each motion to assess RTSA function:

1. **Glenohumeral joint positional changes**. The location of the glenohumeral joint centre of rotation (GH_{cor}) was measured relative to the origin of the scapular co-ordinate system (Figure 3.13) for the normal and reverse shoulders, and humeral head position (HH_{pos}) was measured relative to GH_{cor} for the reverse shoulders. As these were geometric properties established during model-set development, they were not measured with respect to a motion.

2. **Deltoid elongation (DE)**. DE was based on the NSM muscle length calculations for the normal and reverse shoulder model-sets. The elongation (in %) of the anterior, middle and posterior compartments of the deltoid were reported as a function of a given motion. Elongation was calculated as the change in muscle length between the reverse and normal shoulder, divided by the muscle length of the normal shoulder. An overall DE was calculated by arithmetically averaging the elongation in each of the deltoid compartments during each step of a motion. The peak of the overall DE was the primary measure for this outcome.

3. **Deltoid moment arm (DMA)**. DMA was based on the NSM muscle moment arm calculations for the normal and reverse shoulder model-sets. Moment arms are a measure of the effectiveness of a muscle to contribute to a motion (An et al. 1983; Sherman et al. 2013). The moment arms (in mm) of the three deltoid compartments for both model-sets were reported as a function of a given motion. An overall DMA was calculated by arithmetically averaging the moment arms of the deltoid compartments during each motion increment. The arithmetic mean of the overall DMA in the reverse shoulder was the primary measure for this outcome.

4. **Deltoid force (DF)**. DF was based on the results of the NSM load-sharing algorithm for the normal and reverse shoulder model-sets. These correspond to the exertion generated by the muscles during a motion and the summation of all the muscle forces is aligned with joint contact forces. The muscle forces (in N) of the three deltoid compartments for both model-sets were reported as a function of a given motion. An overall DF was calculated by arithmetically summing the muscle forces of the deltoid compartments during each motion increment.

5. **Joint contact force (JCF)**. JCF was based on the NSM joint force calculations for the normal and reverse shoulder model-sets. The GH joint contact force was projected into the glenoid reference frame for the normal shoulders and the glenosphere reference frame for the reverse shoulders. The resultant of the force (in N) was calculated and decomposed into its constitutive components; compression, superoinferior (SI) and anteroposterior (AP) shear.

6. **Stability ratio (SR)**. SR was measured using the JCF of the reverse shoulder. In this instance, the JCF was projected into the humeral cup reference frame and, during each step of a motion, SR was calculated by dividing the geometric stability ratio (SR_g, Equation 3.13 and Figure 3.36) by the ratio (R_{cs}) between the compression (F_c) and the shear (F_s) forces (Equation 3.14). If the arithmetic mean SR throughout the motion was greater than 1, R_{cs} was smaller than SR_g and the trajectory of the contact force was within the humeral cup, the compressive

force was greater than the shear force, and the joint was considered stable. The arithmetic mean SR was the primary outcome for this measure.

$$SR_g = tan\,(\theta_{hc}) = tan\left(arccos(\frac{R_{hc} - d_{hc}}{R_{hc}})\right) \tag{3.13}$$

$$F_c = F_{GH}^{Y} \qquad F_s = \sqrt{(F_{GH}^{X})^2 + (F_{GH}^{Z})^2} \qquad R_{cs} = \frac{F_c}{F_s} \qquad SR = \frac{SR_g}{R_{cs}} \tag{3.14}$$

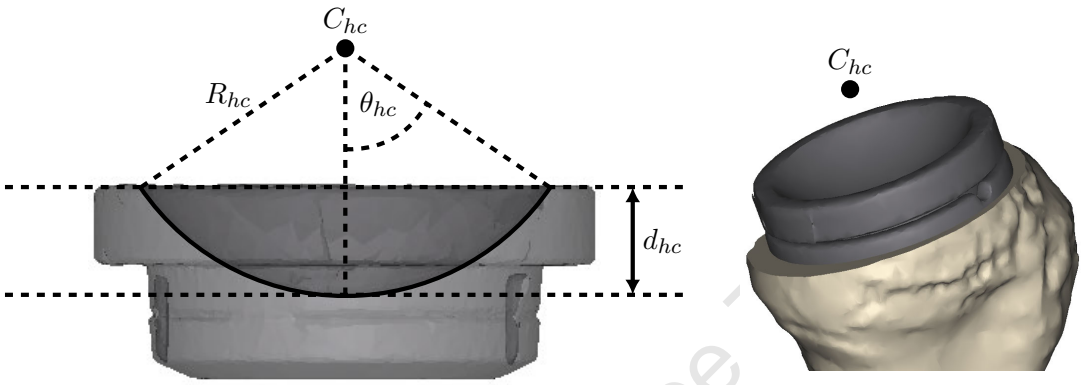

Figure 3.36 The geometric stability ratio makes use of the same parameters used by the prosthetic glenohumeral joint constraint. Here, the maximum geometric stability ratio is the tangent of the angle between the inner rim of the humeral cup and the deepest point in the humeral cup (Equation 3.13). The SR_g for the ⌀38 humeral cup is 1.48 (R_{hc} = 19 mm and d_{hc} = 10.65 mm)

7. **Impingement-free range of motion (IFROM)**. IFROM was calculated using the IDA and is the extent of a motion (in °) that is unobstructed by both intra- or extra-articular impingement. The maximum IFROM obtainable was 120° for ABD, FF and SPE, 60° for IR20 and IR90 and 90° for ER20 and ER90. The motions were simulated in 1° increments to refine the impingement detection process.

Note that for DE, DMA, and DF the individual contributions of the fascicles used to represent the anterior and posterior deltoid (Table 3.1) were averaged during each motion increment to obtain a generalised representation of these deltoid compartments.

3.3.3 Data processing

Descriptive statistics of the outcome measures were evaluated, and the data were represented using the subject average (with 95% confidence intervals) and box plots. In addition, the subject-averaged DE, DMA and JCF (in the glenoid, glenosphere and humeral cup reference frames) were plotted as functions of each motion.

3.4 Results

3.4.1 Glenohumeral joint positional changes

The subject-averaged locations of GH_{cor} and HH_{pos} for the normal and reverse shoulders are shown in Table 3.4. For the reverse shoulders, GH_{cor} was medialised by -29.55 mm (95% CI: -29.52, -25.96) and HH_{pos} was inferiorly translated by -26.74 mm (95% CI: -27.86, -25.63).

Table 3.4 Subject-averaged glenohumeral joint centre of rotation and humeral head position (in mm). Note that confidence intervals have been omitted, and the Diff column represents the difference between GH_{cor} for the normal and reverse shoulders

	GH_{cor}			HH_{pos}
	Normal	**Reverse**	**Diff**	**Reverse**
X-axis (Mediolateral)	-1.81	-29.55	**-27.74**	-1.08
Y-axis (Superoinferior)	-21.70	-24.38	-2.68	**-26.74**
Z-axis (Anteroposterior)	-41.57	-36.48	5.09	-0.12

3.4.2 Deltoid elongation

The elongation of the three deltoid compartments (and the overall deltoid) of the reverse shoulder during each of the assessed motions is shown in Figure 3.37.

Elongation for all three compartments of the deltoid during ABD, FF and SPE was at a maximum at the beginning of the motions and progressively decreased with increased elevation. Peak overall DE was 13.3% (95% CI: 12.2, 14.5) for ABD, 12.4% (95% CI: 11.3, 13.5) for FF and 13.5% (95% CI: 12.2, 14.7) for SPE (Figure 3.38). Conversely, during the rotational motions, smaller changes in elongation were observed, with peak elongations typically occurring at the end of the motion. Elongation during the rotational motions was also found to be a function of humeral elevation. At 90° of abduction the deltoid in the reverse shoulder was slightly shorter than in the normal shoulder. Peak overall DE was 10.4% (95% CI: 9.2, 11.5) for IR20, 9.5% (95% CI: 8.5, 10.5) for ER20, -0.8% (95% CI: -2.1, 0.5) for IR90 and -1.5% (95% CI: -2.7, -0.3) for ER90 (Figure 3.38).

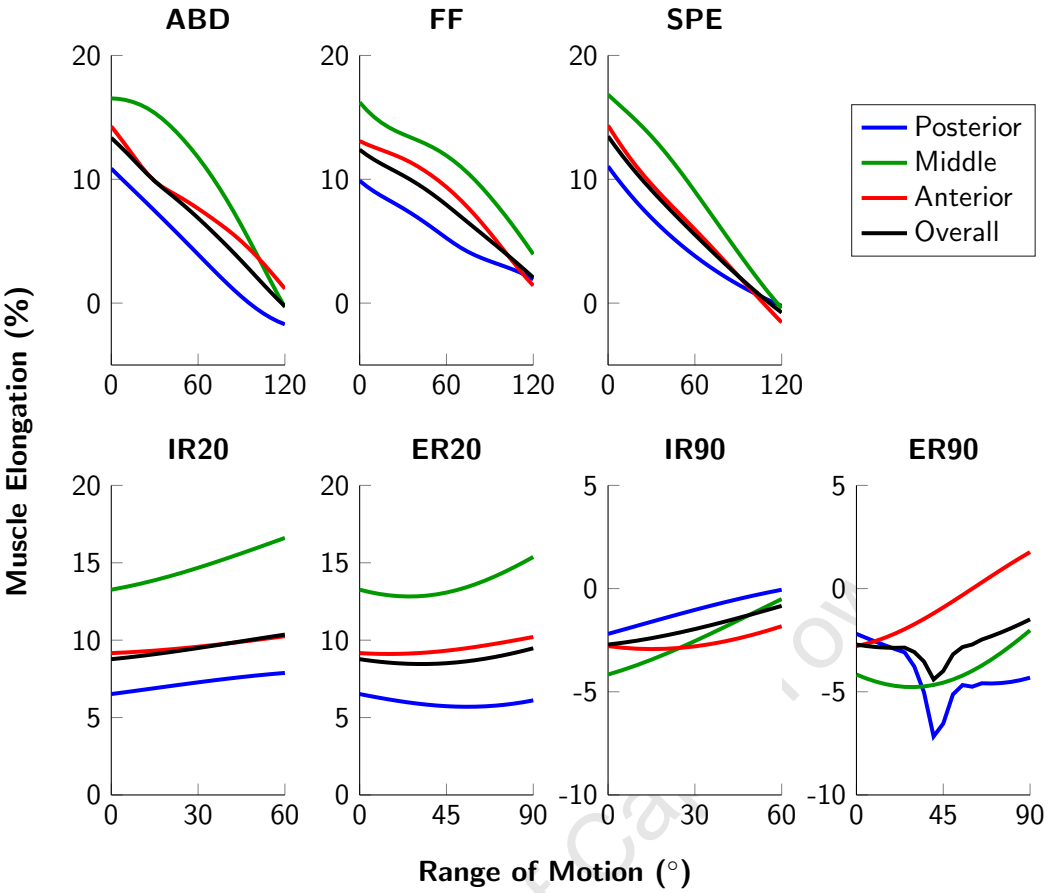

Figure 3.37 Subject-averaged deltoid elongation of the reverse shoulder. Note the posterior deltoid irregularity during ER90 is attributed to a muscle wrapping abnormality (see Section 3.5.8.2)

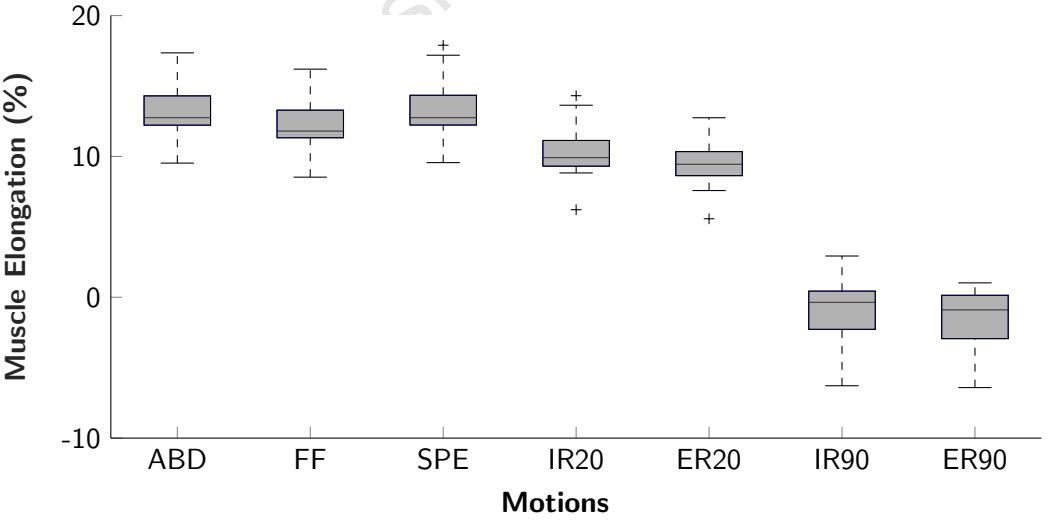

Figure 3.38 Box plots of peak overall deltoid elongation of the reverse shoulder. The box represents the interquartile range, the bar within the box represents the median value, and outliers are denoted by the "+" symbol

3.4.3 Deltoid moment arm

The moment arms of the deltoid for the normal and reverse shoulders are shown in Figure 3.39, and box plots of the mean overall DMA of the reverse shoulder are shown in 3.40. For ABD, FF and SPE positive values corresponded to agonistic moment arms and negative values corresponded to antagonistic moment arms. For the rotational moments, positive values corresponded to moment arms that internally rotate the arm and negative values corresponded to moment arms that externally rotate the arm. During ABD, FF and SPE, the moment arms of all three compartments increased throughout the motions and, consequently, the increase in mean overall DMA was 16.3 mm (95% CI: 15.2, 17.4), 14.5 mm (95% CI: 13.6, 15.5) and 17.7 mm (95% CI: 16.6, 18.7), respectively. The deltoid in the normal and reverse shoulder both produced external moment arms in IR20 and IR90. The mean overall DMA in the reverse shoulder increased externally by -2.7 mm (95% CI: -3.0, -2.4) and -2.5 mm (95% CI: -2.9, -2.2) for IR20 and IR90, respectively. The deltoid in the reverse shoulder transitioned from an external rotator to an internal rotator throughout ER20 and ER90. As a result, the mean overall DMA in the reverse shoulder increased internally by 0.6 mm (95% CI:0.3, 0.9) and 1.3 mm (95% CI: 1.0, 1.5) for ER20 and ER90, respectively.

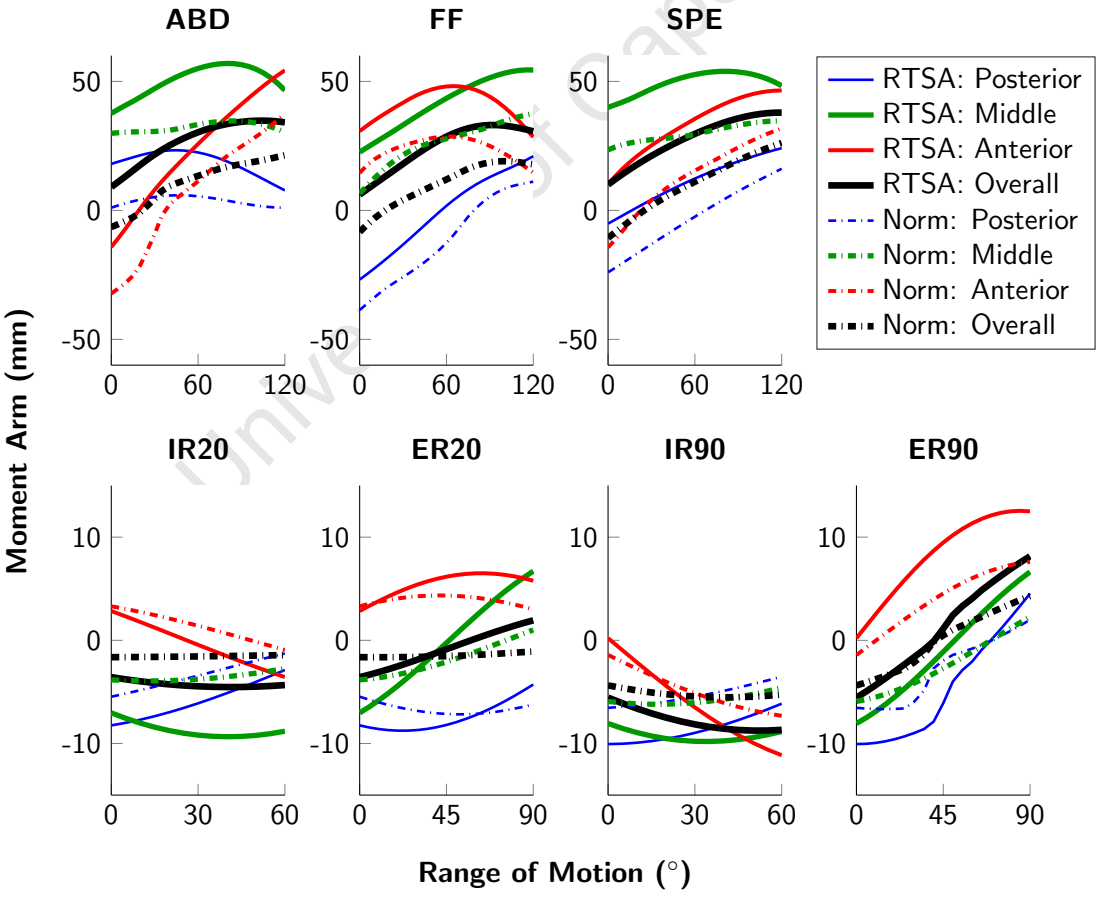

Figure 3.39 Subject-averaged deltoid moment arms of the normal and reverse shoulder. For the humeral elevations/rotations, positive and negative values correspond to the agonistic/internal and antagonistic/external moment arms, respectively

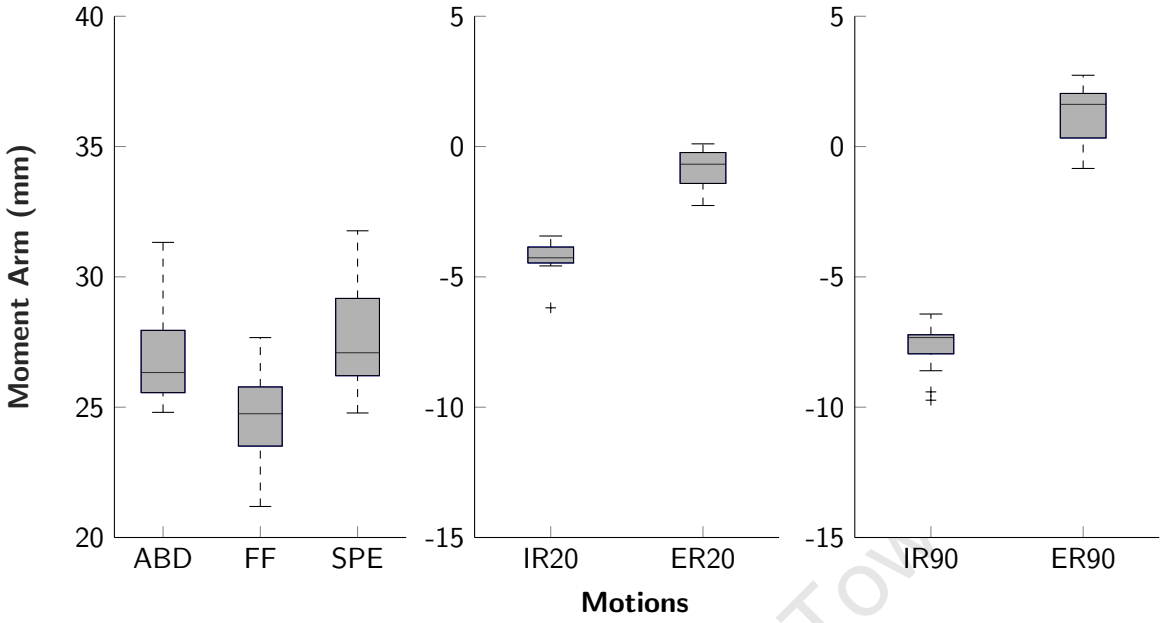

Figure 3.40 Box plots of mean overall DMA of the reverse shoulder

3.4.4 Deltoid forces

Despite a massive rotator cuff tear, stable solutions for the simulations were obtained by the load-sharing algorithm of the NSM and the forces generated by the deltoid for the normal and reverse shoulders are shown in Figure 3.41. For all the motions except FF and IR90, the mean overall deltoid force was increased in the reverse shoulder compared to the normal shoulder. These changes to mean overall deltoid force are shown in Table 3.5.

Table 3.5 Subject-averaged change in mean overall DF (in N) of the reverse shoulder (with 95% confidence intervals

Motion	DF Change (in N)
ABD	13.4 (5.4, 21.5)
FF	-48.4 (-65.7, -31.1)
SPE	118.0 (102.3, 133.7)
IR20	129.6 (110.1, 149.1)
ER20	70.8 (59,7, 81.8)
IR90	-63.1 (-73.3, -52.9)
ER90	38.6 (25.0, 52.3)

The primary source of the increases for SPE, IR20, and ER90 can be attributed to the change in anterior deltoid force; whereas, the ABD increase can be attributed to the change in posterior deltoid force. Conversely, the decrease in FF is primarily due to the change in anterior deltoid force and the decrease in IR90 is due to changes in the middle and posterior deltoid forces.

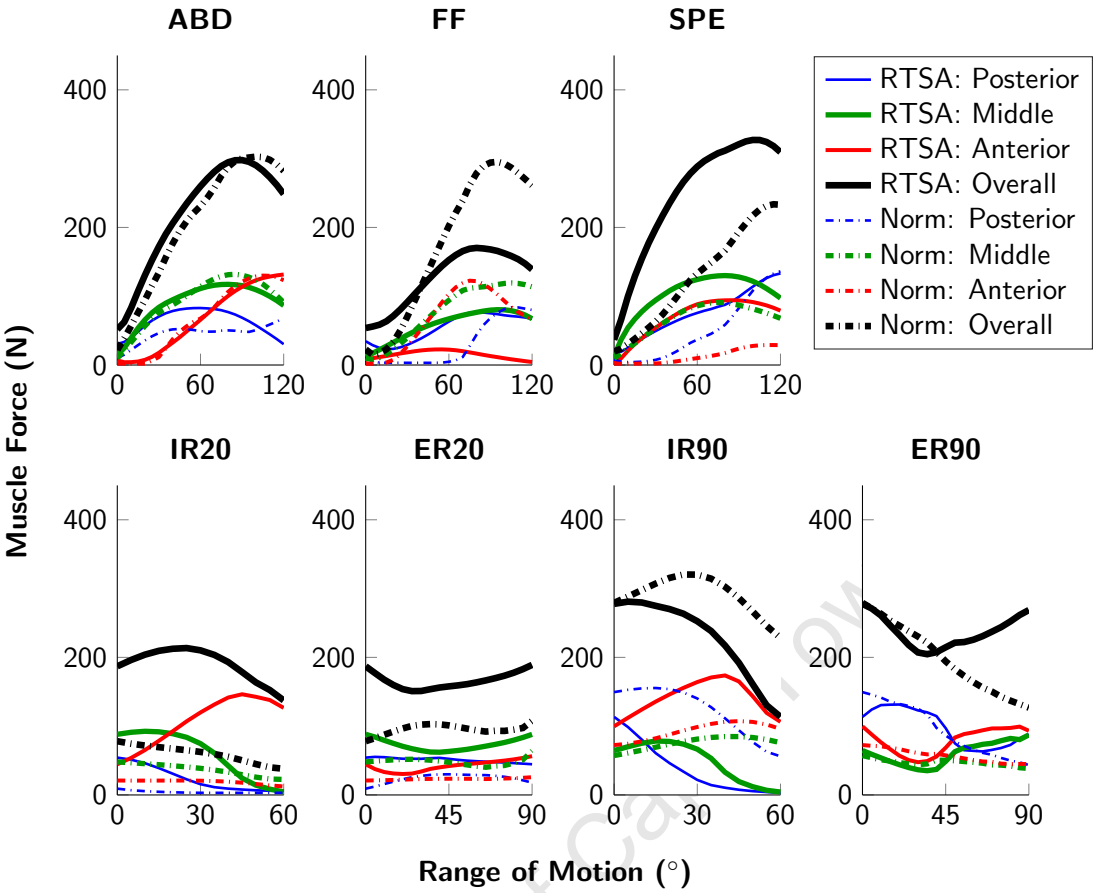

Figure 3.41 Subject-averaged deltoid forces of the normal and reverse shoulder

3.4.5 Joint contact force

The JCF of the normal and reverse shoulders during each of the assessed motions are shown in Figure 3.42. Positive values in these graphs correspond to joint compression and shear of the joint in the superior and anterior directions, and negative values correspond to the opposite directions.

The resultant JCF decreased in the reverse shoulder during each motion (Table 3.6). For both the normal and reverse shoulder, joint compression was the primary component of the resultant force during ABD, FF and SPE and it decreased throughout these motions in the reverse shoulder. SI shear was predominately directed inferiorly in the normal shoulder during ABD and FF, and became superiorly directed in the reverse shoulder. Whereas, during SPE, SI shear was negligible in the normal shoulder and was superiorly directed in the reverse shoulder. AP shear also changed in the reverse shoulder, going from posterior to anterior in ABD and from posterior to negligible in SPE.

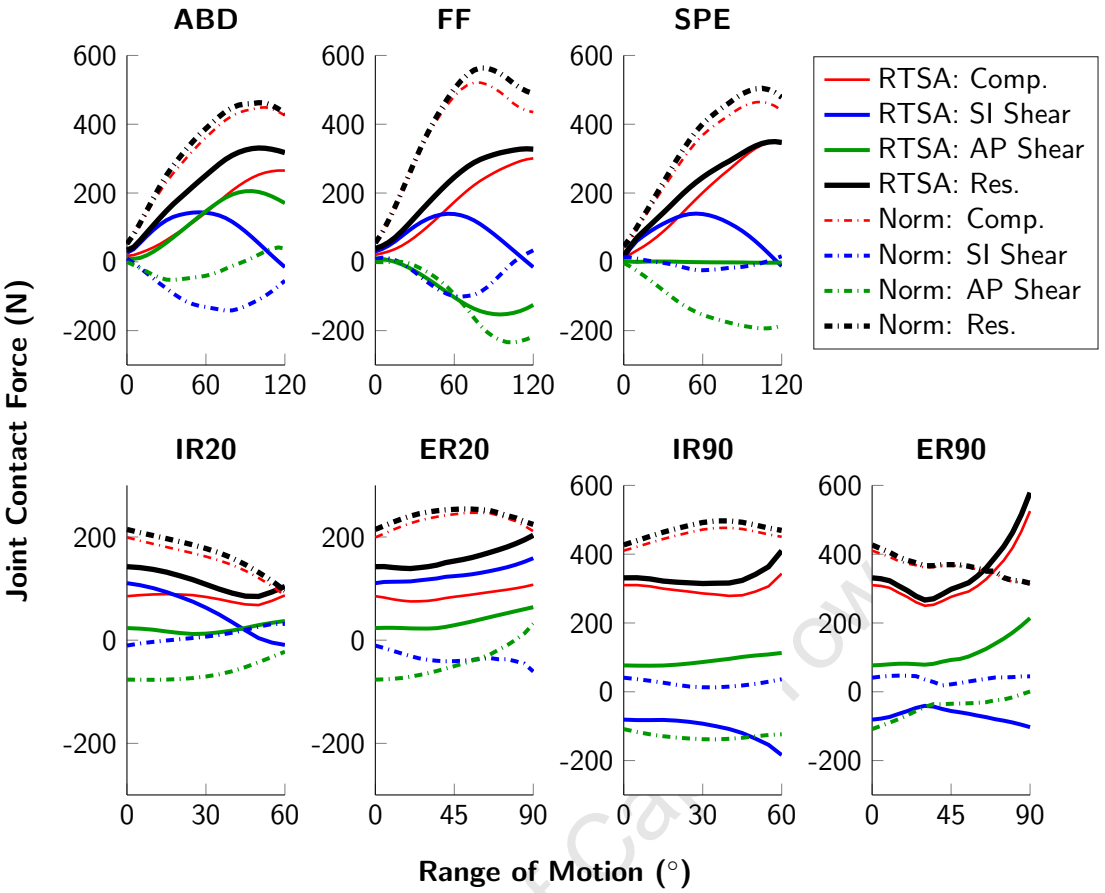

Figure 3.42 Subject-averaged JCF of the normal and reverse shoulder. JCF in the normal shoulder was evaluated in the glenoid reference frame and JCF in the reverse shoulder was evaluated in the glenosphere reference frame. Note that Res. refers to the resultant JCF

The primary component of the resultant JCF was compression for both normal and reverse shoulders during the rotational motions, except for ER20. In this instance the SI shear and compression were both primary components of the resultant force. It is evident that JCF was a function of humeral elevation, with IR90 and ER90 producing noticeably larger forces compared to IR20 and ER20. Additionally, the resultant JCF in reverse shoulder was greater than the normal shoulder by the end of ER90.

Table 3.6 Subject-averaged decrease in peak resultant JCF (in %) of the reverse shoulder (with 95% confidence intervals)

Motion	JCF Decrease (%)
ABD	28.9 (25.7, 32.1)
FF	42.2 (40.1, 44.4)
SPE	30.5 (28.0, 33.0)
IR20	32.1 (26.5, 37.7)
ER20	21.3 (18.2, 24.4)
IR90	18.0 (9.8, 26.2)
ER90	-35.5 (-47.6, -23.5)

3.4.6 Stability ratio

The compression and shear forces of the prosthetic glenohumeral joint (in the humeral cup reference frame) during each of the assessed motions are shown in Figure 3.43. The compressive component of the JCF was greater than the shear component for all assessed motions, therefore, all the motions had a mean SR of greater than 1.

ABD, FF and SPE exhibited similar distributions for compression and shear, both of which increased during the motion. The corresponding mean SR was 5.7 (95% CI: 5.5, 6.0), 6.7 (95% CI: 6.3, 7.1) and 5.9 (95% CI: 5.4, 6.4) for ABD, FF and SPE, respectively. During IR20 and IR90 the compressive force in the joint decreased whilst the shear force increased, and, by the end of both motions, these two forces were nearly equivalent. Consequently, these motions had the smallest mean SR values, 3.9 (95% CI: 3.2, 4.7) and 3.6 (95% CI: 3.5, 3.7) for IR20 and IR90, respectively. During ER20 both compression and shear remained somewhat constant and the corresponding mean SR was 5.9 (95% CI: 5.6, 6.3). Joint compression during ER90 fluctuated and peaked at the end of motion, whereas, shear remained constant until increasing slightly by the end of the motion, therefore, the mean SR for this motion was 4.5 (95% CI: 4.4, 4.6). Box plots of mean SR of the reverse shoulder are shown in Figure 3.44.

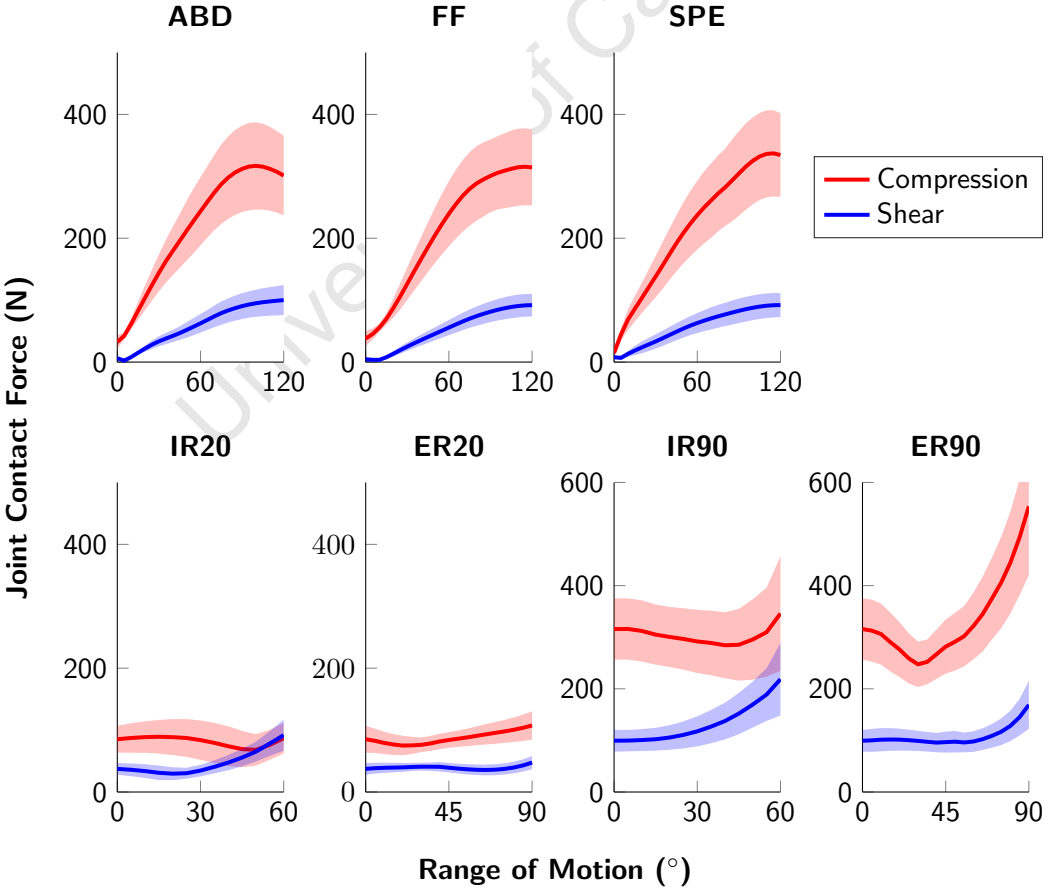

Figure 3.43 Joint compression and shear forces in the humeral cup. Solid lines represent subject-averaged forces and translucent areas represent the corresponding one standard deviation

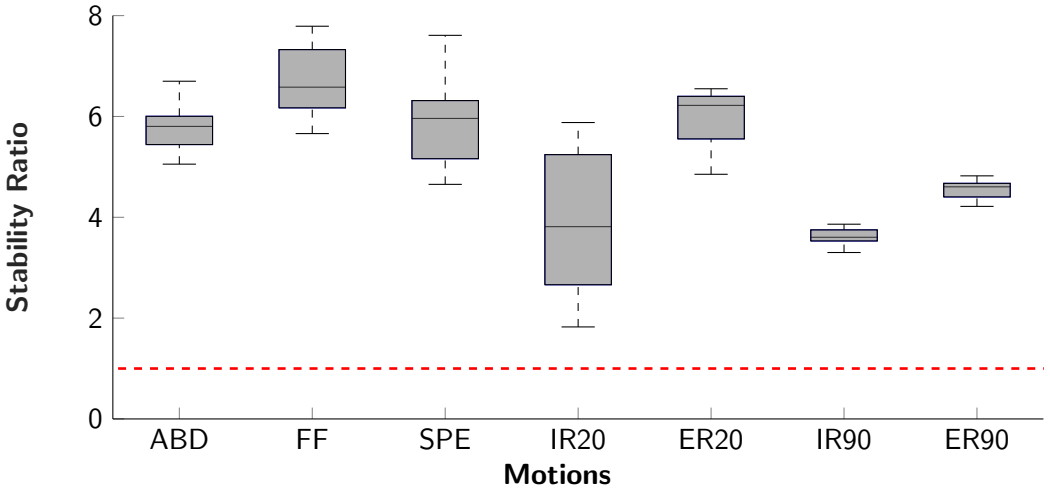

Figure 3.44 Box plots of the mean SR of the reverse shoulder. Note that none of the motions exhibited a stability ratio of less than 1 (dotted red line)

3.4.7 Impingement-free range of motion

Box plots of the IFROM results are shown in Figure 3.45. The mean IFROM for ABD, FF and SPE were 55.3° (95% CI: 43.6, 66.9), 83.5° (95% CI: 74.0, 93.1) and 98.3° (95% CI: 90.0, 106.5), respectively. For the rotational motions, IFROM decreased with increased humeral elevation. Mean IFROM for IR20 was 34.6° (95% CI: 19.5, 49.7) and decreased to 25.9° (95% CI: 17.6, 34.3) for IR90. Whereas, the mean IFROM was 20.1° (95% CI: 6.2, 33.97) for ER20 and decreased to 1.6° (95% CI: 0, 3.8) for ER90.

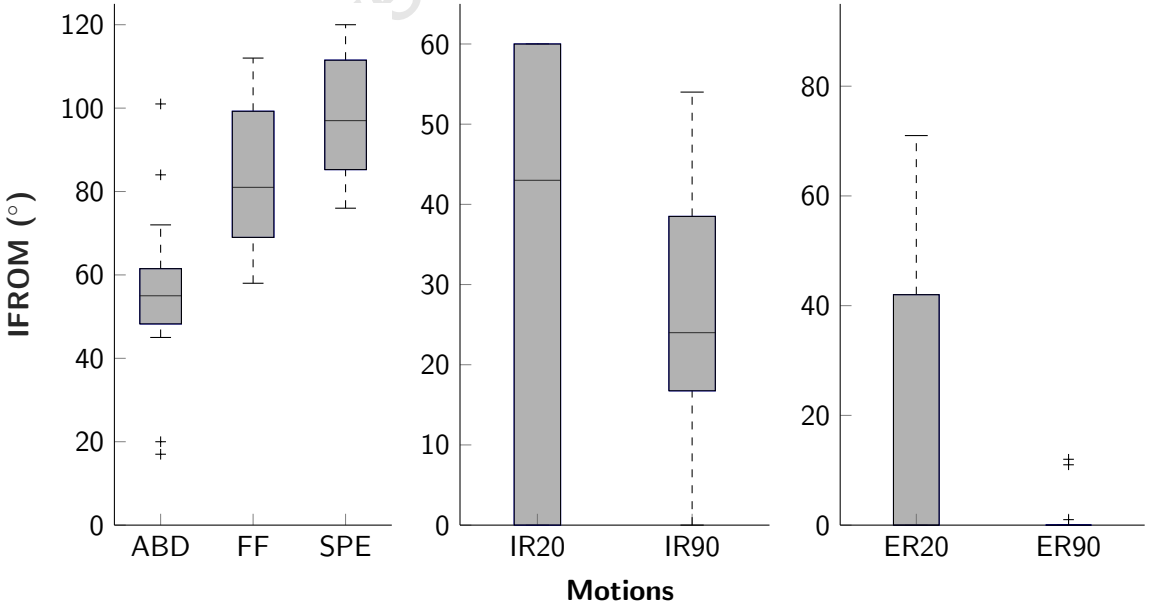

Figure 3.45 Box plots of reverse shoulder IFROM

3.5 Discussion

3.5.1 Glenohumeral joint positional changes

As mentioned in Section 2.4, RTSA medialises the centre of rotation of the glenohumeral joint and lowers the position of the humerus. Both criteria were met during the development of the reverse shoulder model-set as GH_{cor} was medialised by -29.55 mm and HH_{pos} was inferiorly translated by -26.74 mm. However, the magnitudes of these changes are dependent on the design of the prosthesis and can have intra-operative variation. For example, the results of the current study are aligned with those of Saltzman et al. (2010), who reported a 28.0 mm $\pm$ 3.3 medialisation of the GH_{cor} when using the Delta prosthesis. Comparatively, 20.9 mm $\pm$ 3.9 and 17.3 mm $\pm$ 1.8 medialisations have been reported for the Biomet and Tornier prostheses, respectively (Ackland et al. 2010; Henninger et al. 2012b).

3.5.2 Deltoid elongation

Peak elongation of the deltoid was observed when the arm was fully adducted (0° of humeral elevation) and was found to be an average of 13.1% across ABD, FF and SPE (Figure 3.38). This result compares favourably with the literature. A clinical follow-up by Jobin et al. (2012) found that the deltoid elongated by 17% and biomechanical studies by De Wilde et al. (2004) and Roche et al. (2013) found that the deltoid elongated by 12.9% to 16.4%.

Elongation of the deltoid is necessary to re-tension the muscle and alter its biomechanics such that it can restore shoulder function (Boileau et al. 2005). However, there are concerns regarding excessive elongation. If the deltoid is over-tensioned, it may induce acromial stress fractures, neurological damage or abnormal activation of the muscle (Boileau et al. 2006; Lädermann et al. 2009; Hamid et al. 2011; Levy et al. 2013; Walker et al. 2014). Despite the acknowledgement of this concern, there appears to be no general consensus regarding the quantification of excessive elongation, rather, suggestions have been made that 10% to 20% elongation should be targeted (Roche et al. 2013). Consequently, in order to be conservative during the analyses conducted in the subsequent chapters, elongation of the overall deltoid greater than 20% was viewed as excessive.

3.5.3 Deltoid moment arms

RTSA changes the biomechanics of the deltoid through medialisation of the glenohumeral joint centre of rotation and inferior translation of the humerus. In doing so, the moment arm of the deltoid is increased during motions that elevate the arm (Boileau et al. 2005). Table 3.7 compares the peak moment arms of the middle deltoid predicted in the current study during ABD, FF and SPE with those reported in biomechanical studies.

Table 3.7 Peak moment arm (in mm) of the middle deltoid in the reverse shoulder during ABD, FF and SPE

Study	ABD	FF	SPE
Current study	57.0	54.5	53.9
van der Helm (1998)	52.0		
De Wilde et al. (2004)			59.4
Terrier et al. (2008)			50.0
Kontaxis and Johnson (2009)	55.1	52.8	55.3
Ackland et al. (2010)	47.0	28.0	

Overall, these results compare well, with the greatest differences in the moment arms observed between the current study and Ackland et al. (2010) for ABD and FF. This is likely attributed to differing research techniques. Ackland et al. (2010) utilised the University of Melbourne cadaveric shoulder model (Section 3.4.2) and suggested that the moment arms they reported may be smaller due to lower muscle volumes typically found in elderly cadavers.

Smaller moment arms were produced during the rotational motions compared to ABD, FF and SPE. In general, these moment arms were antagonistic; the deltoid acted as an external rotator during internal rotation and transitioned from an external rotator to an internal rotator during external rotation. Similar findings regarding the decreased magnitude and trend of the deltoid moment arms during rotation were reported using the University of Melbourne cadaveric shoulder model (Ackland and Pandy 2011; Ackland et al. 2012). They also observed that the deltoid was predominately an external rotator when the arm was abducted.

3.5.4 Deltoid forces

Compared to the normal shoulder, the overall deltoid force in the reverse shoulder was increased in majority of the motions simulated, except for FF and IR90 as indicated in Table 3.5. This finding is in opposition to the DMA results, which suggest that the deltoid should exert less force during elevation due to an increased moment arm. For ABD and SPE, this discrepancy can be explained by the deltoid in the reverse shoulder producing forces that counteract the massive rotator cuff tear (Kontaxis 2009). Conversely, for FF, there was a noticeable decrease in overall deltoid force and may be attributed to the teres minor contributing to the motion due to the prosthesis changing the line of action of this muscle (Kontaxis 2009). In the current study the mean teres minor force was 2.2 N (95% CI: 1.6, 2.9) for the normal shoulder; comparatively, the teres minor produced a mean force of 38.2 N (95% CI: 32.6, 43.8) for the reverse shoulder (note: this data, along with the forces generated by the other upper extremity muscles, were calculated during the NSM simulations).

With regards to the humeral rotations, these motions were dependent on the effect of arm weight, which increased with increased elevation. At 20° of abduction, the effect of arm weight was small and the reverse shoulder was able to produce IR20 and ER20 with somewhat uniform increases in the forces produced by all the deltoid compartments. Whereas, at 90° of abduction, due to an

increased effect of arm weight, large differences in overall deltoid force can be observed towards the end of IR90 and ER90. This suggests that, without a rotator cuff, the deltoid might struggle to produce the achieve these positions.

It should be acknowledged that comparisons of deltoid forces to biomechanical literature are difficult due to differences in rotator cuff configurations. For example, a cadaveric study by Henninger et al. (2012b) reported an approximate 70 N reduction in the cumulative deltoid force in the reverse shoulder at 60° of SPE and a modelling study by Liou et al. (2017) reported a 112 N reduction in peak overall deltoid force in the reverse shoulder during SPE. However, in both instances, the rotator cuff muscles were preserved and, as a consequence, the load required to elevate the reverse shoulder was shared amongst these muscles and the deltoid.

3.5.5 Joint contact force

The peak of the resultant JCF was found to decrease during all the motions, except for ER90 as indicated in Table 3.6. As JCF is representative of the summation of the muscle forces, these decreases were mainly caused by the removal of the rotator cuff. In the normal shoulder, the rotator cuff helps to stabilise the joint by pulling the head of the humerus towards the glenoid fossa, thereby compressing the joint and producing inferior shear (Ackland et al. 2011). There are a number of studies that have characterised JCF changes in the reverse shoulder during ABD, FF and SPE. Table 3.8 highlights these results in comparison to those of the current study.

Table 3.8 Decrease in peak resultant joint contact force (in %) for the reverse shoulder during ABD, FF and SPE

Study	ABD	FF	SPE
Current Study	28.9	42.2	30.5
Terrier et al. (2008)			50.0
Kontaxis and Johnson (2009)	32.9	20.0	41.0
Ackland et al. (2011)		52.7	54.7
Hoenecke et al. (2014)			37.0
Liou et al. (2017)	27.8	20.1	

As can be seen, there is a relatively large range in the reported decreases in the resultant JCF of the reverse shoulder. These range may be attributed to factors like differences in research techniques (cadaveric versus musculoskeletal simulations), post-surgical rotator cuff status and prosthesis design. Taking this range into consideration, the JCF results of the current study agree with literature.

There is limited biomechanical data available for JCF during the rotational movements, making direct comparisons difficult. Liou et al. (2017) measured joint forces during rotation; however, they kept the rotator cuff intact and performed the rotation at only 10° of humeral abduction. Both of these factors diminish the comparability between studies as the rotator cuff contributes to joint stability and, as can be seen in Figure 3.42, humeral elevation increases JCF as the joint must counteract the weight of the arm. That being said, Werner et al. (2005) observed that the deltoid

is unable to control external rotation when the arm is elevated in the reverse shoulder and this may explain why there was a marked increase in the overall deltoid force and resultant JCF at the end of ER90 (Figures 3.41 and 3.42, respectively) and suggests that an RTSA recipient with a massive rotator cuff tear may find this motion difficult (or impossible) to achieve.

3.5.6 Stability Ratio

Cadaveric studies have estimated joint stability by calculating the force required to anteriorly dislocate the joint (Henninger et al. 2012a; Clouthier et al. 2013). The application of a force in this manner is analogous to the shear force in the humeral cup. Henninger et al. (2012a) found that force required to dislocate the joint was approximately 290 N when the arm was at rest. Whereas, Clouthier et al. (2013) found that the dislocating force was approximately 190 N at 45° of humeral elevation. In comparison, the peak shear force in ABD, FF and SPE was only 100.1 N (95% CI: 86.2, 113.9) in the current study. Therefore, dislocation of the joint in this instance was unlikely as the average shear force was well below these dislocation forces, and the corresponding SR values were considered reasonable.

3.5.7 Impingement-free range of motion

Impingement in the reverse shoulder is heavily dependent on both the shape of the scapula in the vicinity of the glenohumeral joint and the design and placement of the prosthesis. The effect of scapula shape is exemplified by the IFROM results of the current study, especially for the rotational motions. While the mean IFROM in IR20 was 34.6°, the box plots highlighted the subject-specific variability; some models exhibited motion that was completely free from impingement, whereas, others were susceptible to impingement throughout the motion. Figure 3.46 provides an example of the differences between the shapes of two scapula in the model-set and its effect on impingement. The subject on the left has flattened infraglenoid tubercle and, as a consequence, the humeral cup is impinged upon the bone at 45° of IR20. On the other hand, the subject on the right has a recessed infraglenoid tubercle and the cup did not impingement upon the bone at the same position.

Taking these factors into consideration, the subject-averaged IFROM results of the current study align with the findings in literature. Kontaxis and Johnson (2009) utilised the Delta III prosthesis and reported an average IFROM of 59.8° (out of a possible 150°) across ABD, FF and SPE. Whereas, Berhouet et al. (2014a) utilised the Biomet prosthesis and reported an average IFROM of 93.3° (out of a possible 150°) across the same motions. The corresponding metric for the current study falls in between these two values, at 79.0° (out of a possible 120°). Table 3.9 provides a comparison between the results of the current study and literature for the IFROM characteristics observed at 20° of humeral elevation.

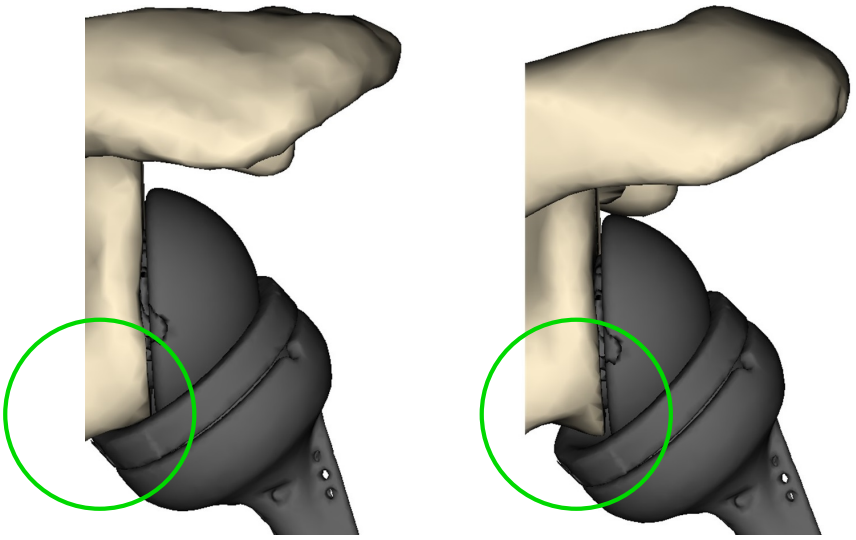

Figure 3.46 Differences in impingement profiles of two subjects in the model-set at 45° of IR20. The region where impingement may occur during IR20 is indicated by the circles

Table 3.9 Average IFROM results (in °) for internal and external rotation at 20° of humeral abduction

Study	Humeral version	Subjects	Prosthesis	IR20	ER20
Current study	20° Retroversion	15	Delta XTEND	34.6	25.9
Gulotta et al. (2012)	20° Retroversion	6	Biomet Comprehensive	61.0	48.0
Berhouet et al. (2013)	Native	40	Aequalis Reversed	33.8	31.1
Kontaxis et al. (2017)	20° Retroversion	30	Biomet Comprehensive	68.2	57.5

The rotational IFROM results for the current study are slightly smaller than those found in literature. However, the same trend of increased IFROM in internal rotation compared to external rotation when the humerus was implanted at 20° of retroversion was observed across all the studies. Additionally, the differences in IFROM magnitudes can be explained by differences in prosthesis design. The Biomet Comprehensive prosthesis has a lateralised centre of rotation and uses a 135° neck-shaft angle. In comparison, the Delta XTEND prosthesis is a Grammont-style prosthesis, with a medialised centre of rotation and a 155° neck-shaft angle. As a result, the humeral cup of the Biomet prosthesis is shifted away from scapula and is less likely to impinge upon the infraglenoid tubercle than the Delta XTEND during rotation at low elevation angles.

Figure 3.45 demonstrated a decrease in rotational IFROM when the arm was abducted compared to when it was adducted. This trend was also identified by Berhouet et al. (2014a). In their study, which utilised the Biomet Comprehensive prosthesis, rotational IFROM decreased from 135° when the arm was adducted to 12° when the arm was adducted. Similarly, during the current study, rotational IFROM decreased from an average of 60.5° when the arm was adducted to 21.7° when the arm was abducted.

3.5.8 Limitations

There are limitations that need to be taken into consideration when interpreting the results of this chapter. These can be broadly categorised into limitations originating from the reverse shoulder model-set, the NSM and the impingement-detection algorithm.

3.5.8.1 Reverse shoulder model-set

The CT scans of healthy shoulders (with no radiographic evidence of osteoarthritis) were used to construct the reverse shoulder model-set. Patients with osteoarthritis may require additional reaming to achieve neutral version of the glenoid resection angle. This would further medialise the centre of rotation of the GH joint and may have an impact on functional outcomes. In addition, the CT scans were sourced from the SICAS Medical Image Repository and, consequently, were only representative of a single demographic. Studies have demonstrated anatomical variations of the scapula and humerus between demographics (Matsumura et al. 2016; Zhang et al. 2016; Dey et al. 2018). These may affect the implantation of the prostheses during the surgery and its functional outcomes.

A single implant size was used for all the subjects in the reverse shoulder model-set. While commercially-available implants offer size variations to address anthropometric differences, a fixed size was chosen to isolate the effect of prosthesis modifications on the outcome measures. Consequently, these results are specific to the Delta XTEND prosthesis and the effect of the modified prosthesis configurations may not be applicable to other prosthesis designs.

20° of retroversion was used to resect the humeral head and, as mentioned in Section 2.4.3.6, a consensus regarding which version angle to use has not been established. However, 20° of retroversion is believed to be an adequate compromise for deltoid biomechanics and impingement characteristics (Stephenson et al. 2011; Gulotta et al. 2012; Roche et al. 2013; Berton et al. 2015).

A massive rotator cuff tear was simulated during the development of the reverse shoulder model-set as it was representative of the primary indication for RTSA. However, due to the expanding indications for the prosthesis, surgeons often attempt to preserve as much of the rotator cuff as possible and this can lead to differing post-surgical configurations of the rotator cuff between patients. As such, the current study was an assessment of the worst-case scenario for the prosthesis and did not consider different rotator cuff configurations.

The models created during the reverse shoulder model-set development process are partially patient-specific as only the humerus and scapula were reconstructed from the CT scans and scaled to fit the default geometry of the NSM. Ideally, the other bones (clavicle, thorax, radius and ulna) should be reconstructed and incorporated into the NSM using the original scale of each subject. However, this would have been a time-consuming process that may not have yielded substantially different results.

3.5.8.2 Newcastle shoulder model

The NSM simplifies the musculature of the shoulder by modelling the muscles as elastic strings, and by dividing the broad muscles into numerous strings that are indicative of their anatomical division into fascicles. Charlton and Johnson (2006) found that this technique can have an impact on how the load-sharing protocol calculates the forces required by the muscles to enact a motion in comparison to other shoulder models developed by van der Helm and Veenbaas (1991) and Veeger et al. (1997) that did not compartmentalise the broad muscles. They also identified differences in the physiological cross-sectional areas of the muscles (which are used to determine the maximal forces that can be generated by the muscles) between the NSM and these other shoulder models, and this could alter simulation results. The NSM is unable to account for the effect of inertia during rapid arm movement. Consequently, a low speed, quasi-static approach was used to mitigate inertial effects. This limits the use of the NSM for the analysis of ballistic motion (such as cricket bowling or baseball pitching). However, given the nature of RTSA, recipients of the prosthesis are unlikely to perform these types of motions. In addition, the NSM neglects translation of the glenohumeral joint in the normal shoulder model-set. This may have a slight effect on the results of the simulations using the normal shoulder model-set.

The NSM uses basic geometric shapes to approximate the bone geometries around which the muscles wrap. These shapes, and the way OpenSim calculates the pathways of the muscles around the wrapping objects, can cause a muscle to incorrectly unwrap or adopt an impossible trajectory at certain points of a motion (Figure 3.47). Marsden et al. (2008) and Kontaxis (2009) have documented this problem and it continues to be a challenge for researchers, with some opting for volumetric muscle models (Webb et al. 2014). However, these models are currently complex and computationally expensive.

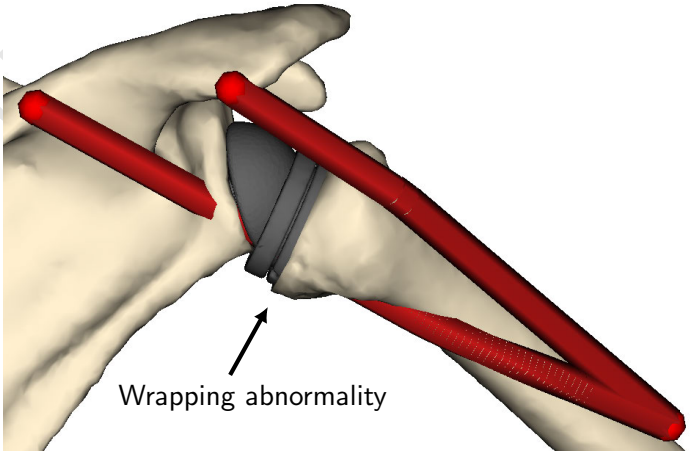

Figure 3.47 Wrapping abnormality of the posterior deltoid during forward flexion. Note that one of the strings unwrapped from the humeral head and was forced to pass through the bones and prosthetic components

The kinematics used to simulate the motions were derived from the measurements of healthy subjects (Barnett et al. 1999; Marchese and Johnson 2000). This was a warranted compromise as Kontaxis and Johnson (2009) demonstrated highly variable post-RTSA kinematic and, consequently, no regression equations have been developed to generalise scapulothoracic and clavicular kinematics in the reverse shoulder. To circumvent this issue, Kontaxis and Johnson (2009) recommended the usage of patient-specific data. However, as the collection of this data were outside the scope of the thesis, two options were available. The first option was to implement no scapulothoracic and clavicular kinematics (as is typical of cadaveric studies) and the second option was to use healthy kinematics (limited to 120°, based on the findings of Kwon et al. (2012)). The latter option was chosen as, even if healthy shoulder kinematics under-estimate reverse shoulder kinematics, its usage was more representative of *in-vivo* conditions than the former option. That being said, it should still be acknowledged that kinematic differences may have an effect on muscle activity and joint contact forces and could be the cause of abnormal deltoid function (Walker et al. 2014).

3.5.8.3 Impingement detection algorithm

The IDA uses a sphere to approximate the lateral surface of the humeral head for the sake of computational efficiency. Consequently, the sphere may slightly over or underestimate the exact point at which extra-articular impingement occurs. An example of this phenomenon was shown in Figure 3.26(c) during the description of the IDA.

3.6 Conclusion

This chapter has described the NSM, and the development of the IDA and the normal and reverse shoulder model-sets. These were used to assess the functional outcomes of the reverse shoulder during seven standardised motions that either elevated or rotated the humerus and form the basis for activities of daily living. The outcome measures evaluated during each of these motions were glenohumeral joint positional changes, deltoid elongation, deltoid moment arms, glenohumeral joint contact forces, stability ratio and impingement-free range of motion.

The results of this assessment reaffirm the fundamental design philosophy of RTSA; that is, the ability of the prosthesis to adequately restore function to a rotator cuff deficient shoulder. This was accomplished by reversing the orientation of the glenohumeral joint and modifying the location of its centre of rotation. In doing so, the biomechanics of the deltoid are altered, and it restore mobility and stability to a shoulder with an irreparably damaged rotator cuff. However, these modifications also resulted in intra- and extra-articular impingement, which can negatively impact the long-term viability of the joint replacement.

In addition, these results were compared to biomechanical literature of a similar nature. A generally good agreement was observed for all the outcome measures evaluated during the motions

that elevated the arm, and for IFROM, DE and DMA during the rotational motions. In these instances, the differences between the findings of the current study and literature can be attributed to factors such as research techniques, anatomical variability and prosthesis design. In contrast, the JCF and SR outcome measures evaluated during the rotational motions were not adequately corroborated due to a scarcity of equivalent biomechanical literature.

In Chapter 4 these functional outcomes will be used as default (or control) values, against which the effect of the prosthesis modifications will be compared. Consequently, modifications will be characterised as either having a beneficial, detrimental or negligible impact on reverse shoulder function. In turn, this characterisation will help to determine the optimised configuration of the prosthesis, as will be discussed in Chapter 5.

Chapter 4

Effect of modifying prosthesis configuration on reverse shoulder functional outcomes[1]

4.1 Introduction

Reverse total shoulder arthroplasty (RTSA) modifications have been proposed to address complications that negatively impact its functional outcomes and longevity. These modifications, as highlighted in Section 2.4.3, alter the design and configuration of the prosthesis and have biomechanical trade-offs (Gutiérrez et al. 2008a; Kontaxis and Johnson 2009; Roche et al. 2013; Hoenecke et al. 2014; Hettrich et al. 2015; Liou et al. 2017). In general, trade-offs occur due to an antagonistic relationship between the effect a modification has on impingement characteristics and the kinematic and kinetic properties of the reverse shoulder (Kontaxis and Johnson 2009). The aim of this chapter is to comprehensively evaluate the biomechanical effect of modifying RTSA configuration on functional outcomes using the assessment framework that was established in Chapter 3.

4.2 Materials and methods

4.2.1 Assessment framework

A flowchart of the assessment framework is shown in Figure 4.1. It highlights the manner in which outcome measures (Section 4.2.4) were evaluated for each model in the reverse shoulder model-set during motions simulated by the Newcastle Shoulder Model (NSM) and impingement detection algorithm (IDA), where N_i was the total number of models in the set and N_k was the total number of motions simulated (Section 4.2.3). The framework was expanded to include the capability of assessing both the default and modified configurations (Section 4.2.2) of the prosthesis (where N_j the total number of modified configurations assessed).

[1] An aspect of this chapter was evaluated in a study titled "Effect of humeral tray placement on impingement-free range of motion and muscle moment arms in reverse shoulder arthroplasty". It was presented at the 2017 Orthopaedic Research Society Annual Meeting and it is currently under review with Clinical Biomechanics (Appendix B).

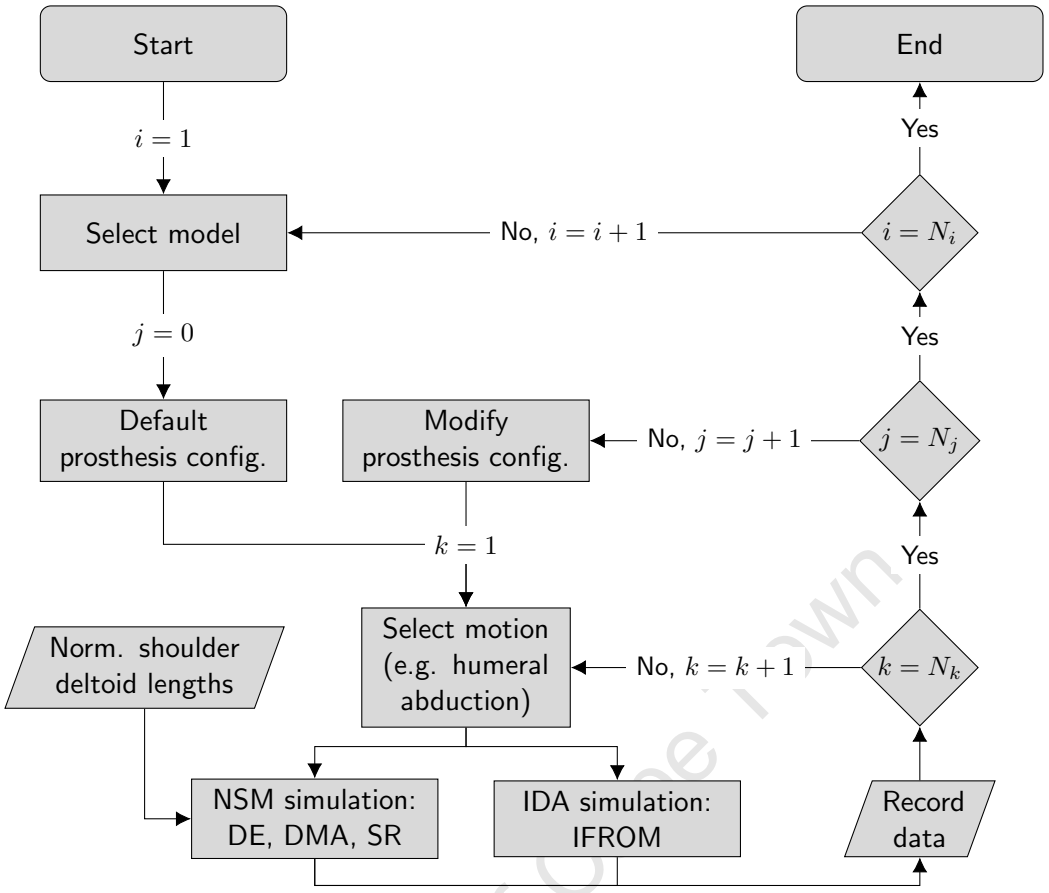

Figure 4.1 Flowchart of the assessment framework. $N_i = 15$, $N_j = 36$ (Section 4.2.2) and $N_k = 7$

4.2.2 Prosthesis modifications

Prosthesis modifications were incorporated into the reverse shoulder model-set and evaluated using the NSM and IDA. The OpenSim Application Programming Interface (API) was used to apply the modifications to the musculoskeletal models. When provided with translational or rotational inputs, the API can programmatically alter a given parameter within the default configuration of the musculoskeletal model and calculate the new muscle lengths, vectors and moment arms using the updated configuration of the model and the protocol shown in Figure 3.9. These new properties are then used by the other components of the NSM to calculate the modified muscle and joint contact forces. As each model is temporarily constructed in MATLAB by the API, once the protocol has been completed, the modifications made to the models are removed and they are reset to their default configurations. The IDA functions in a similar manner. When given translational or rotational inputs, it can calculate the impingement-free range of motion for the modified configurations. The algorithm also resets the models to their default configurations after completing the assessment. Usage of the OpenSim API and IDA in this manner enabled the streamlined and systematic assessment of prosthesis modifications with minimal user input and without the need for creating a model for each modified configuration and subject in the model-set.

4.2.2.1 Glenosphere modifications

The position of the glenosphere on the reamed glenoid surface was modified using seven parameters. These parameters were applied to the default configuration of each musculoskeletal model using the implanted co-ordinate system of the scapular implant component. One of the parameters applied a translation along the X_{gs} axis (Figure 4.2). This corresponded to a lateral offset of the glenosphere, and was implemented at 5 and 10 mm increments.

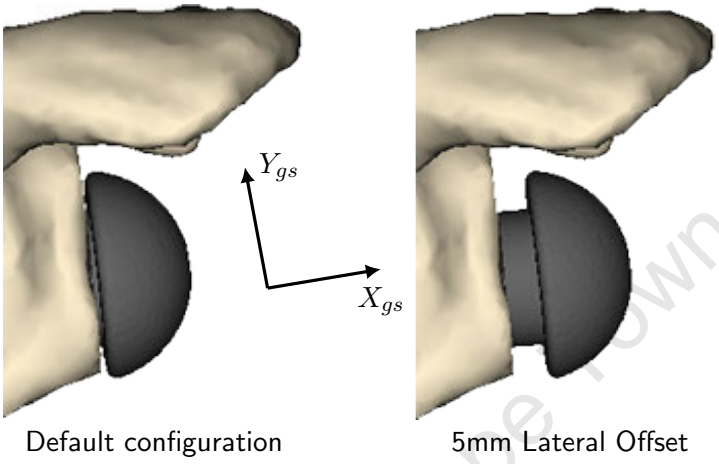

Figure 4.2 A comparison between the default configuration and the glenosphere lateral offset

Five of the parameters applied eccentric translations along the Y_{gs} and X_{gs} axes (Figure 4.3):

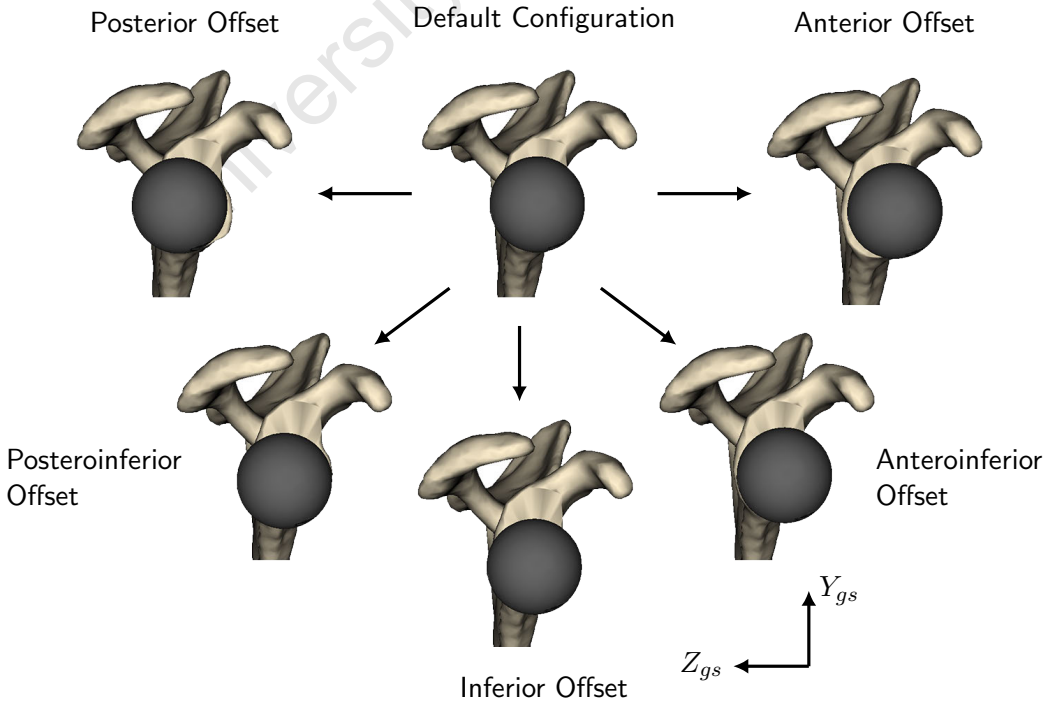

Figure 4.3 A comparison between the default configuration and 5mm offsets applied in the $Y_{gs}Z_{gs}$ plane

These parameters corresponded to the anterior, antero-inferior, inferior, postero-inferior and posterior translational offsets of the glenosphere, and were implemented at 5 and 10 mm increments. No superior offsets were assessed due to prior research by Kelly et al. (2008) who recommended placement of the glenosphere in the inferior portion of the glenoid to maximise functional outcomes. The final glenosphere modification parameter applied a rotation about the Z_{gs} axis to inferiorly tilt the glenosphere (Figure 4.4). This offset was implemented at 10° and 20° degree increments.

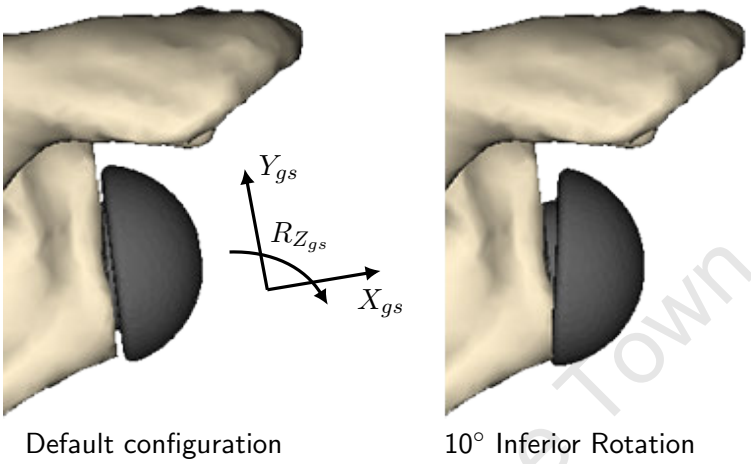

Figure 4.4 A comparison between the default configuration and the glenosphere inferior tilt

4.2.2.2 Humeral tray modifications

The position of the humeral tray on the resected humeral head was modified using nine parameters. Two of the parameters applied a translation along the Y_h axis of the humeral co-ordinate system (Figure 4.5). This resulted in a change in the depth of the humeral tray relative to the humeral head. This offset was implemented using 2.5 and 5 mm increments that increased or decreased the depth.

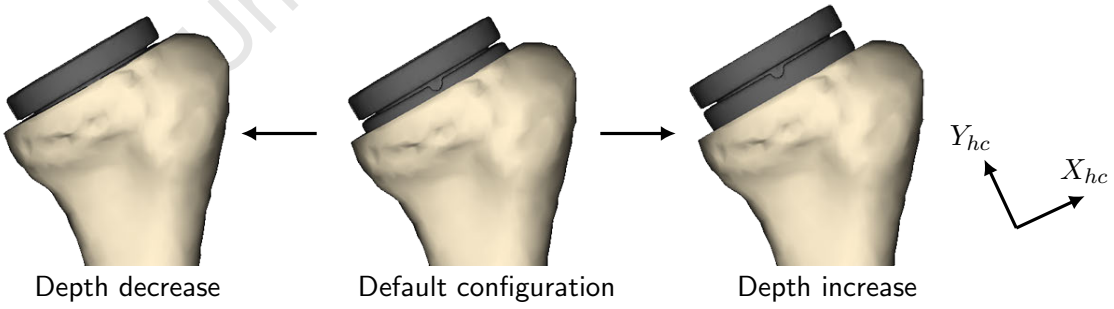

Figure 4.5 A comparison between the default configuration and 2.5 mm humeral tray depth offsets

The remaining eight parameters applied translations along the X_{hc} and Y_{hc} axes of the humeral component implanted co-ordinate system. This resulted in lateral (L), posterolateral (PL), posterior (P), posteromedial (PM), medial (M), anteromedial (AM), anterior (A) and anterolateral (AL) offsets of the humeral tray (Figure 4.6). These offsets were implemented at 2.5 and 5 mm increments.

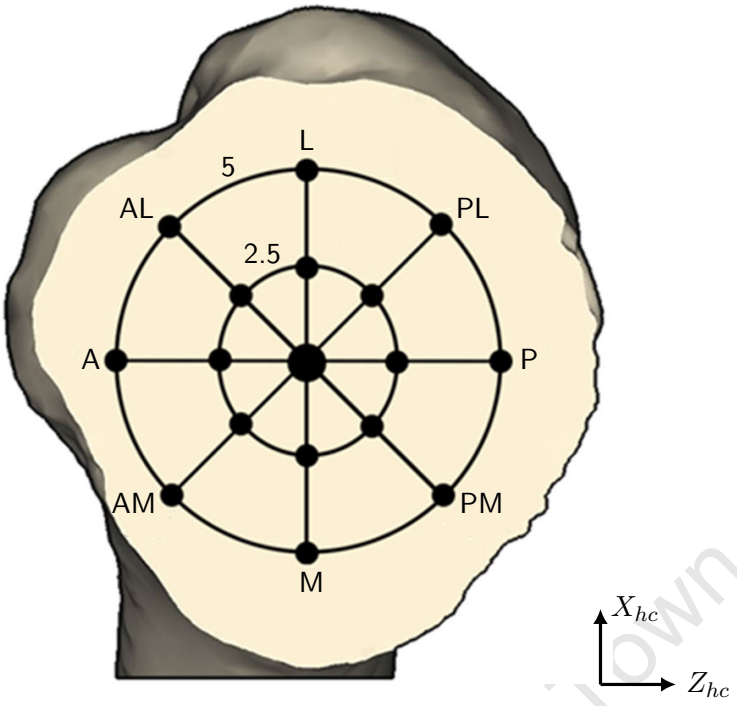

Figure 4.6 Humeral tray placements projected onto a resected humeral head. The central black dot represents the default configuration and the offset black dots represent the tray placement offsets. The concentric circles indicate the 2.5 and 5 mm offset distances.

Figure 4.7 provides an example of the effect of these offsets on the interface between the humeral tray and the resected humeral head. The position of the stem in the humeral shaft was not affected by the tray offsets.

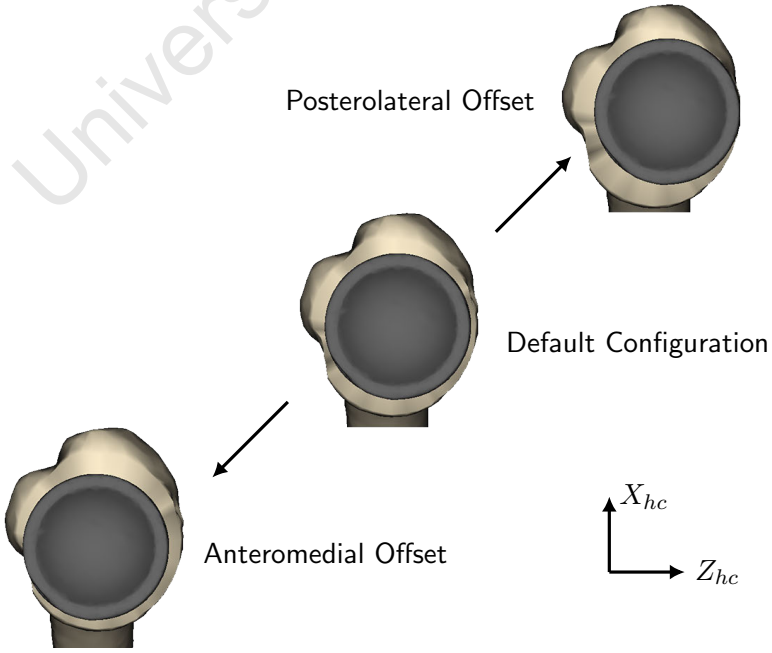

Figure 4.7 Example of the effect of 2.5 mm humeral tray placement offsets

4.2.2.3 Greater tuberosity modification

The position of the greater tuberosity was modified by increasing the radius of the spherical humeral head wrapping object. Figure 4.8 highlights the effect of this modification on the middle deltoid muscle and was implemented at 5 and 10 mm increments.

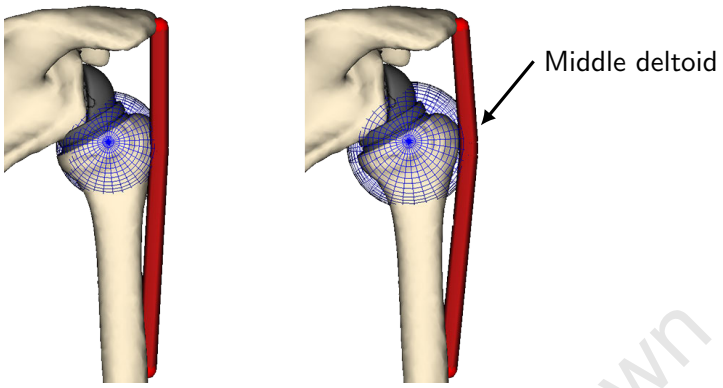

Figure 4.8 A comparison between the default configuration and the greater tuberosity offset

4.2.2.4 Modified configurations summary

Table 4.1 provides a summary of the 36 modified configurations evaluated using the assessment framework (18 modified parameters × 2 incrementally increasing offset levels).

Table 4.1 Modified RTSA parameters

Location	Type	Offset	Acronym	Increments	
Glenosphere	Translation (mm)	Lateral	GS_L	5	10
		Anterior	GS_A		
		Anteroinferior	GS_AI		
		Inferior	GS_I		
		Posteroinferior	GS_PI		
		Posterior	GS_P		
	Rotation (°)	Inferior	GS_IR	10	20
Humeral tray	Depth change (mm)	Decrease	HTD_D	2.5	5
		Increase	HTD_I		
	Translation (mm)	Lateral	HTT_L		
		Posterolateral	HTT_PL		
		Posterior	HTT_P		
		Posteromedial	HTT_PM		
		Medial	HTT_M		
		Anteromedial	HTT_AM		
		Anterior	HTT_A		
		Anterolateral	HTT_AL		
Greater tuberosity	Radius (mm)	Increase	GT_RI	5	10

4.2.3 Motions

The same motions that were used in Chapter 3 were implemented here. These included abduction (ABD), forward flexion (FF), scapular plane elevation (SPE), internal rotation at 20° and 90° of humeral elevation (IR20 and IR90), and external rotation at 20° and 90° of humeral elevation (ER20 and ER90). For additional information regarding these motions, refer to Section 3.3.1.

4.2.4 Outcome measures

The outcome measures evaluated in this chapter were peak elongation of the overall deltoid (DE, in %), mean overall deltoid moment arm (DMA, in mm), mean stability ratio (SR) and impingement-free range of motion (IFROM, in °). Additional information regarding these outcome measures can be found in Section 3.3.2.

With regards to effect of the prosthesis modifications, each outcome measure had a different response. If a modification increased DE, this was detrimental as it could induce excessive elongation. If a modification increased DMA (for all the motions, except external rotation), this was beneficial as it was indicative of a reduced effort required to produce a motion. Whereas, due to way rotation was defined, decreased DMA for external rotation was beneficial. If a modification increased SR, this was beneficial as it was indicative of an increase in joint compression or a decrease in joint shear (or some combination of both). If a modification increased IFROM, this was beneficial as it represented a decrease in the incidence of impingement.

4.2.5 Data processing

Data processing was conducted differently for DE compared to the other outcome measures. DMA, SR, and IFROM for the modified configurations were evaluated relative to the default configuration and analysed using a data binning process. Whereas, DE was evaluated in isolation, and analysed using a thresholding process.

4.2.5.1 Thresholding process: DE

The effect of the modified configurations on DE was analysed using a thresholding process. For each motion, the peak DE data from the default and modified configurations (at both offset levels) of each subject in the model-set were collected. If the absolute peak DE was greater than 20% for any permutation, it was assigned a value of 1. The sum of this tally was calculated across the subjects for each motion. If this tally (out of a possible 15) was greater than 1 for a given modification and motion, it was assumed that the modification may have a consistently negative effect as it had an impact on more than one subject. Whereas, if the tally was only 1, it may not have a consistently negative effect as the increased DE was probably due to anatomical variability.

Subsequently, the tally of each modified parameter was summed for all the motions. This sum, out of possible 105 (15 multiplied by 7, the number of motions), was illustrative of the impact a modified configuration had on DE for the assessed motions. Complementary to this tally, the difference between the default configuration and each modified configuration was calculated, and this data were used to construct box plots.

4.2.5.2 Data binning process: DMA, SR, and IFROM

For each combination of outcome measure and motion, the data from the default and modified configurations (at both offset levels) of each subject in the model-set were collected. The difference between the default configuration and each modified configuration was calculated, and this data were used to construct box plots. This differential data were then used by a data binning process (Figure 4.9) to categorise the relative effect of the modified configurations.

For each outcome measure, the differential data were compartmentalised into three groups based on motion type. The first group included the motions that elevated the humerus (ABD, FF and SPE), the second group included the motions that internally rotated the humerus (IR20 and IR90) and the third group included the motions that externally rotated the humerus (ER20 and ER90). Within each group, the sign (positive or negative) and absolute value of each data point were recorded. The absolute values were then arranged into ascending order and placed into five bins. Each bin was assigned a value between 0 and 1 in 0.25 increments; where the first bin contained the modifications with the smallest differences and had a value of 0, and the last bin contained the modifications with the largest differences and had a value of 1. Subsequently, the binned data were assigned their corresponding signs and rearranged into the original order. The median of the binned data in the model-set was then calculated for each modified configuration and recorded.

These medians were representative of the typical effect a modification had on each combination of outcome measure and motion within the model-set. The range of values obtainable was -1 to 1; where negative values corresponded to modifications that had a detrimental impact, positive values corresponded to modifications that had a beneficial impact, and bin values of 0 corresponded to modifications with a negligible impact. The data were analysed further by summing the median score of every motion for each outcome measure and modification. This motion-summed score was indicative of the impact a modified configuration had on a given outcome measure for the assessed motions. As a result, the maximum range of values obtainable by a modification for a given outcome measure was between -7 to 7 (the median score multiplied by 7, the number of motions assessed). Finally, these scores were summed for each outcome measure. This cumulative score was indicative of the impact a modification had on overall RTSA shoulder function. In this instance, the maximum range of values obtainable was -21 to 21 (the motion-summed score multiplied by 3, the number of outcome measures). The cumulative score, in conjunction with the assessment of deltoid elongation, illustrated the relative effectiveness of each modification.

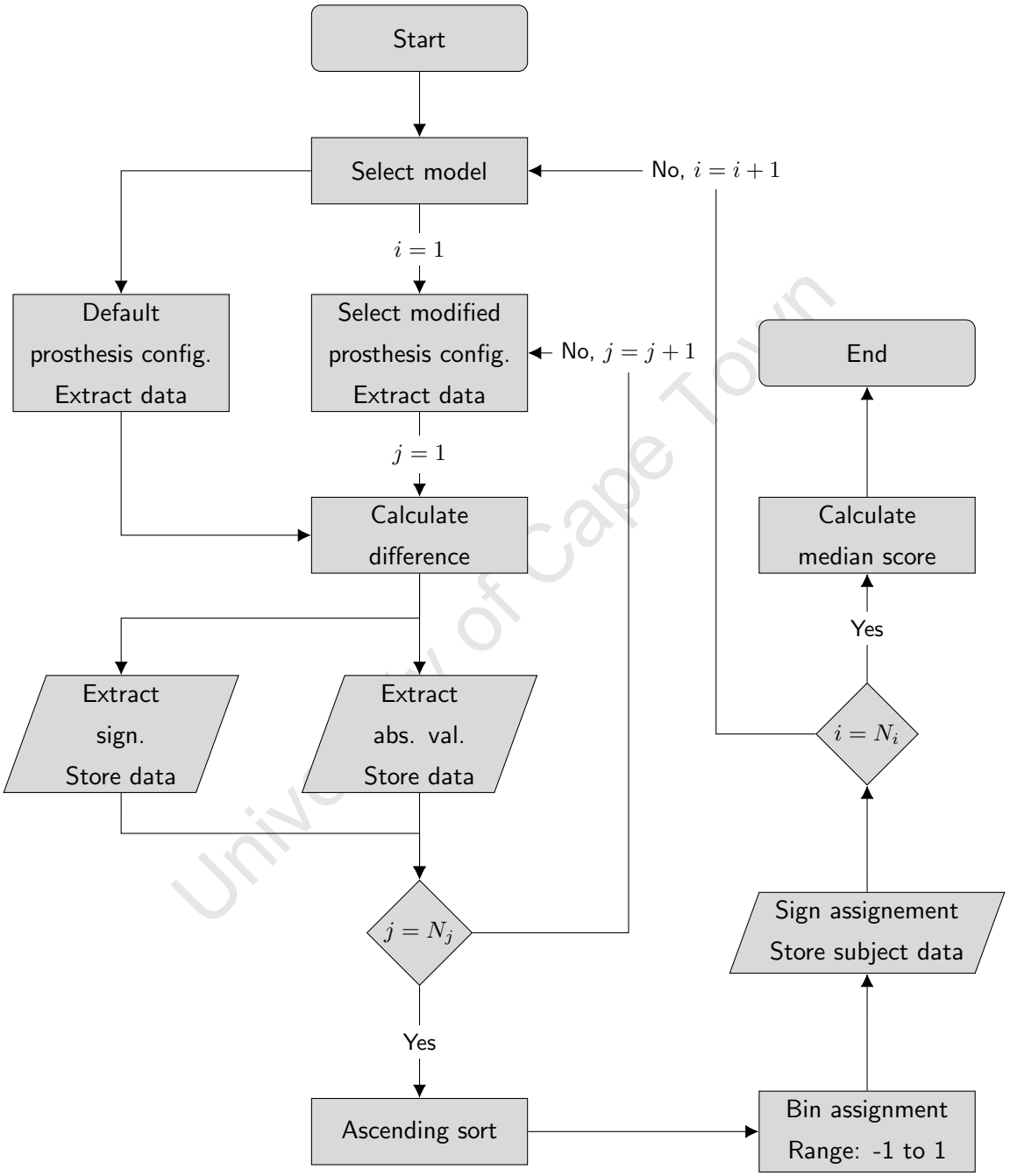

Figure 4.9 Flowchart of the data processing technique used to calculate the median binned score for a given combination of outcome measure and motion

4.3 Results

4.3.1 Deltoid elongation

The tallied data for excessive peak DE (Table 4.2) showed that consistent excessive elongation (>20%) was present at the second offset level for the anteroinferior, inferior and posteroinferior translations of the glenosphere, with the inferior translation having the highest overall tally (11 out of a possible 105 incidences). These incidences were only identified during the motions that fully adducted the humerus (ABD, FF and SPE). Figure 4.10 provides an example of the changes to peak DE due to a modified configuration for each of the motions. Figure 4.11 uses this same format to illustrate the changes to peak DE for each combination of modified configuration and motion using a uniform y-axis scale for each sub-figure.

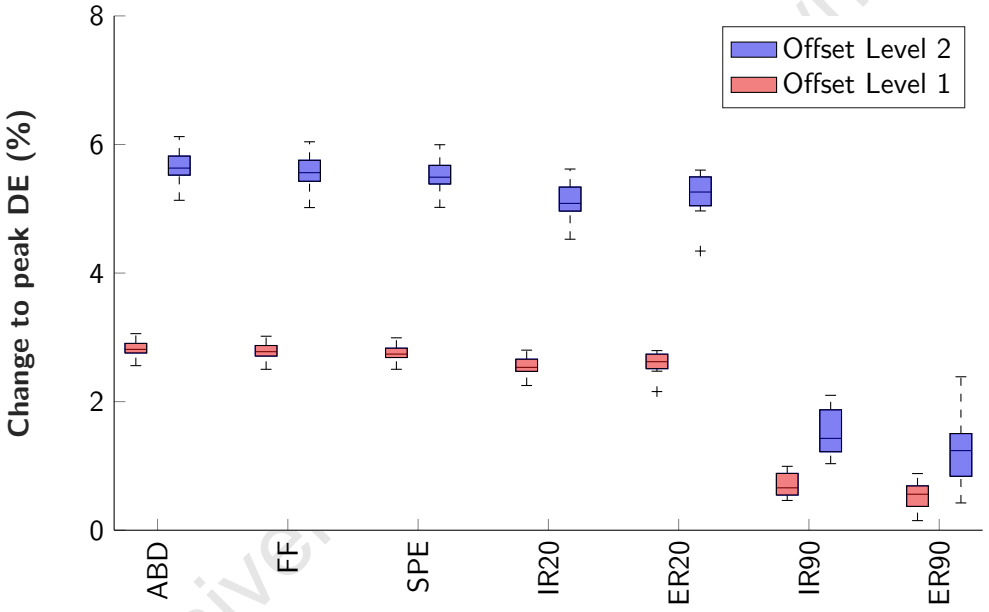

Figure 4.10 Box plots of the changes to peak DE (in %) due to the inferior translation of the glenosphere at both offset levels for each motion

Table 4.2 Tallied data for DE greater than 20%. Note that instances of consistent DE are highlighted in grey

	Offset Level 1								Offset Level 2							
Config.	**ABD**	**FF**	**SPE**	**IR20**	**ER20**	**IR90**	**ER90**	**Sum**	**ABD**	**FF**	**SPE**	**IR20**	**ER20**	**IR90**	**ER90**	**Sum**
GS_L	.	.	.	.	.	.	.	.	.	.	.	.	.	.	.	.
GS_A	.	.	.	.	.	.	.	.	.	.	.	.	.	.	.	.
GS_AI	.	.	**1**	.	.	.	.	**1**	**3**	**2**	**3**	.	.	.	.	**8**
GS_I	**1**	.	**1**	.	.	.	.	**2**	**4**	**3**	**4**	.	.	.	.	**11**
GS_PI	.	.	.	.	.	.	.	.	**3**	**1**	**2**	.	.	.	.	**6**
GS_P	.	.	.	.	.	.	.	.	.	.	.	.	.	.	.	.
GS_IR	.	.	.	.	.	.	.	.	.	.	.	.	.	.	.	.
HTD_D	.	.	.	.	.	.	.	.	.	.	.	.	.	.	.	.
HTD_I	.	.	.	.	.	.	.	.	**1**	.	**1**	.	.	.	.	**2**
HTT_L	.	.	.	.	.	.	.	.	.	.	.	.	.	.	.	.
HTT_PL	.	.	.	.	.	.	.	.	.	.	.	.	.	.	.	.
HTT_P	.	.	.	.	.	.	.	.	.	.	.	.	.	.	.	.
HTT_PM	.	.	.	.	.	.	.	.	.	.	.	.	.	.	.	.
HTT_M	.	.	.	.	.	.	.	.	.	.	.	.	.	.	.	.
HTT_AM	.	.	.	.	.	.	.	.	.	.	.	.	.	.	.	.
HTT_A	.	.	.	.	.	.	.	.	.	.	.	.	.	.	.	.
HTT_AL	.	.	.	.	.	.	.	.	.	.	.	.	.	.	.	.
GT_RI	.	.	.	.	.	.	.	.	.	.	.	.	.	.	.	.

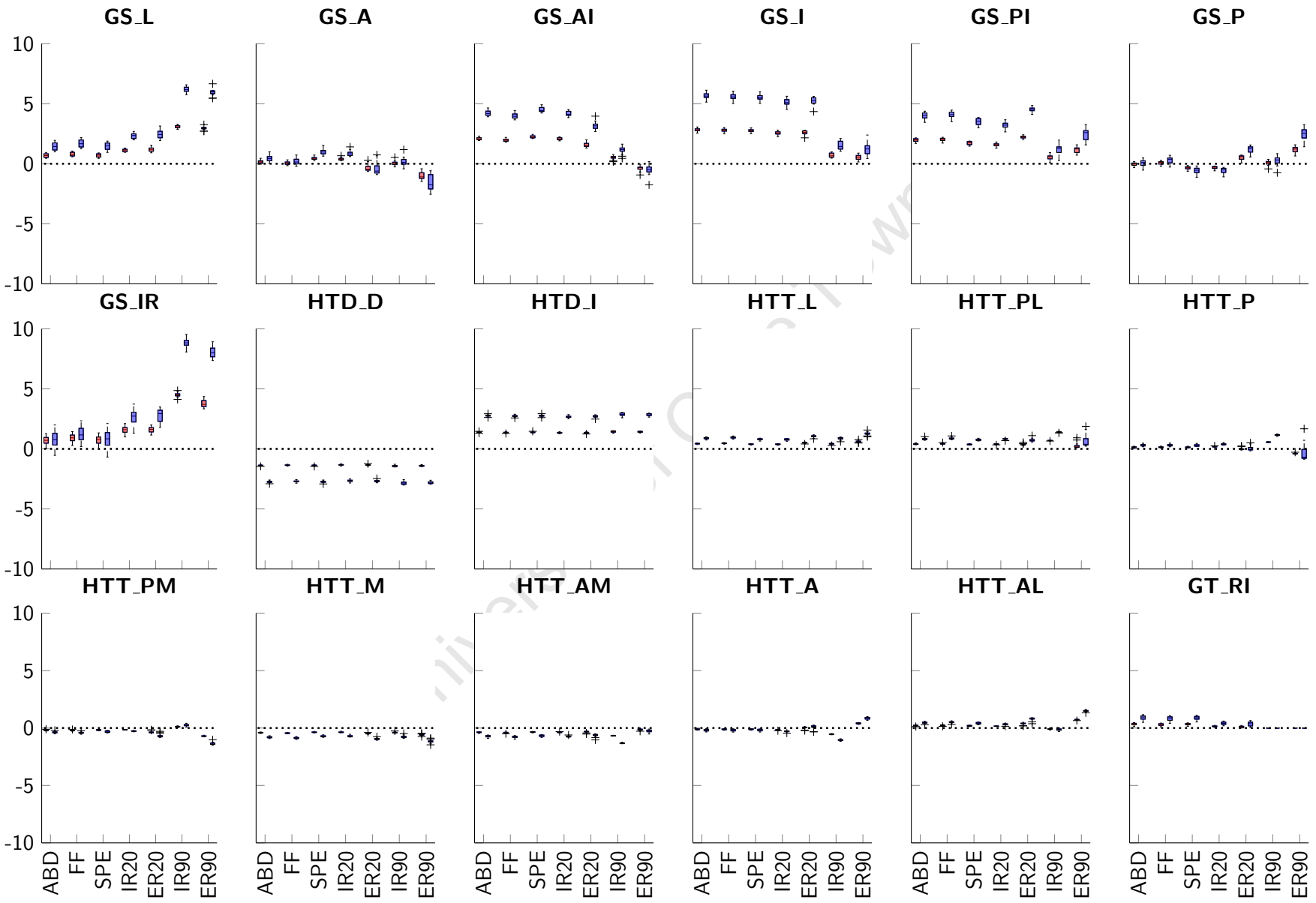

Figure 4.11 Box plots of the changes to peak DE (in %). Each sub-figure represents a modified configuration and the columns within each sub-figure represent a motion. In each column, red and blue boxes indicate the first and second offset levels, respectively. Note, the figure is a vector graphic and can be magnified for greater detail

4.3.2 Deltoid moment arm

Box plots of the changes to overall mean DMA due to a modified configuration for each motion is exemplified in Figure 4.12. Figure 4.13 uses this format to illustrate the changes to the overall mean DMA for each combination of modified configuration and motion using a uniform y-axis scale for each sub-figure. In addition, the corresponding binned data for these changes can be found in Table 4.4. From these results it was evident that anteroinferior translation of the glenosphere had the most beneficial impact at both offset levels. Whereas, humeral tray translation in the anteromedial and anterior direction had the most detrimental impact at the first and second offset level, respectively. These results also showed that the humeral tray and the greater tuberosity modifications had a relatively small impact on overall mean DMA compared to the glenosphere modifications.

Table 4.3 highlights the range of the changes to mean overall DMA values found for the three motion activity groups defined in Section 4.2.5.

Table 4.3 Range of the changes to mean overall DMA values (in mm). The data are from the second offset level and presented with subject-averaged means (and 95% confidence intervals)

Group		Range		Offset	Motion
ABD, FF & SPE	Min	-8.39	(-8.93, -7.84)	GS_IR	SPE
	Max	5.28	(5.12, 5.44)	GS_AI	ABD
IR20 & IR90	Min	-1.71	(-1.78, -1.63)	GS_AI	IR90
	Max	1.26	(1.18, 1.35)	GS_IR	IR20
ER20 & ER90	Min	-1.67	(-1.73, -1.62)	GS_P	ER90
	Max	1.65	(1.58, 1.71)	GS_A	

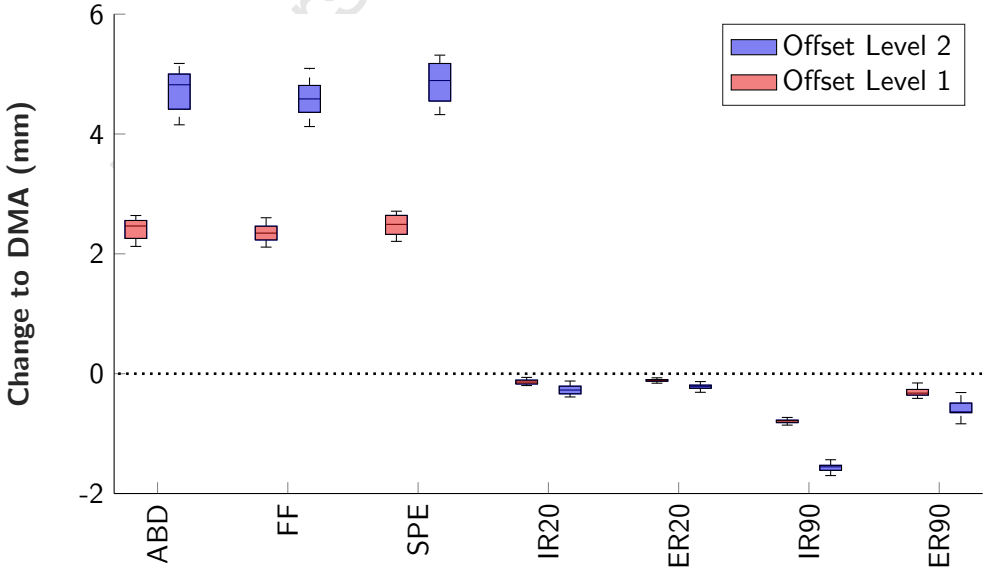

Figure 4.12 Box plots of the changes to mean overall DMA (in mm) due to the inferior translation of the glenosphere at both offset levels for each motion

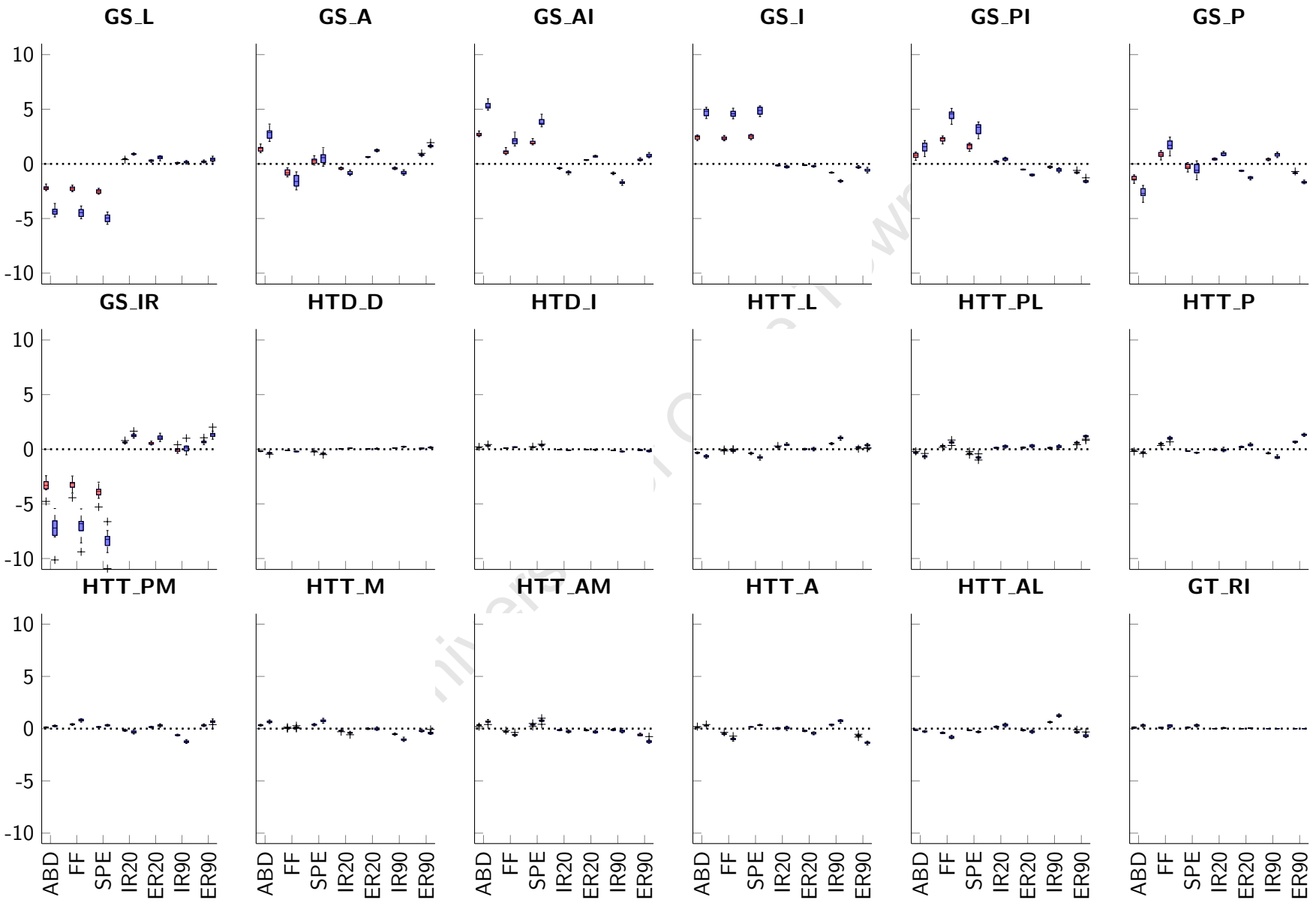

Figure 4.13 Box plots of the changes to mean overall DMA (in mm). Each sub-figure represents a modified configuration and the columns within each sub-figure represent a motion. In each column, red and blue boxes indicate the first and second offset levels, respectively. Note, the figure is a vector graphic and can be magnified for greater detail

Table 4.4 Changes to mean overall DMA: median binned data

	Offset Level 1								Offset Level 2							
Config.	**ABD**	**FF**	**SPE**	**IR20**	**ER20**	**IR90**	**ER90**	**Sum**	**ABD**	**FF**	**SPE**	**IR20**	**ER20**	**IR90**	**ER90**	**Sum**
GS_L	-0.75	-0.75	-1	0.75	0.5	0	0.25	**-1**	-1	-1	-1	1	0.75	0.25	0.5	**-0.5**
GS_A	0.75	-0.75	0.25	-0.75	0.75	-0.5	1	**0.75**	1	-0.75	0.5	-1	1	-1	1	**0.75**
GS_AI	1	0.75	0.75	-0.5	0.5	-1	0.5	**2**	1	0.75	1	-1	0.75	-1	0.75	**2.25**
GS_I	1	0.75	1	-0.25	0	-1	-0.5	**1**	1	1	1	-0.5	-0.25	-1	-0.75	**0.5**
GS_PI	0.5	0.75	0.75	0.25	-0.5	-0.5	-0.75	**0.5**	0.75	1	1	0.75	-1	-0.75	-1	**0.75**
GS_P	-0.75	0.75	-0.25	0.75	-0.75	0.75	-1	**-0.5**	-1	0.75	-0.5	1	-1	1	-1	**-0.75**
GS_IR	-1	-1	-1	0.75	0.5	0	0.75	**-1**	-1	-1	-1	1	1	0.25	1	**0.25**
HTD_D	0	0	-0.25	0	0	0.25	0	**0**	-0.25	-0.25	-0.5	0	0	0.5	0.25	**-0.25**
HTD_I	0	0	0	0	0	0	0	**0**	0.25	0	0.25	0	0	-0.25	-0.25	**0**
HTT_L	-0.25	0	-0.5	0.25	0	0.75	0.25	**0.5**	-0.5	0	-0.5	0.75	0	1	0.5	**1.25**
HTT_PL	-0.25	0.25	-0.5	0.25	0.25	0	0.75	**0.75**	-0.5	0.5	-0.75	0.5	0.5	0.5	1	**1.75**
HTT_P	0	0.5	0	0	0.25	-0.5	0.75	**1**	-0.25	0.75	-0.25	0	0.5	-0.75	1	**1**
HTT_PM	0	0.5	0	-0.25	0.25	-0.75	0.5	**0.25**	0.25	0.75	0.25	-0.5	0.5	-1	0.75	**1**
HTT_M	0.25	0	0.5	-0.25	0	-0.75	-0.25	**-0.5**	0.5	0	0.75	-0.5	0	-1	-0.5	**-0.75**
HTT_AM	0.25	-0.25	0.5	-0.25	-0.25	0	-0.75	**-0.75**	0.5	-0.5	0.75	-0.5	-0.5	-0.25	-1	**-1.5**
HTT_A	0	-0.5	0	0	-0.25	0.5	-0.75	**-1**	0.25	-0.75	0.25	0	-0.5	0.75	-1	**-1**
HTT_AL	0	-0.5	0	0.25	-0.25	0.75	-0.5	**-0.25**	-0.25	-0.75	-0.25	0.5	-0.5	1	-0.75	**-1**
GT_RI	0	0	0	0	0	0	0	**0**	0.25	0.25	0.25	0	0	0	0	**0.75**

4.3.3 Stability ratio

Box plots of the changes to mean SR due to a modified configuration for each motion is exemplified in Figure 4.14. Figure 4.15 uses this format to illustrate the changes to overall mean SR for each combination of modified configuration and motion using a uniform y-axis scale for each sub-figure. In addition, the corresponding binned data for these changes can be found in Table 4.6. These results showed that posteromedial translation of the humeral tray had the most beneficial impact as it was the only modification that increased SR at both offset levels for all the motions. Conversely, antero-lateral humeral tray translation (which was diametrically opposite to the posteromedial translation) had the most detrimental impact as it decreased SR at both offset levels for all the motions. Unlike DMA, humeral tray translations and the greater tuberosity modification had noticeable impacts on SR.

Table 4.5 highlights the range of the changes to mean mean SR values found for the three motion activity groups.

Table 4.5 Range of the changes to mean SR values. The data are from the second offset level and presented with subject-averaged means (and 95% confidence intervals)

Group		Range		Offset	Motion
ABD, FF & SPE	Min	-1.46	(-1.78, -1.13)	GS_IR	SPE
	Max	3.32	(2.23, 4.40)	GS_P	FF
IR20 & IR90	Min	-2.04	(-2.52, -1.56)	HTT_A	IR20
	Max	4.28	(2.36, 6.20)	HTT_P	IR90
ER20 & ER90	Min	-0.72	(-0.86, -0.58)	HTT_L	ER20
	Max	1.65	(1.32, 1.97)	GT_RI	ER90

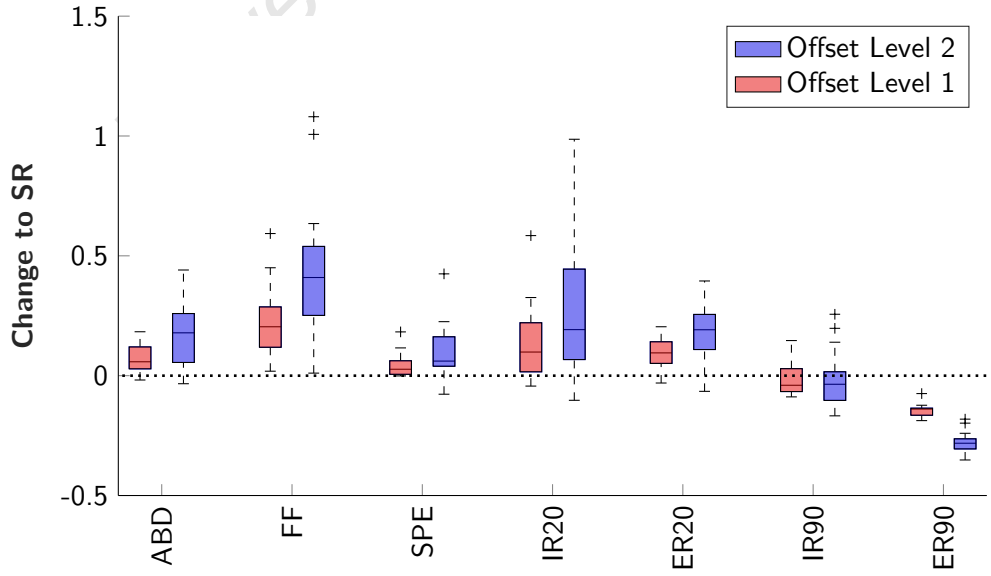

Figure 4.14 Box plots of the changes to mean SR due to the inferior translation of the glenosphere at both offset levels for each motion

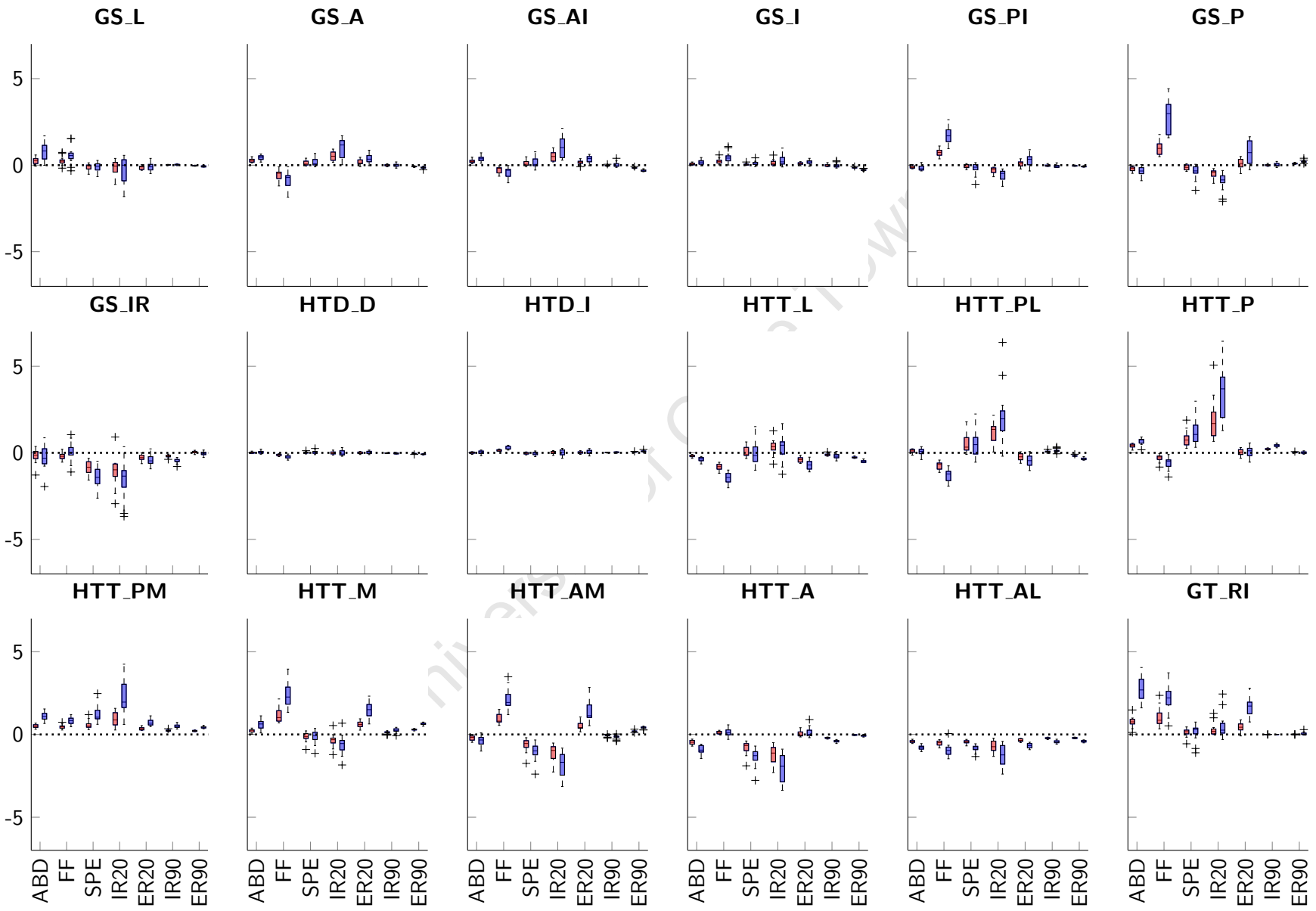

Figure 4.15 Box plots of the changes to mean SR. Each sub-figure represents a modified configuration and the columns within each sub-figure represent a motion. In each column, red and blue boxes indicate the first and second offset levels, respectively. Note, the figure is a vector graphic and can be magnified for greater detail

Table 4.6 Changes to mean SR: median binned data

	Offset Level 1								Offset Level 2							
Config.	**ABD**	**FF**	**SPE**	**IR20**	**ER20**	**IR90**	**ER90**	**Sum**	**ABD**	**FF**	**SPE**	**IR20**	**ER20**	**IR90**	**ER90**	**Sum**
GS_L	0.25	0.25	0	0	-0.25	0	0	**0.25**	0.75	0.75	0	0	-0.25	0	-0.25	**1**
GS_A	0.25	-0.75	0	0.75	0.5	0	-0.25	**0.5**	0.5	-0.75	0.25	1	0.75	0	-0.25	**1.5**
GS_AI	0.25	-0.25	0	0.75	0.5	0	-0.5	**0.75**	0.5	-0.5	0	1	0.75	0	-0.75	**1**
GS_I	0	0.25	0	0.25	0.25	0	-0.5	**0.25**	0.25	0.5	0	0.5	0.5	0	-0.75	**1**
GS_PI	0	0.75	0	-0.5	0.25	0	0	**0.5**	-0.25	1	-0.25	-0.75	0.75	-0.25	-0.25	**0**
GS_P	-0.25	1	-0.25	-0.75	0.25	0	0.25	**0.25**	-0.5	1	-0.5	-0.75	1	0	0.5	**0.75**
GS_IR	-0.25	-0.25	-0.75	-1	-0.75	-0.5	0	**-3.5**	-0.25	0	-1	-1	-0.75	-0.75	0	**-3.75**
HTD_D	0	-0.25	0	0	0	0	0	**-0.25**	0	-0.25	0	-0.25	0	0	-0.25	**-0.75**
HTD_I	0	0.25	0	0	0	0	0	**0.25**	0	0.5	0	0	0	0	0.25	**0.75**
HTT_L	-0.25	-0.75	0	0.5	-0.75	-0.25	-0.5	**-2**	-0.5	-1	-0.25	0.75	-1	-0.5	-1	**-3.5**
HTT_PL	0	-0.75	0.5	1	-0.5	0.25	-0.5	**0**	0	-1	0.75	1	-1	0.25	-0.75	**-0.75**
HTT_P	0.5	-0.25	0.75	1	0	0.5	0	**2.5**	0.75	-0.75	1	1	0.5	0.75	0	**3.25**
HTT_PM	0.75	0.5	0.75	1	0.75	0.5	0.5	**4.75**	1	0.75	1	1	1	0.75	0.75	**6.25**
HTT_M	0.25	1	0	-0.75	1	0.25	0.75	**2.5**	0.75	1	0	-0.75	1	0.5	1	**3.5**
HTT_AM	-0.25	1	-0.75	-1	0.75	0	0.5	**0.25**	-0.5	1	-1	-1	1	-0.25	0.75	**0**
HTT_A	-0.5	0	-0.75	-1	0	-0.5	0	**-2.75**	-1	0	-1	-1	0	-0.75	-0.25	**-4**
HTT_AL	-0.5	-0.5	-0.5	-0.75	-0.75	-0.5	-0.5	**-4**	-0.75	-1	-0.75	-1	-1	-0.75	-0.75	**-6**
GT_RI	0.75	0.75	0.25	0.5	0.75	0	0	**3**	1	1	0.5	0.5	1	0	0	**4**

4.3.4 Impingement-free range of motion

Box plots of the changes to IFROM due to a modified configuration for each motion is provided in Figure 4.16. Figure 4.17 uses this format to illustrate the changes to IFROM for each combination of modified configuration and motion a uniform y-axis scale for each sub-figure. In addition, the corresponding binned data for these changes can be found in Table 4.8. These results showed that inferior translation of the glenosphere had the most beneficial impact as it increased IFROM at both offset levels during all the motions, except for ER90 (which was generally unaffected by the prosthesis modifications). Conversely, posterior translation of the glenosphere had the most detrimental impact as it decreased IFROM at both offset levels during the same motions. Additionally, these results illustrate the negligible impact humeral tray modifications had on IFROM; with only some changes to IFROM identified in IR90 and ER90. For example, medialisation of the humeral tray markedly increased IFROM. However, this finding was subject-specific and, consequently, the median change to IFROM was negligible within the model-set.

Table 4.7 highlights the range of the changes to IFROM values found for the three motion activity groups.

Table 4.7 Range of the changes to IFROM values (in °). The data are presented with subject-averaged means (and 95% confidence intervals)

Group		Range		Offset	Level	Motion
ABD, FF & SPE	Min	-60.60	(-70.31, -50.89)	GS_P	2	FF
	Max	62.80	(52.58, 73.02)	GS_I	2	ABD
IR20 & IR90	Min	-34.60	(-49.68, -19.52)	GS_P	2	IR20
	Max	25.40	(10.32, 40.48)	GS_AI	1	IR20
ER20 & ER90	Min	-13.47	(-23.30, -3.63)	GS_A	1	ER20
	Max	68.80	(55.20, 82.38)	GS_PI	2	ER20

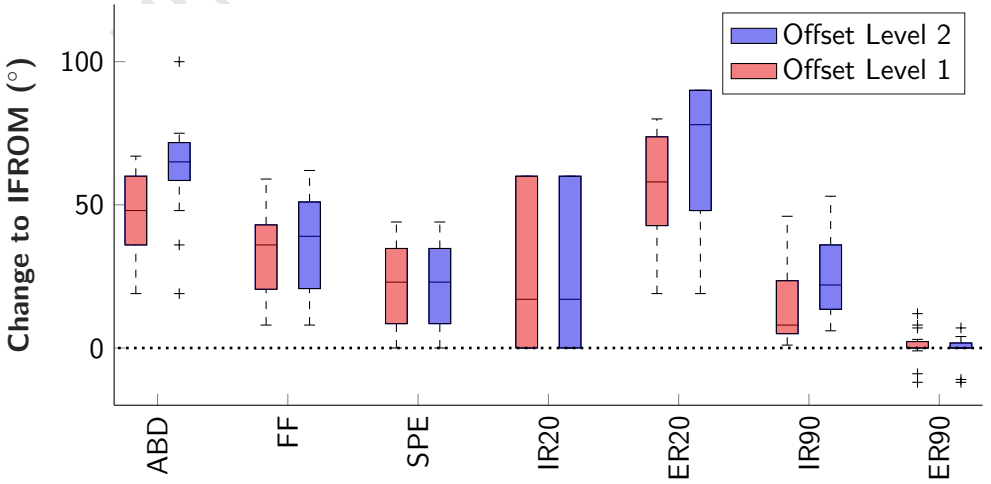

Figure 4.16 Box plots of the changes to mean IFROM (in °) due to the inferior translation of the glenosphere at both offset levels for each motion activity

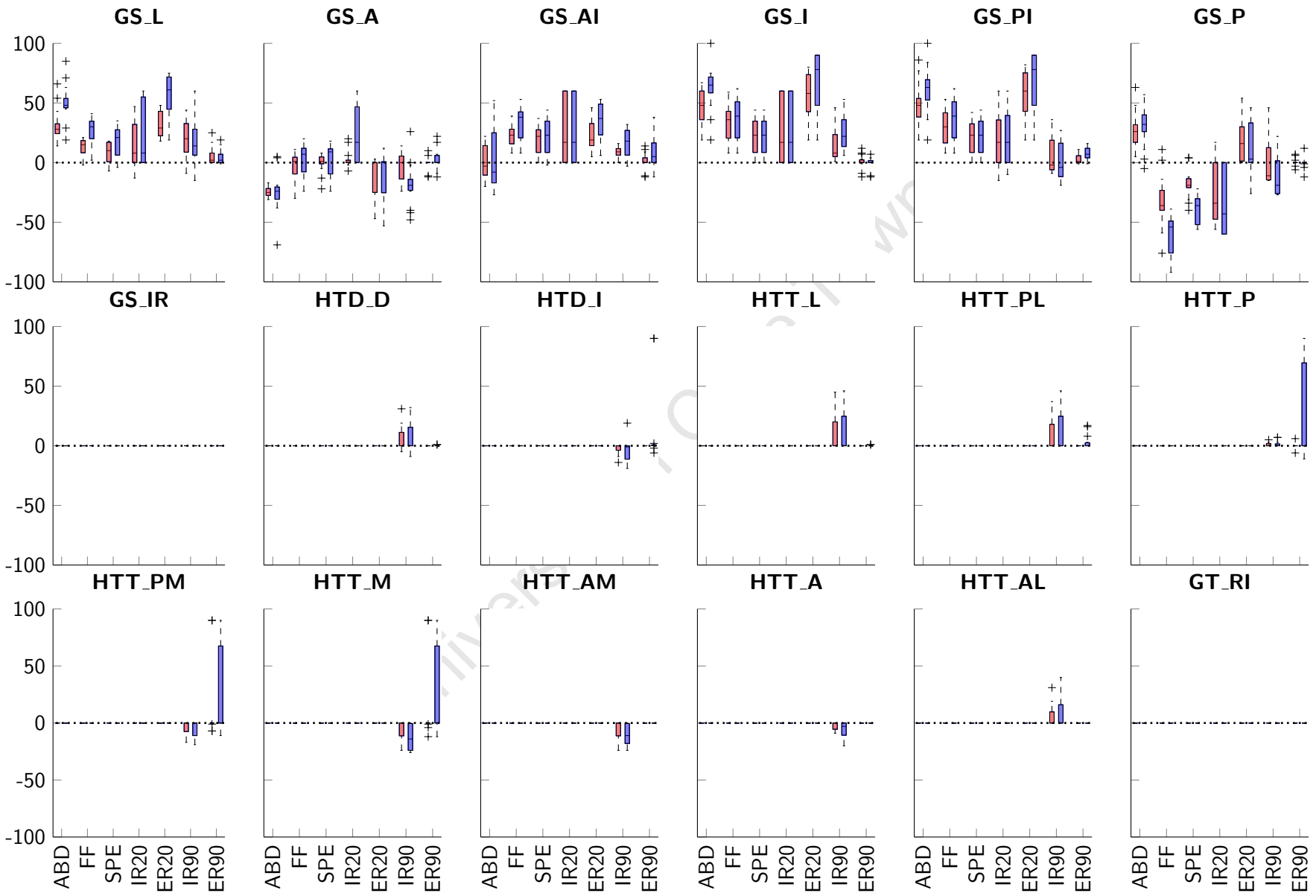

Figure 4.17 Box plots of the changes to IFROM (in °). Each sub-figure represents a modified configuration and the columns within each sub-figure represent a motion. In each column, red and blue boxes indicate the first and second offset levels, respectively. Note, the figure is a vector graphic and can be magnified for greater detail

Table 4.8 Changes to IFROM: median binned data. — indicates an outcome not measured for a given modified configuration

	Offset Level 1								Offset Level 2							
Config.	**ABD**	**FF**	**SPE**	**IR20**	**ER20**	**IR90**	**ER90**	**Sum**	**ABD**	**FF**	**SPE**	**IR20**	**ER20**	**IR90**	**ER90**	**Sum**
GS_L	0.5	0	0	0.25	0.5	0.5	0	**1.75**	1	0.5	0.25	0.25	1	0.25	0	**3.25**
GS_A	-0.25	0	0	0	0	0	0	**-0.25**	-0.5	0	0	0.5	0	-0.5	0	**-0.5**
GS_AI	0	0.25	0.25	0.5	0.5	0.25	0	**1.75**	0	0.75	0.25	0.5	0.75	0.5	0	**2.75**
GS_I	1	0.75	0.25	0.75	0.75	0.25	0	**3.75**	1	0.75	0.5	0.75	1	0.75	0	**4.75**
GS_PI	1	0.5	0.25	0.75	1	0	0	**3.5**	1	0.75	0.5	0.75	1	0	0.25	**4.25**
GS_P	0.5	-0.75	-0.25	-1	0.5	-0.25	0	**-1.25**	0.75	-1	-0.75	-1	0.25	-0.75	0	**-2.5**
GS_IR	—	—	—	—	—	—	—	—	—	—	—	—	—	—	—	—
HTD_D	0	0	0	0	0	0	0	**0**	0	0	0	0	0	0	0	**0**
HTD_I	0	0	0	0	0	0	0	**0**	0	0	0	0	0	0	0	**0**
HTT_L	0	0	0	0	0	0	0	**0**	0	0	0	0	0	0	0	**0**
HTT_PL	0	0	0	0	0	0	0	**0**	0	0	0	0	0	0	0	**0**
HTT_P	0	0	0	0	0	0	0	**0**	0	0	0	0	0	0	0	**0**
HTT_PM	0	0	0	0	0	0	0	**0**	0	0	0	0	0	0	0	**0**
HTT_M	0	0	0	0	0	0	0	**0**	0	0	0	0	0	-0.25	0	**-0.25**
HTT_AM	0	0	0	0	0	0	0	**0**	0	0	0	0	0	-0.25	0	**-0.25**
HTT_A	0	0	0	0	0	0	0	**0**	0	0	0	0	0	0	0	**0**
HTT_AL	0	0	0	0	0	0	0	**0**	0	0	0	0	0	0	0	**0**
GT_RI	—	—	—	—	—	—	—	—	—	—	—	—	—	—	—	—

4.3.5 Overall effect of modifying the prosthesis configuration

A summary of the outcome measures for each modified configuration is provided in Table 4.9. The DE columns contained the tallies of excessive elongation (out of 105) at the two offset levels. The DMA, SR, and IFROM columns contained the motion-summed scores (out of 7) at the two offset levels. The overall columns contain the overall score of the DMA, SR, and IFROM scores (out of 21), with the configurations that had a net positive effect highlighted in grey.

Table 4.9 Outcome measures summary: motion-summed data. — indicates an outcome not measured for a given configuration and * indicates a configuration that caused excessive DE

	Offset Level 1					Offset Level 2				
Config.	**DE**	**DMA**	**SR**	**IFROM**	**Overall**	**DE**	**DMA**	**SR**	**IFROM**	**Overall**
GS_L		-1	0.25	1.75	**1**		-0.5	1	3.25	**3.75**
GS_A		0.75	0.5	-0.25	**1**		0.75	1.5	-0.5	**1.75**
GS_AI	1	2	0.75	1.75	**4.5**	8	2.25	1	2.75	**6***
GS_I	2	1	0.25	3.75	**5**	11	0.5	1	4.75	**6.25***
GS_PI		0.5	0.5	3.5	**4.5**	6	0.75	0	4.25	**5***
GS_P		-0.5	0.25	-1.25	**-1.5**		-0.75	0.75	-2.5	**-2.5**
GS_IR		-1	-3.5	—	**-4.5**		0.25	-3.75	—	**-3.5**
HTD_D		0	-0.25	0	**-0.25**		-0.25	-0.75	0	**-1**
HTD_I		0	0.25	0	**0.25**	2	0	0.75	0	**0.75**
HTT_L		0.5	-2	0	**-1.5**		1.25	-3.5	0	**-2.25**
HTT_PL		0.75	0	0	**0.75**		1.75	-0.75	0	**1**
HTT_P		1	2.5	0	**3.5**		1	3.25	0	**4.25**
HTT_PM		0.25	4.75	0	**5**		1	6.25	0	**7.25**
HTT_M		-0.5	2.5	0	**2**		-0.75	3.5	-0.25	**2.5**
HTT_AM		-0.75	0.25	0	**-0.5**		-1.5	0	-0.25	**-1.75**
HTT_A		-1	-2.75	0	**-3.75**		-1	-4	0	**-5**
HTT_AL		-0.25	-4	0	**-4.25**		-1	-6	0	**-7**
GT_RI		0	3	—	**3**		0.75	4	—	**4.75**

At the first offset level, both the inferior translation of the glenosphere and the posteromedial translation of the humeral tray had the most beneficial impact on overall functional outcomes. For the inferior translation of the glenosphere, this was due to IFROM improvements whereas, for the posteromedial translation of the humeral tray, this was primarily attributed to SR improvements. The most detrimental impact on overall functional outcomes was caused by the inferior rotation of the glenosphere due to decreases in SR and DMA.

At the second offset level, the posteromedial translation of the humeral tray had the most beneficial impact due to further improvements to SR. While additional inferior translation of the glenosphere did improve overall prosthesis function, it did cause excessive deltoid elongation and made it an unsuitable candidate for further analysis. Due to marked decreases in DMA and SR, the anterolateral translation of the humeral tray replaced the inferior rotation of the glenosphere as the worst modification at the second offset level.

4.4 Discussion

4.4.1 Deltoid moment arm

As the moment arm of a muscle is a measure of the effectiveness of its contribution to a motion (An et al. 1983; Sherman et al. 2013), changes to DMA as a result of the modifying the prosthesis configuration would have an effect on everyday capabilities of RTSA recipients. For example, an increased DMA during humeral elevation would decrease the effort required by the deltoid muscle (by increasing its lever arm), allowing for easier interactions with their environment at, over above, shoulder height.

4.4.1.1 Humeral elevations

The modified configurations were found to have an effect on either the deltoid offset distance or the wrapping of the deltoid around the greater tuberosity. These factors play a role in determining DMA. Increasing deltoid offset distance alters the distance between the glenohumeral joint centre of rotation and the effective muscle centre and, in doing so, the moment arm increases when the humerus is abducted (Boileau et al. 2005). Whereas, increasing deltoid wrapping alters the vector between the effective muscle centre and the origin of the muscle, thereby decreasing the moment arm when the humerus is adducted (Kontaxis and Johnson 2009; Costantini et al. 2015).

Lateralisation and inferior rotation of the glenosphere both increased deltoid wrapping and, thereby, decreased DMA during the initiation of humeral elevation (Figure 4.18(c)). For example, 5 mm of glenosphere lateralisation decreased the mean overall DMA by 9.1% during SPE in the current study. Comparatively, Hoenecke et al. (2014) reported a 12.4% decrease during the same assessment. This DMA decrease was also associated with an increase in the force required by the deltoid to elevate the humerus (Henninger et al. 2012b; Costantini et al. 2015). Conversely, inferior translation of the glenosphere increased DMA by increasing deltoid offset distance when. In the current study, mean overall DMA increased by an average of 9.1% and 17.8% in ABD, FF and SPE for the 5 and 10 mm offsets, respectively. However, due to the additional lowering of the humerus caused by the inferior translation of the glenosphere (especially at the 10 mm offset, Table 4.2), the deltoid was excessively elongated and, therefore, should not be implemented.

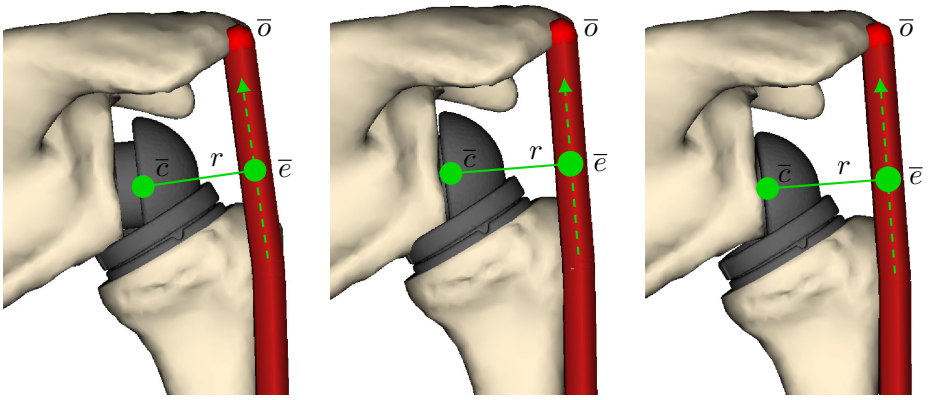

(a) Lateral glenosphere (b) Default configuration (c) Inferior glenosphere

Figure 4.18 Comparison of deltoid muscle orientations when the humerus was neutrally positioned. The lateral glenosphere (left) reduced the moment arm (r) by altering the direction vector between the effective muscle centre ($\overline{e}$) and the muscle origin ($\overline{o}$) when the humerus was adducted. Whereas, the inferior glenosphere (right) had no effect on the moment arm as wrapping was unaffected when the arm is adducted. However, when the deltoid unwraps from the greater tuberosity once the humerus was elevated, the offset distance between the centre of rotation and effective muscle centre increased due to the inferior glenosphere placement

Unlike the inferior glenosphere translation, the anterior and posterior glenosphere offsets altered DMA by changing the wrapping of the deltoid. Consequently, the combined offsets (anteroinferior or posteroinferior) altered DMA by combining the effects of deltoid offset distance and deltoid wrapping. These combinations were more effective than the anterior or posterior offsets (but not as effective as the inferior offset) due to the inclusion of some inferior translation. As shown in Table 4.2, even the moderate amount of inferior translation incorporated into these combined offsets can result in excessive deltoid elongation and make these offsets unsuitable.

Humeral tray translations altered the position of the humerus relative to the tray. In doing so, the offset distance of the deltoid changes. For example, lateralisation of the tray medialises the humerus and slightly decreases deltoid offset distance, thereby decreasing DMA. Due to the manner in which they were implemented, the effect of tray translations exhibited a symmetrical pattern. The offsets that medialised the humerus (HTT_L, HTT_PL and HTT_AL) decreased DMA and the offsets that lateralised the humerus (HTT_M, HTT_PM and HTT_AM) increased DMA. A similar pattern was identified by Berhouet et al. (2014a) during their assessment of humeral tray placement for the Biomet prosthesis. They also remarked that the effect of tray placement on moment arms was small in comparison to the glenosphere modifications and this finding helped to corroborate the results of Figure 4.13.

Changes to humeral tray depth also altered the position of the humerus; a decrease in tray depth raised the position of the humerus (thereby decreasing DMA) and an increase in tray depth lowered the humerus (thereby increasing DMA). However, as with the tray translations, the effect of these changes to humerus position was much smaller than the change caused by the glenosphere modifications and, as such, had a reduced overall effect on DMA.

The greater tuberosity radius increase shifted the deltoid away from the centre of rotation. In doing so, it fulfilled the same function as humeral lateralisation and increased DMA when the humerus was adducted. However, once the humerus was abducted the deltoid no longer wraps on the humeral head and the beneficial effect of the modification was lost. Therefore, the impact of the modification on mean overall DMA was negligible at the first offset level and minimal at the second.

4.4.1.2 Humeral rotations

As can be seen in Table 4.4, the DMA during the rotational motions typically had the opposite response to the modifications compared to the motions that elevated the humerus. For example, the medial translation of the humeral tray increased DMA during ABD and SPE, and decreased DMA during IR20, IR90 and ER90. These responses were likely caused by the modifications having the opposite effect on the direction vector between the muscle origin and the effective muscle centre while the humerus was rotating. Consequently, none of the modifications were able to increase DMA during all the motions, and the largest overall score for this outcome measure was only 2.25 out of 7 at the second offset level of the anteroinferior glenosphere translation.

4.4.2 Stability ratio

Stability ratio is a measure of the prosthetic glenohumeral joint stability. The closer the value is to 1, the more likely the direction vector of the joint contact force is situated near the rim of the humeral cup and, thus, may dislocate the joint (which would need to be remedied through revision surgery). Therefore, modified prosthesis configurations that increase SR are beneficial.

By definition, stability ratio was affected by changes to the relationship between compression and shear in the humeral cup. Terrier et al. (2008) and Ackland et al. (2011) have demonstrated that the force produced by the deltoid in the reverse shoulder is one of the main contributors to the joint contact forces and, as such, changes to DMA influence stability. In general, SR can be improved either by modifying the joint contact force such that the increase to compression is greater than the increase to shear, or by modifying the joint contact force such that the decrease to shear is greater than the decrease to compression. The former change to SR is typically a result of decreased DMA and the latter change is typically a result of increased DMA.

During ABD, FF and SPE, glenosphere lateralisation decreased DMA, increased the force requirements of the deltoid and, in turn, increased joint compression and shear. The 5 mm offset increased SR by an average of 2.1% in ABD, FF and SPE due to an average increase in compression and shear of 5.1% and 2.7%, respectively. Similar increases in joint forces due to glenosphere lateralisation were also identified in previous biomechanical studies; Giles et al. (2015) and Liou et al. (2017) reported 9.0% and 7.2% in the resultant joint forces at equivalent glenosphere offsets, respectively. However, the increased stability has the potential to be counteracted by the introduction

of a bending moment at the glenosphere due to the centre of rotation being moved away from the bone-implant interface, as can be seen in Figure 4.18(a) (Henninger et al. 2012a; Hoenecke et al. 2014; Costantini et al. 2015).

Inferior translation of the glenosphere increased DMA, decreased the force requirements of the deltoid and, in turn, decreased joint compression and shear. The 5 mm offset increased SR by an average of 1.7% in ABD, FF and SPE due to an average decrease in compression and shear of -0.7% and -2.3%, respectively. This increase in SR agreed with the work of Clouthier et al. (2013), who found that this modification increased the force required to dislocate the shoulder.

Humeral tray modifications also followed the trend of DMA and SR interaction. For example, tray lateralisation (humeral medialisation) decreased DMA during ABD, FF and SPE, increased deltoid force requirements and increased joint compression and shear. However, the increases to shear were greater than the increase to compression, and SR decreased. Conversely, tray medialisation increased DMA, decreased deltoid force requirements and decreased joint compression and shear. In this instance, the decreases to shear were greater than the decreases to compression, and the SR increased.

As highlighted in the previous section, the greater tuberosity radius increase had a minimal impact on mean overall DMA due to the unwrapping of the deltoid at high elevation angles. Despite this finding, this modification had a marked impact on joint stability. This can be attributed to the changes in joint contact forces while the modification was in effect at the lower ranges of humeral elevation. This region was the least stable (Costantini et al. 2015) and, as a result, this modification had a noticeable impact on SR. During 0° to 45° degrees of humeral elevation in ABD, FF and SPE compression increased by an average of 8.0% and shear decreased by an average of -18.6% for the 10 mm radius increase, respectively. In addition, the unwrapping of the deltoid when the humerus was abducted explains why the modification had no effect on SR during IR90 and ER90.

4.4.3 Impingement-free range of motion

Impingement can have an effect on range of motion during everyday activities (Garcia et al. 2015), propagate scapular notching (which, in turn, can expose the screws used to anchor the glenosphere to the scapula and loosen the metaglene), and wears away at the humeral cup. These are detrimental to the long-term outcomes of RTSA recipients (Farshad and Gerber, 2010) and, as such, modified configurations that increase IFROM are beneficial.

Changes to IFROM were predominately obtained by modified configurations that translated the glenosphere. As shown in Figure 4.19, IFROM improvements were achieved by shifting the humeral cup away from the reamed glenoid, thereby reducing intra-articular impingement. The current study found that inferiorly translating the glenosphere had the greatest beneficial impact on IFROM, with the 5 mm and 10 mm offsets improving IFROM by an average of 34.1° and 40.3° in ABD, FF

and SPE, respectively. To a lesser extent, glenosphere lateralisation also improved IFROM, with 17.9° and 31.6° improvements obtained for the same metrics stated previously. These findings compare well with literature, Kontaxis and Johnson (2009) and De Wilde et al. (2010) observed that inferior translation of the glenosphere was more effective than glenosphere lateralisation at reducing impingement. Clinical follow-up studies also observed a reduced severity of scapular notching due to inferior glenosphere placement (Simovitch et al. 2007; Mizuno et al. 2012).

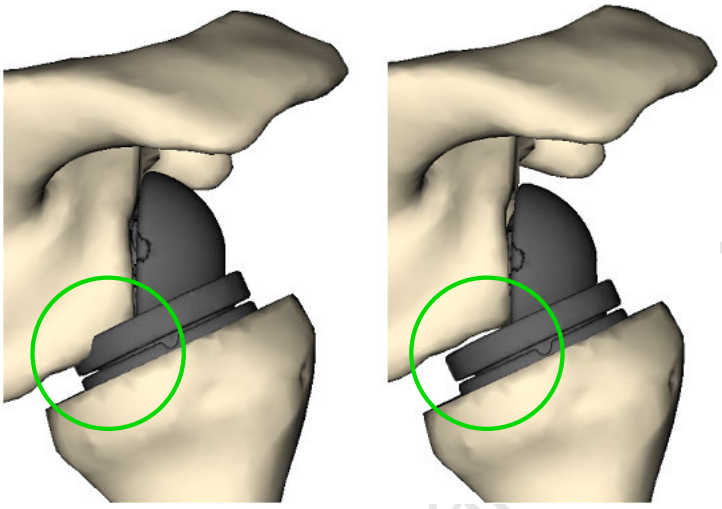

(a) Default configuration (b) Inferior glenosphere

Figure 4.19 Comparison of intra-articular impingement profiles between the default (left) and the inferiorly translated glenosphere (right) configurations. Note that, for this subject, intra-articular impingement when the humerus was adducted was mitigated with the 5 mm inferior translation of the glenosphere

These modifications had the same beneficial effect on IFROM during rotation with the humerus adducted, due to the shift of the humeral cup away from the reamed glenoid. For example, the current study found that 5 mm of inferior glenosphere translation increased IFROM by 25.4° during IR20 and 56.1° during ER20. These findings are corroborated by Berhouet et al. (2014b) and Li et al. (2013), who identified 28.5° and 46.2°, and 25.2° and 60.0° increases in IR20 and ER20, respectively. Additionally, these modifications increased IFROM during rotation at 90° of humeral elevation by shifting the humerus away from the acromion and coracoid process thereby reducing extra-articular impingement (Figure 4.20). It should also be noted that IFROM was not measured for the inferior rotation of the glenosphere due to the way the modification was applied. In contrast, previous studies have been shown that it may have an effect on impingement (Nyffeler et al. 2005; De Wilde et al. 2010; Gutiérrez et al. 2007). However, this effect was small in comparison to the other glenosphere modifications and Edwards et al. (2012), after a one-year follow-up, suggested that it does not decrease the incidence of scapular notching.

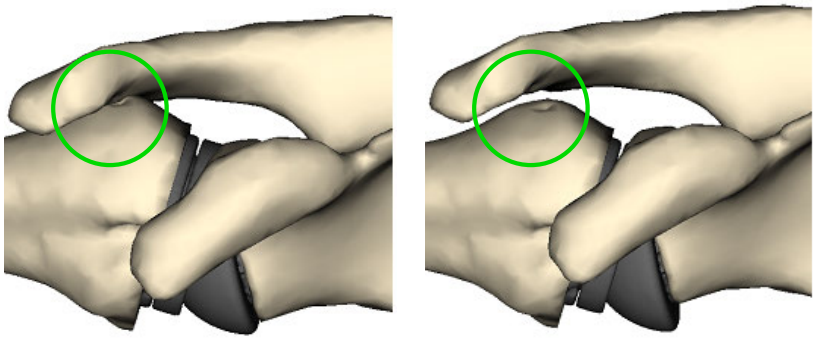

(a) Default configuration (b) Inferior glenosphere

Figure 4.20 Comparison of extra-articular impingement profiles between the default (left) and the inferiorly translated glenosphere (right) configurations. Note that, for this subject, extra-articular impingement between the humerus and acromion when the humerus was at 90° of humeral elevation and neutrally rotated was minimised with the 5 mm inferior translation of the glenosphere

With regards to the effect of humeral tray translations on IFROM, biomechanical studies have found that it can reduce extra-articular impingement when the humerus is elevated (Berhouet et al. 2014a; Lädermann et al. 2015). This was achieved by altering the position of the humerus relative to tray thereby moving it away from or towards the acromion or coracoid process. Berhouet et al. (2014a) and Lädermann et al. (2015) demonstrated that a medial tray placement (which lateralised the humerus) increased extra-articular impingement when the humerus was elevated. Due to limiting elevation of the humerus to 120° and the utilisation of a 155° neck-shaft angle, changes to IFROM were only observed during IR90 and ER90 in the current study, and not during ABD, FF and SPE as previously demonstrated. A decrease in the rotational IFROM was identified in the current study when the 5 mm medial tray offset was implemented (-4.9° in IR90 and -13.4° in ER90). Changing humeral tray depth also only changed rotational IFROM when the humerus was elevated. In this instance, the position of the humerus was either moved inferiorly or superiorly and, therefore, contact with the acromion was affected. However, as shown in Table 4.9, the overall effect of humeral tray modifications on impingement was negligible relative to the glenosphere translations.

4.4.4 Limitations

The limitations of this chapter can be categorised into those concerning the implementation of the prosthesis modifications and the data processing techniques. The limitations of Chapter 3 are also applicable in this chapter due to the nature of the assessments conducted.

4.4.4.1 Prosthesis modifications

Some of prosthesis modifications that were described in Section 2.4.3 were not evaluated in this chapter. As the Delta XTEND prosthesis (DePuy-Synthes 2013) acted as the basis for the default

configuration, a fixed humeral stem neck-shaft angle of 155° was used. In addition, a fixed diameter of 38 mm was used for the glenosphere and humeral cup, along with a fixed cup depth of 10.65 mm. These factors were not modified due to practical limitations, a 135° humeral stem design is not available for the Delta XTEND and alterations to the diameter and cup depth would require the development of their own models for each subject due to current method of modifying the prosthesis configuration. Therefore, each subject would require more than one model in the model-set and this would over-complicate the assessment procedure.

Onlay tray movement was prescribed to the humeral components of the prosthesis to simulate tray translations. As the Delta XTEND is an inlay prosthesis, this was an idealised implementation that assumed there was a separation between the stem and tray. For the purposes of musculoskeletal modelling, this was a reasonable assumption to make as the overall impact of the tray translations was the alteration of the humerus relative to the tray. However, the practical implementation of this modification would require the conversion of the Delta XTEND from an inlay to an onlay.

Comparably, augmentations to the greater tuberosity have not yet been practised by surgeons and, as such, this modification is currently an idealised implementation of the concept. If the modification proves to be beneficial for the optimised configuration of the prosthesis, that could motivate the development of a practical implementation. In addition, this modification was not assessed using the IDA as it did not change the position of the humerus or prosthetic components.

There was a disconnect between the virtual surgery and the programmatic application of the modifications, with the former taking place in Mimics and the latter taking place in OpenSim (using its API) and the IDA. This inhibited the accurate programmatic simulation of different resection angles. An attempt was made at this with the inferior rotation of the glenosphere, however, as can be seen in Figure 4.4, the API was only able to rotate the prosthesis and could not revise the resection angle (which would be required for a more realistic assessment of the modification). As a result, this rotation may not represent a realistic placement of the prosthesis and IFROM was not measured for this parameter. It was due to this disconnect that retroversion angle for the humeral head resection was not used as a modifiable parameter.

4.4.4.2 Data processing

The data for each outcome measure typically take the form of an mean; for example, the mean moment arm of the overall deltoid. Analysing data in this manner can be reductive as it takes an outcome measure that has dimensionality (as it is a function of motion) and reduces it to a single number with zero dimension. A technique like statistical parametric mapping preserves the dimensionality of the data by analysing the full set of data points (Pataky 2010). This has the potential to provide a much deeper insight into the effect a modification has on an outcome measure for a given motion. However, due to the volume of data generated during the assessment of 36 modifications, 3 outcome measures and 7 motions, some form of data reduction is required to

adequately synthesize and process the data. Therefore, future iterations of the assessment framework alternatively could use the data from a specific point in a given motion, instead of the mean, to determine the targeted effect of prosthesis modifications. These points could be prescribed by an orthopaedic team looking to address patient-specific criteria.

4.5 Selecting prosthesis modifications for optimisation

The modified configurations with an overall beneficial were identified in Table 4.9 and re-iterated in Table 4.10. The 5 mm posteromedial translation of the humeral tray obtained the highest score (7.25 out of 21).

Table 4.10 Overall effect of the modified configurations (score out of 21). * represents configurations with excessive DE

Config.	Offset Level 1	Offset Level 2
GS_L	1	3.75
GS_A	1	1.75
GS_AI	4.5	*
GS_I	5	*
GS_PI	4.5	*
HTD_I	0.25	0.75
HTT_PL	0.75	1
HTT_P	3.5	4.25
HTT_PM	5	7.25
HTT_M	2	2.5
GT_RI	3	4.75

In Chapter 5, modifications will be systematically combined to find a configuration of the prosthesis that optimise RTSA functional outcomes. As such, any superfluous modifications need to be removed to streamline the simulations and minimise unnecessary computational time.

The second offset level of glenosphere lateralisation, greater tuberosity radius increase and humeral tray modifications improved functional outcomes without any detriment to deltoid elongation. Therefore, evaluating both offset levels is unnecessary as the second offset can maximise the impact of these modifications. The effect of the humeral tray depth increase and the medial and posterolateral translations of the tray were small relative to the other humeral tray modifications and, will not be assessed. With regards to the eccentric translations of the glenosphere, only the first offset level can be used for three out of the four translations due to excessive deltoid elongation at the second level. As with the humeral tray modifications, the anterior translation of the glenosphere had a reduced effect on functional outcomes in comparison to the other glenosphere modification and, as such, will not be assessed.

Based on this selection process, only the following modifiable parameters will be assessed in Chapter 5:

1. Glenosphere lateralisation - 10 mm offset
2. Glenosphere eccentric translations - 5 mm offsets:
   (a) Anteroinferior
   (b) Inferior
   (c) Posteroinferior
3. Humeral tray translations - 5 mm offsets:
   (a) Posterior
   (b) Posteromedial
4. Greater tuberosity radius increase - 10 mm offset

4.6 Conclusion

The ability of the NSM and IDA, using the reverse shoulder model-set, to assess the effect of modifying prosthesis configuration on the functional outcomes of RTSA has been demonstrated in this chapter. Modifications to the intra-operative placement of the glenosphere and humeral tray, and the radius of the greater tuberosity were individually incorporated into the NSM using the OpenSim API and a custom-made protocol for the IDA. A total of 18 modifiable parameters of the prosthesis were assessed at two incrementally increasing offset levels (for a total of 36 modified configurations) using the assessment framework that was established in Chapter 3 and expanded upon in this chapter.

Each modified configuration was evaluated relative to the default and its effect on functional outcomes was compared to biomechanical literature. Not all the modifications implemented in the current study have been investigated previously, with prior studies placing a greater emphasis on the analysis of lateral or inferior translation of the glenosphere, and medial or lateral translation of the humeral tray. That being said, the underlying effect of each modified configuration on the reverse shoulder was investigated. This broadened the comparability of the current study to the available literature and, in general, a good agreement was observed, especially for the motions that elevated the humerus. As with the Chapter 3, differences between the findings of the current study and literature could be attributed to anatomical variability and the implementation of differing prosthesis designs and research techniques.

The relative effect of each modification was assessed using a data binning process and, consequently, they were characterised as having a beneficial, detrimental, or negligible impact on each

combination of primary outcome measure (DMA, SR, and IFROM) and motion. Additionally, a thresholding process was used to identify any incidences of consistent excessive elongation of the deltoid and eliminate the corresponding modifications from further consideration. At the first offset level, the inferior translation of the glenosphere and the posteromedial translation of the humeral tray both had the greatest overall beneficial effect, conversely, the inferior rotation of the glenosphere had the greatest detrimental effect.

19 of the 36 modified configurations were found to have an overall beneficial impact on the functional outcomes of RTSA. After a streamlining process, a subset of 7 parameters was selected for use in Chapter 5 to determine an optimised configuration of the prosthesis. This subset included four glenosphere modifications, two humeral tray modifications and one greater tuberosity modification.

Chapter 5

Optimising prosthesis configuration

5.1 Introduction

Previous investigations into the effect of reverse total shoulder arthroplasty (RTSA) modifications have generally been performed on a single modifiable parameter (Gutiérrez et al. 2008b; De Wilde et al. 2010; Henninger et al. 2012b; Berhouet et al. 2014a; Chae et al. 2015; Costantini et al. 2015; Kontaxis et al. 2017). This approach has allowed for incremental additions to the biomechanical understanding of the prosthesis. However, it is hypothesised that the simultaneous application of multiple parameters can improve function to a greater extent than the application of its constitutive components in isolation. Therefore, the aim of this chapter is to systematically combine a set of parameters and evaluate the effect of these configurations on reverse shoulder functional outcomes to determine an optimised prosthesis configuration.

This evaluation will be conducted using the assessment framework (established in Chapter 3 and expanded upon in Chapter 4, Figure 4.1) and data processing techniques (established in Chapter 4). In addition, a factor analysis will be performed in an attempt to further characterise the biomechanical trade-offs between impingement and the kinematic and kinetic properties of the reverse shoulder.

5.2 Materials and methods

5.2.1 Prosthesis modifications

As with the Chapter 4, modifications were incorporated into the reverse shoulder model-set and evaluated using the NSM and IDA. However, rather than applying an individual modification, combinations of modifications were incorporated into the model-set and the overall effect of this modified configuration was assessed. The findings of the previous chapter demonstrated that only a subset the modifiable parameters had a beneficial impact on reverse shoulder function. This subset (re-iterated in Table 5.1) included the default configuration, one lateral glenosphere translation, three eccentric glenosphere translations, two humeral tray translations and one greater tuberosity radius increase.

These parameters were systematically combined, along with the default configuration of each modification, to establish 48 configurations of the prosthesis (2×4×3×2) and a new nomenclature was created for these configurations. The lateral glenosphere translations were assigned descriptors A1 and A2, the eccentric glenosphere translations were assigned B1 to B4, the humeral tray translations were assigned C1 to C3 and the greater tuberosity radius increases were assigned D1 and D2. This nomenclature allowed for a concise description of a modified configuration. For example, A1B1C1D1 referred to the default configuration and A2B3C1D2 referred to a configuration that implemented a 10 mm lateral translation of the glenosphere, a 5 mm inferior translation of the glenosphere, no change to the humeral tray translation and a 10 mm increase of the greater tuberosity radius.

Table 5.1 Modifiable parameters and configuration nomenclature

Location	Type	Offset	Inc. (mm)	Nomenclature
Glenosphere	Translation	Default	0	A1
		Lateral	10	A2
		Default	0	B1
		Anteroinferior	5	B2
		Inferior	5	B3
		Posteroinferior	5	B4
Humeral Tray	Translation	Default	0	C1
		Posterior	5	C2
		Posteromedial	5	C3
Greater tuberosity	Radius	Default	0	D1
		Increase	10	D2

5.2.2 Motions

The same motions that were used in Chapters 3 and 4 were implemented here. These included abduction (ABD), forward flexion (FF), scapular plane elevation (SPE), internal rotation at 20° and 90° of humeral elevation (IR20 and IR90), and external rotation at 20° and 90° of humeral elevation (ER20 and ER90). For additional information regarding these motions, refer to Section 3.3.1

5.2.3 Outcome measures

The same outcome measures evaluated in Chapter 4 were evaluated here. These included peak elongation of the overall deltoid (DE, in %), mean overall deltoid moment arm (DMA, in mm), mean stability ratio (SR) and impingement-free range of motion (IFROM, in °). An increase in DE was detrimental and increases in DMA, SR, and IFROM were beneficial, except for DMA during ER20 and ER90, where decreases were beneficial.

Complementary to these outcome measures, the positional changes to the glenohumeral joint due to the default and optimised configurations were evaluated. Additional information regarding these outcome measures can be found in Section 3.3.2.

5.2.4 Data processing

5.2.4.1 Thresholding process: DE

As in Section 4.2.5.1, a thresholding process was implemented to determine if any of the modified configurations consistently exhibited signs of excessive peak DE (greater than 20% in relation to the normal shoulders) during the assessed motions.

5.2.4.2 Data binning process: DMA, SR, and IFROM

As in Section 4.2.5.2, a data binning process was used to evaluate the effect of the modified configurations on each combination of primary outcome measure (DMA, SR, and IFROM) and motion in relation to the default configuration. Through the process, each combination of outcome measure and motion was assigned a value between -1 to 1 in 0.25 increments. This value was the median of the binned data in the model-set and demonstrated the typical effect of a modified configuration. Negative values indicated a detrimental effect and positive values indicated a beneficial effect. These median scores were summed for each motion and for each outcome measure. This cumulative score (which ranged from -21 to 21), in conjunction with the thresholding process, illustrated the overall effect of a modification and was used to determine the optimal configuration of the prosthesis for the given modified parameters.

5.2.4.3 Detailed analysis of the optimised configuration

To understand the effect of the optimised configuration, an analysis similar to Section 3.3.3 was performed. Descriptive statistics of the DE, DMA, SR, IFROM and the glenohumeral joint positional changes were calculated for the default and optimised configurations during each motion. This data were represented using subject averages with 95% confidence intervals. Additionally, the subject-averaged DE, DMA and GH joint contact forces (in the humeral cup reference frame) were plotted as functions of each motion for both configurations.

5.2.4.4 Factor analysis

Factor analysis was performed on the data collected from the binning process (Abdi et al. 2013). This analysis was supplementary to the binning process and was carried out to reduce the data to assess the variability of the outcome measures due to the modified configurations. The median

binned data for DMA, SR, and IFROM for each motion was collated for each modified configuration and assembled into a 47×21 matrix, where each row represented a configuration and each column represented one of the 21 outcome measures. Factor analysis was performed on this matrix using IBM SPSS Statistics for Windows (version 25, IBM Corp., USA). Principal component analysis was used to extract the factors (principal components) from the data and a varimax rotation was performed to orthogonally rotate the loadings of each measured outcome.

5.3 Results

5.3.1 Deltoid elongation

The tallied data of excessive peak DE is shown in Table 5.2. Excessive DE was especially apparent for the configurations that simultaneously implemented numerous parameters. The highest summed tally was identified for the A2B3C2D2 configuration, which induced excessive peak DE in just under a third of all the models during ABD, FF and SPE. Using the assumption that a sum of greater than 1 for a given motion was indicative of consistent excessive DE, the number of usable modified configurations reduced from 47 to 21.

Table 5.2 Tallied data for DE greater than 20%. Note that instances of consistent DE are highlighted in grey

No.	Config.	ABD	FF	SPE	IR20	ER20	IR90	ER90	Sum
1	A1B1C1D2	·	·	·	·	·	·	·	·
2	A1B1C2D1	·	·	·	·	·	·	·	·
3	A1B1C2D2	·	·	·	·	·	·	·	·
4	A1B1C3D1	·	·	·	·	·	·	·	·
5	A1B1C3D2	·	·	·	·	·	·	·	·
6	A1B2C1D1	·	·	**1**	·	·	·	·	**1**
7	**A1B2C1D2**	**2**	·	**2**	·	·	·	·	**4**
8	**A1B2C2D1**	**1**	·	**2**	·	·	·	·	**3**
9	**A1B2C2D2**	**2**	·	**2**	·	·	·	·	**4**
10	A1B2C3D1	·	·	**1**	·	·	·	·	**1**
11	**A1B2C3D2**	**1**	·	**2**	·	·	·	·	**3**
12	**A1B3C1D1**	**1**	·	**1**	·	·	·	·	**2**
13	**A1B3C1D2**	**2**	**1**	**3**	·	·	·	·	**6**
14	**A1B3C2D1**	**2**	·	**2**	·	·	·	·	**4**
15	**A1B3C2D2**	**4**	**2**	**4**	·	·	·	·	**10**
16	**A1B3C3D1**	**1**	·	**1**	·	·	·	·	**2**
17	**A1B3C3D2**	**2**	·	**2**	·	·	·	·	**4**
18	A1B4C1D1	·	·	·	·	·	·	·	·
19	A1B4C1D2	**1**	·	**1**	·	·	·	·	**2**
20	A1B4C2D1	·	·	**1**	·	·	·	·	**1**
21	**A1B4C2D2**	**2**	·	**2**	·	·	·	·	**4**
22	A1B4C3D1	·	·	·	·	·	·	·	·
23	A1B4C3D2	**1**	·	**1**	·	·	·	·	**2**
24	A2B1C1D1	·	·	·	·	·	·	·	·
25	A2B1C1D2	·	·	**1**	·	·	·	·	**1**
26	A2B1C2D1	·	·	·	·	·	·	·	·
27	A2B1C2D2	**1**	·	**1**	·	·	·	·	**2**
28	A2B1C3D1	·	·	·	·	·	·	·	·
29	A2B1C3D2	·	·	·	·	·	·	·	·
30	**A2B2C1D1**	**2**	·	**3**	·	·	·	·	**5**
31	**A2B2C1D2**	**3**	**2**	**3**	·	·	·	·	**8**
32	**A2B2C2D1**	**4**	**1**	**4**	·	·	·	·	**9**
33	**A2B2C2D2**	**4**	**4**	**4**	·	·	·	·	**12**
34	**A2B2C3D1**	**1**	·	**3**	·	·	·	·	**4**
35	**A2B2C3D2**	**4**	**2**	**4**	·	·	·	·	**10**
36	**A2B3C1D1**	**3**	**1**	**3**	·	·	·	·	**7**
37	**A2B3C1D2**	**3**	**3**	**3**	·	·	·	·	**9**
38	**A2B3C2D1**	**4**	**4**	**4**	·	·	·	·	**12**
39	**A2B3C2D2**	**4**	**4**	**4**	**1**	·	·	·	**13**
40	**A2B3C3D1**	**3**	**1**	**3**	·	·	·	·	**7**
41	**A2B3C3D2**	**4**	**3**	**4**	·	·	·	·	**11**
42	**A2B4C1D1**	**1**	·	**2**	·	·	·	·	**3**
43	**A2B4C1D2**	**3**	**3**	**3**	·	·	·	·	**9**
44	**A2B4C2D1**	**3**	**1**	**3**	·	·	·	·	**7**
45	**A2B4C2D2**	**4**	**4**	**4**	·	·	·	·	**12**
46	A2B4C3D1	**1**	·	**1**	·	·	·	·	**2**
47	**A2B4C3D2**	**4**	**2**	**3**	·	·	·	·	**9**

5.3.2 DMA, SR, and IFROM

The binned data for each combination of outcome measure and motion for the 47 modified configurations is shown in Table 5.4. In addition, this table includes the motion-summed scores (out of 7) for each combination of outcome measure and modified configuration, and the overall score (out of 21). The configurations that did not excessively elongate the deltoid were highlighted in grey. Sections 5.3.3 and 5.3.4 will go into detail regarding these results.

Table 5.3 highlights the range of changes to each outcome measure for the three motion groups defined in Section 4.2.5.2. The DMA values ranged from -5.33 mm during SPE to 3.75 mm during FF; the SR values ranged from -0.82 during FF to 17.74 during ABD, and that the IFROM values ranged from -1.53° during IR90 to 69.8° during ER20.

Table 5.3 Range of the changes to each outcome measure. The data are presented with subject-averaged means (and 95% confidence intervals)

Measure	Group	Range			Motion	No.	Config
DMA (mm)	ABD, FF & SPE	Min	-5.33	(-5.51, -5.15)	SPE	25	A2B1C1D2
		Max	3.75	(3.65, 3.85)	FF	16	A1B3C2D2
	IR20 & IR90	Min	-2.21	(-2.28, -2.14)	IR90	14	A1B3C1D3
		Max	1.36	(1.26, 1.45)	IR20	46	A2B4C2D2
	ER20 & ER90	Min	-2.17	(-2.31, -2.03)	ER90	31	A2B2C1D2
		Max	0.79	(0.75, 0.83)		18	A1B4C1D1
SR	ABD, FF & SPE	Min	-0.82	(-1.04, -0.60)	FF	7	A1B2C1D2
		Max	17.74	(9.82, 25.67)	ABD	29	A2B1C2D3
	IR20 & IR90	Min	-0.5	(-0.90, -0.11)	IR20	42	A2B4C1D1
		Max	11.27	(7.85, 14.69)	IR20	10	A1B2C2D2
	ER20 & ER90	Min	-0.22	(-0.26, -0.18)	ER90	30	A2B2C1D1
		Max	5.18	(3.95, 6.41)	ER20	29	A2B1C2D3
IFROM (°)	ABD, FF & SPE	Min	-1.13	(-3.56, 1.29)	SPE	2	A1B1C1D3
		Max	64.67	(53.09, 76.24)	ABD	36	A2B3C1D1
	IR20 & IR90	Min	-1.53	(-8.28, 5.21)	IR90	8	A1B2C1D3
		Max	34.07	(25.69, 42.44)		37	A2B3C1D2
	ER20 & ER90	Min	-1.07	(-3.34, 1.20)	ER90	26	A2B1C1D3
		Max	69.8	(56.02, 83.58)	ER20	42	A2B4C1D1

Table 5.4 Median binned data of the changes to each outcome measure for the modified configurations. The rows highlighted in grey represented the binned data for the usable configurations

	DMA							SR							IFROM							Sums			
No.	ABD	FF	SPE	IR20	ER20	IR90	ER90	ABD	FF	SPE	IR20	ER20	IR90	ER90	ABD	FF	SPE	IR20	ER20	IR90	ER90	DMA	SR	IFROM	Overall
1	0	0	0	0	0	0	0	0.75	0.75	0	0.25	0.75	0	0	0	0	0	0	0	0	0	0	2.5	0	2.5
2	0	0	0	0	0.25	-0.5	1	0.25	-0.25	0.5	1	0	0.25	0	0	0	0	0	0	0	0	0.75	1.75	0	2.5
3	0	0.25	0	0	0.25	-0.5	1	1	0.25	1	1	1	0.25	0	0	0	0	0	0	0	0	1	4.5	0	5.5
4	0	0	0	0	0	-0.75	0.5	0.5	0.25	0.5	0.75	0.75	0.5	0.75	0	0	0	0	0	0	0	-0.25	4	0	3.75
5	0	0	0	0	0.25	-0.75	0.5	1	0.75	0.75	1	1	0.5	0.75	0	0	0	0	0	0	0	0	5.75	0	5.75
6	0.75	0	0.25	-0.25	0.25	-0.5	0.25	0	0	0	0.5	0.25	0	-0.25	0	0	0	0.25	0.25	0	0	0.75	0.5	0.5	1.75
7	0.75	0.25	0.5	-0.25	0.25	-0.5	0.25	0.75	0.5	0	0.75	0.75	0	-0.25	0	0	0	0.25	0.25	0	0	1.25	2.5	0.5	4.25
8	0.5	0.5	0.25	-0.25	0.75	-1	1	0.25	-0.25	0.5	1	0.25	0.25	-0.25	0	0	0	0.25	0.25	0.25	0	1.75	1.75	0.75	4.25
9	0.75	0.5	0.25	-0.25	0.75	-1	1	0.75	0	1	1	0.75	0.25	-0.25	0	0	0	0.25	0.25	0.25	0	2	3.5	0.75	6.25
10	0.75	0.25	0.5	-0.5	0.5	-1	1	0.5	0	0.5	1	0.75	0.5	0.5	0	0	0	0.25	0.25	0	0	1.5	3.75	0.5	5.75
11	1	0.5	0.5	-0.5	0.5	-1	1	1	0.5	0.75	1	1	0.5	0.5	0	0	0	0.25	0.25	0	0	2	5.25	0.5	7.75
12	0.5	0.5	0.5	0	0	-0.5	-0.25	0	0	0	0	0.25	0	-0.25	0.75	0.5	0	0.25	0.5	0.25	0	0.75	0	2.25	3
13	0.75	0.5	0.75	0	0	-0.5	-0.25	1	0.75	0	0.75	0.75	0	-0.25	0.75	0.5	0	0.25	0.5	0.25	0	1.25	3	2.25	6.5
14	0.5	1	0.5	0	0.25	-1	1	0.25	0	0.5	1	0.25	0.25	-0.25	0.75	0.5	0	0.25	0.5	0.25	0	2.25	2	2.25	6.5
15	0.5	1	0.5	0	0.25	-1	1	0.75	0.25	0.75	1	0.75	0.25	-0.25	0.75	0.5	0	0.25	0.5	0.25	0	2.25	3.5	2.25	8
16	0.75	0.75	0.75	-0.25	0	-1	0.25	0.5	0.5	0.5	0.75	0.75	0.5	0.5	0.75	0.5	0	0.5	0.5	0	0	1.25	4	2.25	7.5
17	0.75	1	0.75	-0.25	0	-1	0.25	1	0.75	0.75	1	1	0.5	0.5	0.75	0.5	0	0.5	0.5	0	0	1.5	5.5	2.25	9.25
18	0	0.5	0.25	0	-0.5	0	-0.75	0	0.25	0	-0.25	0.25	0	0	0.75	0.5	0	0.25	0.5	0	0	-0.5	0.25	2	1.75
19	0	0.5	0.25	0	-0.5	0	-0.75	0.75	1	0	0	1	0	0	0.75	0.5	0	0.25	0.5	0	0	-0.5	2.75	2	4.25
20	0	0.75	0.25	0	0	-0.75	0.5	0.25	0	0.5	1	0.25	0.25	0	0.75	0.5	0	0.25	0.5	0	0	0.75	2.25	2	5
21	0	1	0.25	0	0	-0.75	0.5	1	0.5	0.75	1	1	0.25	0	0.75	0.5	0	0.25	0.5	0	0	1	4.5	2	7.5
22	0	0.75	0.25	0	-0.25	-1	0	0.25	0.75	0.5	0.75	0.75	0.5	0.75	0.75	0.5	0	0.25	0.75	0	0	-0.25	4.25	2.25	6.25
23	0.25	1	0.5	0	0	-1	0	1	0.75	0.5	1	1	0.5	0.75	0.75	0.5	0	0.25	0.75	0	0	0.75	5.5	2.25	8.5
24	-1	-1	-1	0.5	0.5	0	0.25	0.25	0.25	0	0	0	0	0	0.75	0.5	0	0.25	0.5	0	0	-1.75	0.5	2	0.75
25	-1	-1	-1	0.75	0.5	0	0.25	1	0.5	0.25	0	1	0	0	0.75	0.5	0	0.25	0.5	0.25	0	-1.5	2.75	2.25	3.5
26	-1	-1	-1	0.75	0.75	-0.25	1	0.5	0	0.5	1	0	0.5	0	0.75	0.5	0	0.5	0.5	0.25	0	-0.75	2.5	2.5	4.25
27	-1	-0.75	-1	0.75	0.75	-0.25	1	1	0	1	1	1	0.5	0	0.75	0.5	0	0.5	0.5	0.25	0	-0.5	4.5	2.5	6.5
28	-1	-1	-1	0.5	0.75	-0.75	0.75	0.75	0.5	0.5	0.75	0.75	0.5	0.5	0.75	0.5	0	0.5	0.5	0.25	0	-1.75	4.25	2.5	5
29	-1	-0.75	-1	0.75	0.75	-0.75	0.75	1	0.25	0.75	0.75	1	0.5	0.75	0.75	0.5	0	0.5	0.5	0.25	0	-1.25	5	2.5	6.25
30	-0.25	-1	-0.75	0.25	0.75	-0.25	0.5	0.25	0	0	0	0	0	-0.5	1	0.5	0.25	0.5	0.75	0.5	0.5	-0.75	-0.25	4	3
31	-0.25	-0.75	-0.5	0.25	0.75	-0.25	0.5	1	0.5	0.25	0.25	1	0	-0.25	1	0.5	0.25	0.5	0.75	0.5	0.5	-0.25	2.75	4	6.5
32	-0.5	-0.5	-1	0.25	1	-0.75	1	0.5	0	0.5	1	0.5	0.5	-0.25	1	0.5	0.25	0.75	0.75	0.75	0.25	-0.5	2.75	4.25	6.5
33	-0.25	-0.25	-0.75	0.5	1	-0.75	1	1	0	1	1	1	0.5	-0.25	1	0.5	0.25	0.75	0.75	0.75	0.25	0.5	4.25	4.25	9
34	-0.25	-0.5	-0.5	0.25	1	-1	1	0.75	0.25	0.5	0.75	0.75	0.5	0.5	1	0.75	0.25	0.75	0.75	0.5	0	0	4	4	8
35	0	-0.25	-0.5	0.25	1	-1	1	1	0.25	0.75	0.75	1	0.5	0.5	1	0.75	0.25	0.75	0.75	0.5	0	0.5	4.75	4	9.25
36	-0.25	-0.5	-0.5	0.5	0.5	-0.25	0	0.25	0.25	0	0	0	0	-0.5	1	0.75	0.25	0.75	0.75	0.75	0.25	-0.5	0	4.5	4
37	-0.25	-0.25	-0.25	0.5	0.5	-0.25	0	1	0.75	0	0	1	0	-0.25	1	0.75	0.25	0.75	0.75	0.75	0.5	0	2.5	4.75	7.25
38	-0.5	0	-0.75	0.5	0.5	-0.75	1	0.5	0	0.5	1	0	0.25	-0.25	1	0.75	0.25	0.75	1	0.75	0.25	0	2	4.75	6.75
39	-0.25	0	-0.5	0.75	0.5	-1	1	1	0.25	0.75	1	1	0.5	-0.25	1	0.75	0.25	0.75	1	1	0.25	0.5	4.25	5	9.75
40	-0.25	0	-0.25	0.25	0.5	-1	0.75	0.75	0.5	0.5	0.75	0.75	0.5	0.5	1	0.75	0.25	0.75	1	0.75	0	0	4.25	4.5	8.75
41	0	0	-0.25	0.5	0.75	-1	0.75	1	0.5	0.75	0.75	1	0.5	0.5	1	0.75	0.25	0.75	1	0.75	0	0.75	5	4.5	10.25
42	-1	-0.5	-1	0.75	0	0	-0.25	0.25	0.5	0	0	0	0	-0.25	1	0.75	0.25	0.5	1	0.5	0	-2	0.5	4	2.5
43	-0.75	-0.25	-0.75	0.75	0	0	-0.25	1	0.75	0	0	1	0	0	1	0.75	0.25	0.5	1	0.5	0	-1.25	2.75	4	5.5
44	-1	0	-1	0.75	0	-0.5	0.75	0.5	0.25	0.5	1	0	0.25	0	1	0.75	0.25	0.75	1	1	0	-1	2.5	4.75	6.25
45	-1	0	-0.75	1	0.25	-0.5	0.75	1	0.25	0.75	1	1	0.25	0	1	0.75	0.25	0.75	1	1	0	-0.25	4.25	4.75	8.75
46	-0.75	-0.25	-0.75	0.75	0	-1	0	0.75	0.75	0.25	0.75	0.75	0.5	0.5	1	0.75	0.25	0.75	1	0.5	0	-2	4.25	4.25	6.5
47	-0.5	0	-0.5	0.75	0.25	-1	0	1	0.5	0.5	0.75	1	0.5	0.5	1	0.75	0.25	0.75	1	0.5	0	-1	4.75	4.25	8

5.3.3 Optimisation process

The motion-summed and overall scores for the modified configurations are re-iterated in Figure 5.1. This scatter plot illustrates the distribution of the results using dots to represent the scores obtained by one or more modified configuration. The red dots represent the configurations with excessive peak DE and the blue dots represent the usable configurations. The numbers next to the blue dots indicate the configurations that obtained the highest and lowest scores.

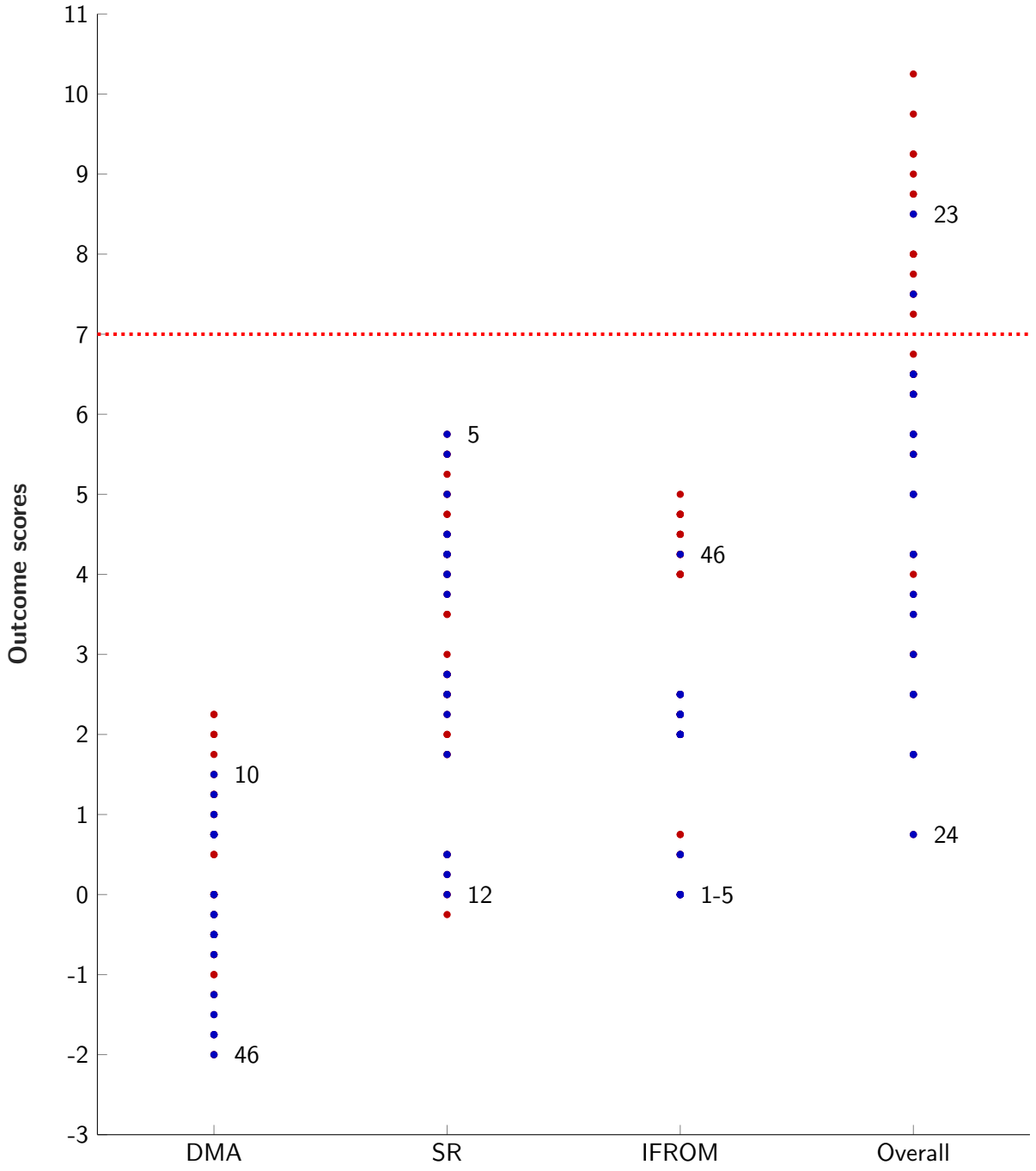

Figure 5.1 Scatter plot of the motion-summed and overall scores for the modified configurations. The dotted red line indicates the maximum score obtainable for the individual outcome measure

An excerpt of Table 5.4 is shown below; in this table the usable modified configurations that optimised each outcome measure and the overall performance (identified in Figure 5.1) were re-iterated. The outcome measure optimised in each instance is highlighted in grey.

Table 5.5 Scores (and percentages) of the usable modified configurations that optimised each outcome measure and the overall performance

		DMA		SR		IFROM		Overall	
No.	**Config.**	/7	%	/7	%	/7	%	/7	%
10	A1B2C3D1	1.5	21.4	3.75	53.6	0.5	7.1	5.75	27.4
5	A1B1C3D2	0	0	5.75	82.1	0	0	5.75	27.4
46	A2B4C3D1	-2	-28.6	4.25	60.7	4.25	60.7	6.5	31
23	A1B4C3D2	0.75	10.7	5.5	78.6	2.25	32.1	8.5	40.5
16	A1B3C3D1	1.25	17.9	4	57.1	2.25	32.1	7.5	35.7

The highest DMA score was 1.5 out of 7. This was obtained by a configuration that implemented two parameters: the anteroinferior translation of the glenosphere (B2) and the posteromedial translation of the humeral tray (C2). In this instance, the configuration improved DMA to a varying degree during all the motions except internal rotation.

The highest SR score was 5.75 out of 7. This was obtained by a configuration that implemented two parameters: the posteromedial translation of the humeral tray (C3) and the increase to the greater tuberosity radius (D2). This configuration improved SR to a varying degree during each motion. However, it did so at the expense of negligible changes to DMA and IFROM.

The highest IFROM score was 4.25 out of 7. This was obtained by a configuration that implemented three parameters: the lateral translation of the glenosphere (A2), the posteroinferior translation of the glenosphere (B4) and the posterior translation of the humeral tray. While this configuration maximised IFROM during all the motions except ER90 (where it had a negligible change) and had a moderately beneficial impact on SR, it had a negative overall effect on DMA and thereby diminished its overall performance.

The overall performance was optimised by the A1B4C3D2 configuration. It scored 8.5 out of 21 and implemented three parameters: the posteroinferior translation of the glenosphere, the posteromedial translation of the humeral tray and the increase to the greater tuberosity radius. Whilst this configuration did not maximise any of the individual outcome measures (Table 5.6), it improved SR by 5.5 (which was 0.25 less than the highest SR score) and had a moderately beneficial impact on IFROM, as it improved four of the seven motions. It only had a slight beneficial effect on DMA, as this outcome measure was negligibly affected during three motions (IR20, IR90 and ER90) and decreased during another (IR90).

Rather than opting to emphasise a single outcome measure with the optimal configuration, a balanced configuration was identified. The A1B3C3D1 configuration had the second highest overall performance of the usable configurations and, as shown in Table 5.6, maintained an overall beneficial effect on SR and IFROM, whilst improving upon the overall DMA score.

Consequently, the A1B3C3D1 configuration (which inferiorly translated the glenosphere by 5 mm and posteromedially translated the humeral tray by 5 mm) was selected as the optimised configuration as opposed to the A1B4C3D2 configuration.

Table 5.6 Comparison of the outcome measures for the two candidate optimised configurations: A1B4C3D2 and A1B3C3D1

Config.	Outcome	ABD	FF	SPE	IR20	ER20	IR90	ER90	Sum
A1B4C3D2	DMA	0.25	1	0.5	0	0	-1	0	0.75
	SR	1	0.75	0.5	1	1	0.5	0.75	5.5
	IFROM	0.75	0.5	0	0.25	0.75	0	0	2.25
A1B3C3D1	DMA	0.75	0.75	0.75	-0.25	0	-1	0.25	1.25
	SR	0.5	0.5	0.5	0.75	0.75	0.5	0.5	4
	IFROM	0.75	0.5	0	0.5	0.5	0	0	2.25

5.3.4 Optimised configuration functional changes

5.3.4.1 Glenohumeral joint positional changes

The subject-averaged locations of GH_{cor} and HH_{pos} for the default and optimised configurations are shown in Table 5.7. The differences between the default and optimised configurations were attributed to the implementation of the 5 mm inferior translation of the glenosphere (which translated the glenosphere along its Y_{gs} axis) and the 5 mm posteromedial translation of the humeral tray (which translated the humeral tray along its X_{hc} by 3.52 and Z_{hc} by -3.47).

Table 5.7 Subject-averaged glenohumeral joint centre of rotation and humeral head position for the default and optimised configurations (in mm). Note that confidence intervals have been omitted

	GH_{cor}			HH_{pos}		
	Default	Optimised	Diff	Default	Optimised	Diff
X-axis (ML)	-29.55	-29.55	0.00	-1.08	2.44	3.52
Y-axis (SI)	-24.38	-29.38	-5.00	-26.74	-26.94	-0.19
Z-axis (AP)	-36.48	-36.48	0.00	-0.12	-3.59	-3.47

5.3.4.2 Deltoid elongation

The changes to the peak DE due to the optimised configuration (A1B3C3D1) are illustrated in Figure 5.2. Peak DE increased in all motions except ER90, where it essentially remained unchanged. As mentioned in Section 5.3.1, excessive peak DE was identified in one subject during ABD and SPE, and this can be observed by the upper bound of the corresponding box plots. However, as is also evident, the average peak elongation of the deltoid during all the motions was below the 20% threshold.

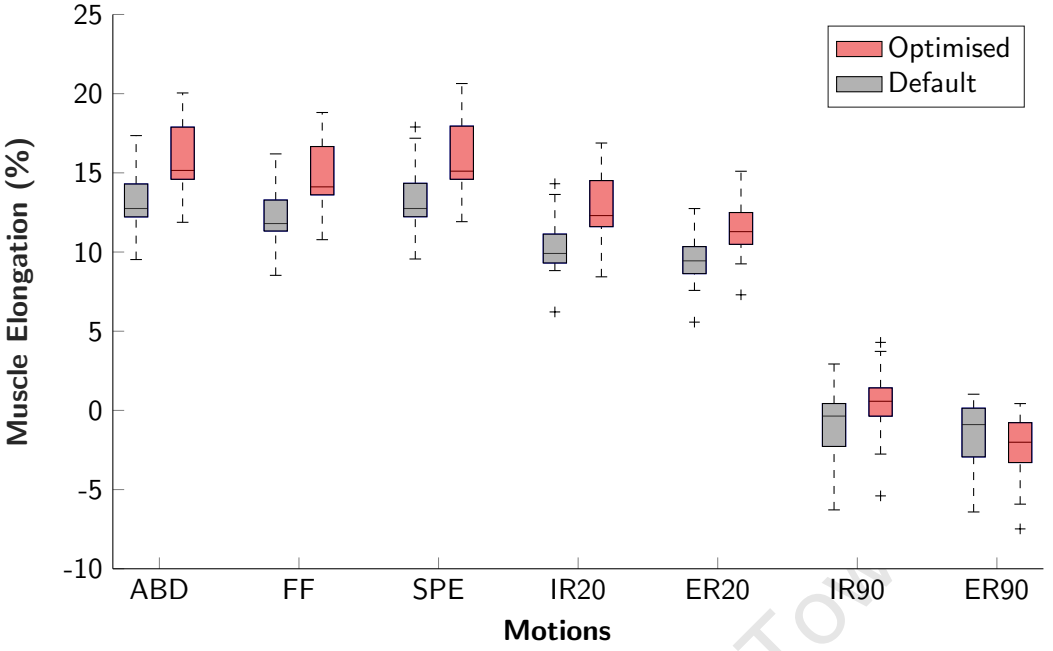

Figure 5.2 Box plots of the peak deltoid elongation for the default and optimised configurations. The grey box plots (left) represent the default configuration and the red box plots (right) represent the optimised configuration

5.3.4.3 Deltoid moment arm

The changes to DMA due to the optimised configuration are illustrated in Figure 5.3. The moment arm of the overall deltoid was increased throughout ABD, FF and SPE due to the optimised configuration. The overall DMA was decreased throughout both internal rotations and thereby increased the capability of the muscle to externally rotate the humerus. However, this change was more apparent during IR90 than IR20. With regards to the external rotations, the overall deltoid in both instances transitioned from an external rotator to an internal rotator over the course of both motions. Consequently, the effect of the optimised configuration transitioned from beneficial at the start of both motions to detrimental by the end of both motions and the resultant change to the overall deltoid was negligible for ER20 and marginal for ER90. These functional changes that took place throughout the motions were summarised using the mean of the overall DMA, and the corresponding box plots of these results can be found in Figure 5.4.

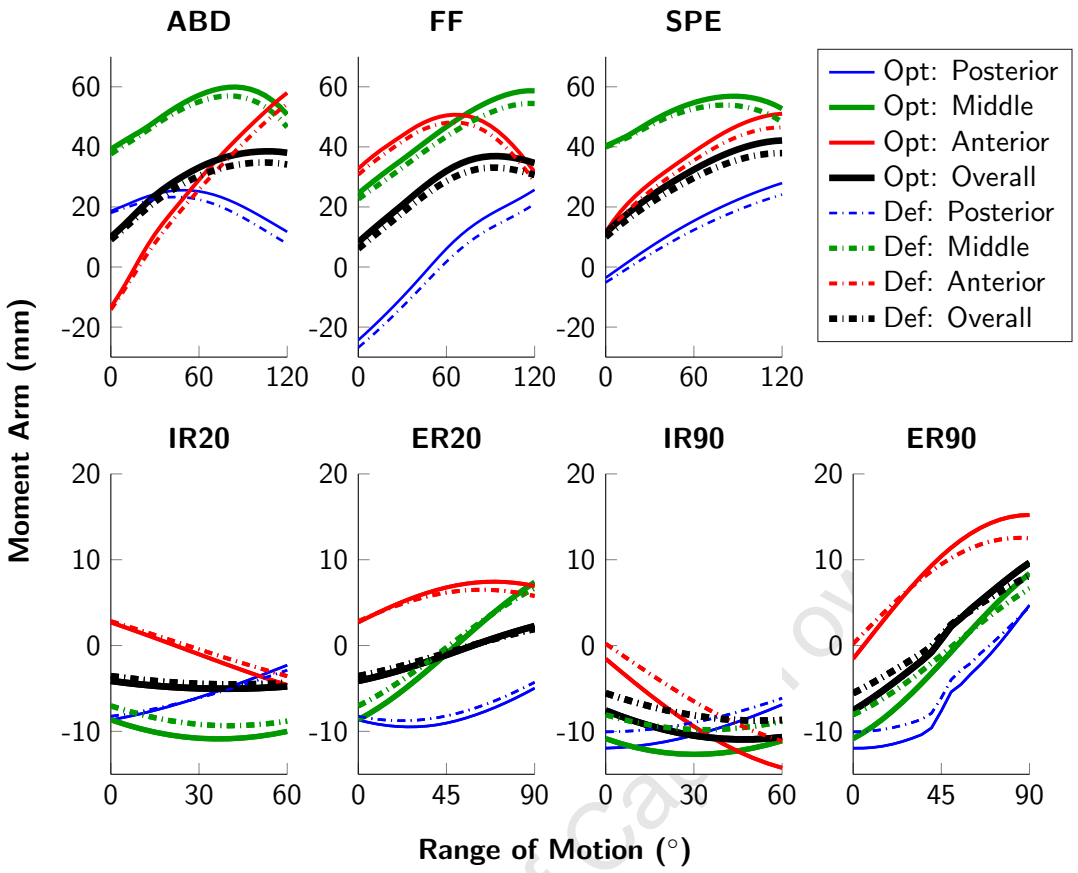

Figure 5.3 Subject-averaged DMA of the default and optimised configuration. For the humeral elevations/rotations, positive and negative values correspond to the agonistic/internal and antagonistic/external moment arms, respectively

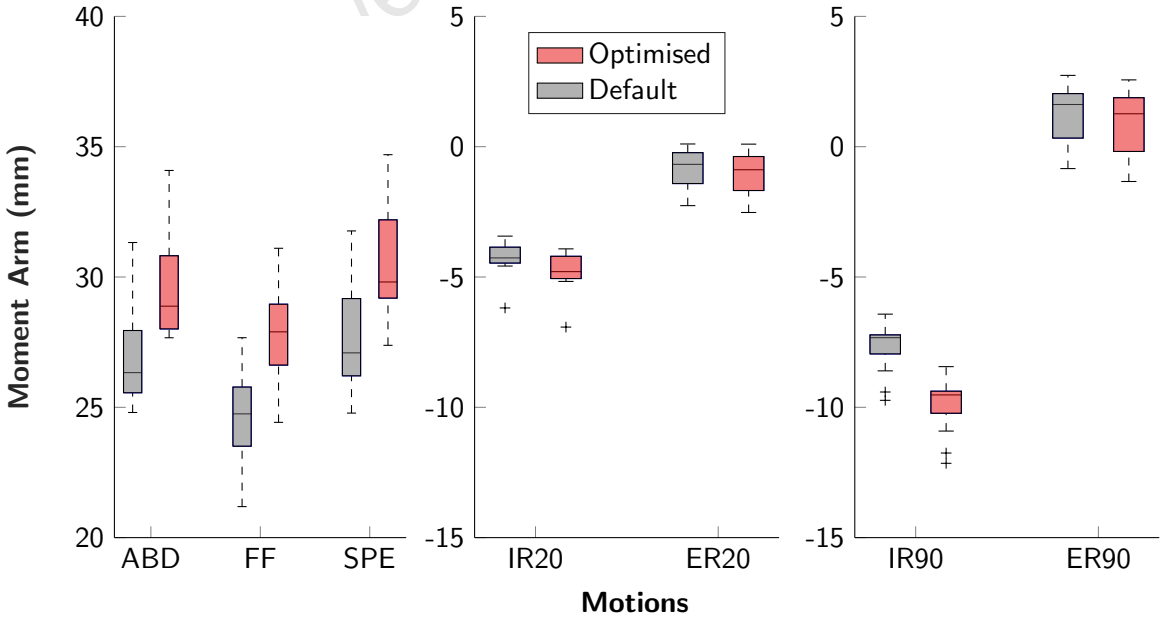

Figure 5.4 Box plots of the mean overall DMA of the default and optimised configurations

5.3.4.4 Stability ratio

The SR changes can be found in Figure 5.5. The optimised configuration increased SR during all the motions.

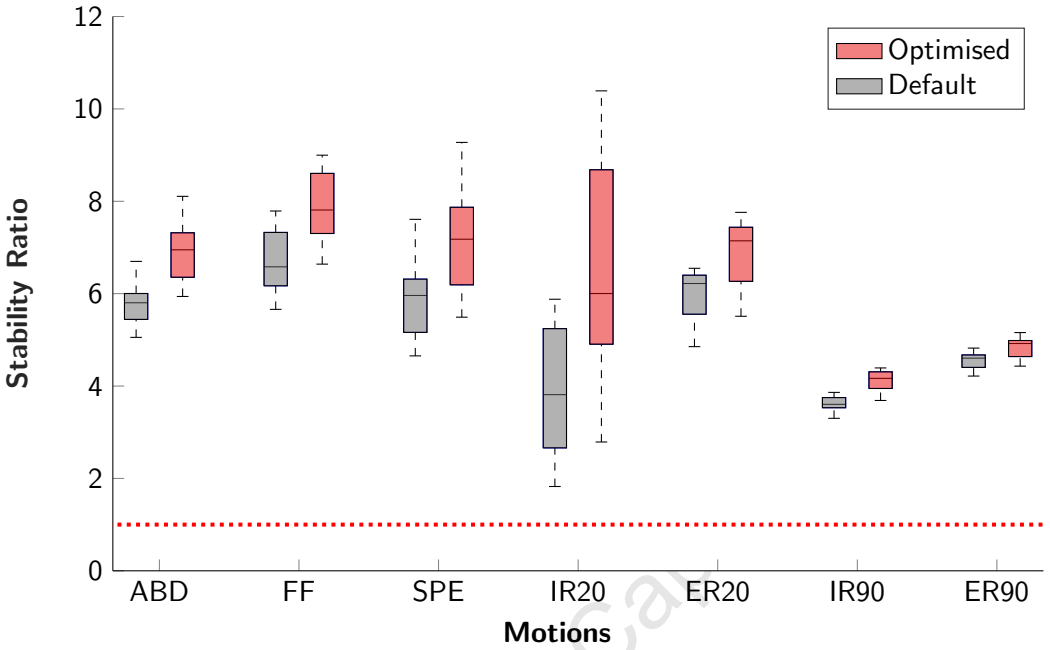

Figure 5.5 Box plots of the mean SR of the default and optimised configurations

As highlighted previously, SR is dependent on the interplay between the compression and shear joint contact forces throughout the course of each motion. The graphs in Figure 5.6 demonstrate that the increase in SR during ABD, FF and SPE for the optimised configuration was due to slight decreases in the shear forces. The SR changes during IR20 were more pronounced due to the simultaneous increase in compression and decrease in shear. However, this result had a large degree of variability due to the compression and shear forces nearly converging by the end of the motion for some of the subjects. Similar simultaneous changes to the joint forces were observed for ER20, except, in this instance, the changes were more consistent as the forces were separated throughout the motion. SR only slightly increased during IR90 and ER90 as the beneficial decrease to the shear forces were somewhat counteracted by the detrimental decrease to the compression forces.

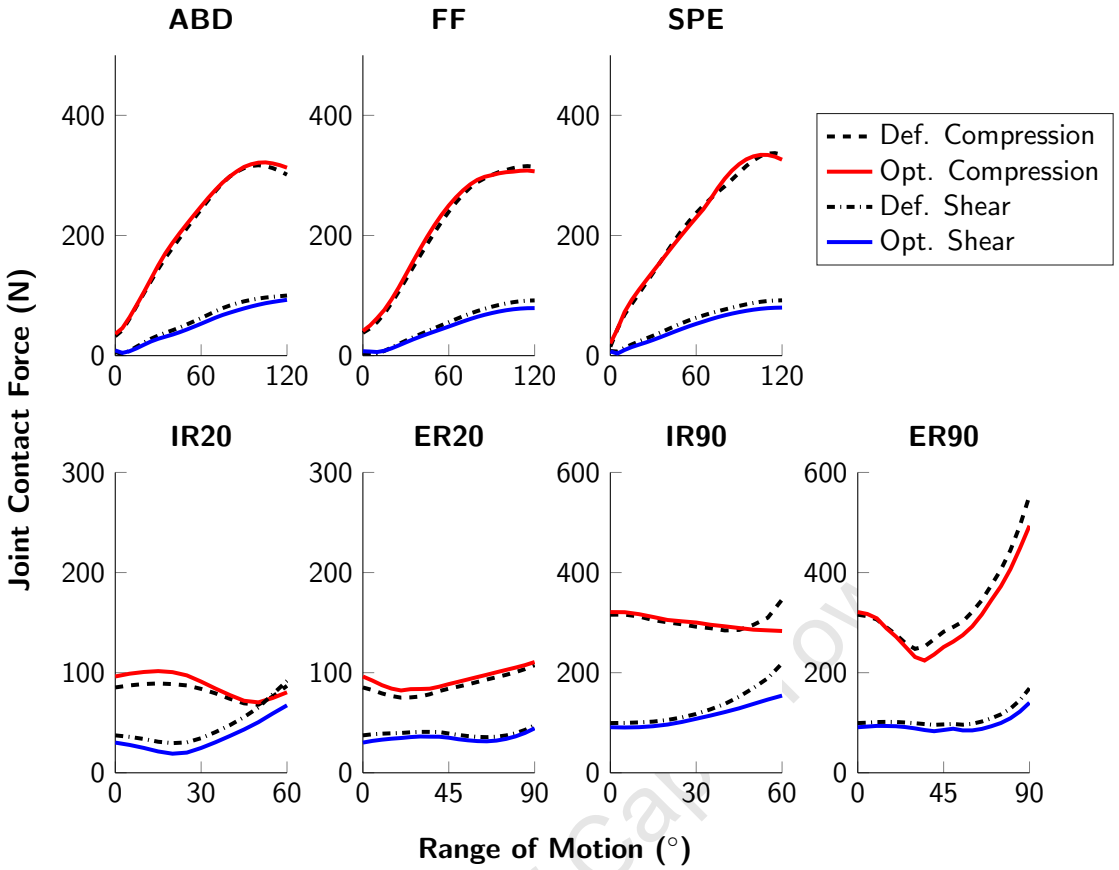

Figure 5.6 Compression and shear joint contact forces of the default and optimised configurations. The subject-averaged forces for the optimised configuration are represented by solid lines and by dashed lines for the default configuration

5.3.4.5 Impingement-free range of motion

The changes to IFROM are shown in Figure 5.7. The optimised configuration had a noticeable impact on IFROM during all the motions except IR90 and ER90. Excluding a single outlier, no impingement was detected for SPE and IR20 for the optimised configuration, and this was denoted by the lines at 120° and 60° for SPE and IR20, respectively. Mean IFROM increased by 47.87°, 32.80° and 56.10° during ABD, FF and ER20, respectively; whereas, mean IFROM only increased by 5.07° during IR90 and 0.27° during ER90.

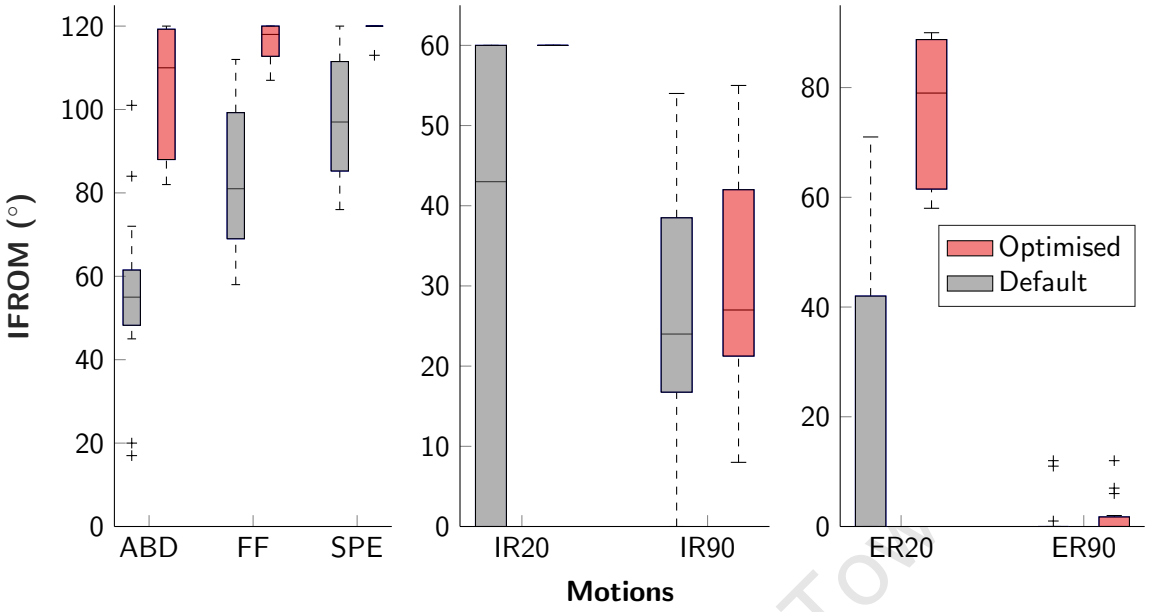

Figure 5.7 Box plots of IFROM for the default and optimised configurations

5.3.5 Factor analysis

Principal component analysis of all 47 modified configurations demonstrated that 88.16% of the variance of the data collected can be explained using five principal components (Table 5.8).

Table 5.8 Explained variance of the principal component analysis

Component	% of Variance	Cumulative %
1	26.64	26.64
2	21.52	48.16
3	17.40	65.56
4	12.07	77.63
5	10.54	88.16

The rotated component matrix of the reduced data-set is shown in Table 5.9. Here, the principal component (PC) that had the greatest loading (smallest absolute difference to 1) with each combination of outcome measure and motion was highlighted in grey.

Additionally, a scatter plot of the PC1 and PC2 loadings for each combination of outcome measure and motion is shown in Figure 5.8. A qualitative assessment of the loading matrix and scatter plot indicated that the first principal component (PC1) was loaded by the IFROM outcome measure for majority of the motions, whereas, PC2 was partially loaded by both DMA and SR and PC3 and PC4 were partially loaded by DMA and SR, respectively.

Table 5.9 Loading matrix of the rotated components

		Principal Component				
Outcome	**Motion**	**PC1**	**PC2**	**PC3**	**PC4**	**PC5**
DMA	ABD	-0.39	0.09	-0.87	0.02	0.15
	FF	-0.11	0.08	-0.90	0.02	-0.27
	SPE	-0.39	-0.05	-0.90	0.05	-0.11
	IR20	0.60	-0.06	0.73	0.06	-0.05
	ER20	0.08	0.58	0.42	0.02	0.55
	IR90	-0.15	-0.78	0.49	-0.09	0.17
	ER90	-0.09	0.89	0.17	-0.13	0.29
SR	ABD	0.11	0.26	0.13	0.90	0.08
	FF	0.15	-0.46	-0.14	0.73	-0.33
	SPE	-0.05	0.88	0.01	0.23	-0.08
	IR20	-0.08	0.88	-0.20	0.04	-0.14
	ER20	-0.02	0.20	-0.09	0.93	-0.05
	IR90	0.13	0.83	0.01	0.21	-0.37
	ER90	-0.06	0.33	0.01	0.42	-0.69
IFROM	ABD	0.91	-0.13	0.18	0.04	0.00
	FF	0.93	-0.13	0.17	0.05	-0.10
	SPE	0.81	0.03	0.21	0.07	0.36
	IR20	0.88	0.21	0.20	0.06	0.19
	ER20	0.97	-0.04	0.11	0.03	-0.01
	IR90	0.80	0.16	0.25	-0.01	0.38
	ER90	0.32	-0.14	0.08	0.05	0.78

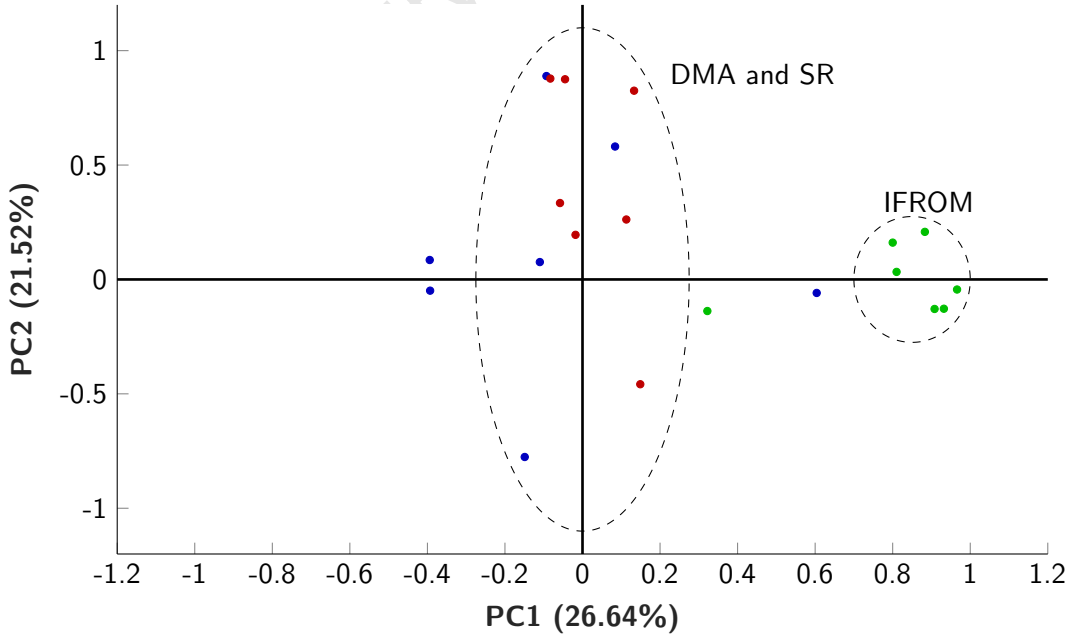

Figure 5.8 Scatter plot of the loadings of principal components 1 and 2. The dots are representative of each combination of outcome measure and motion; and DMA, SR, and IFROM are indicated by blue, red and green dots, respectively. Ellipses represent the identification of outcome measure clusters by visual inspection

5.4 Discussion

5.4.1 Optimisation process

The modified configurations evaluated during the optimisation process were systematically combined from four types of modifiable parameters, for a total of 48 configurations (1 default configuration and 47 modified configurations). This process was streamlined thanks to the findings of the previous chapter, which characterised the unique effect of each modified configuration on RTSA functional outcomes and determined those that had negligible, or detrimental overall effect. If the modifications were not characterised as such, the total number of configurations assessed in this chapter would have increased from 48 to 25245.

Once all 48 configurations were evaluated using the assessment framework, a thresholding process further decreased the number of usable configurations by determining which of those were susceptible to excessive peak elongation of the deltoid. This process identified 26 modified configurations that consistently elongated the deltoid by more than 20% compared to the normal shoulder and these configurations implemented multiple modifications, which predominately included lateralisation of the glenosphere (A2) and one of the eccentric glenosphere translations (B2, B3 or B4). In Chapter 4, 10 mm of eccentric glenosphere translation was found to over-stretch the deltoid and, therefore, it should not be unexpected that, when the 5 mm eccentric translations were used in conjunction with the other modification types, the resulting configuration would have caused excessive elongation. It should also be noted that the thresholding process eliminated the configuration with the highest overall score. The A2B3C3D2 (No. 41) configuration scored 10.25 out of 21 by implementing all four modification types to improve DMA by 0.75, SR by 5 and IFROM by 4.5. However, it accomplished these improvements at the expense of elongating the deltoid in 20% of the reverse shoulder models during FF and 26.67% of the models during ABD and SPE.

Relatively low scores were obtained by the 21 usable configurations, with a median overall score of 5 out of 21. As mentioned previously, this was due to three factors. Firstly, the deltoid elongation threshold; secondly, the biomechanical trade-off between the antagonistic outcome measures (Gutiérrez et al. 2008a; Kontaxis and Johnson 2009; Hoenecke et al. 2014; Hettrich et al. 2015; Liou et al. 2017); and, thirdly, the differing requirements for the motions that elevated the humerus compared to those that rotated the humerus. The second factor can be exemplified in the current study using the A1B1C3D2 configuration (No. 5). This configuration was found to have the highest SR score of the usable configurations. However, it did so without having any appreciable impact on DMA and IFROM. The third factor was identified in the Chapter 4 and was especially apparent for the deltoid moment arm, which essentially had the inverse response for the elevation and rotation motions. For example, the A2B1C1D1 (No. 24) configuration had a detrimental impact on the ABD, FF and SPE moment arms, and had a beneficial impact on the IR20, ER20 and ER90 moment arms. Consequently, this configuration had a negative DMA score of -1.75.

The optimised configuration (A1B3C3D1) was selected primarily based on this biomechanical trade-off factor. While it did not obtain the highest overall score for the usable configurations (which was accomplished by the A1B4C3D2 configuration), it managed to adequately balance the three primary outcome measures. As shown in Table 5.5, A1B3C3D1 had the second highest DMA score of the usable modified configurations (1.25 out of 7), had the same IFROM score as A1B4C3D2 (2.25 out of 7), and had a slightly decreased SR score (4 out of 7, compared to 5.5 out of 7). Additionally, when considering the practicalities of these two configurations, it can be assumed that the intra-operative implementation of A1B3C3D1 (which utilises two modification types) would be more straightforward than A1B4C3D2 (which utilises three modification types).

Figure 5.9 illustrates the changes to the placement of the prosthesis due to the optimised configuration. The current implementation of the optimised configuration does not take a potential lack of sufficient bone stock at the infraglenoid tubercle region for the fixation of the inferior screw into account as the virtual implantation of the glenosphere was simplified through the omission of the fixations screws (Section 3.2.2.5). To circumvent this issue, built-in eccentricity (Section 2.4.3.3) of the glenosphere could utilised if this optimised configuration were to be manufactured.

Finally, it should be acknowledged that the optimised configuration determined in the current study was a generalised solution for all the subjects in the reverse model-set. It is possible that a subject-specific implementation of the assessment framework may have determined different optimised configurations for each model in the set. However, as this was the first iteration of the assessment framework, a population-based was followed to characterise the generally prosthesis configurations that had a typically beneficial or detrimental impact on reverse shoulder function.

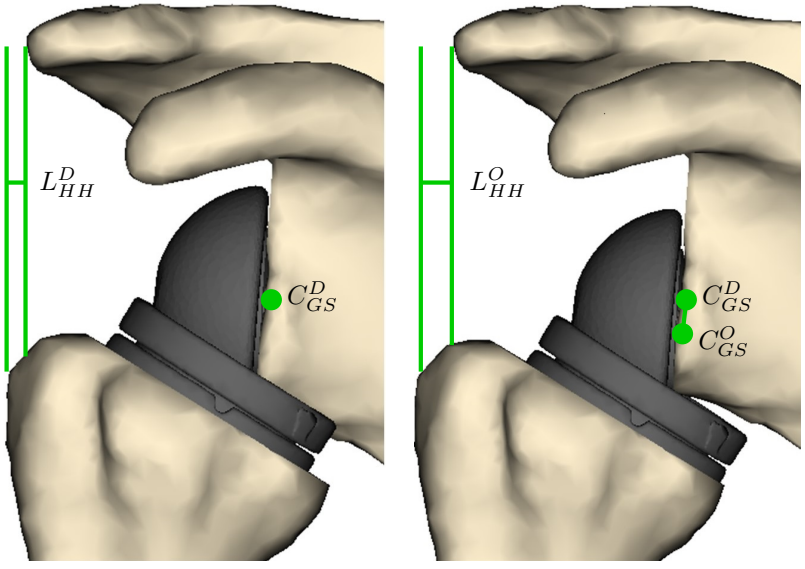

(a) Default configuration (b) Optimised configuration

Figure 5.9 Comparison between the default and optimised prosthesis configurations. Note that the optimised configuration inferiorly translated the glenosphere centre of rotation (C^{O}_{GS}) by 5 mm and lateralised the humeral head (L^{O}_{HH}) by 3.52 mm by medialising the humeral cup

5.4.2 Optimised configuration functional changes

The optimised configuration (A1B3C3D1) had a beneficial effect on 15 of the 21 outcome measures. For the six other outcome measures (IFROM at 90° of humeral elevation and DMA during IR20, ER20 and IR90), the configuration either had a negligible or detrimental impact. Due to a limitation of the binning process (discussed in Section 5.4.4), the change to IFROM during SPE due to the optimised configuration was considered negligible. However, detailed analysis of A1B3C3D1 revealed that no impingement was detected for this motion and, as such, the configuration did have a beneficial impact on this outcome measure.

The optimised configuration was constructed from two modifiable parameters. A comparison between the isolated and combined effect of these parameters demonstrated the ability of these parameters to work in unison to improve the functional outcomes of the reverse shoulder. The inferior translation of the glenosphere improved DMA (by increasing the deltoid offset distance) and IFROM (by shifting the humeral cup away from the glenoid), and had a nominal positive effect on SR. Whereas, the posteromedial translation of the humeral tray improved SR (by primarily reducing joint shear), nominally improved DMA, and had a negligible effect on IFROM. Consequently, the optimised configuration mutually benefited from both parameters and improved function to a greater extent than the isolated application of either. An example of this interaction is highlighted in Figure 5.10; here box plots of the three primary outcome measures during ABD are constructed for the default, GS_I, HTT_PM and optimised configurations.

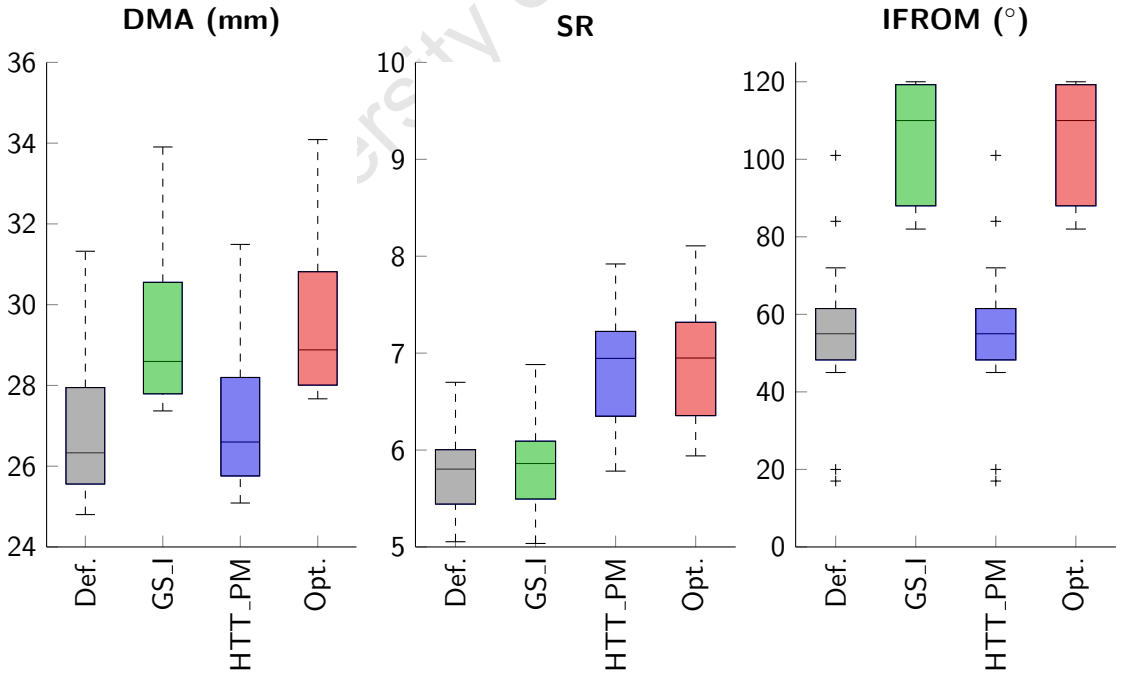

Figure 5.10 Comparison between the changes to the functional outcomes of the reverse shoulder due to the optimised configuration and its constitutive modifications during ABD. The box plots from left to right represent the default, GS_I, HTT_PM and optimised configurations

As it appears that there have been no studies documenting the effect of combining humeral tray translation with eccentric glenosphere translation, the findings of the current study cannot be directly compared to prior research. However, based on the comparisons performed in previous chapter, and the good agreement observed between the findings of the current study and the available literature, it can be presumed that the functional changes due to the optimised configuration are reasonable.

5.4.3 Factor analysis

Factor analysis of the 47 modified configurations found that IFROM was aligned with the first principal component and that DMA and SR were both partially aligned with the second principal component. From these findings it can be inferred that the effect of a configuration on DMA and SR was inter-dependent, and that its effect on IFROM was independent from these two outcome measures. This separation of outcome measures helps to demonstrate the antagonistic relationship between impingement and the kinematic and kinetic properties of the reverse shoulder from an alternate, data-driven perspective. It also suggests that IFROM (as it was clustered around the first principal component), had a deterministic outcome due to prosthesis configuration changes; whereas, changes to DMA and SR due to were more variable.

5.4.4 Limitations

The limitations of this chapter were derived from the data processing techniques. In addition, the limitations of the previous two chapters are applicable here due to the continued use of the same assessment framework.

The binning process was dependent on the number of input configurations. Therefore, the magnitudes of the median binned data of the outcome measures for certain configurations were not comparable between chapters, as the previous chapter assessed 36 modified configurations and 47 were assessed here. For example, the A2B1C1D1 configuration only implemented a 10 mm lateralisation of the glenosphere, thereby making it equivalent to the second offset level of the GS_L configuration in the previous chapter. Despite this equivalence, Table 5.10 illustrates the different scores that were obtained from the same modification.

Table 5.10 Median binned data comparison

Confg.	DMA	SR	IFROM	Overall
GS_L	-0.5	1	3.25	3.75
A2B1C1D1	-1.75	0.5	2	0.75

While the magnitudes differed, the effect (detrimental or beneficial) of a configuration was preserved between chapters. These magnitude differences are a drawback of the current formulation of the binning process as it prohibited direct comparison between the scores of both chapters and required that the comparisons take place during detailed analyses.

The binning process also used three motion groups: a group for the motions that elevated the humerus (ABD, FF and SPE), a group for the motions that internally rotated the humerus and a group for the motions that externally rotated the humerus. A limitation of these groupings was identified for IFROM as it was the only outcome measure that had an upper and lower bound. As can be seen in Figure 5.7, IFROM during SPE for the default configuration was 98.3° and the optimised configuration essentially removed the occurrence of impingement for this motion. Comparatively, IFROM during ABD for the default configuration was 55.3° and increased to 103.1° with the optimised configuration. This discrepancy resulted in the binning process undervaluing the changes to IFROM for SPE as they were limited by the available range of motion and were not as large as those for ABD.

A prerequisite for factor analysis is that the input data share a common scale and are typically inter-correlated (Abdi and Williams 2010). In order to perform the factor analysis the binned data were assumed to meet this criteria, as the outcome measures were classified according to relative effect sizes on a uniform scale of -1 to 1. This was a broad assumption to make. However, as only a qualitative assessment of the outputs from the factor analysis was performed it can be justified.

5.5 Conclusion

The systematic combination and assessment of multiple prosthesis parameters were performed in this chapter. 48 configurations of the prosthesis were derived from four parameter types: lateral glenosphere translation, eccentric glenosphere translation, humeral tray translation and greater tuberosity radius increase. These configurations were evaluated using the assessment framework that was established and utilised in Chapters 3 and expanded upon in 4.

The effect of the 47 modified configurations was assessed relative to the default configuration and characterised using data processing techniques. A thresholding process identified 21 configurations that did not excessively elongate the deltoid, and a data binning process identified an optimised configuration of the prosthesis within this subset. The optimised configuration implemented a 5 mm inferior translation of the glenosphere and a 5 mm posteromedial translation of the humeral tray. While this configuration did not obtain the highest overall score, it provided balanced, moderate improvements to most of the primary outcome measures. Based on findings of the data binning technique, this configuration improved DMA, SR, and IFROM by 17.9%, 57.1% and 32.1%, respectively compared to the default configuration. A detailed analysis of the functional changes to the reverse shoulder due this configuration help to contextualise the extent to which it changed the outcome measures. A factor analysis of the binned data demonstrated a separation between the effect of prosthesis configuration on IFROM compared to DMA and SR. This observation provides further backing to the biomechanical trade-offs that occur because of RTSA.

These biomechanical trade-offs and differing functional requirements of the motions (humeral elevations compared to humeral rotations) indicate that, as a long-term goal for this area of research,

RTSA prosthesis configuration should be optimised based on subject-specific criteria. Ideally, these criteria (such as the anatomical variability of the bone geometry, or rotator cuff status) should be pre-operatively established by the orthopaedic team and used to facilitate the optimisation process conducted using this assessment framework. For example, a configuration could be selected that provides balanced improvements to function (as performed here), or a configuration that either targets improvements to a particular motion or functional outcome.

In summary, out of 21 usable modified configurations, the simultaneous implementation of inferior glenosphere translation and posteromedial humeral tray translation provided an optimal improvement to RTSA functional outcomes. The net functional gain due to this configuration was greater than those obtained by the implementation of either modifiable parameter in isolation, thereby supporting the initially presented hypothesis. However, biomechanical trade-offs are still present with this configuration, as it was unable to have a beneficial effect on all the outcome measures.

Chapter 6

Effect of the optimised prosthesis configuration on muscle fatigue[1]

6.1 Introduction

As mentioned in Chapter 2, reverse shoulder arthroplasty suffers from several complications, these include impingement, dislocation, metaglene loosening, acromial stress fractures, and abnormal muscle function. These complications, except for abnormal muscle function, are commonly reported (Simovitch et al. 2007; Garberina and Williams 2008; Molé and Favard 2007; Levy et al. 2013). Abnormal function of the deltoid is often overlooked and, consequently, may be considered a secondary complication (Walker et al. 2014). However, as the deltoid becomes a crucial muscle in rotator cuff deficient reverse shoulders, the potential degradation of its function can have a detrimental effect on functional outcomes. It has the potential to be compromised either due to incorrect tensioning of the muscle during the surgery or due to an increased susceptibility to fatigue during prolonged periods of use.

A drawback of majority of the existing biomechanical models of the normal and reverse shoulder is their time independent nature (Liou et al. 2017). The models typically lack the ability to take into consideration the effect of extended periods of use on muscle and joint function. The aim of this chapter is to incorporate a means of assessing muscle fatigue into the Newcastle Shoulder Model (NSM). In doing so, the effect of fatigue during standardised shoulder functions is to be evaluated in order to establish a foundational baseline. Subsequently, the modified NSM is used to compare the response of the default and optimised prosthesis configurations to the onset of muscle fatigue during prolonged periods of use.

[1] An aspect of this chapter was evaluated in a study titled "Simulating the combined effect of muscle fatigue and muscle weakness in reverse shoulder arthroplasty: modifications to the Newcastle Shoulder Model". It was presented XXVI Congress of the International Society of Biomechanics.

6.2 Materials and methods

6.2.1 Fatigue model

The fatigue model used in this study was based on the work of Xia and Frey-Law (2008). It is a three-compartment model that assumes the fibres of a given muscle are in one of three states at any given time: resting (M_R), active (M_A) or fatigued (M_F). These states describe the differing manner in which the motor units in a muscle are recruited when it is activated (Liu et al. 2002).

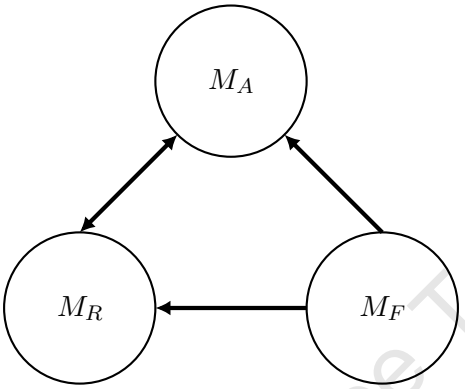

Figure 6.1 Schematic diagram of the interaction between the three muscle states (Xia and Frey-Law 2008). According to this model, a muscle is some combination of resting (M_R), active (M_A), and fatigued (M_F) at any given time

Equations 6.1 to 6.3 are used to quantify the fibres states in the model. A value for each state (ranging from 0 to 1, such that they sum to 1) is provided as an initial condition and the model iteratively calculates the evolution of these states as a function of time. As the experimental determination of the recovery and fatigue rates for the shoulder were outside the scope of the thesis, they were sourced from literature.

$$\frac{dM_R}{dt} = R \cdot M_F - C(t) \tag{6.1}$$

$$\frac{dM_A}{dt} = C(t) - F \cdot M_A \tag{6.2}$$

$$\frac{dM_F}{dt} = F \cdot M_A - R \cdot M_F \tag{6.3}$$

Where:

- R is a recovery rate, $R = 0.00168$ for the shoulder (Frey-Law et al. 2012)
- F is a fatigue rate, $F = 0.0182$ for the shoulder (Frey-Law et al. 2012)
- $C(t)$ is an activation-deactivation drive that is dependent on muscle excitation (E) and activation (A) levels, Where:

- If $E \geqslant A$ and $E - M_A \leqslant M_R$, then $C(t) = E - M_A$
- If $E \geqslant A$ and $E - M_A > M_R$, then $C(t) = M_R$
- If $E < A$, then $C(t) = E - M_A$

The model was incorporated into the Hill muscle model component of the NSM (Figure 6.2). During each step of a given motion (which had a 0.13 second time increment) a muscle fatigue factor, $f_{MF} = 1 - M_F$, was calculated and multiplied to the maximum force generating capabilities (F_{cap}) of the muscles that surround the glenohumeral joint.

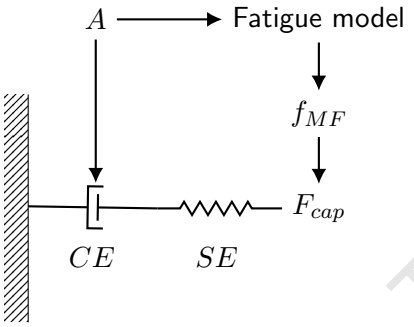

Figure 6.2 Modified Hill muscle model that includes the muscle fatigue model

The fatigable muscles of the reverse shoulder included the latissimus dorsi, pectoralis major, deltoid, teres minor, teres major, coracobrachialis, short head of the biceps and triceps brachii. Using these modified constraints, the load-sharing protocol calculated the force contributions of each muscle over time and, in doing so, could estimate the effect of fatigue.

The fatigue model was incorporated into the NSM in a manner that allowed for the assessment of non-fatigable or fatigable muscles. In the non-fatigable instance, the fatigue factor (f_{MF}) was set to a constant of 1.

6.2.2 Motions

Nine motions were simulated during the assessment of fatigue:

1. Held abduction (ABDh): humeral elevation in the frontal plane from 0° to 30°, 0° to 60° and 0° to 90°. Once these elevation angles were reached, the shoulder was held in place for a total of 180 seconds.
2. Held forward flexion (FFh): humeral elevation in the sagittal plane from 0° to 30°, 0° to 60° and 0° to 90°. Once these elevation angles were reached, the shoulder was held in place for a total of 180 seconds.
3. Held scapular plane elevation (SPEh): humeral elevation in the scapular plane from 0° to 30°, 0° to 60° and 0° to 90°. Once these elevation angles were reached, the shoulder was held in place for a total of 180 seconds.

These motions were simulated for non-fatigable muscles (NFM) and fatigable muscles (FM), using the default and optimised configurations of the prosthesis, for a total of 36 simulations per model in the reverse shoulder model-set. For the fatigable muscles, the motions were assumed to start from rest and the initial conditions of the muscle fibres were: $M_R = 1$ and $M_A = M_F = 0$.

6.2.3 Outcome measures

Four outcomes measures were evaluated during each simulation:

1. **Fibre state (FS)**. The distribution of the muscle fibre states was calculated as a function of time using the fatigue model.

2. **Muscle force (MF)**. The force generated by the muscles (in N) were calculated as functions of time using the NSM and the modified muscle force constraints. The anterior, middle and posterior deltoid muscle forces are shown in this chapter and additional muscle forces can be found in Appendix C.

3. **Joint contact force (JCF)**. Joint contact forces were calculated as functions of time using the NSM and the modified muscle force constraints for the reverse shoulder model-set. The GH joint contact force was projected into the glenosphere reference frame. The resultant of the force (in N) was calculated and it was decomposed into its constitutive components: compression, superoinferior (SI) and anteroposterior (AP) shear.

4. **Time to initiate fatigue (TIF)**. The time taken to initiate fatigue (in seconds, s) was derived from the JCF outcome measure. It represented the point where the load-sharing protocol calculated a new distribution of the resultant joint contact forces due to the onset of fatigue during the held motions.

6.2.4 Data processing

The fibre state, and the subject-averaged muscle and joint contact forces were plotted as functions of time for the default and optimised configurations during each motion. Descriptive statistics for the TIF outcome measure were calculated for the default and optimised configurations during each motion, and this data were represented using subject averages (with 95% confidence intervals) and box plots.

Preliminary Shapiro-Wilk tests on the TIF outcome measure using SPSS found that not all the data were normally distributed. Consequently, non-parametric Wilcoxon signed rank tests were performed to statistically analyse the differences between the TIF of the prosthesis configurations for each motion, and between the TIF of the three elevation angles (30° compared to 60°, 60° compared to 90° and 30° compared to 90°). Statistical significance was observed when $P < 0.05$.

6.3 Results

6.3.1 Fibre state

The distribution of the muscle fibre states is shown in Figure 6.3. These fibre states were consistent across all the fatigable muscles, motions and prosthesis configurations.

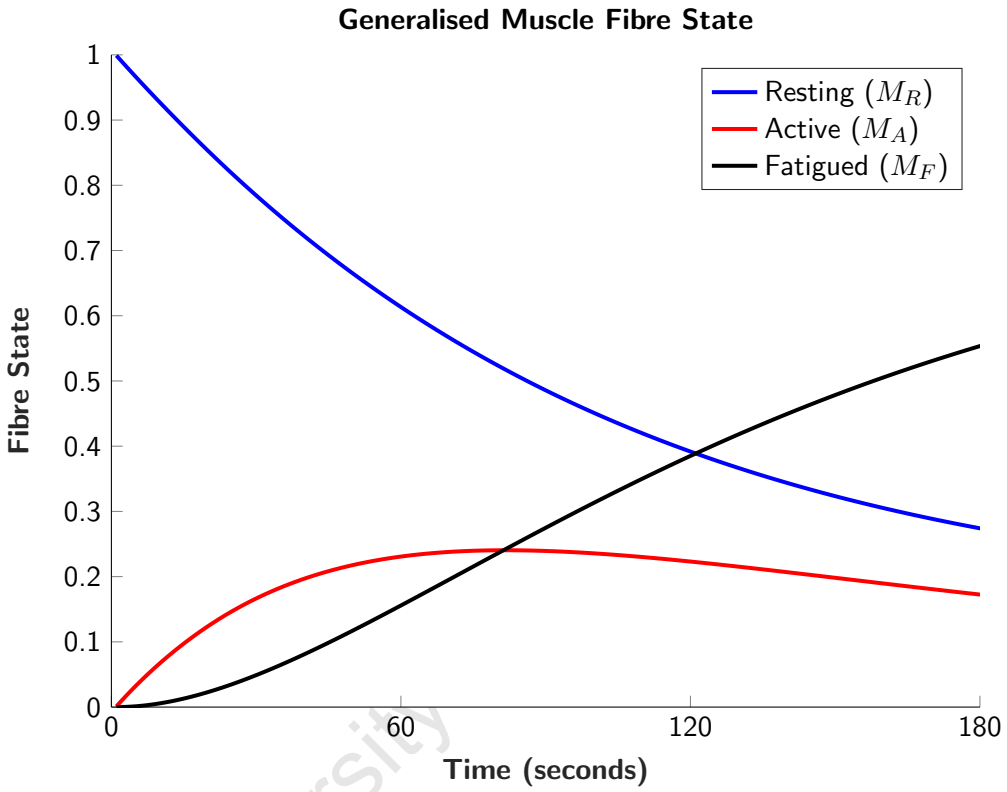

Figure 6.3 Distributions of the muscle fibre states over the duration of the held motions

The active fibre state increased from the start of the motion until it reached a maximum at approximately 80 seconds, after which it began to slowly decrease; whereas, the fatigued fibre state increased over the duration of the held motions. The resting fibre state, in response to these changes, progressively decreased during the motions. By the end of the 180 seconds, the fibre states in each muscle had evolved from the initial conditions to $M_R = 0.27$, $M_A = 0.17$ and $M_F = 0.56$.

6.3.2 Muscle forces

The subject-averaged forces generated by the deltoid of the default and optimised configurations, for the non-fatigable and fatigable muscles, during ABDh, FFh and SPEh are shown in Figures 6.4 to 6.6. For these figures, each row represents a humeral elevation angle (30°, 60° or 90°), the black lines indicate the default configuration, the red lines indicate the optimised configuration, solid lines indicate the fatigable muscles and dotted lines indicate the non-fatigable muscles.

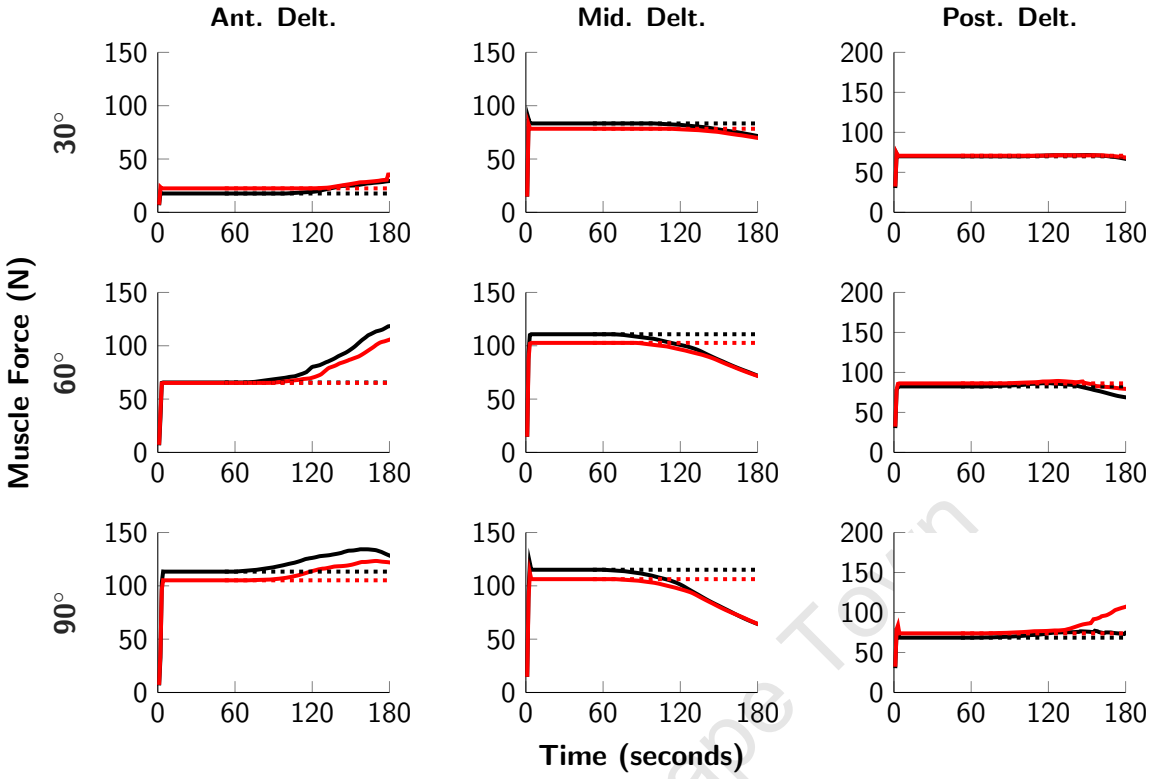

Figure 6.4 Subject-averaged muscle forces during ABDh

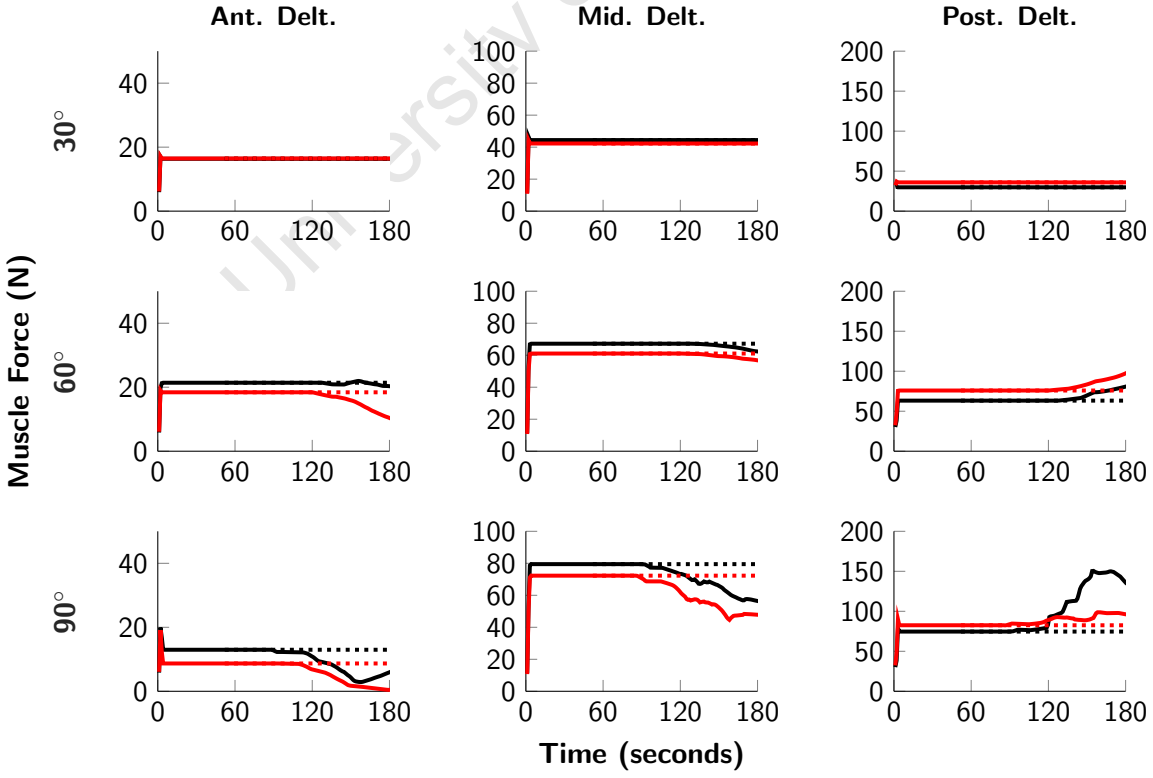

Figure 6.5 Subject-averaged muscle forces during FFh

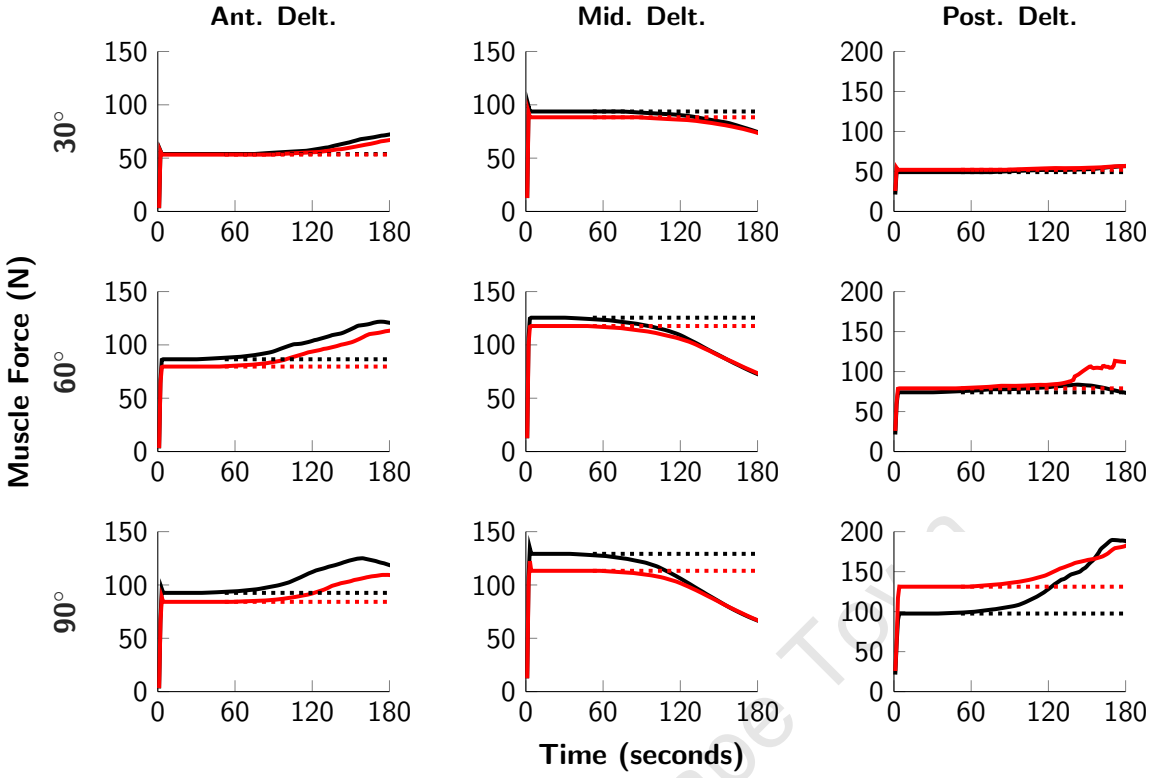

Figure 6.6 Subject-averaged muscle forces during SPEh

The deltoid forces during each held motion increased with increasing humeral elevation. Once the elevation angles were obtained for each motion, these forces remained constant until fatigue initiated. Fatigue primarily caused a progressive decrease in the middle deltoid force and the time of its initiation varied based on the motion, elevation angle and prosthesis configuration (see Section 6.3.4 for further details). FFh at 30° was the only simulation that was unaffected by fatigue for both prosthesis configurations as the muscle forces did not change over the course of the 180 seconds.

The initiation of fatigue also propagated motion-specific changes to the anterior and posterior deltoid, and some of the other muscles (Appendix C). For example, by the end of FFh at 90°, the anterior deltoid muscle force decreased, and the posterior deltoid muscle force increased. Conversely, both the anterior and posterior deltoid forces increased by the end of SPEh at 90°.

Table 6.1 summarises the subject-averaged force generated by middle deltoid muscle after completing each motion. The middle deltoid force for the non-fatigable muscles (which corresponds to the force required to initially elevate the humerus) was decreased for optimised configuration compared to the default. For the fatigable muscles, the difference in middle deltoid force due to prosthesis configuration at the end of each motion was comparatively reduced (except for FFh, which maintained equivalent differences).

Table 6.1 Subject-averaged middle deltoid force (in N) after 180 seconds. Note that confidence intervals have been omitted and the Diff columns represent the percentage difference between the default and optimised configurations for the non-fatigable and fatigable muscles

		NFM			FM		
Motion	**Angle (°)**	**Default**	**Optimised**	**Diff (%)**	**Default**	**Optimised**	**Diff (%)**
ABD	30	83.36	78.38	-6.0	71.32	69.57	-2.5
	60	110.80	102.69	-7.3	71.49	71.31	-0.3
	90	115.09	106.27	-7.7	63.78	63.90	0.2
FF	30	44.42	42.27	-4.8	44.42	42.27	-4.8
	60	67.20	61.05	-9.2	62.23	56.65	-9.0
	90	79.48	72.27	-9.1	56.26	47.78	-15.1
SPE	30	93.73	88.30	-5.8	74.09	73.31	-1.1
	60	125.50	117.69	-6.2	72.12	72.92	1.1
	90	129.18	113.27	-12.3	66.18	66.47	0.4

6.3.3 Joint contact force

The subject-averaged joint contact forces of the default and optimised configurations, for the non-fatigable and fatigable muscles, during ABDh, FFh and SPEh are shown in Figures 6.7 to 6.9. These figures follow the same style convention used for the muscle force plots.

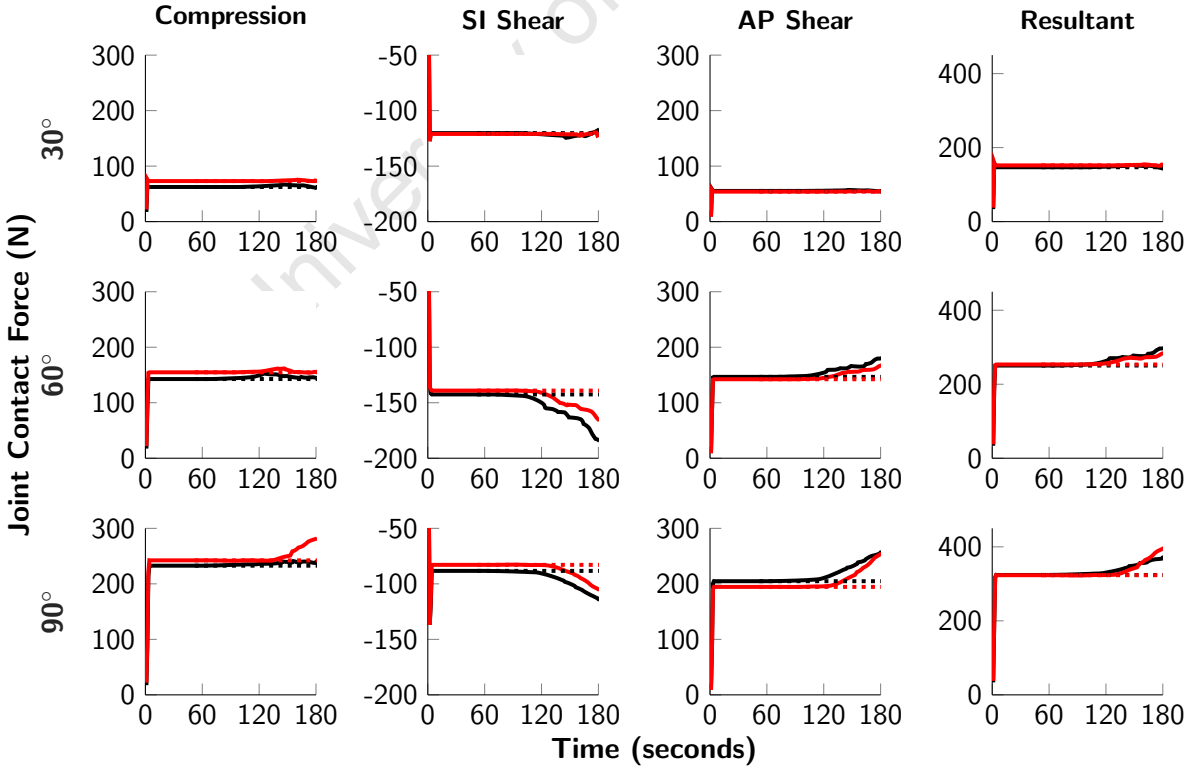

Figure 6.7 Subject-averaged joint contact forces during ABDh

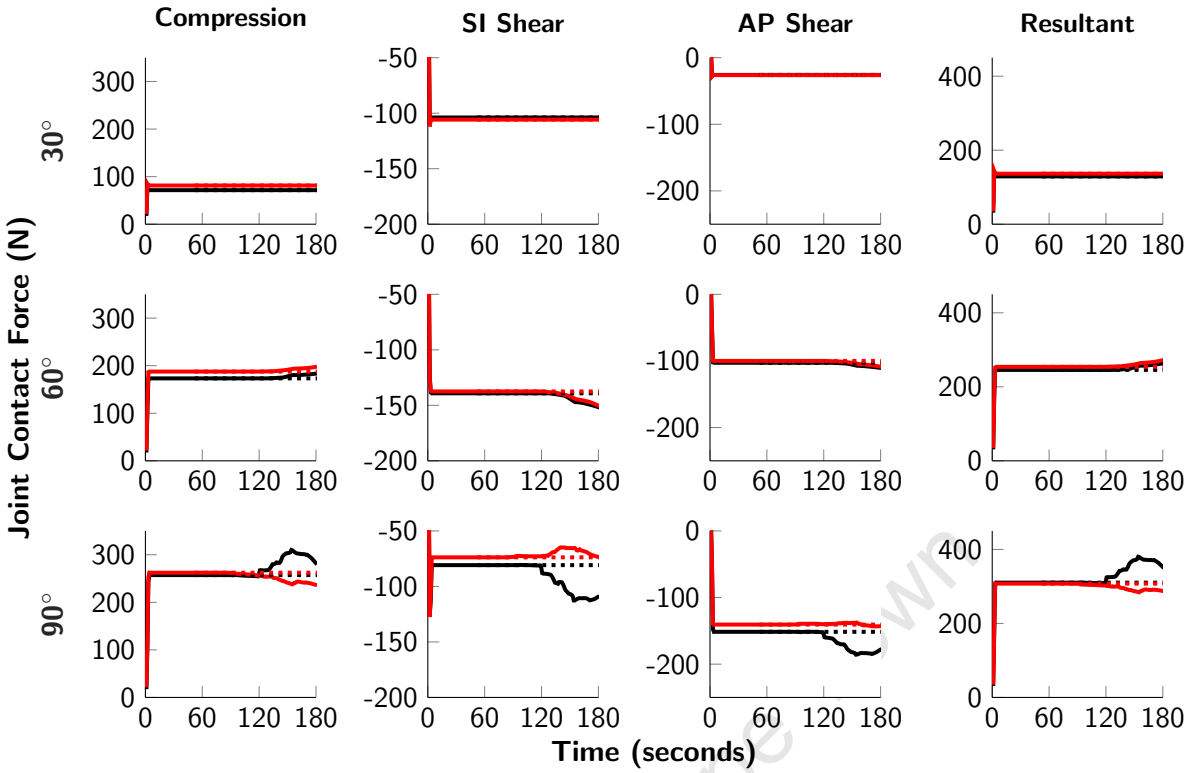

Figure 6.8 Subject-averaged joint contact forces during FFh

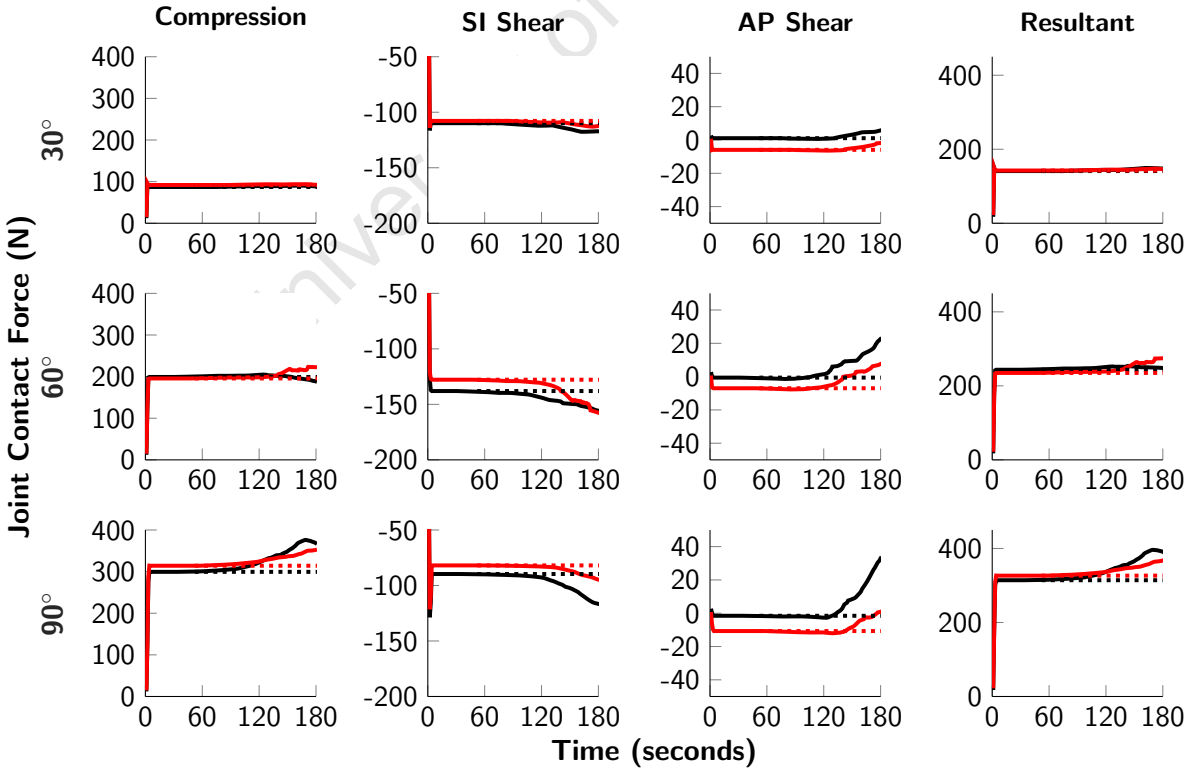

Figure 6.9 Subject-averaged joint contact forces during SPEh

As with the muscle forces, the resultant joint contact force increased with increasing humeral elevation and, once the elevation angles were obtained, these forces remained constant until fatigue initiated. Fatigue primarily resulted in an increase in the resultant joint contact force due to motion-specific changes in joint compression and shear, which became apparent with increased elevation. For ABDh and SPEh, fatigue generally increased compression, anterior shear and inferior shear. For FFh, fatigue increased compression, posterior shear and inferior shear (except for FFh at 90° using the optimised configuration, which had the opposite response).

Table 6.2 summarises the subject-averaged resultant joint contact force after completing each motion. The optimised configuration had a greater impact on joint contact forces for the fatigable muscles compared to the non-fatigable muscles at the end of ABDh, SPEh and FFh at 90°.

Table 6.2 Subject-averaged resultant joint contact force (in N) after 180 seconds. Note that confidence intervals have been omitted and the Diff columns represent the percentage difference between the default and optimised configuration for the non-fatigable and fatigable muscles

		NFM			FM		
Motion	**Angle (°)**	**Default**	**Optimised**	**Diff (%)**	**Default**	**Optimised**	**Diff (%)**
ABD	30	146.99	151.99	3.4	142.87	153.00	7.1
	60	250.54	253.36	1.1	297.64	284.58	-4.4
	90	324.03	323.33	-0.2	371.13	396.84	6.9
FF	30	129.24	136.49	5.6	129.24	136.49	5.6
	60	245.66	253.99	3.4	263.67	272.65	3.4
	90	310.25	307.60	-0.9	349.83	287.16	-17.9
SPE	30	141.05	142.51	1.0	147.88	146.09	-1.2
	60	243.53	234.96	-3.5	247.62	274.55	10.9
	90	314.21	326.57	3.9	389.84	368.36	-5.5

6.3.4 Time to initiate fatigue

Table 6.3 and Figure 6.10 show the subject-averaged time taken to initiate fatigue for the default and optimised configurations during each motion. For ABDh and SPEh, the optimised configuration extended the time taken to initiate fatigue. These extensions increased with increasing elevation; for example, the optimised configuration extended TIF for SPEh at 30° by 3.8% ($P = 0.005$) and at 90° by 16.1% ($P < 0.001$). Conversely, the optimised configuration reduced TIF for FFh; at 60° it was reduced by 0.8% ($P = 0.275$) and at 90° it was reduced by -2.6% ($P = 0.008$).

In addition, significant differences ($P < 0.001$) were observed for all the comparisons between the three elevation angles for each motion and both prosthesis configurations.

Table 6.3 Subject-averaged time taken to initiate fatigue (in s) for the default and optimised configurations. Note that confidence intervals have been omitted and the Diff column represents the percentage difference the configurations. * indicates statistical significance ($P < 0.05$)

		TIF (s)			
Motion	**Angle (°)**	**Default**	**Optimised**	**Diff (%)**	**P-value**
ABDh	30	164.59	167.99	2.1	0.027*
	60	131.50	141.13	7.3	< 0.001*
	90	116.45	127.30	9.3	< 0.001*
FFh	30	180.00	180.00	0.0	N/A
	60	165.75	164.35	-0.8	0.275
	90	130.91	127.50	-2.6	0.008*
SPEh	30	153.95	159.79	3.8	0.005*
	60	114.27	123.92	8.4	< 0.001*
	90	105.28	122.24	16.1	< 0.001*

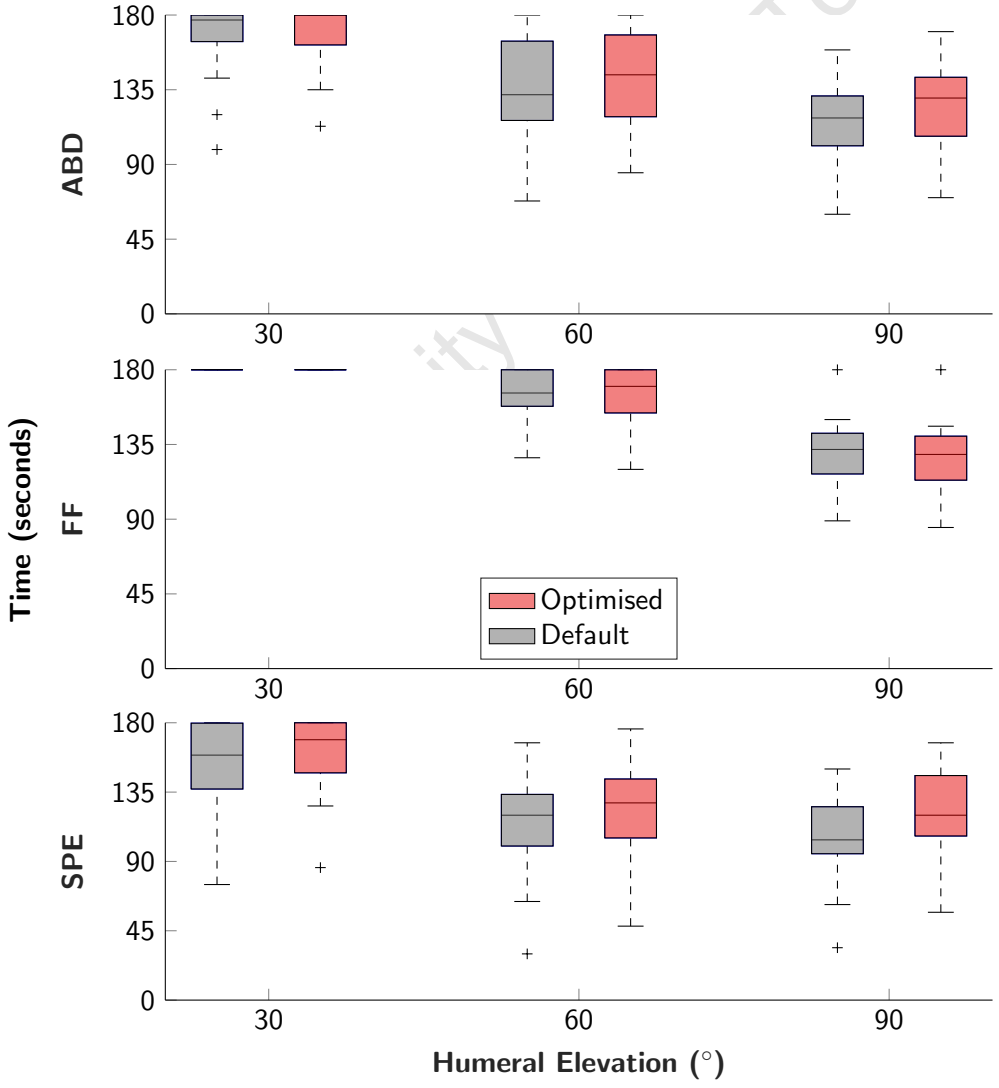

Figure 6.10 Subject-averaged time taken to initiate fatigue

6.4 Discussion

6.4.1 Characterising muscle fatigue in the reverse shoulder

The inclusion of the three-compartment fatigue model into the NSM propagated muscle fatigue during prolonged elevation of the arm. This was predominately characterised by a progressive decrease in the force generated by the middle deltoid after the initiation of fatigue. The time taken to initiate fatigue was motion-specific and dependent on the elevation angle, with fatigue occurring the fastest for SPEh at 90°, as it had the highest resultant joint contact force of all the motions evaluated.

As the deltoid is the primary abductor in a rotator cuff deficient reverse shoulder, fatigue-propagated decreases to the middle deltoid force were undesirable as it caused an increase in the forces generated by some of the surrounding muscles (beyond their non-fatigable levels) to maintain function. For example, after an average of 116.5 seconds of ABDh at 90°, the middle deltoid force in the default configuration began to decrease and, in response, the forces generated by the anterior deltoid, posterior deltoid, scapular trapezius, clavicular pectoralis major, coracobrachialis and short head of the biceps increased relative to their non-fatigable counterparts.

This compensatory mechanism of the surrounding muscles was identified in all the motions that experienced fatigue and was more apparent with increased elevation. However, the extent to which the muscles adapted to fatigue was motion-specific. This can be exemplified by the posterior deltoid in the default configuration. The posterior deltoid force exhibited a minimal response to fatigue during abduction held at 90°, conversely, during FFh and SPEh at the same elevation angle, the forces it generated were almost doubled by the end of both motions.

In an ideal scenario, this compensatory mechanism would ensure that the non-fatigable level of the joint contact forces was maintained after the initiation of fatigue. Evidently, this was not the case as the joint contact forces were altered over time, thereby indicating the unbalanced nature of the mechanism. For the default configuration, the resultant force increased by the end of the motions at 60° and 90° of elevation. This was caused by the net increase in muscle force due to the compensatory mechanism outweighing the net decrease in muscle force due to fatigue. Consequently, it can be envisaged that, if the arm was held for a longer period, muscle fatigue would eventually cause a severe imbalance in the muscle forces and adequate shoulder function would not be able to be maintained.

6.4.2 Effect of the optimised configuration on muscle fatigue

In general, the forces initially generated by the deltoid were decreased using the optimised prosthesis configuration; this was to be expected due to the deltoid moment arm increases illustrated in Figure 5.3. A decrease in deltoid muscle forces prior to the initiation of fatigue was desirable as it resulted in reduced effort required to enable shoulder function. Conversely, the progressive effects of muscle

fatigue on the middle deltoid were undesirable due to the force imbalance and the potential loss of function.

Due to the initial change in middle deltoid forces during ABDh and SPEh, the optimised configuration was able to extend the time to initiate fatigue by an average of 10.7 and 16.8 seconds, respectively at 90° of elevation. However, due to fatigue, the middle deltoid force in both prosthesis configurations converged by the end of these motions. Conversely, the forces generated by the compensatory muscles (with the exception of the posterior deltoid during ABDh) for the optimised configuration were reduced compared to those of the default configuration by the end of these motions. This suggests that the optimised configuration may be able to maintain shoulder function for a slightly longer period of continued use.

The time taken to initiate fatigue was reduced by an average of 3.5 seconds for FFh at 90° of elevation using the optimised configuration. This can be attributed to the optimised configuration having a smaller effect on the deltoid muscle forces during FFh compared to ABDh and SPEh, and the activation of the teres minor during forward flexion in the reverse shoulder (Appendix C, Figure C.6, Kontaxis (2009)). The teres minor force, like the middle deltoid force, was subject to progressive decreases due to onset of muscle fatigue. These factors, alongside smaller increases to the posterior deltoid force for the optimised configuration after the initiation of fatigue, resulted in a decreased resultant joint contact force by the end of FFh at 90° compared to its non-fatigable counterpart.

Taking into consideration the volume of activities performed daily (some of which may involve prolonged elevation of the shoulder), these changes in the time taken to initiate fatigue due to the optimised configuration have the potential to accumulate to have a beneficial effect on the long-term outcomes of the reverse shoulder that offset the need for revision surgery (such as a reduced likelihood of acromial stress fractures or metaglene loosening).

6.4.3 Limitations

The limitations of the NSM (Section 3.5.8.2) remain applicable and, as this was the first attempt at incorporating a fatigue model into the NSM, there were additional limitations that should be taken into consideration.

Muscle fatigue is a multi-dimensional phenomenon that is driven by neural and neuromuscular mechanisms (Enoka and Stuart 1992). As the three-compartment model is a numerical model, a number of these factors were not considered. The distribution of the fibre states was generic, and a uniform fatigue factor was applied to all the fatigable muscles; this is unlikely to represent a real-world scenario as each muscle would probably have a different response to fatigue. The fatigue model was also incorporated after the kinematic calculations of the NSM. Consequently, this was an open-loop implementation of the fatigue model and, therefore, it could not take into consideration the effect fatigue may have on joint kinematics.

As a time-dependent muscle fatigue model was incorporated into the NSM, the effect of fatigue during prolonged periods of use was assessed. Therefore, predefined humeral elevations (30°, 60°, and 90° of ABD, FF, and SPE) were simulated over 180 seconds. Consequently, there was a mismatch between these held motions and the motions used in the preceding chapters to determine the optimised configuration. This means the optimised configuration might not optimally counteract the effect of muscle fatigue and a different combination of prosthesis modifications may have a better performance in this context. However, as the optimised configuration was able to extend the time to initiate fatigue, the improvements offered by a different prosthesis configuration is likely to be small.

6.5 Conclusion

This chapter presents the first attempt at incorporating a muscle fatigue model into the NSM. The basis for the fatigue model was the three-compartment model that assumes that the fibres of a muscle are either resting, active or fatigued at any given time. The fatigue model was incorporated into the Hill muscle model component of the NSM and a fatigue factor was applied to the maximum force generating capabilities of the muscles surrounding the glenohumeral joint.

The effect of muscle fatigue was characterised during periods of prolonged use of the reverse shoulder at varying humeral elevations. These assessments identified a compensatory mechanism for the shoulder muscles in response to the initiation of fatigue. Fatigue propagated a progressive decrease in the force generated by the middle deltoid, and some of the surrounding muscles increased the forces they generated beyond their baseline levels. While this adaptation helped maintain shoulder function after the initiation of fatigue, the compensation between muscle force decreases and increases were unbalanced. This resulted in changes to the joint contact forces that may coincide with the eventual loss of shoulder function after further use.

Optimisation of the prosthesis configuration led to an advantageous reduction in middle deltoid forces prior to the onset of fatigue. Consequently, the time taken to initiate fatigue was extended for this configuration during held abduction and scapular plane elevation. In addition, the changes experienced by the compensatory muscles were typically smaller than those of the default configuration by the end of each motion. The cumulative effect of these changes may improve long-term reverse shoulder outcomes that offset the need for revision surgery.

In summary, the incorporation of time-dependent muscle fatigue into a musculoskeletal model has the potential to provide additional insights into the post-surgical behaviour of the reverse shoulder. For example, it could help to establish rehabilitation strategies that target the compensatory muscles and, as demonstrated here, can be used for the comparison between prosthesis configurations. However, additional assessments using other modalities (such as electromyographic analysis) should be performed to verify the results of this chapter and potentially establish muscle-specific fatigue factors.

Chapter 7

Effect of the optimised prosthesis configuration on implant micromotion

7.1 Introduction

Improper fixation of the implant components (metaglene and fixation screws) on the reamed glenoid surface can result in loosening of the implants (Molé and Favard 2007; Gerber et al. 2009). If micromotion at the bone-implant interface is in the range of 28 to 150 micrometres, it is suggested that satisfactory osseointegration of the implants cannot be achieved (Favre et al. 2011). This loosening can deteriorate the functional outcomes of the reverse shoulder and, in severe situations, requires a revision surgery that makes use of bone grafts to provide a sufficient surface area for stable fixation (Gerber et al. 2009). Previous biomechanical studies have used finite element (FE) analysis to quantify micromotion and assess the effect of prosthesis modifications on it (Virani et al. 2008; Favre et al. 2011; Chae et al. 2016; Elwell et al. 2017). However, these studies have assigned the scapula (or scapula substitute) with material properties for surrogate bone specimens (such as Sawbones) or apply bodyweight loads. As such, the studies may not adequately represent the physiological loading conditions that are typically experienced by the glenohumeral joint in the reverse shoulder during standardised motions (Terrier et al. 2008; Kontaxis and Johnson 2009; Ackland et al. 2011).

The aim of this chapter is to create a finite element model-set of the reverse shoulder to quantify the micromotion experienced at the bone-implant interface of the reverse shoulder using more representative parameters. The FE models were derived from the reverse shoulder models used in the previous chapters; the models utilised the sub-bodyweight glenohumeral joint contact forces calculated by the NSM simulations of the standardised motions and based the material properties of the scapula on the originating CT scan data. These FE simulations were conducted on the default and optimised RTSA configurations to further understand the effect of the optimised configuration.

7.2 Materials and Methods

7.2.1 Finite element model-set

The virtual surgeries performed in Section 3.2.2.5 acted as a baseline for the construction of the finite element (FE) models. As the NSM simulations did not take the metaglene screws into consideration, they were omitted during the development of the reverse shoulder model-set. Consequently, the virtual surgeries were adapted in Mimics to incorporate a superior and an inferior screw. As shown in Figure 7.1, the locking fixation screws were modelled as cylinders with a diameter of 4.5 mm (Chae et al. 2016; Elwell et al. 2017). This screw configuration has been found to achieve adequate fixation and obtained the best screw purchase inside the scapula (James et al. 2013).

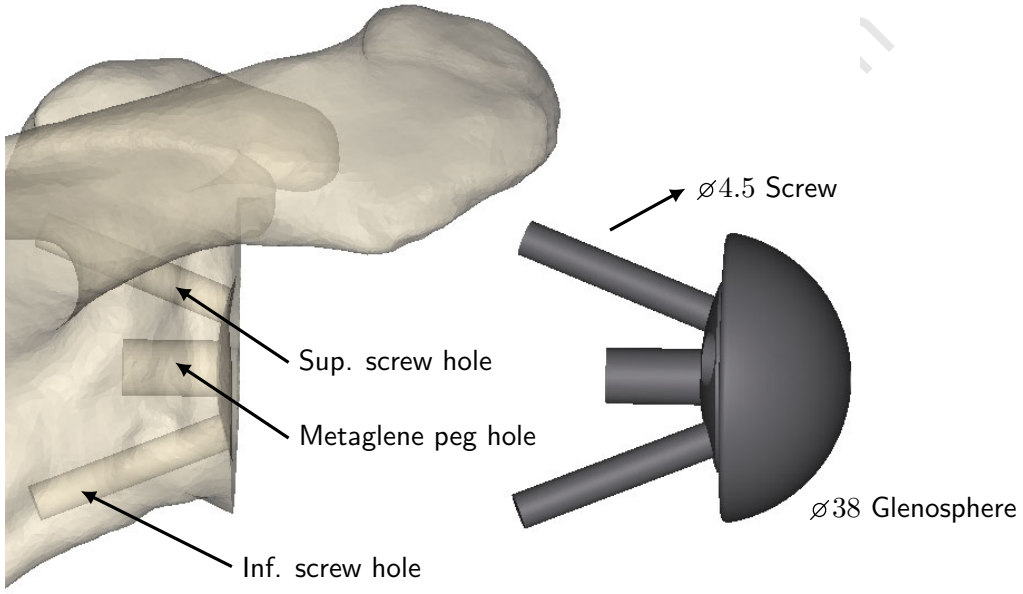

Figure 7.1 Adapted virtual surgery of the scapula to include the inferior and superior screws (visualised in Mimics)

Due to practical limitations regarding FE modelling, only 5 of the 15 models in the reverse shoulder model-set were used to create the FE model-set. These subjects (Table 7.1) were selected as they produced low, average, and high resultant joint contact forces relative to the overall cohort (see Appendix D for additional information).

Table 7.1 Anthropometric characteristics of the FE subjects

FE Subject	NSM Subject	Sex	Age (years)	Height (m)	Weight (kg)
1	1	M	69	1.69	59
2	3	M	56	1.85	85
3	4	F	45	1.65	54
4	5	F	57	1.66	45
5	12	F	60	1.54	45
	Mean ($\pm$ 1 SD):	2M/3F	57 $\pm$ 9	1.68 $\pm$ 0.11	57.60 $\pm$ 16.45

As micromotion at the bone-implant interface (the interface between the implant components and the scapula) was assessed, the FE model-set only included the scapula and scapular implant components (all of which were orientated in the scapular co-ordinate system). Each model in the set consisted of the default and optimised configurations. A concept design of the glenosphere used in the optimised configuration is shown in Figure 7.2. The glenosphere was modified to inferiorly translate the centre of rotation by 5 mm without changing the placement of the metaglene and the superior and inferior screws.

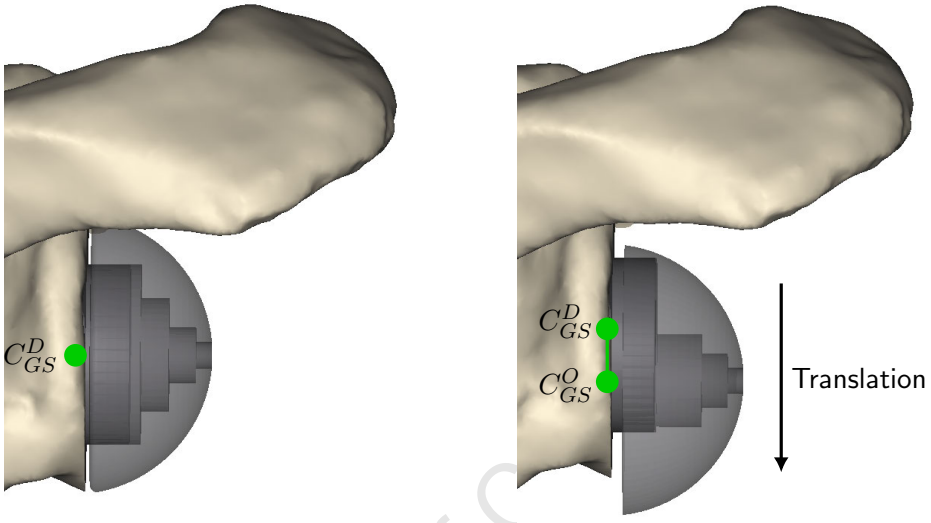

(a) Design of the glenosphere in the default configuration

(b) Concept design of the glenosphere in the optimised configuration

Figure 7.2 Comparison between the glenosphere used in the default and optimised configurations (visualised in Mimics). The design of the glenosphere in the optimised configuration inferiorly translates the centre of rotation (C^O_{GS}) without changing the placement of the metaglene and screws

During the development of the reverse shoulder model-set the scapula and humerus geometries of each subject were scaled to match the default geometries of the NSM. However, for the finite element model-set, the original scale of the scapula was required to assign it material properties (see the next section for further details). As such, the scapula and updated implant components were rescaled to the original subject scales using the inverse of Equation 3.4 after completing the adapted virtual surgeries.

7.2.2 Material properties

The metaglene and screws were assigned a Young's Modulus of 113.8 GPa and a Poisson's ratio of 0.3 to represent a linearly elastic and isotropic titanium alloy (Ti6Al4V). As the joint contact force was applied to the centre of rotation (rather than on the surface of the glenosphere as a distributed load, see Section 7.2.6), it was modelled as a rigid body in order to facilitate load transfer to the

metaglene and fixation screws (Ribeiro et al. 2011) and, as such, the glenosphere was not prescribed material properties.

The reamed scapula was modelled as linearly elastic, isotropic and non-homogeneous material. Each element of a given scapula was assigned a Poisson's ratio of 0.3 and a Young's Modulus that was based on the Hounsfield units of the bone in the originating CT scan (Zannoni et al. 1999). As the CT scans were not calibrated, a linear interpolation (Equation 7.1) was utilised to estimate the density of each element (Sharma and Robertson 2013).

$$\rho^{element} = \frac{0.8}{HU^{max}} \cdot HU^{element} + \rho^{water} \tag{7.1}$$

Where:

- $\rho^{element}$ is the density of each element in the scapula
- ρ^{water} is the density of water (1 g/cm^3)
- $HU^{element}$ is the Hounsfield unit of each element in the scapula
- HU^{max} is the maximum Hounsfield unit of the scapula

$\rho^{element}$ was then used to calculate the Young's Modulus of each element using the following equation:

$$E^{element} = E_0 \cdot \left(\frac{\rho^{element}}{\rho_0}\right)^2 \tag{7.2}$$

Where:

- $E^{element}$ is the Young's Modulus of each element in the scapula
- $E_0 = 15$ GPa (Büchler et al. 2002)
- $\rho_0 = 1.8$ g/cm^3

The scapula material assignment was performed using Bonemat (Taddei et al. 2007) by transforming the reamed scapula back into the native CT scan frame using the inverse of Equations 3.5. The material assignment did not differentiate between cortical and cancellous bone; an example of the output of this process is shown in Figure 7.3.

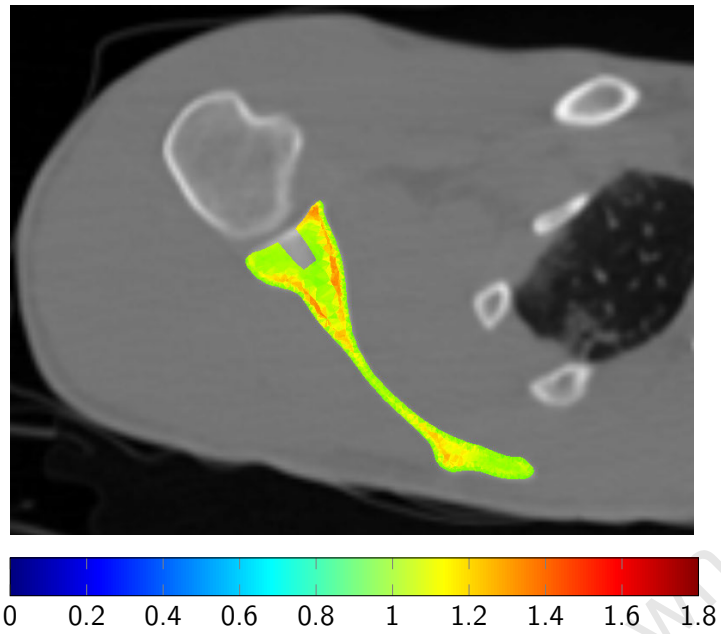

Figure 7.3 Transverse cross-section of the reamed scapula with the estimated elemental densities ($\rho^{element}$) represented by a heat map (visualised in Bonemat)

7.2.3 Meshing

The meshes of each component in the FE model were created in 3-matic (Materialise, Leuven, Belgium) using linear tetrahedral (C3D4) elements. A transitional mesh was implemented for the scapula; with a fine mesh near the bone-implant interface, and a coarse mesh elsewhere (Figure 7.4).

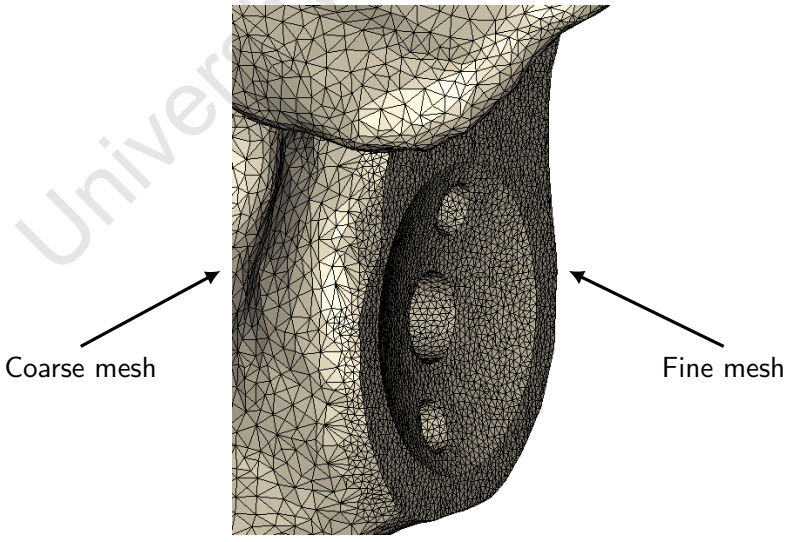

Figure 7.4 Comparison between the fine and coarse mesh edge lengths (visualised in 3-matic). A fine mesh was used near the bone-implant interface, and a coarse mesh was used elsewhere

A mesh convergence study was performed on one of the FE models to determine the optimal edge lengths for both the fine and coarse meshes. Using a fixed coarse mesh edge length of 2 mm, the fine mesh edge length was decreased from 1 mm to 0.75 and 0.5 mm. An evaluation

of the differences in the micromotion outcome measure for a standardised loading parameter was used to determine the optimal fine mesh edge length (see Section 7.2.6 and 7.2.8). Subsequently, the optimal coarse mesh edge length (4, 2 or 1 mm) was determined using a similar process whilst maintained the previously calculated fine mesh edge length. In addition, the edge length of the implant components matched the fine mesh edge length for each of the six mesh permutations simulated (3 fine mesh permutations $\times$ 3 coarse mesh permutations). The study found that the optimal edge lengths for the fine and coarse mesh were 0.75 and 2 mm, respectively (see Section 7.3.1.2 for additional information).

7.2.4 Contact

The contact between the implant components (the glenosphere, metaglene and fixation screws) was modelled using surface-to-surface tie constraints. The contact between the implant components (superior and inferior screws, central peg and back-face of metaglene) and the scapula was modelled as finite sliding, surface-to-surface interactions that had normal and tangential behaviours (Viceconti et al. 2000; Bernakiewicz and Viceconti 2002). The normal behaviour modelled "hard" contact between the components using an automatically calculated stiffness value. The tangential behaviour modelled friction between the components using an isotropic penalty method; a coefficient of friction (μ_S) of 1.7 between the screws and the scapula was used (Chae et al. 2016), and a coeffecient of friction (μ_M) of 0.743 between the metaglene and the scapula was used (Virani et al. 2008). A sensitivity analysis into the effect of different combinations of friction coefficients was performed using the FE model-set of the default configuration. The permutations used in the analysis were broadly derived from Elwell et al. (2017) and are shown in Table 7.2. A total of 20 simulations were performed (5 models $\times$ 4 friction permutations) using a standardised loading parameter and the aim of the analysis was to ensure that the FE model responded to the coefficients of friction in a logical manner that was consistent with Elwell et al. (2017).

Table 7.2 Permutations of friction coefficients evaluated in the friction sensitivity analysis

	Permutation			
Friction coefficient	**1**	**2**	**3**	**4**
μ_S	1.7	0.743	0.743	1.7
μ_M	0.743	0	0.743	1.7

7.2.5 Boundary conditions

As shown in Figure 7.5, a fixed boundary condition was placed along the medial border of each scapula to prevent translation and rotation.

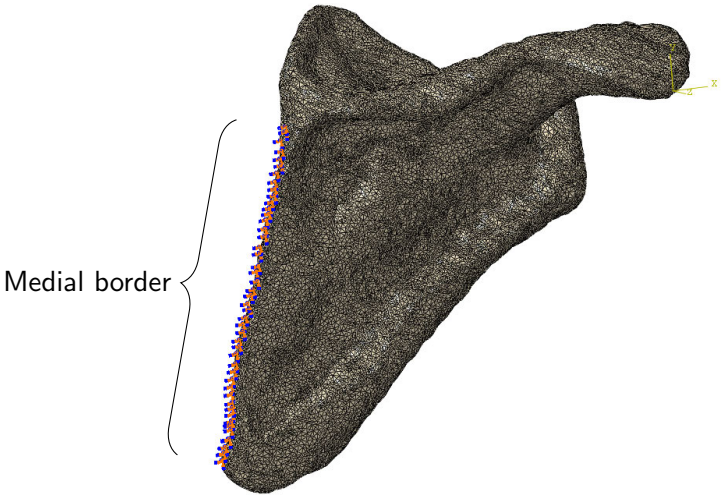

Figure 7.5 The locations of the fixed boundary conditions along the medial border of the scapula (visualised in Abaqus/CAE)

7.2.6 Loading parameters

The glenohumeral joint contact force (JCF) was applied as a concentrated force to the centre of rotation of the glenosphere (C^D_{GS} or C^O_{GS}, Figure 7.2). As mentioned in Section 7.2.2, the glenosphere was modelled as a rigid body in order to transfer the joint contact force from the glenosphere to the other components of the FE model. The constitutive components of the joint contact force (Figure 7.6) were joint compression (which was projected onto the X-axis of the concentrated force) and joint superoinferior and anteroposterior shear (which were projected onto the Y-axis and Z-axis of the concentrated force, respectively). As with the previous sign conventions, the compressive force and the superior and anterior shear forces had positive values and negative values corresponded to the opposite directions.

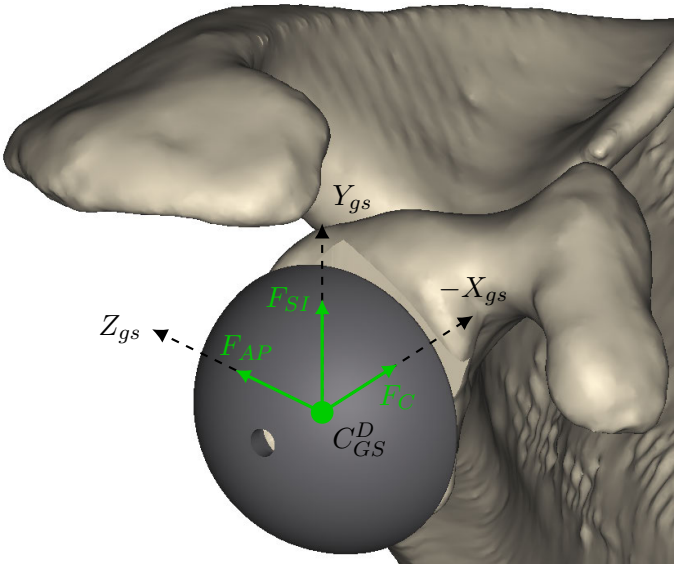

Figure 7.6 Decomposition of the GH joint contact force into its constitutive components (visualised in Mimics)

A sensitivity analysis into the effect of different loading parameters was performed using the FE model-set of the default configuration. As shown in Table 7.3, the permutations used in the analysis included subject-specific body weight (BW) forces that were applied predominately in the compressive and superior shear directions. Load application in this manner is prescribed by the ASTM standard and has been used in previous FE studies (Virani et al. 2008; Favre et al. 2011; Denard et al. 2017; Elwell et al. 2017). A total of 25 simulations were performed (5 models $\times$ 5 loading permutations) and the aim of the analysis was to ensure that the models responded in a logical manner prior to the application of the motion-specific joint contact forces. Note that the first permutation was used as the standardised loading parameter for the mesh convergence study and friction sensitivity analysis.

Table 7.3 Permutations of the loads (in BW) evaluated in the loading sensitivity analysis

	Permutation				
JCF Component	**1**	**2**	**3**	**4**	**5**
X: Compression	1	1	2	1	1
Y: SI Shear	0	1	2	-1	0.5
Z: AP Shear	0	0	0	0	-0.5

After the sensitivity analysis, motion- and subject-specific joint contact forces were simulated using the FE model-set of the default and optimised configurations. Table 7.4 demonstrates the typical loading parameters of the simulations using subject-averaged joint contact forces (refer to Appendix D for the subject-specific data). These were derived from the results of the NSM simulations and included the joint contact force at 30°, 60° and 90° of elevation during abduction (ABD), forward flexion (FF) and scapular plane elevation (SPE). A total of 90 simulations were performed (5 models $\times$ 2 prosthesis configurations $\times$ 9 loading permutations) in this instance.

7.2.7 FE analysis

The FE analysis was carried out using Abaqus Standard (version 6.14-1, Dassault Systèmes Simulia Corp., RI, USA) in its non-linear geometry mode. 51 simulations were performed during the preliminary mesh convergence study and sensitivity analyses, and 90 simulations were performed during the primary analysis. The runtime of each simulation during the primary analysis was 17.6 $\pm$ 9.2 minutes using a 64-bit Microsoft Windows 7-based desktop computer with an Intel Core i7 3.4GHz processor (operated in multi-processor parallelisation mode) and 16 GB of RAM.

7.2.8 Outcome measures

Two outcomes were measured during the assessment of the effect of prosthesis configuration on bone-implant micromotion: contact status and micromotion.

Table 7.4 Subject-averaged joint contact forces (in N) for the nine physiological loading conditions and two prosthesis configurations. Note that standard deviations have been omitted

Config.	Motion	Angle (°)	Compression	SI Shear	AP Shear	Resultant
Default	ABD	30	-36.06	123.22	46.38	136.51
		60	-83.00	160.61	141.36	229.49
		90	-151.24	124.19	217.18	292.34
	FF	30	-68.71	102.86	-22.07	125.66
		60	-180.21	135.54	-74.21	237.39
		90	-271.11	79.71	-89.01	296.28
	SPE	30	-73.05	108.71	6.44	131.13
		60	-169.56	141.10	24.92	221.99
		90	-269.63	107.71	52.42	295.04
Optimised	ABD	30	-43.95	121.75	46.20	137.43
		60	-94.32	156.96	138.88	229.82
		90	-163.30	120.09	211.91	293.25
	FF	30	-78.02	106.20	-20.02	133.29
		60	-193.77	136.15	-67.73	246.31
		90	-272.03	74.51	-76.18	292.16
	SPE	30	-77.98	106.49	1.90	132.00
		60	-167.58	130.51	20.28	213.37
		90	-282.56	100.66	49.27	303.97

1. **Contact status**. Contact status is a measure indicative of the contact occurring at the bone-implant interface. Contact status evolves from full contact at the beginning of each simulation, to partial contact by the end of each simulation. The manner in which partial contact occurs was interpreted as the qualitative effect of the load applied during the simulation.

2. **Micromotion (MM)**. Micromotion is a quantitative measure of the degree of separation (in μm) occurring in the normal and tangential directions at the bone-implant interface. In Abaqus, the COPEN parameter contains the separation of each node for the implant components in the normal direction and the CSLIP1 and CSLIP2 parameters contain the separation of each node for the implant components in the tangential directions. Custom-made Python (version 2.7, Python Software Foundation, DE, USA) and MATLAB scripts were used to extract this data from the Abaqus output files and calculate micromotion for each node on the metaglene and the superior and inferior screws using Equation 7.3.

$$MM_{node} = \sqrt{(COPEN_{node})^2 + (CSLIP1_{node})^2 + (CSLIP2_{node})^2} \tag{7.3}$$

From these nodal micromotions, the peak and mean micromotion of each implant was determined for each FE model. These were the primary measures for this outcome.

7.2.9 Data processing

Descriptive statistics of mean and peak micromotion were evaluated for each combination of physiological loading condition and implant component (metaglene and inferior and superior fixation screws) in both prosthesis configurations (for a total of 90 evaluations), and the data were represented using the subject average (with one standard deviation) and box plots. In addition, the subject-averaged percentage differences between the default and optimised prosthesis configurations for peak and mean micromotion of each loading permutation were calculated.

Preliminary Shapiro-Wilk tests using SPSS found that not all of the data were normally distributed. Consequently, non-parametric Wilcoxon rank-sum tests were performed to statistically analyse the differences between the micromotion results of the prosthesis configurations and between the micromotion results of the three elevation angles (30° compared to 60°, 60° compared to 90° and 30° compared to 90°). Statistical significance was observed when $P < 0.05$.

7.3 Results

7.3.1 Preliminary FE modelling

7.3.1.1 Material properties

Transverse sections of each reamed scapula with the estimated elemental densities are shown in Figure 7.7. The cross-sections were made at the midpoint of the metaglene central peg hole for each subject. Note that the shoulder of subject 4 was hunched whilst being scanned and, consequently, had a transverse section that was not consistent with the other subjects.

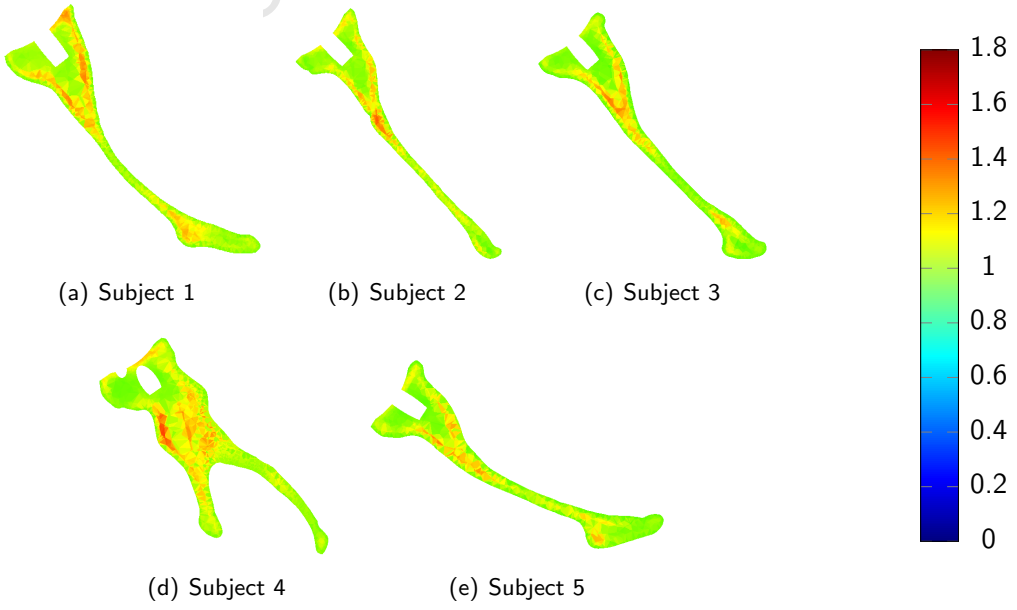

(a) Subject 1 (b) Subject 2 (c) Subject 3

(d) Subject 4 (e) Subject 5

Figure 7.7 Transverse section of each scapula, (elemental densities represented by heat maps)

A summary of the subject-specific material property assignments is shown in Table 7.5. The subject averaged Young's Modulus ranged from 4536.54 ± 263.45 MPa to 14164.20 ± 247.36 MPa.

Table 7.5 Subject-specific material properties

		Density (g/cm^3)		Young's Modulus (MPa)	
Subject	$\mathbf{HU^{max}}$	$\rho^{\mathbf{min}}$	$\rho^{\mathbf{max}}$	$\mathbf{E^{min}}$	$\mathbf{E^{max}}$
1	1475.00	1.02	1.75	4791.80	14215.35
2	1550.00	0.95	1.72	4226.60	13741.12
3	1634.00	0.96	1.75	4300.21	14235.18
4	1566.00	1.01	1.76	4777.48	14394.69
5	1510.00	0.99	1.75	4586.61	14234.68
Mean:	1547	0.99	1.75	4536.54	14164.2
Std:	± 60	± 0.029	± 0.015	± 263.45	± 247.36

7.3.1.2 Mesh convergence

Table 7.6 demonstrates the effect of changing the fine mesh edge length on mean and max micromotion. Using the 0.5 mm edge length as a baseline, a component-averaged difference of mean and max micromotion of 4.1% and 0.5% was calculated for the 0.75 mm configuration. In comparison, a 7.0% and 2.2% component-averaged difference was calculated for the 1 mm configuration. Given the acceptably small change to micromotion and a 32.0% decrease in the total number of elements (which increases computational efficiency), 0.75 mm was selected for the fine mesh edge length.

Table 7.6 Percentage micromotion relative to the 0.5 mm fine mesh edge length baseline. n_e indicates the total number of elements in each FE model

		Component micromotion (%)			
Edge Length (mm)	**Measure**	**Metaglene**	**Sup. Screw**	**Inf. Screw**	**Mean**
0.5	Mean	100	100	100	100
(n_e = 287397)	Peak	100	100	100	100
0.75	Mean	95.0	96.5	96.2	95.9
(n_e = 195502)	Peak	99.1	102.5	97.0	99.5
1	Mean	89.2	95.8	94.0	93.0
(n_e = 162402)	Peak	94.2	102.7	96.5	97.8

Similarly, Table 7.7 demonstrates the effect of changing the coarse mesh edge length on mean and max micromotion. Using the 1 mm edge length as a baseline, a component-averaged difference of mean and max micromotion of 2.7% and 0.5% was calculated for the 2 mm configuration. In comparison, a 3.5% and 2.9% component-averaged difference was calculated for the 4 mm configuration. The 2 mm coarse mesh edge length was selected as it had an acceptably small change to micromotion and decreased the number of scapula elements by 60.8%. Due to these selections, the average number of elements for the scapula and implant components were 229655 ± 71555 (61180 ± 18038 nodes) and 41520 ± 9266 (13559 ± 2976 nodes), respectively.

Table 7.7 Percentage micromotion relative to the 1 mm coarse mesh edge length baseline. n_s indicates the number of scapula elements

		Component micromotion (%)			
Edge Length (mm)	**Measure**	**Metaglene**	**Sup. Screw**	**Inf. Screw**	**Mean**
1	Mean	100	100	100	100
($n_s = 392577$)	Peak	100	100	100	100
2	Mean	99.2	94.3	98.6	97.3
($n_s = 153906$)	Peak	103.3	94.1	101.2	99.5
4	Mean	94.8	94.8	99.9	96.5
($n_s = 137130$)	Peak	102.5	86.3	102.6	97.1

7.3.1.3 Friction sensitivity analysis

The subject-averaged effect of varying the friction coefficients between the screws and the scapula (μ_s) and the metaglene and the scapula (μ_m) is shown in Table 7.8. The first permutation ($\mu_s = 1.7$ and $\mu_m = 0.743$) acted as the baseline and the results indicated that the micromotion was affected by changes to the friction coefficients. The second permutation had the smallest coefficients of friction ($\mu_s = 0.743$ and $\mu_m = 0$) and experienced the most micromotion (a 41.9% increase in component-averaged micromotion). Comparatively, the forth permutation had the largest coefficients of friction ($\mu_s = 1.7$ and $\mu_m = 1.7$) and experienced the least micromotion (a 16.5% decrease in component-averaged micromotion). The trend of these changes to micromotion due to alterations of the coefficient of friction were found to be consistent with those of Elwell et al. (2017).

Table 7.8 Subject-averaged percentage micromotion relative to the friction coefficient baseline (permutation 1). Note that standard deviations have been omitted for clarity

				Component micromotion (%)			
Friction coefficients			**Measure**	**Metaglene**	**Sup. Screw**	**Inf. Screw**	**Mean**
Permutation 1	μ_s = 1.7		Mean	100	100	100	100
	μ_m = 0.743		Peak	100	100	100	100
2	μ_s = 0.743		Mean	154.1	134.4	137.3	141.9
	μ_m = 0		Peak	169.7	162.0	125.7	152.5
3	μ_s = 0.743		Mean	102.1	106.9	118.1	109.0
	μ_m = 0.743		Peak	105.8	104.3	121.0	110.4
4	μ_s = 1.7		Mean	72.5	88.2	89.8	83.5
	μ_m = 1.7		Peak	68.9	78.2	98.7	81.9

7.3.1.4 Load sensitivity analysis

Figure 7.8 provides an example of the contact status at the beginning of each simulation. For each subject, full contact was made between the implant holes in the scapula and the implant components.

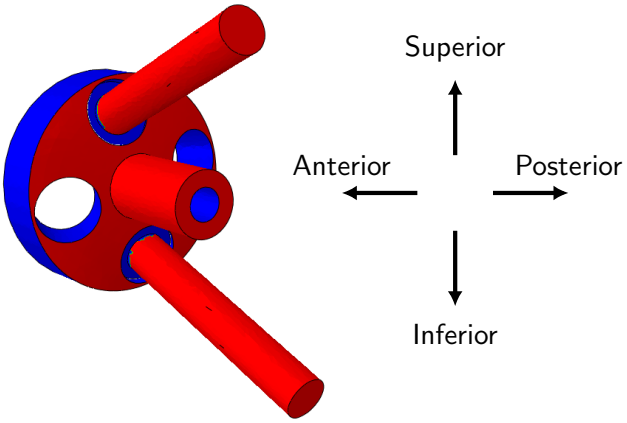

Figure 7.8 Tri-tone heat map of the contact status of the implant components at the beginning of each simulation. Blue indicates regions of no contact, red indicates regions of full (sticking) contact and green indicates regions of transitional (slipping contact)

Subsequently, Figure 7.9 demonstrates the contact status of the different loading permutations for a given subject at the end of each simulation.

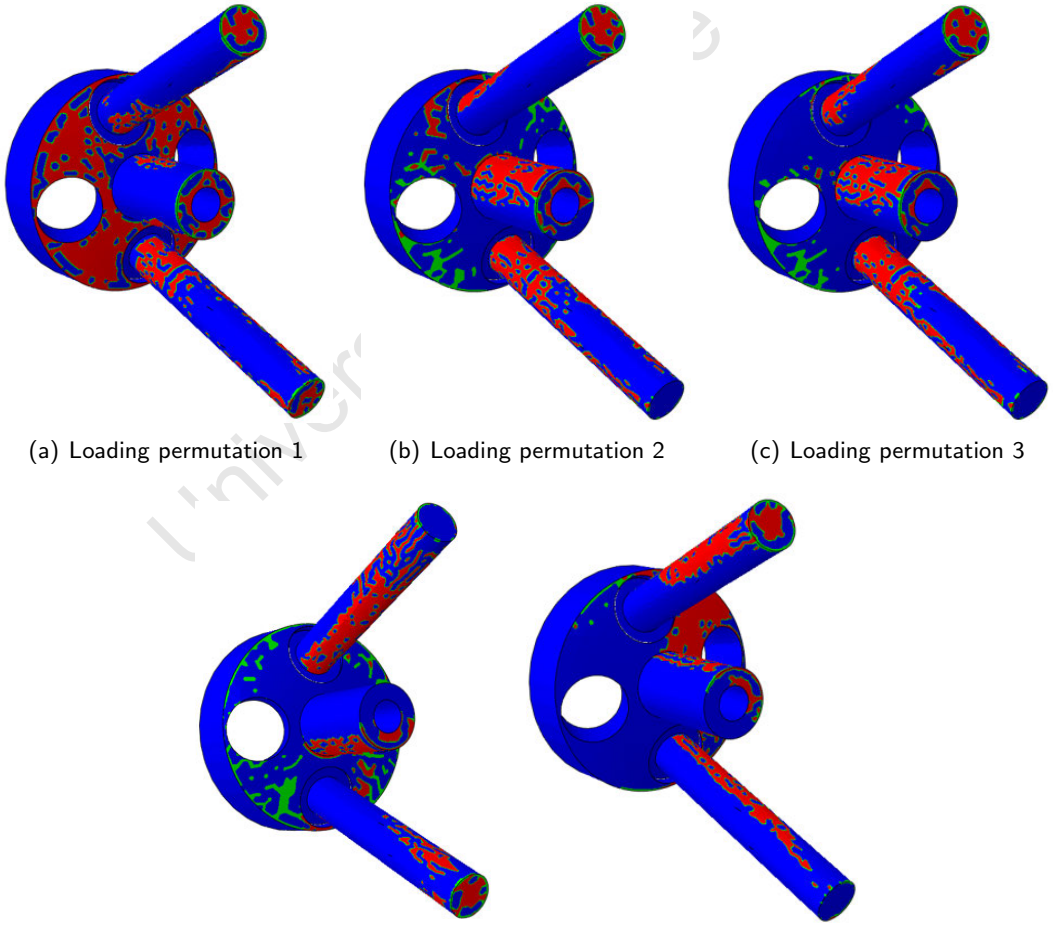

(a) Loading permutation 1 (b) Loading permutation 2 (c) Loading permutation 3

(d) Loading permutation 4 (e) Loading permutation 5

Figure 7.9 Tri-tone heat map of the contact status of the implant components for each loading permutation for a given subject

Similar contact patterns were observed across all subjects and demonstrated that micromotion was affected by the load application orientations. The first loading permutation applied a compressive force. As a result, contact was predominately maintained at back surface of the metaglene and along portions of the metaglene central peg and fixation screws. The second and third loading permutations applied compressive and superior shear forces. These caused a superior translation of the implant and resulted in the preservation of contact around the superior portions of the fixation screws and metaglene central peg. The forth loading permutation applied compressive and inferior shear forces. It had the opposite effect as loading permutations 3 and 4, as the implant was translated inferiorly, and contact was preserved around the inferior portions of the fixation screws and metaglene central peg. The fifth permutation applied a compressive force and shear forces in the superior and posterior directions. These combined loads simultaneously superiorly translated the implants and pushed the components into the posterosuperior portion of the interface between the metaglene and the reamed glenoid surface. This resulted in the preservation of contact at the posterosuperior portions of the metaglene back surface, metaglene central peg and fixation screws.

The results shown in Table 7.9 quantify the micromotion experienced due to the different loading permutations. The first loading permutation experienced the least micromotion. The second and third permutations demonstrated the sensitivity of the models to the magnitude of the applied load as micromotion increased with increased loading (component-averaged peak micromotion increased from 2.71 to 4.71 μm). In addition, there was an uneven distribution of micromotion at the fixation screws in both instances, with the inferior screw experiencing greater micromotion than the inferior screw (3.49 μm compared to 1.43 μm for the inferior and superior screws in permutation 2, respectively).

Table 7.9 Subject-averaged micromotion (in μm) for the loading permutations. Note that standard deviations have been

		Load (BW)				Component micromotion (in μm)			
		X	Y	Z	Measure	Metaglene	Sup. Screw	Inf. Screw	Mean
Permutation	1	1	0	0	Mean	0.21	0.11	0.13	0.15
					Peak	0.74	0.50	0.86	0.70
	2	1	1	0	Mean	0.73	0.29	0.40	0.47
					Peak	3.22	1.43	3.49	2.71
	3	1.5	1.5	0	Mean	1.17	0.51	0.59	0.75
					Peak	6.29	2.66	5.17	4.71
	4	1	-1	0	Mean	0.77	0.30	0.26	0.44
					Peak	3.92	1.64	2.04	2.53
	5	1	0.5	-0.5	Mean	0.73	0.34	0.41	0.49
					Peak	3.51	2.44	3.16	3.04

The fourth permutation demonstrated the sensitivity of the FE models to the direction of the applied load as micromotion of the inferior fixation screw was reduced in this permutation compared

to the second (2.04 μm compared to 3.49 μm). The fifth permutation, due to the combined loading applied, experienced a more even distribution of fixation screw micromotion (3.16 μm and 2.44 μm for the inferior and superior screws, respectively). Overall, it was also observed that metaglene micromotion was greater than fixation screw micromotion.

7.3.2 Contact status

The contact status of the implant components in the default and optimised configurations for the physiological loading conditions for a given subject is shown in Figure 7.10. As with the load sensitivity analysis, similar contact patterns were observed across all subjects. Contact status was observed to be dependent on both the motion and elevation angle for both prosthesis configurations.

The JCF during ABD was comprised of compression and superior and anterior shear. Contact was preserved along the superior portions of the fixation screws and the metaglene central peg. Contact increased with increasing elevation angle, with the most apparent increase occurred at the metaglene central peg. Contact at the back surface of the metaglene differed between prosthesis configurations. The default configuration maintained some contact around its anteroinferior portion and the optimised configuration maintained some contact around its anterosuperior portion.

The JCF during FF was comprised of compression and superior and posterior shear. Contact was preserved along the superoposterior portions of the fixation screws and the metaglene back surface and central peg. Contact increased with increasing elevation angle, with the most apparent increase occurred at the back surface of the metaglene. In addition, contact along the metaglene central peg changed from superoposterior to posterior with increased elevation angle. At 30° and 60° of elevation, increased contact was identified for the optimised configuration around the anteroinferior portion of the metaglene back surface compared to the default configuration.

The JCF during SPE was comprised of compression, superior shear and a small amount of anterior shear (compared to ABD). As such, contact was preserved along the superior portions of the fixation screws and the metaglene central peg and around the back surface of the metaglene. Contact increased with increasing elevation angle, with the most apparent increases occurring at the metaglene. At 30° of elevation the optimised configuration had increased contact around the anteroinferior portion of the metaglene back surface compared to the default configuration.

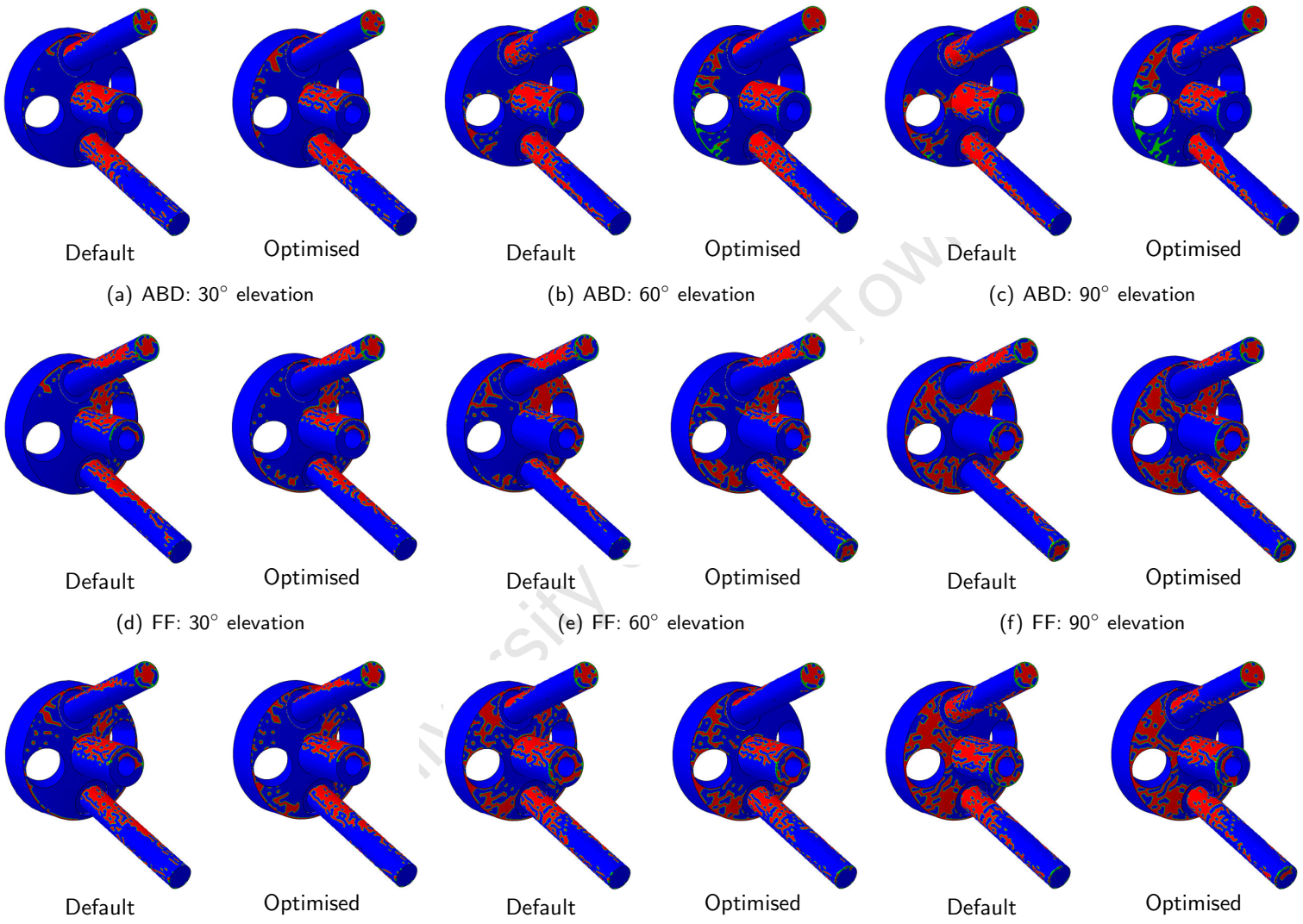

(a) ABD: 30° elevation (b) ABD: 60° elevation (c) ABD: 90° elevation

(d) FF: 30° elevation (e) FF: 60° elevation (f) FF: 90° elevation

(g) SPE: 30° elevation (h) SPE: 60° elevation (i) SPE: 90° elevation

Figure 7.10 Tri-tone heat map of the contact status of the implant components in the default (left) and optimised (right) configurations for the physiological loading conditions for a given subject

7.3.3 Micromotion

The mean and peak micromotion of the implant components of the default and optimised prosthesis configuration during each physiological loading condition are illustrated in Figures 7.11 and 7.12. As with contact status, it is evident from these box plots that micromotion was dependent on the motion and elevation angle for both prosthesis configurations.

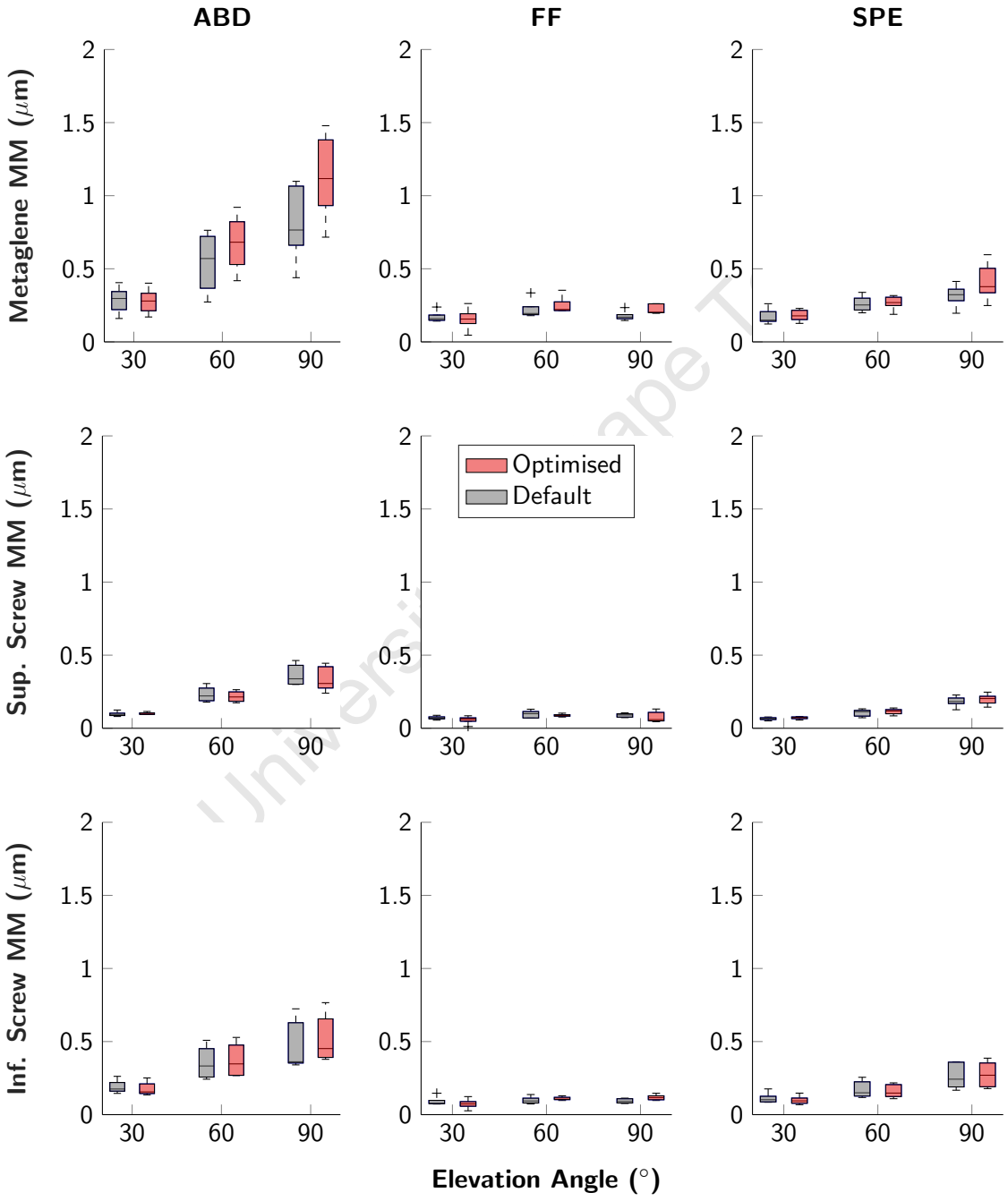

Figure 7.11 Box plots of mean micromotion (MM) of the implant components in the default and optimised configurations for the physiological loading conditions

ABD resulted in the greatest mean and peak micromotion, and the metaglene was subject to the most micromotion of the three implant components. Table 7.10 summarises the results of the comparisons between the default and optimised configuration. Motion and elevation angle specific percentage differences were identified in each comparison and a statistically significant difference was observed for the peak micromotion of the superior screw during 30° of SPE.

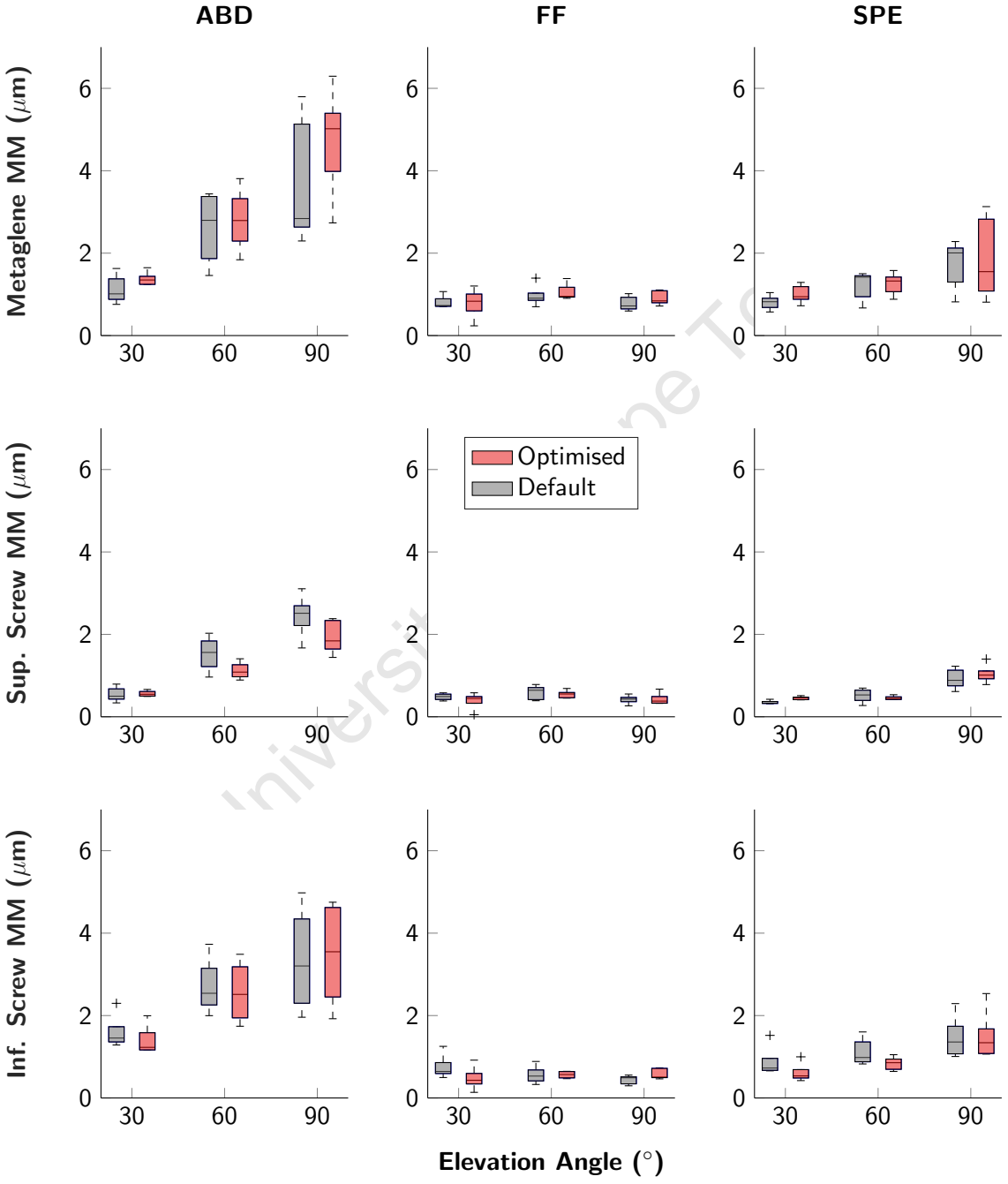

Figure 7.12 Box plots of peak micromotion (MM) of the implant components in the default and optimised configurations for the physiological loading conditions

Table 7.10 Comparisons of mean and peak micromotion of the implant components between the default and optimised configurations. * indicates statistical significance ($P < 0.05$)

			Mean		Peak	
	Motion	**Angle (°)**	**Diff (%)**	**P-value**	**Diff (%)**	**P-value**
Metaglene	ABD	30	-2.7	0.841	22.0	0.222
		60	24.2	0.686	7.1	0.886
		90	38.5	0.222	26.7	0.421
	FF	30	-8.0	1.000	-2.7	0.841
		60	13.0	0.095	9.7	0.421
		90	26.9	0.056	17.3	0.310
	SPE	30	4.4	0.690	25.6	0.151
		60	3.4	0.841	3.6	1.000
		90	30.0	0.222	8.7	1.000
Sup. Screw	ABD	30	4.1	0.310	2.8	0.690
		60	-6.5	0.686	-26.9	0.200
		90	-7.2	0.548	-20.8	0.095
	FF	30	-18.8	0.310	-19.4	0.690
		60	-7.9	0.841	-7.3	1.000
		90	-12.2	0.548	2.3	0.841
	SPE	30	8.9	0.421	29.5	0.032*
		60	8.6	0.690	-11.1	0.548
		90	7.2	0.690	12.1	0.690
Inf. Screw	ABD	30	-7.1	0.548	-12.1	0.222
		60	5.1	0.886	-5.1	0.886
		90	9.7	0.310	4.4	1.000
	FF	30	-18.8	0.421	-36.4	0.095
		60	12.4	0.222	0.6	0.690
		90	25.4	0.095	32.9	0.151
	SPE	30	-12.1	0.421	-30.0	0.095
		60	-7.3	0.690	-25.3	0.222
		90	3.4	1.000	1.5	1.000

The effect of elevation angle on mean and peak micromotion for the implant components in the default and optimised configuration is shown in Table 7.11. Both configurations were sensitive to changes in elevation angles for ABD and SPE, with statistical significances observed in majority of comparisons between 30° and 60°, and 30° and 90°. In contrast, fewer statistical significances were observed for FF (with no statistical significances observed for the metaglene in both configurations) and for the comparison between 60° and 90°. The optimised configuration was also more sensitive to differences between 30° and 60° of elevation compared to the default configuration.

Table 7.11 Statistical comparisons of mean and peak micromotion of the implant components at different elevation angles. * indicates statistical significance ($P < 0.05$)

Mean micromotion (P-value)

Component	Motion	Default			Optimised		
		30 vs 60	60 vs 90	30 vs 90	30 vs 60	60 vs 90	30 vs 90
Metaglene	ABD	0.111	0.190	0.008*	0.016*	0.063	0.008*
	FF	0.095	0.095	0.548	0.095	0.421	0.151
	SPE	0.056	0.310	0.016*	0.032*	0.095	0.008*
Sup. Screw	ABD	0.016*	0.063	0.008*	0.016*	0.032	0.008*
	FF	0.095	0.841	0.056	0.032	0.548	1.000
	SPE	0.016*	0.016*	0.008*	0.008*	0.008*	0.008*
Inf. Screw	ABD	0.032*	0.413	0.008*	0.016*	0.286	0.008*
	FF	0.421	1.000	0.421	0.095	0.690	0.095
	SPE	0.056	0.151	0.016*	0.032*	0.095	0.008*

Peak micromotion (P-value)

Component	Motion	Default			Optimised		
		30 vs 60	60 vs 90	30 vs 90	30 vs 60	60 vs 90	30 vs 90
Metaglene	ABD	0.032*	0.413	0.008*	0.016*	0.111	0.008*
	FF	0.310	0.222	0.690	0.151	0.310	0.841
	SPE	0.151	0.151	0.056	0.222	0.548	0.151
Sup. Screw	ABD	0.016*	0.032*	0.008*	0.016*	0.016*	0.008*
	FF	0.421	0.310	0.421	0.151	0.095	0.690
	SPE	0.151	0.032	0.008*	0.841	0.008*	0.008*
Inf. Screw	ABD	0.032*	0.730	0.016	0.032*	0.286	0.016*
	FF	0.222	0.421	0.032*	0.222	0.841	0.222
	SPE	0.095	0.222	0.056	0.095	0.008*	0.008

7.4 Discussion

7.4.1 Contact status

The assessment of contact status provided qualitative insight into the effect of the joint contact forces on micromotion at the bone-implant interface. It demonstrated that the location of contact was dependent on the magnitude and direction of the joint contact force. The load sensitivity analysis showed that increased forces decreased contact and that the shear components of the joint contact force had a greater influence on contact than compression. The latter observation is in line with the findings regarding stability ratio reported in the previous chapters.

The application of the physiological loading conditions showed that the orientation and elevation of the joint influenced contact. The greatest difference in joint contact forces between ABD, FF and SPE was AP shear. ABD had the largest AP shear and, as a result, it had the least contact at the three elevation angles. Conversely, the AP shear in FF and SPE was in the same order of magnitude

for each elevation angle. Therefore, similar amounts of contact were observed for both motions, although their locations slightly differed. From a qualitative perspective it appeared that the contact preserved in each motion increased with increased elevation angle; suggesting that micromotion at the bone-implant interface decreased at higher elevation angles. However, the micromotion results demonstrated that this was not the case and this is discussed further in the next section.

With regards to the prosthesis configurations, it appeared that the optimised configuration did not drastically change the amount of contact preserved. However, slight changes to location of the contact were identified for the metaglene. These differences were most likely due to the change in glenosphere centre of rotation and differences in joint contact force. For example, the optimised configuration increased compression and decreased posterior shear during 30° of FF and, consequently, some contact was preserved around the anteroinferior portion of the metaglene back surface.

7.4.2 Micromotion

Subject-averaged peak micromotion ranged from 0.35 $\pm$ 0.04 μm for the superior screw in the default configuration at 30° of SPE to 4.71 $\pm$ 1.30 μm for the metaglene in the optimised configuration at 90° of ABD. These values are not within the 28 to 150 μm range reported by Favre et al. (2011),who validated their FE results using the University of Zurich testing rig (Section 2.5.3.3) and high-resolution image analysis, and are smaller than those that have been previously reported. For a standard implantation of the prosthesis, Chae et al. (2016) reported peak micromotion of 16.2 μm, Elwell et al. (2017) reported mean micromotion of 55 μm, Virani et al. (2008) reported 57 μm of micromotion and Favre et al. (2011) reported 120 μm of micromotion. These highly variable findings can be attributed to a lack of consensus regarding study design. Table 7.12 highlights the differences between some of the parameters used in these previous studies and the current study.

Due to these differences the interpretation of absolute micromotion values calculated by FE simulations is challenging without experimental validation. To date, it appears that there have been no experimental studies that have been able to accurately recreate the *in-vivo* conditions of the reverse shoulder and measure micromotion at the bone-implant interface. However, the evaluation of relative differences in micromotion using FE modelling remains valid and insightful, as the only parameter to differ between simulations is the independent variable under investigation. For example, Elwell et al. (2017) evaluated the effect of glenosphere lateralisation on micromotion and, while the absolute micromotion calculated may differ from *in-vivo* micromotion as they did not perform experimental validation, the differences in micromotion values between prosthetic configurations is information that can help to drive future prosthetic developments.

Comparing the results of the current study, it was evident that ABD produced more micromotion than FF and SPE for all three implant components. This observation agreed with that of contact status and is likely caused by the relatively large AP shear force generated during this motion.

Table 7.12 Comparison of parameters used during FE modelling of RTSA

Study	Model type	Bone properties	Contact	Loading
Virani (2008)	ASTM[1]	Bone surrogate	Screw: tie constraint Meta.: $\mu_m = 0.743$	BW Comp. and BW Sup. Shear
Favre (2011)	ASTM	Bone surrogate	Screw: tie constraint Meta.: tie constraint	BW Comp. and BW Sup. Shear
Chae (2016)	Scapula[2]	Cortical and Cancellous layers	Screw: $\mu_s = 1.7$ Meta.: $\mu_m = 1.7$	BW Axial Load
Elwell (2017)	Scapula	CT scan	Screw: $\mu_s = 0.8$ Meta. $\mu_m = 0$	BW Comp. and BW Sup. Shear
Current study	Scapula	CT scan	Screw: $\mu_s = 1.7$ Meta. $\mu_m = 0.743$	Sub-BW JCF

[1] Refers to the modelling of the testing rig used by ASTM

[2] Refers to the modelling of the prosthesis virtually implanted in the scapula

In general, the micromotion of the metaglene was greater than that of the fixation screws. This was due to differences in friction coefficients and the surface area at the respective bone-implant interfaces. As a result of the superior shear applied in each loading condition, the inferior fixation screw experienced more micromotion than the superior screw. A similar finding was observed during the load sensitivity analysis, and this suggests that the modifications to the inferior screw (such as diameter or length changes) may help to mitigate micromotion.

The elevation angle comparisons also identified differences between 30° and 60° and 30° and 90°, but typically not between 60° and 90°. The compressive force relative to the shear forces increased with increased elevation, thereby stabilising the joint and mitigating some of the differences between micromotion at 60° and 90° of elevation. That being said, the greatest amount of micromotion was generally identified at 90° of elevation due to the shear forces peaking at this angle. This is contrasts with the findings of Chae et al. (2016), who observed higher micromotion at 30° of SPE compared to 60° and 90°. However, in their study they utilised 0.7 and 1 BW axial loads at each of these angles. Comparatively, an average of 0.23, 0.39 and 0.52 BW resultant joint contact forces were used in the current study at the same elevation angles to represent the more physiologically representative loading conditions of the reverse shoulder.

There were discrepancies between the interpretations of contact status and micromotion. The findings of the contact status (which is a qualitative metric) suggest that higher elevation angles are more stable, however, as demonstrated in this section, this is not the case. This is because the magnitude changes of the joint contact force as the humerus is elevated obfuscate the interpretation of contact status in isolation. Rather, contact status is only indicative of the directional effect of the joint contact force and must be used in conjunction with micromotion (which is a quantitative metric) during the analysis and interpretation of the FE simulations.

While there were differences in mean and peak micromotion between the prosthesis configurations, virtually none of them were statistically significant and the impact of the optimised configuration on micromotion was minimal. Consequently, the beneficial effect of the optimised configuration on impingement-free range of motion, deltoid moment arms and joint stability during ABD, FF and SPE could obtained without a detrimental impact on micromotion at the bone-implant interface.

7.4.3 Limitations

The limitations of the analysis conducted in this chapter stem from the CT scans used to create the scapula models and practicalities of FE modelling.

As discussed previously, the CT scans of healthy shoulders were the basis for both the reverse shoulder model-set (used by the NSM) and the FE model-set. This may have affected the virtual surgery and the placement of the implant components as additional reaming may be required to achieve neutral version of the reamed glenoid surface. Additionally, the densities assigned to the scapula may be over-estimated in comparison to those found in the recipients of RTSA. The recipients typically have osteoarthritis and are likely to have different bone densities. The CT scans were also not calibrated, and a linear interpolation was used to estimate the elemental bone density. Therefore, these factors can potentially exaggerate the strength of the scapula and the micromotion at the bone-implant interface may be under-estimated.

Compared to the reverse shoulder model-set (which had 15 models), only five models were created for the FE model-set. This reduced model-set size was due to time constraints and practicalities of the initial FE model development. A larger FE model-set has the potential to refine and strengthen the inferences made during the current study. FE modelling practicalities were also evident during the mesh convergence study. The mesh convergence study required the creation of meshes for each permutation of the scapula and implant components (for the fine mesh assessment). This meant that six FE models had to be created for each subject and, consequently, the study was limited to one subject.

In conjunction with the model-set limitations, the FE models included simplifications that have an effect on the outcomes of the simulations. Firstly, tie constraints were used for the contact between the glenosphere and metaglene, and the metaglene and fixation screws. This would have an effect on the propagation of the joint contact force. Secondly, the fixation screws were modelled as cylinders and, as a result, the contact surface area at the bone-screw interface was reduced and this would have an impact on micromotion. Thirdly, the soft tissue encapsulating the scapula and glenohumeral joint was neglected. These can stabilise the glenohumeral joint and would necessitate more representative boundary conditions. While these simplifications mean that the FE models do not accurately represent the *in-vivo* conditions of the prosthesis, they are in line with those implemented in previous FE studies into reverse shoulder arthroplasty (Virani et al. 2008; Chae et al. 2016; Elwell et al. 2017).

7.5 Conclusion

A finite element model-set of the reverse shoulder has been developed in this chapter to evaluate micromotion at the bone-implant interface for the default and optimised configuration of the prosthesis. It was based on the reverse shoulder model-set constructed in Chapter 3 and included the reamed scapula, two fixation screws (inferior and superior), metaglene and glenosphere. The modelling parameters (such as material properties, contact between components and boundary conditions) were obtained from previous studies of a similar nature, and physiological loads (derived from the findings of the Chapters 3 and 5) were applied to the centre of rotation of the glenosphere.

After preliminary mesh convergence and sensitivity analyses, nine loading conditions (three motions at three elevation angles) were simulated using the FE model-set, for a total of 90 simulations. Contact and micromotion at the bone-implant interface were evaluated after each of these simulations. The micromotion values reported in the current study were smaller than those reported in literature. However, this was likely due to highly variable study designs, and an argument can be made that the evaluation of the relative differences between the simulations remains valid.

These evaluations demonstrated that micromotion was dependent on the motion and elevation angle for both prosthesis configurations, with 90° of ABD producing the overall largest amount of micromotion for the implant components. In addition, an uneven distribution of micromotion was identified between the fixation screws, as the inferior screw was subject to more micromotion than the superior screw. This observation indicates that design modifications to the inferior screw may help to mitigate micromotion.

Minimal differences between the effect of the default and optimised configuration on micromotion were observed when comparing the results. This is beneficial and suggests that the benefits to impingement-free range of motion, deltoid moment arms and joint stability were obtained without detrimentally affecting micromotion at the bone-implant interface. However, validation of these findings using equivalent experimental techniques would be required going forward.

Chapter 8

Conclusions and recommendations

8.1 Conclusions

The aim of this thesis was to identify an optimised reverse total shoulder arthroplasty (RTSA) configuration. This was accomplished by investigating a variety of modified prosthesis configurations and identifying the subset of configurations that had a beneficial impact on functional outcomes of the reverse shoulder. These were then systematically combined to determine a configuration that optimised functional outcomes. Subsequently, the overall performance of this optimised configuration was evaluated by assessing supplementary outcomes of the prosthesis. The sections that follow provide a summary of the main conclusions drawn throughout these processes.

8.1.1 Assessing the effect of modifying prosthesis configuration

A biomechanical assessment framework was established in Chapter 3 to evaluate the functional outcomes of a default configuration of the reverse shoulder. The framework utilised the Newcastle Shoulder Model (NSM), a custom-made impingement detection algorithm (IDA), and model-sets for the normal and reverse shoulder. The framework evaluated glenohumeral joint positional changes, deltoid elongation, deltoid moment arm (DMA), joint contact force, stability ratio (SR, which was derived from the joint contact force), and impingement-free range of motion (IFROM). Apart from the positional changes to the glenohumeral joint, these outcome measures were evaluated during seven motions that simulated different types of humeral elevation and rotation. These evaluations were performed on each subject in the model-set to take anatomical variability into consideration.

The results of these evaluations were aligned with the observations of previous literature regarding the prosthesis. RTSA medialised the glenohumeral joint centre of rotation and lowered the position of the humerus. In doing so, the deltoid was elongated and the moment arm of the deltoid was increased during humeral elevations. Joint contact force was reduced in the reverse shoulder as the compressive forces provided by the rotator cuff in the normal shoulder were diminished. Stability of the semi-constrained prosthesis was dependent on the ratio between the compressive and shear components of joint contact force in the humeral cup. This ratio was greater than one for all the assessed motions, indicating that the joint was stable, as joint compression was greater than joint

shear. Due to the non-anatomic nature of the prosthesis, impingement occurred between the scapula and humeral cup, and the scapula and humerus. The extent to which impingement occurred was dependent on the anatomy of each subject and this caused large variations in the results of this outcome measure.

Once the baseline of reverse shoulder functional outcome was established in Chapter 3, the effect of modifying prosthesis configuration was evaluated in Chapter 4 using an expanded assessment framework. 36 modified configurations, derived from 18 modifiable parameters and two offset levels, were assessed using the framework. These modifications included changes to the intra-operative placement of the glenosphere and humeral tray, and an augmentation to the radius of the greater tuberosity. A thresholding process determined the configurations that induced excessive deltoid elongation, thereby eliminating them from further consideration. A binning process characterised the effect of each modified configuration on the primary outcome measures (DMA, SR, and IFROM) as beneficial, detrimental, or negligible, relative to the default configuration. 19 of the 36 modified configurations had a net beneficial effect on the functional outcomes without excessively elongating the deltoid. From these 19 configurations, a subset of 7 modifiable parameters was selected for use during the optimisation process.

The results of Chapter 4 also demonstrated the biomechanical trade-off that occurs in the reverse shoulder, as no single modified configuration was able to simultaneously maximise all the functional outcomes. This was due to an antagonistic relationship between impingement and the kinematic and kinetic properties of the reverse shoulder and the differing functional requirements for the motions that elevated the humerus compared to those that rotated the humerus.

8.1.2 Optimising prosthesis configuration

The systematic combination of multiple prosthesis parameters was performed in Chapter 5 to establish 47 modified configurations of the prosthesis. These configurations were evaluated using the expanded assessment framework and the data processing techniques (developed in Chapter 4). Even though none of the constitutive modifications excessively elongated the deltoid, only 21 of the 47 combined configurations did not cause excessive deltoid elongation. Each of the primary outcome measures were maximised by different configurations. Consequently, the configuration that was selected to optimise RTSA function provided balanced, moderate improvements to the primary outcome measures, rather than emphasising a single outcome measure. The optimised configuration simultaneously inferiorly translated the glenosphere by 5 mm and posteromedially translated the humeral tray by 5 mm. This configuration mutually benefited from the positive effects of both modifications. The glenosphere translation improved deltoid moment arms and impingement-free range of motion; and the humeral tray translation improved joint stability. This configuration had a beneficial (or negligible) impact on majority of the outcome measures, except for the deltoid moment arms during internal rotation, which were detrimentally affected.

These exceptions, along with the relatively low overall scores obtained by the usable modified configurations and the factor analysis performed on the binned data, re-iterate observations regarding the biomechanical trade-offs of RTSA due to the antagonistic relationship between functional outcomes and the differing requirements of the motions. It suggests that a generalised maximisation of function, accounting for a variety of outcome measures and motions, is not possible and that, in the long-term, targeted improvements based on the patient-specific requirements may become best practice for the orthopaedic community.

8.1.3 Evaluating optimised configuration performance

Muscle fatigue and implant micromotion were assessed for the default and optimised configurations of the prosthesis to provide insight into the overall performance of the prosthesis.

A time-dependent three-compartment muscle fatigue model was incorporated into the NSM to characterise the effect of fatigue on reverse shoulder function during prolonged periods of humeral elevation. Fatigue propagated a progressive decrease in the force generated by the middle deltoid over the course of each motion, especially at higher elevations. In order to compensate for this decrease and maintain adequate shoulder function, the forces generated by some of the surrounding muscles increased beyond their baseline levels. While this compensatory mechanism help to maintain function after the initiation of fatigue, the changes to the muscle forces were unbalanced and it had an effect on the joint contact forces that could potentially lead to an eventual loss of function with continued use at higher elevations. The optimised configuration decreased the force required by the deltoid to initially elevate the humerus. Consequently, the time taken to initiate fatigue was extended using this configuration and the changes to the forces generated by the compensatory muscles were typically smaller by the end of the motions. This suggests that the optimised configuration can mitigate the negative effects of muscle fatigue compared to the default configuration.

A finite element model-set was created to assess micromotion at the bone-implant interface. Joint contact forces calculated in the previous chapters were used as the input parameters for the analysis of loading conditions that represented various humeral elevations. The micromotion experienced by the implant components (metaglene and inferior and superior fixation screws) was dependent on the motion and elevation angle. Component micromotion varied due to differing friction coefficients and surface areas at the interface. Additionally, the inferior fixation screw experienced more micromotion than its superior counterpart due to the superior shear component of the applied joint contact forces. Micromotion was dependent on the loading condition due to changes in the distribution of joint compression and shear. 90° of abduction produced the largest amount of micromotion for the implant components and this was likely due to the relatively large antero-posterior shear forces generated during the motion. The optimised configuration was found to have a minimal effect on micromotion. This was beneficial as it suggests that the benefits to IFROM, DMA, SR, and muscle fatigue were obtained without detrimental affecting implant micromotion.

8.2 Recommendations

The following sections provide recommendations for future studies that can be pursued in light of the findings of this thesis. These recommendations include the validation of the results using experimental techniques, improvements to the assessment framework and its associated techniques, and the establishment of a subject-specific pre-operative planning protocol. In addition, it should be noted that the assessment framework has the potential to be extended to a variety of RTSA-related clinical problems, provided it is given the necessary input parameters; examples of these problems include the efficacy of RTSA to treat glenoid biconcavity, the implications of latissimus dorsi tendon transfer on reverse shoulder function, and comparisons between RTSA functional outcomes when performing unguided surgery versus guided surgery that utilises pre-operative planning technologies.

8.2.1 Experimental validations

Currently, the means of validating the results of the assessment framework has involved comparisons to biomechanical literature. While these comparisons have demonstrated an alignment with the current understanding of RTSA biomechanics and the effects of prosthesis modifications, a next step towards the realisation of the optimised configuration could be the experimental validation of the findings of this thesis. Ideally, three aspects should be validated: the changes to functional outcomes due to the optimised configuration, and the findings of the muscle fatigue and finite element analyses. In each of these instances, these experiments would either validate the results of the musculoskeletal or finite element modelling, thereby propagating further developments of a prosthesis design, or necessitate possible adjustments to the modelling techniques and the re-iteration of the assessments.

8.2.1.1 Validate the functional outcome changes due to the optimised configuration

A cadaveric shoulder model, like those described in Section 2.5.1, could either be used or developed to experimentally calculate muscle moment arms, stability ratio, and impingement for the default and optimised configuration of the prosthesis. The usage of one of these models could stem from the establishment of a collaboration with the corresponding research institute, or a custom-made model could be made at the university.

8.2.1.2 Validate the findings of the muscle fatigue analysis

An EMG analysis on RTSA recipients could be performed to investigate the effect of muscle fatigue during prolonged elevation of the arm. In conjunction, muscle-specific fatigue factors could be established to improve the fidelity of the muscle fatigue model, which used a generalised muscle fatigue factor.

8.2.1.3 Validate the findings of the finite element analysis

A mechanical testing rig, like those described in Section 2.5.3, could either be used or developed to experimentally calculate micromotion at the bone-implant interface for the default and optimised configuration of the prosthesis. As with the cadaveric shoulder model, usage could stem from collaborations, or a custom-made model could be made at the university.

8.2.2 Enhance the assessment framework

Subsequent iterations of the assessment framework should incorporate parameters that make the simulations more representative of *in-vivo* conditions. Some of the key parameters include: pre-operative CT scans, reverse shoulder kinematics, activities of daily living and post-surgical rotator cuff status.

8.2.2.1 Pre-operative CT scans

Recipients of RTSA typically have osteoarthritis and their scapula and humerus can be deformed. These deformations may alter the reaming and resection processes used during the virtual surgery, and establish reverse shoulder models that are more representative than those developed using the CT scans of healthy shoulders. Additionally, calibrated pre-operative CT scans would provide a better approximation of the scapula material properties used during finite element analysis.

8.2.2.2 Reverse shoulder kinematics

As mentioned previously, the kinematics of reverse shoulders differ from healthy shoulders. The evaluation of RTSA recipients using a motion-capture system would establish a kinematic data-set for standardised motions and activities of daily living that are specific to the prosthesis.

8.2.2.3 Activities of daily living

The functional outcomes of activities of daily living (ADLs) differ from standardised activities as they require the combined humeral elevations and rotations. As such, the impact of a prosthesis modification on the functional outcomes during standardised activities may not be reflected during ADLs (Kontaxis et al. 2017). ADLs have been measured by Murray and Johnson (2004) and include tasks that involved hygiene, feeding, and the use of everyday objects. Therefore, their inclusion in the assessment framework, alongside standardised activities, would enhance the determination of an optimised configuration.

8.2.2.4 Post-surgical rotator cuff status

The indications for RTSA have expanded due to good preliminary clinical outcomes. As a result, patients with partially intact rotator cuffs can be prescribed RTSA and surgeons are often able to preserve these muscles during the surgery. Including different post-surgical rotator cuff statuses in the assessment framework would broaden its scope and optimised configurations of the prosthesis could be determined for a variety of rotator cuff tear scenarios.

8.2.2.5 Clinically-driven weighting factors

The current iteration of the assessment framework is unbiased and does not favour any particular motion or outcome measure. However, this could be changed by using weighting factors (applied to the median binned data scores) to bias the analysis towards a prescribed condition, thereby eliminating the problems raised by the antagonistic relationship between functional outcomes and the differing requirements of the motions. For example, a surgeon could favour improvements to IFROM over DMA and SR changes, and give the IFROM scores a positive weighting and the DMA and SR scores a reduced or zero weightings. The assessment framework would then determine a different subset of beneficial configuration modification, which, in turn, would establish a prosthesis configuration that is optimised for IFROM.

8.2.3 Evaluate additional prosthesis modifications

The prosthesis modifications not included in this thesis should be incorporated into subsequent assessments to provide a complete evaluation of all possible prosthesis configurations. These modifications include changes to glenosphere diameter, glenosphere inclination angle (which was only partially assessed in Chapter 4), humeral stem neck-shaft angle, humeral head resection version and humeral cup depth. These were omitted due to limitations surrounding the use of the Delta XTEND prosthesis and the reverse shoulder model-set development process, which was conducted manually.

A means of parameterising the virtual surgery to accommodate adjustments to the resection angles and different prosthesis geometries should be investigated. In doing so, the model-set development process could be automated, thereby removing the current disconnect between the virtual surgery and the application of the prosthesis modifications using the OpenSim API.

8.2.4 Refine the assessment techniques

Refinements to the assessment techniques used during this thesis may be an esoteric exercise depending on one's perspective and desired outputs from the process. If one is looking to achieve the most representative biomechanical model of the reverse shoulder possible these recommendations are of

interest. However, if one is more interested with using the process as a means of evaluating the relative differences between configurations of the reverse shoulder configuration, these recommendations may add unnecessary complexity.

8.2.4.1 Musculoskeletal modelling

The musculature of the NSM is modelled as a series elastic strings that can wrap around basic geometric shapes that approximate bone geometries. Whilst modelling in this manner is common in the field of biomechanics, it neglects the volumetric nature of muscles, muscle on muscle interactions and unwrapping problems that can occur at certain humeral orientations. A departure from this technique would be challenging but has the potential to yield more accurate muscle and joint contact force predictions. A divergent path of future developments could be finite element modelling of the muscles. This technique has been shown to take these neglected factors into consideration (Webb et al. 2014), and could more accurately predict muscle and joint contact forces at the expense of decreased computational efficiency.

8.2.4.2 Impingement detection

The current iteration of the IDA may slightly over or under-estimate extra-articular impingement as it uses a sphere and a plane to approximate the lateral surface of the humeral head. It could be improved by using these geometric primitives to constraint the region in which the algorithm checks the distance between each vertex of the humerus and scapula. While this may take longer to simulate, it could better calculate the exact point at which this type of impingement occurs.

8.2.4.3 Data processing

The current data processing techniques are reductive as the dimensionality of the data (which is a function of motion) are removed when calculating means. This could be avoided by using newer techniques like statistical parametric mapping to preserve dimensionality (Pataky 2010). However, careful implementation of such a technique would be required to ensure that the assessment framework can sufficiently synthesise and process the data to characterise the effect of the prosthesis modifications.

8.2.5 Establish a subject-specific pre-operative planning protocol

The flowchart in Figure 8.1 proposes a strategy for subject-specific pre-operative planning. It represents an idealised scenario that could be the ultimate long-term goal of future RTSA prosthesis optimisation research. In this instance, the protocol determines an optimised prosthesis configuration (from a set of prescribed modifiable parameters) for each patient based on pre-operative criteria

established by the orthopaedic team. For example, the protocol could select a configuration that provides balanced improvements to function (as done in this thesis), or it could select a configuration that either targets a particular motion or maximises improvements to IFROM, or DMA and SR.

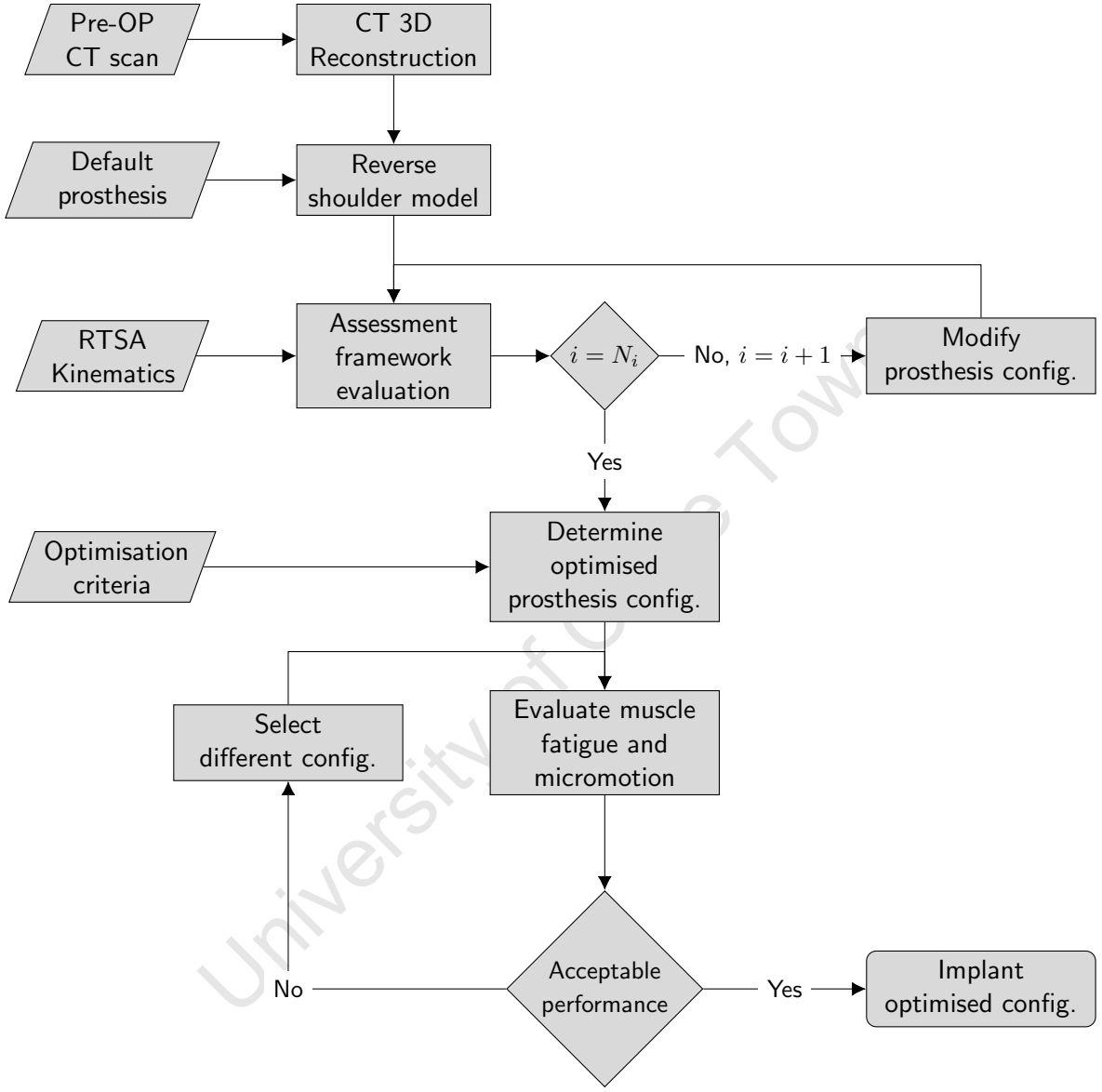

Figure 8.1 Flowchart of the proposed subject-specific pre-operative planning protocol

8.3 Summary

An optimised configuration of RTSA has been presented in this thesis. On average, the optimised configuration improved functional outcomes of a rotator cuff deficient reverse shoulder by implementing a 5 mm inferior translation of the glenosphere and a 5 mm posteromedial translation of the humeral tray. This novel combination of prosthesis modifications, without excessively elongating the deltoid, had a beneficial effect on deltoid moment arms, glenohumeral joint stability and impingement-free range of motion during humeral elevations. The optimised configuration also mitigated muscle fatigue by decreasing the force required by the deltoid to initially elevate the humerus and it did not negatively affect implant micromotion. Future studies should look to experimentally validate these findings, determine their clinical significance, and enhance both the assessment technique and framework.

References

Abdi, H. and L.J. Williams (2010). "Principal component analysis". In: *Wiley Interdisciplinary Reviews: Computational Statistics* 2.4, pp. 433–459.

Abdi, H., L.J. Williams, and D. Valentin (2013). "Multiple factor analysis: Principal component analysis for multitable and multiblock data sets". In: *Wiley Interdiscip. Rev. Comput. Stat.* 5.2, pp. 149–179.

Ackland, D.C. and M.G. Pandy (2011). "Moment arms of the shoulder muscles during axial rotation". In: *J. Orthop. Res.* 29.5, pp. 658–667.

Ackland, D.C., S. Roshan-Zamir, M. Richardson, and M.G. Pandy (2010). "Moment arms of the shoulder musculature after reverse total shoulder arthroplasty". In: *J. Bone Joint Surg. Am.* 92, pp. 1221–1230.

Ackland, D.C., S. Roshan-Zamir, M. Richardson, and M.G. Pandy (2011). "Muscle and joint-contact loading at the glenohumeral joint after reverse total shoulder arthroplasty". In: *J. Orthop. Res.* 29.12, pp. 1850–1858.

Ackland, D.C., M. Richardson, and M.G. Pandy (2012). "Axial Rotation Moment Arms of the Shoulder after Reverse Total Arthroplasty". In: *J. Bone Joint Surg. Am.* 94, pp. 1886–1895.

An, K.N., Y. Ueba, E.Y. Chao, W.P. Cooney, and R.L. Linscheid (1983). "Tendon excursion and moment arm of index finger muscles". In: *J. Biomech.* 16.6, pp. 419–425.

ASTM-International (2014). *Standard Test Methods for Dynamic Evaluation of Glenoid Loosening or Disassociation*. West Conshohocken, PA, USA: ASTM International.

Barnett, N.D., R.D.D. Duncan, and G.R. Johnson (1999). "The measurement of three dimensional scapulohumeral kinematics - a study of reliability". In: *Clin. Biomech.* 14.4, pp. 287–290.

Berhouet, J., P. Garaud, and L. Favard (2013). "Influence of glenoid component design and humeral component retroversion on internal and external rotation in reverse shoulder arthroplasty: A cadaver study". In: *Orthopaedics and Traumatology: Surgery and Research* 99.3, pp. 887–894.

Berhouet, J., A. Kontaxis, L. Gulotta, E. Craig, R. Warren, J. Dines, and D. Dines (2014a). "Effects of the humeral tray component positioning for onlay reverse shoulder arthroplasty design: a biomechanical analysis". In: *J. Shoulder Elbow Surg.* 24.4, pp. 569–577.

Berhouet, J., P. Garaud, and L. Favard (2014b). "Evaluation of the role of glenosphere design and humeral component retroversion in avoiding scapular notching during reverse shoulder arthroplasty". In: *J. Shoulder Elbow Surg.* 23.2, pp. 151–158.

Bernakiewicz, M. and M. Viceconti (2002). "The role of parameter identification in finite element contact analyses with reference to orthopaedic biomechanics applications". In: *J. Biomech.* 35, pp. 61–67.

Berton, A., L.V. Gulotta, P. Stefano, P. Florio, U.G. Longo, V. Denaro, and A. Kontaxis (2015). "The effect of humeral version on teres minor muscle moment arm, length, and impingement in reverse shoulder arthroplasty during activities of daily living". In: *J. Shoulder Elbow Surg.* 24.4, pp. 578–586.

Boileau, P., D. Watkinson, A.M. Hatzidakis, and F. Balg (2005). "Grammont reverse prosthesis: Design, rationale, and biomechanics". In: *J. Shoulder Elbow Surg.* 14.1, pp. 174–161.

Boileau, P., D. Watkinson, AM. Hatzidakis, and I. Hovorka (2006). "Neer Award 2005: The Grammont reverse shoulder prosthesis: Results in cuff tear arthritis, fracture sequelae, and revision arthroplasty". In: *J. Shoulder Elbow Surg.* 15.5, pp. 527–540.

Boileau, P., G. Moineau, Y. Roussanne, and K. O'Shea (2011). "Bony increased-offset reversed shoulder arthroplasty minimizing scapular impingement while maximizing glenoid fixation". In: *Clin. Orthop.* 469.9, pp. 2558–2567.

Broström, L.A., R. Wallenstein, E. Olsson, and D. Anderson (Apr. 1992). "The Kessel prosthesis in total shoulder arthroplasty. A five-year experience". In: *Clin. Orthop.* Pp. 155–160.

Büchler, P., N.A. Ramaniraka, L.R. Rakotomanana, J.P. Iannotti, and A. Farron (2002). "A finite element model of the shoulder: Application to the comparison of normal and osteoarthritic joints". In: *Clinical Biomechanics* 17.9-10, pp. 630–639.

Chae, S.W., J. Lee, S.H. Han, and S.Y. Kim (2015). "Inferior tilt fixation of the glenoid component in reverse total shoulder arthroplasty: A biomechanical study". In: *Orthopaedics and Traumatology: Surgery and Research* 101.4, pp. 421–425.

Chae, S.W., H. Lee, S.M. Kim, J. Lee, S.H. Han, and S.Y. Kim (2016). "Primary stability of inferior tilt fixation of the glenoid component in reverse total shoulder arthroplasty: A finite element study". In: *J. Orthop. Res.* 34.6, pp. 1061–1068.

Charlton, I.W. (2003). "Model for the prediction of the forces at the glenohumeral joint". PhD thesis. Newcastle University.

Charlton, I.W. and G.R. Johnson (2001). "Application of spherical and cylindrical wrapping algorithms in a musculoskeletal model of the upper limb". In: *J. Biomech.* 34.9, pp. 1209–1216.

Charlton, I.W. and G.R. Johnson (2006). "A model for the prediction of the forces at the glenohumeral joint". In: *Proc. Inst. Mech. Eng. H* 220.8, pp. 801–812.

Chou, J., S.F. Malak, I.A. Anderson, T. Astley, and P.C. Poon (2009). "Biomechanical evaluation of different designs of glenospheres in the SMR reverse total shoulder prosthesis: Range of motion and risk of scapular notching". In: *J. Shoulder Elbow Surg.* 18.3, pp. 354–359.

Clouthier, A.L., M.A. Hetzler, G. Fedorak, J.T. Bryant, K.J. Deluzio, and R.T. Bicknell (2013). "Factors affecting the stability of reverse shoulder arthroplasty: A biomechanical study". In: *J. Shoulder Elbow Surg.* 22.4, pp. 439–444.

Corke, P.I. (1996). "A robotics toolbox for MATLAB". In: *IEEE Robot. Autom. Mag.* 3.1, pp. 24–32.

Costantini, O., D.S. Choi, A. Kontaxis, and L.V. Gulotta (2015). "The effects of progressive lateralization of the joint center of rotation of reverse total shoulder implants". In: *J. Shoulder Elbow Surg.* 24.7, pp. 1120–1128.

Craig, E.V. (July 2013). *Shoulder Arthritis: An Overview*. URL: https://www.hss.edu/conditions_shoulder-arthritis-overview.asp (visited on 09/17/2015).

Crowninshield, R.D. and R.A. Brand (1981). "A physiologically based criterion of muscle force prediction in locomotion". In: *J. Biomech.* 14.11, pp. 793–801.

Cuff, D., D. Pupello, N. Virani, J. Levy, and M. Frankle (2008). "Reverse Shoulder Arthroplasty for the Treatment of Rotator Cuff Deficiency". In: *J. Bone Joint Surg. Am.* 90.6, pp. 1244–1251.

Day, J., E. Paxton, E. Lau, V.A. Gordon, J.A. Abboud, and G.R. Williams (2015). "Use of reverse total shoulder arthroplasty in the Medicare population". In: *J. Shoulder Elbow Surg.* 24.5, pp. 766–772.

Day, J.S., E. Lau, K.L. Ong, G.R. Williams, M.L. Ramsey, and S.M. Kurtz (2010). "Prevalence and projections of total shoulder and elbow arthroplasty in the United States to 2015". In: *Journal of Shoulder and Elbow Surgery* 19.8, pp. 1115–1120.

De Leva, P. (1996). "Adjustments to Zatsiorsky-Seluyanov's segment inertia parameters". In: *J. Biomech.*

De Wilde, L.F., E.A. Audenaert, and B.M. Berghs (2004). "Shoulder prostheses treating cuff tear arthropathy: A comparative biomechanical study". In: *J. Orthop. Res.* 22.6, pp. 1222–1230.

De Wilde, L.F., D. Poncet, B. Middernacht, and A. Ekelund (2010). "Prosthetic overhang is the most effective way to prevent scapular conflict in a reverse total shoulder prosthesis." In: *Acta Orthop.* 81.6, pp. 719–26.

Delp, S.L., F.C. Anderson, A.S. Arnold, P. Loan, A. Habib, C.T. John, E. Guendelman, and D.G. Thelen (2007). "OpenSim: Open source to create and analyze dynamic simulations of movement". In: *IEEE Trans. Bio-Med. Eng.* 54.11, pp. 1940–1950.

Denard, P.J., E. Lederman, B.O. Parsons, and A.A. Romeo (2017). "Finite element analysis of glenoid-sided lateralization in reverse shoulder arthroplasty". In: *J. Orthop. Res.* 35.7, pp. 1548–1555.

DePuy-Synthes (2013). *Delta XTEND Reverse Shoulder System: Surgical Technique*. DePuy Synthes.

Dey, R., S. Roche, T. Rosch, T. Mutsvangwa, J. Charilaou, and S. Sivarasu (2018). "Anatomic variations in glenohumeral joint: an interpopulation study". In: *J. Shoulder Elbow Surg. Open Access* 2.1, pp. 1–7.

Edwards, T.B., A. Boulahia, J.F. Kempf, P. Boileau, C. Nemoz, and G. Walch (2002). "The influence of the rotator cuff on the results of shoulder arthroplasty for primary osteoarthritis: results of a multicenter study". In: *J. Bone Joint Surg. Am.* 84, pp. 2240–2248.

Edwards, T.B., M.D. Williams, J.E. Labriola, H.A. Elkousy, G.M. Gartsman, and D.P. O'Connor (2009). "Subscapularis insufficiency and the risk of shoulder dislocation after reverse shoulder arthroplasty". In: *J. Shoulder Elbow Surg.*

Edwards, T.B., G.J. Trappey, C. Riley, D.P. O'Connor, H.A. Elkousy, and G.M. Gartsman (2012). "Inferior tilt of the glenoid component does not decrease scapular notching in reverse shoulder

arthroplasty: results of a prospective randomized study." In: *J. Shoulder Elbow Surg.* 21.5, pp. 641–646.

Ek, E.T.H., L. Neukom, S. Catanzaro, and C. Gerber (2013). "Reverse total shoulder arthroplasty for massive irreparable rotator cuff tears in patients younger than 65 years old: Results after five to fifteen years". In: *J. Shoulder Elbow Surg.* 22.9, pp. 1199–1208.

Elwell, J., J. Choi, and R. Willing (2017). "Quantifying the competing relationship between adduction range of motion and baseplate micromotion with lateralization of reverse total shoulder arthroplasty". In: *J. Biomech.* 52, pp. 24–30.

Encore-Medical (2008). *Reverse Shoulder Prosthesis: Surgical Technique*. Encore Medical.

Enoka, R.M. and D.G. Stuart (1992). "Neurobiology of muscle fatigue". In: *J. Appl. Physiol.* 72.5, pp. 1631–1648.

Erickson, B.J., R.M. Frank, J.D. Harris, N. Mall, and A.A. Romeo (2015). "The influence of humeral head inclination in reverse total shoulder arthroplasty: A systematic review". In: *J. Shoulder Elbow Surg.* 24.6, pp. 988–993.

Farshad, M. and C. Gerber (2010). "Reverse total shoulder arthroplasty-from the most to the least common complication." In: *Int. Orthop.* 34.8, pp. 1075–1082.

Favre, P., P.S. Sussmann, and C. Gerber (2010). "The effect of component positioning on intrinsic stability of the reverse shoulder arthroplasty". In: *J. Shoulder Elbow Surg.* 19.4, pp. 550–556.

Favre, P., S. Perala, P. Vogel, S.F. Fucentese, J.R. Goff, C. Gerber, and J.G. Snedeker (2011). "In vitro assessments of reverse glenoid stability using displacement gages are misleading - recommendations for accurate measurements of interface micromotion". In: *Clin. Biomech.* 26, pp. 917–922.

Frankle, M., S. Siegal, D. Pupello, A. Saleem, M. Mighell, and M. Vasey (2005). "The Reverse Shoulder Prosthesis for Glenohumeral Arthritis Associated with Severe Rotator Cuff Deficiency. A Minimum Two-Year Follow-Up Study of Sixty Patients." In: *J. Bone Joint Surg. Am.* 87.8, pp. 1697–1705.

Franklin, J.L., W.P. Barrett, S.E. Jackins, and F.A. Matsen (1988). "Glenoid loosening in total shoulder arthroplasty. Association with rotator cuff deficiency". In: *J. Arthroplasty* 3, pp. 39–46.

Frey-Law, L.A., J.M. Looft, and J. Heitsman (2012). "A three-compartment muscle fatigue model accurately predicts joint-specific maximum endurance times for sustained isometric tasks". In: *Journal of Biomechanics* 45.10, pp. 1803–1808.

Friedman, R., R. Hawthorne, and B. Genez (1992). "The use of computerized tomography in the measurement of glenoid version". In: *J. Bone Joint Surg. Am.* 74.7, pp. 1032–1037.

Gallo, R.A., S.C. Gamradt, C.J. Mattern, F.A. Cordasco, E.V. Craig, D.M. Dines, and R.F. Warren (2011). "Instability after reverse total shoulder replacement". In: *J. Shoulder Elbow Surg.* 20.4, pp. 584–590.

Garberina, M.J. and G.R. Williams (2008). "Polyethylene dissociation after reverse total shoulder arthroplasty: The use of diagnostic arthroscopy". In: *J. Shoulder Elbow Surg.* 17.1, pp. 16–18.

Garcia, G.H., S.A. Taylor, B.J. DePalma, G.T. Mahony, B.M. Grawe, J. Nguyen, J.S. Dines, D.M. Dines, R.F. Warren, E.V. Craig, and L.V. Gullota (2015). "Patient activity levels after reverse total shoulder arthroplasty: what are patients doing?" In: *Am. J. Sports Med.* 43, pp. 2816–2821.

Gerber, C., S.D. Pennington, and R.W. Nyffeler (2009). "Reverse Total Shoulder Arthroplasty". In: *J. Am. Acad. Orthop. Surg.* 17, pp. 284–295.

Giles, J.W., G.D.G. Langohr, J.A. Johnson, and G.S. Athwal (2015). "Implant Design Variations in Reverse Total Shoulder Arthroplasty Influence the Required Deltoid Force and Resultant Joint Load". In: *Clin. Orthop.* 473.11, pp. 3615–3626.

Grammont, P.M. and E. Baulot (1993). "Delta shoulder prosthesis for rotator cuff rupture". In: *Orthopedics* 16, pp. 65–68.

Guery, J., L. Favard, F. Sirveaux, D. Oudet, D. Mole, and G. Walch (2006). "Reverse total shoulder arthroplasty: survivorship analysis of eighty replacements followed for five to ten years". In: *J. Bone Joint Surg. Am.* 88, pp. 1742–1747.

Gulotta, L.V., D. Choi, P. Marinello, Z. Knutson, J. Lipman, T. Wright, F.A. Cordasco, E.V. Craig, and R.F. Warren (2012). "Humeral component retroversion in reverse total shoulder arthroplasty: a biomechanical study". In: *J. Shoulder Elbow Surg.* 21.9, pp. 1121–1127.

Gutiérrez, S., R.M. Greiwe, M.A. Frankle, S. Siegal, and W.E. Lee (2007). "Biomechanical comparison of component position and hardware failure in the reverse shoulder prosthesis". In: *J. Shoulder Elbow Surg.* 16.3, pp. 9–12.

Gutiérrez, S., T.S. Keller, J.C. Levy, W.E. Lee, and Z.P. Luo (2008a). "Hierarchy of stability factors in reverse shoulder arthroplasty". In: *Clin. Orthop.* 466.3, pp. 670–676.

Gutiérrez, S., C.A. Comiskey, Z.P. Luo, D.R. Pupello, and M.A. Frankle (2008b). "Range of impingement-free abduction and adduction deficit after reverse shoulder arthroplasty. Hierarchy of surgical and implant-design-related factors". In: *J. Bone Joint Surg. Am.* 90.12, pp. 2606–2615.

Gutiérrez, S., Z.P. Luo, J. Levy, and M.A. Frankle (2009). "Arc of motion and socket depth in reverse shoulder implants". In: *Clin. Biomech.* 24, pp. 473–479.

Gutiérrez, S., M. Walker, M. Willis, D.R. Pupello, and M.A. Frankle (2011). "Effects of tilt and glenosphere eccentricity on baseplate/bone interface forces in a computational model, validated by a mechanical model, of reverse shoulder arthroplasty". In: *J. Shoulder Elbow Surg.*

Hamid, N., P.M. Connor, J.F. Fleischli, and D.F. D'Alessandro (2011). "Acromial Fracture After Reverse Shoulder Arthroplasty". In: *Am. J. Orthop.* 40.7, E125–E129.

Henninger, H.B., A. Barg, A.E. Anderson, K.N. Bachus, R.Z. Tashjian, and R.T. Burks (2012a). "Effect of deltoid tension and humeral version in reverse total shoulder arthroplasty: A biomechanical study". In: *J. Shoulder Elbow Surg.* 21'.4, pp. 483–490.

Henninger, H.B., A. Barg, A.E. Anderson, K.N. Bachus, R.T. Burks, and R.Z. Tashjian (2012b). "Effect of lateral offset center of rotation in reverse total shoulder shoulder arthroplasty: a biomechanical study". In: *J. Shoulder Elbow Surg.* 21.9, pp. 1128–1135.

Herrmann, S., C. König, M. Heller, C. Perka, and S. Greiner (2011). "Reverse shoulder arthroplasty leads to significant biomechanical changes in the remaining rotator cuff". In: *Journal of Orthopaedic Surgery and Research* 6.1, pp. 1–7.

Hettrich, C.M., V.N. Permeswaran, J.E. Goetz, and D.D. Anderson (2015). "Mechanical tradeoffs associated with glenosphere lateralization in reverse shoulder arthroplasty". In: *J. Shoulder Elbow Surg.* 24.11, pp. 1774–1781.

Hill, A.V. (1938). "The heat of shortening and the dynamic constants of muscle". In: *Proceedings of the Royal Society* 126B, pp. 136–195.

Hoenecke, H.R., C. Flores-Hernandez, and D.D. D'Lima (2014). "Reverse total shoulder arthroplasty component center of rotation affects muscle function". In: *J. Shoulder Elbow Surg.* 23.8, pp. 1128–1135.

Hogfors, C., D. Karlsson, and B. Peterson (1995). "Structure and internal consistency of a shoulder model". In: *J. Biomech.* 28.7, pp. 767–777.

Ingham, E. and J. Fisher (2005). "The role of macrophages in osteolysis of total joint replacement". In: *Biomaterials* 26.11, pp. 1271–1286.

James, J., M.A. Allison, F.W. Werner, D.E. McBride, N.N. Basu, L.G. Sutton, and V.N. Nanavati (2013). "Reverse shoulder arthroplasty glenoid fixation: Is there a benefit in using four instead of two screws?" In: *Journal of Shoulder and Elbow Surgery* 22.8, pp. 1030–1036.

Jobin, C.M., G.D. Brown, M.J. Bahu, T.R. Gardner, L.U. Bigliani, W.N. Levine, and C.S. Ahmad (2012). "Reverse total shoulder arthroplasty for cuff tear arthropathy: The clinical effect of deltoid lengthening and center of rotation medialization". In: *J. Shoulder Elbow Surg.* 21.10, pp. 1269–1277.

Johnson, G.R., D. Spalding, A. Nowitzke, and N. Bogduk (1996). "Modelling the muscles of the scapula morphometric and coordinate data and functional implications". In: *J. Biomech.* 29.8, pp. 1039–1051.

Kelly, J.D., C.S. Humphrey, and T.R. Norris (2008). "Optimizing glenosphere position and fixation in reverse shoulder arthroplasty, Part one: the twelve-mm rule". In: *J. Shoulder Elbow Surg.* 17.4, pp. 595–601.

Kim, S.H., B.L. Wise, Y. Zhang, and R.M. Szabo (2011). "Increasing Incidence of Shoulder Arthroplasty in the United States". In: *J. Bone Joint Surg. Am.* 93.24, pp. 2249–2254.

Kistler, M., S. Bonaretti, M. Pfahrer, R. Niklaus, and P. Büchler (2013). "The virtual skeleton database: an open access repository for biomedical research and collaboration". In: *J. Med. Internet Res.* 15.11, e245.

Kontaxis, A. (2009). "Biomechanical analysis of reverse anatomy shoulder prosthesis". PhD thesis. Newcastle University.

Kontaxis, A. and G.R. Johnson (2008). "Adaptation of scapula lateral rotation after reverse anatomy shoulder replacement." In: *Computer methods in biomechanics and biomedical engineering* 11.1, pp. 73–80.

Kontaxis, A. and G.R. Johnson (2009). "The biomechanics of reverse anatomy shoulder replacement - a modelling study". In: *Clin. Biomech.* 24.3, pp. 254–260.

Kontaxis, A., X. Chen, J. Berhouet, D. Choi, T. Wright, D.M. Dines, R.F. Warren, and L.V. Gulotta (2017). "Humeral version in reverse shoulder arthroplasty affects impingement in activities of daily living". In: *J. Shoulder Elbow Surg.* 26.6, pp. 1073–1082.

Kwon, Y.W., R.E. Forman, P.S. Walker, and J.D. Zuckerman (2010). "Analysis of reverse total shoulder joint forces and glenoid fixation". In: *Bulletin of the NYU Hospital for Joint Diseases* 68.4, pp. 273–280.

Kwon, Y.W., V.J. Pinto, J. Yoon, M.A. Frankle, P.E. Dunning, and A. Sheikhzadeh (2012). "Kinematic analysis of dynamic shoulder motion in patients with reverse total shoulder arthroplasty". In: *J. Shoulder Elbow Surg.* 21.9, pp. 1184–1190.

Lädermann, A., MD. Williams, B. Melis, P. Hoffmeyer, and G. Walch (2009). "Objective evaluation of lengthening in reverse shoulder arthroplasty". In: *J. Shoulder Elbow Surg.* 18.4, pp. 588–595.

Lädermann, A., P.J. Denard, P. Boileau, A. Farron, P. Deransart, A. Terrier, J. Ston, and G. Walch (2015). "Effect of humeral stem design on humeral position and range of motion in reverse shoulder arthroplasty". In: *Int. Orthop.* 39.11, pp. 2205–2213.

Langohr, G.D.G., J.W. Giles, G.S. Athwal, and J.A. Johnson (2015). "The effect of glenosphere diameter in reverse shoulder arthroplasty on muscle force, joint load, and range of motion". In: *J. Shoulder Elbow Surg.* 24.6, pp. 972–979.

Langohr, G.D.G., R. Willing, J.B. Medley, G.S. Athwal, and J.A. Johnson (2016). "Contact mechanics of reverse total shoulder arthroplasty during abduction: The effect of neck-shaft angle, humeral cup depth, and glenosphere diameter". In: *J. Shoulder Elbow Surg.* 25.4, pp. 589–597.

Lettin, A., S. Copeland, and J. Scales (1982). "The Stanmore total shoulder replacement". In: *J. Bone Joint Surg. Br.* 64, pp. 47–51.

Lévigne, C., J. Garret, P. Boileau, G. Alami, L. Favard, and G. Walch (2011). "Scapular notching in reverse shoulder arthroplasty: is it important to avoid it and how?" In: *Clin. Orthop.* 469.9, pp. 2512–2520.

Levy, J. C., N. Virani, D. Pupello, and M. Frankle (2007). "Use of the reverse shoulder prosthesis for the treatment of failed hemiarthroplasty in patients with glenohumeral arthritis and rotator cuff deficiency". In: *J. Bone Joint Surg. Am.* 89-B.2, pp. 189–195.

Levy, J.C., C. Anderson, and A. Samson (2013). "Classification of postoperative acromial fractures following reverse shoulder arthroplasty." In: *J. Bone Joint Surg. Am.*

Li, X., Z. Knutson, D. Choi, D. Lobatto, J. Lipman, E.V. Craig, R.F. Warren, and L.V. Gulotta (2013). "Effects of glenosphere positioning on impingement-free internal and external rotation after reverse total shoulder arthroplasty". In: *Journal of Shoulder and Elbow Surgery* 22.6, pp. 807–813.

Liou, W., Y. Yang, G.R. Petersen-Fitts, D.J. Lombardo, S. Stine, and V.J. Sabesan (2017). "Effect of lateralized design on muscle and joint reaction forces for reverse shoulder arthroplasty". In: *J. Shoulder Elbow Surg.* 26.4, pp. 564–572.

Liu, J.Z., R.W. Brown, and G.H. Yue (2002). "A dynamical model of muscle activation, fatigue, and recovery". In: *Biophys. J.* 82, pp. 2344–2359.

Marchese, S. and G.R. Johnson (2000). "Measuring the kinematics of the clavicle". In: *6th International Symposium of the 3D Analysis of human motion, Cape Town*, pp. 37–40.

Marsden, S.P., D.C. Swailes, and G.R. Johnson (2008). "Algorithms for exact multi-object muscle wrapping and application to the deltoid muscle wrapping around the humerus". In: *Proc. Inst. Mech. Eng. H* 222.7, pp. 1081–1095.

Matsumura, N., S. Oki, K. Ogawa, T. Iwamoto, K. Ochi, K. Sato, and T. Nagura (2016). "Three-dimensional anthropometric analysis of the glenohumeral joint in a normal Japanese population". In: *J. Shoulder Elbow Surg.* 25.3, pp. 493–501.

Melis, B., M. De Franco, A. Lädermann, D. Mole, L. Favard, C. Nerot, C. Maynou, and G. Walch (2011). "An evaluation of the radiological changes around the Grammont reverse geometry shoulder arthroplasty after eight to 12 years." In: *J. Bone Joint Surg. Br.* 93.9, pp. 1240–1246.

Mizuno, N., P.J. Denard, P. Raiss, and G. Walch (2012). "The clinical and radiographical results of reverse total shoulder arthroplasty with eccentric glenosphere". In: *Int. Orthop.* 36.8, pp. 1647–1653.

Molé, D. and L. Favard (2007). "Excentered scapulohumeral osteoarthritis [French]". In: *Rev. Chir. Orthop. Reparatrice Appar. Mot.* 96.6 suppl, pp. 37–94.

Morton, D.A., K.B Foreman, and K.H. Albertine (2011). *The Big Picture: Gross Anatomy*. Ed. by K.H. Albertine. 1st Edition. McGraw-Hill Companies.

Murray, I.A. (1999). "Upper limb kinematics and dynamics during everyday tasks". PhD thesis. Newcastle University.

Murray, I.A. and G.R. Johnson (2004). "A study of the external forces and moments at the shoulder and elbow while performing every day tasks". In: *Clin. Biomech.* 19.6, pp. 586–594.

Neer, C.S. (2011). "The classic: Articular replacement for the humeral head". In: *Clin. Orthop.* 469.9, pp. 2409–2421.

Neer, C.S., E.V. Craig, and H. Fukuda (1983). "Cuff-tear arthropathy". In: *J. Bone Joint Surg. Am.* 65, pp. 1232–1244.

Neumann, D.A. (2002). *Kinesiology of the musculoskeletal system: foundations for physical rehabilitation*. Ed. by D.A. Neumann. 1st Edition. St. Louis: Mosby.

Nicholson, G., E. Strauss, and S. Sherman (2011). "Scapular notching: Recognition and strategies to minimize clinical impact." In: *Clin. Orthop.* 469.9, pp. 2521–2530.

Nikooyan, A. A., H. E.J. Veeger, P. Westerhoff, F. Graichen, G. Bergmann, and F. C.T. van der Helm (2010). "Validation of the Delft Shoulder and Elbow Model using in-vivo glenohumeral joint contact forces". In: *Journal of Biomechanics* 43.15, pp. 3007–3014.

Nyffeler, RW., CM Werner, L. Simmen, and C. Gerber (2004). "Analysis of a retrieved Delta III total shoulder prosthesis". In: *J. Bone Joint Surg. Br.* 86.8, pp. 1187–1191.

Nyffeler, R.W., C.M.L. Werner, and C. Gerber (2005). "Biomechanical relevance of glenoid component positioning in the reverse Delta III total shoulder prosthesis". In: *J. Shoulder Elbow Surg.* 14.5, pp. 524–528.

Oh, J.H., S.J. Shin, M.H. McGarry, J.H. Scott, N. Heckmann, and T.Q. Lee (2014). "Biomechanical effects of humeral neck-shaft angle and subscapularis integrity in reverse total shoulder arthroplasty". In: *J. Shoulder Elbow Surg.* 23.8, pp. 1091–1098.

Pataky, T.C. (2010). "Generalized n-dimensional biomechanical field analysis using statistical parametric mapping". In: *J. Biomech.*

Pattin, C.A., W.E. Caler, and D.R. Carter (1996). "Cyclic mechanical property degradation during fatigue loading of cortical bone". In: *J. Biomech.* 26, pp. 69–79.

Pepper, M., V. Akuthota, and E.C. McCarty (2006). "The pathophysiology of stress fractures". In: *Clin. Sports Med.* 25, pp. 1–16.

Permeswaran, V.N., J.E. Goetz, M.J. Rudert, C.M. Hettrich, and D.D. Anderson (2016). "Cadaveric validation of a finite element modeling approach for studying scapular notching in reverse shoulder arthroplasty". In: *J. Biomech.* 49.13, pp. 3069–3073.

Permeswaran, V.N., A. Caceres, J.E. Goetz, D.D. Anderson, and C.M. Hettrich (2017). "The effect of glenoid component version and humeral polyethylene liner rotation on subluxation and impingement in reverse shoulder arthroplasty". In: *J. Shoulder Elbow Surg.* 26.10, pp. 1718–1725.

Petrillo, S., U.G.. Longo, L.V. Gulotta, A. Berton, A. Kontaxis, T. Wright, and V. Denaro (2016). "Reverse total shoulder arthroplasty: research models". In: *Joints* 4.4, pp. 236–246.

Pollock, R.G., E.D. Deliz, S.J. McIlveen, E.L. Flatow, and L. Bigliani (1992). "Prosthetic replacement in rotator cuff deficient shoulders". In: *J. Shoulder Elbow Surg.* 1, pp. 173–186.

Ponce, B.A., L.O. Oladeji, M.E. Rogers, and M.E. Menendez (2015). "Comparative analysis of anatomic and reverse total shoulder arthroplasty: In-hospital outcomes and costs". In: *Journal of Shoulder and Elbow Surgery* 24.3, pp. 460–467.

Post, M., S.S. Haskell, and M. Jablon (1980). "Total shoulder replacement with a constrained prosthesis". In: *J. Bone Joint Surg. Am.* 62, pp. 327–335.

Ribeiro, N.S., J. Folgado, P.R. Fernandes, and J. Monteiro (2011). "Wear analysis in anatomical and reversed shoulder prostheses". In: *Comput. Methods Biomech Biomed. Eng.* 14.10, pp. 883–892.

Roche, C.P., P. Diep, M. Hamilton, L.A. Crosby, P.H. Flurin, T.W. Wright, J.D. Zuckerman, and H.D. Routman (2013). "Impact of inferior glenoid tilt, humeral retroversion, bone grafting, and design parameters on muscle length and deltoid wrapping in reverse shoulder arthroplasty". In: *Bulletin of the NYU Hospital for Joint Diseases* 71.4, pp. 284–293.

Saltzman, M.D., D.M. Mercer, J.W. Warme, A.L. Bertelsen, and F.A. Matsen III (2010). "A method for documenting the change in center of rotation with reverse total shoulder arthroplasty and its application to a consecutive series of 68 shoulders having reconstruction with one of two different reverse prostheses." In: *J. Shoulder Elbow Surg.* 19.7, pp. 1028–1033.

Sanchez-Sotelo, J. (2009). "Reverse total shoulder arthroplasty". In: *Clin. Anat.* 22.2, pp. 172–182.

Schuenke, M., E. Schulte, and U. Schumacher (2012). *Atlas of Anatomy*. Ed. by A.M. Gilroy, B.R. MacPherson, and L.M Ross. 2nd Edition. Thieme Medical Publishers, Inc.

Sharma, G.B. and D.D. Robertson (2013). "Adaptive scapula bone remodeling computational simulation: Relevance to regenerative medicine". In: *Journal of Computational Physics* 244, pp. 312–320.

Sherman, M.A., A. Seth, and S.L. Delp (2013). "What Is a Moment Arm? Calculating Muscle Effectiveness in Biomechanical Models Using Generalized Coordinates". In: *Proceedings of the ASME 2013 International Design Engineering Technical Conferences & Computers and Information in Engineering Conference*.

Simovitch, R., M. Zumstein, E. Lohri, N. Helmy, and C. Gerber (2007). "Predictors of scapular notching in patients managed with the Delta III reverse total shoulder replacement." In: *J. Bone Joint Surg. Am.* 89.3, pp. 588–600.

Sirveaux, F., L. Favard, D. Oudet, D. Huquet, G. Walch, and D. Mole (2004). "Grammont inverted total shoulder arthroplasty in the treatment of glenohumeral osteoarthritis with massive rupture of the cuff". In: *J. Bone Joint Surg. Br.* 86.3, pp. 388–395.

Spitzer, V.M. and D.G. Whitlock (1998). "The Visible Human dataset: the anatomical platform for human simulation". In: *Anat. Rec.* 253.2, pp. 49–57.

StatsSA (Aug. 2017). *New mid-year estimates reveal ageing population*. URL: http://www.statssa.gov.za/?p=10277 (visited on 01/15/2018).

Stephenson, D.R., J.H. Oh, M.H. McGarry, G.F. Rick Hatch, and T.Q. Lee (2011). "Effect of humeral component version on impingement in reverse total shoulder arthroplasty". In: *J. Shoulder Elbow Surg.* 20.4, pp. 652–658.

Sutton, L.G., F.W. Werner, A.K. Jones, C.A. Close, and V.N. Nanavati (2010). "Optimization of glenoid fixation in reverse shoulder arthroplasty using 3-dimensional modeling". In: *J. Shoulder Elbow Surg.* 19.5, pp. 664–669.

Taddei, F., E. Schileo, B. Helgason, L. Cristofolini, and M. Viceconti (2007). "The material mapping strategy influences the accuracy of CT-based finite element models of bones: an evaluation against experimental measurements". In: *Med. Eng. Phys.* 29.9, pp. 973–979.

Terrier, A., A. Reist, F. Merlini, and A. Farron (2008). "Simulated joint and muscle forces in reversed and anatomic shoulder prostheses". In: *J. Bone Joint Surg. Br.* 90.6, pp. 751–756.

Tornier (2016). *Bio-RSA Bony Increased Offset - Reversed Shoulder Arthroplasty: Surgical Technique*. Tornier.

Tornier (2017). *Aequalis Ascend Flex Convertible Shoulder System: Surgical Technique*. Tornier.

Van der Helm, F.C.T. (1994). "A finite element musculoskeletal model of the shoulder mechanism". In: *J. Biomech.* 27.5, pp. 551–569.

Van der Helm, F.C.T. (1996). "A standardised protocol for motion recordings of the shoulder". In: *1st Conference of the International Shoulder Group (Delft, The Netherlands)*.

Van der Helm, F.C.T. (1998). "The 'reversed' glenohumeral endoprosthesis". In: *J. Biomech.* 31 (Suppl. 1).27.

Van der Helm, F.C.T. and G.M. Pronk (1994). "Analysis of the kinematic and dynamic behavior of the shoulder mechanism". In: *J. Biomech.* 27.5, pp. 527–550.

Van der Helm, F.C.T. and R. Veenbaas (1991). "Modelling the mechanical effects of muscles with large attachment sites: application to the shoulder mechanism". In: *J. Biomech.* 24, pp. 1151–1163.

Van der Helm, F.C.T., G.M. Pronk, H.E.J. Veeger, and L.H.V. van der Wouder (1989). "The rotation center of the glenohumeral joint". In: *Abstracts - International Society of Biomechanics XII Congress*.

Van der Helm, F.C.T., H.E.J. Veeger, Pronk G.M., L.H.V. van der Woude, and R.H. Rozendaal (1992). "Geometry parameters for musculoskeletal modelling of the shoulder mechanism". In: *J. Biomech.* 25.2, pp. 129–144.

Vaupel, Z.M., K.C. Baker, M.D. Kurdziel, and J.M. Wiater (2012). "Wear simulation of reverse total shoulder arthroplasty systems: Effect of glenosphere design". In: *J. Shoulder Elbow Surg.* 21.10, pp. 1422–1429.

Veeger, H.E.J., B. Yu, K.N. An, and R.H. Rozendaal (1997). "Parameters for modelling the upper extremity". In: *J. Biomech.* 30.6, pp. 647–652.

Viceconti, M., R. Muccini, M. Bernakiewicz, M. Baleani, and L. Cristofolini (2000). "Large-sliding contact elements accurately predict levels of bone-implant micromotion relevant to osseointegration". In: *J. Biomech.* 33, pp. 1611–1618.

Virani, N.A., M. Harman, K. Li, J. Levy, D.R. Pupello, and M.A. Frankle (2008). "In vitro and finite element analysis of glenoid bone/baseplate interaction in the reverse shoulder design". In: *J. Shoulder Elbow Surg.* 17.3, pp. 509–521.

Virani, N.A., A. Cabezas, S. Gutiérrez, B.G. Santoni, R. Otto, and M.A. Frankle (2013). "Reverse shoulder arthroplasty components and surgical techniques that restore glenohumeral motion". In: *J. Shoulder Elbow Surg.* 22.2, pp. 179–187.

Walker, D., T. Wright, S. Banks, and A.M. Struk (2014). "Electromyographic analysis of reverse total shoulder arthroplasties". In: *J. Shoulder Elbow Surg.* 23.2, pp. 166–172.

Wall, B., L. Nové-Josserand, D.P. O'Connor, T.B. Edwards, and G. Walch (2007). "Reverse total shoulder arthroplasty: A review of results according to etiology". In: *J. Bone Joint Surg. Am.* 89, pp. 1476–1485.

Webb, J.D., S.S. Blemker, and S.L. Delp (2014). "3D finite element models of shoulder muscles for computing lines of actions and moment arms". In: *Comput Methods Biomech Biomed Engin* 17.8, pp. 829–837.

Werner, CML., P.A. Steinman, M. Gilbart, and C. Gerber (2005). "Treatment of Painful Pseudoparesis Due to Irreparable Rotator Cuff Dysfunction with the Delta III Reverse-Ball-And-Socket Total Shoulder Prosthesis". In: *J. Bone Joint Surg. Am.* 87-A.7, pp. 1476–1485.

Winters, J. (1995). "How detailed should muscle models be to understand multi-joint movement coordination?" In: *Winters, J.* 14.4-5, pp. 401–442.

Winters, J.M. (1990). "Hill-based muscle models: a systems engineering perspective". In: ed. by J.M. Winters and S.L. Woo. Springer-Verlag. Chap. 5, pp. 69–93.

Wong, M.T., G.D.G. Langohr, G.S. Athwal, and J.A. Johnson (2016). "Implant positioning in reverse shoulder arthroplasty has an impact on acromial stresses". In: *J. Shoulder Elbow Surg.* 25.11, pp. 1889–1895.

Wu, G. and P.R. Cavanagh (1995). "ISB recommendations for standardization in the reporting of kinematic data". In: *J. Biomech.*

Wu, G., F.C.T. Van Der Helm, H.E.J. Veeger, M. Makhsous, P. Van Roy, C. Anglin, J. Nagels, A.R. Karduna, K. McQuade, X. Wang, F.W. Werner, and B. Buchholz (2005). "ISB recommendation on definitions of joint coordinate systems of various joints for the reporting of human joint motion - Part II: shoulder, elbow, wrist and hand". In: *J. Biomech.* 38.5, pp. 981–992.

Wylie, J.D (2014). "Functional outcomes assessment in shoulder surgery". In: *World Journal of Orthopedics* 5.5, pp. 623–633.

Xia, T. and L.A. Frey-Law (2008). "A theoretical approach for modeling peripheral muscle fatigue and recovery". In: *Journal of Biomechanics* 41.14, pp. 3046–3052.

Zannoni, C., R. Mantovani, and M. Viceconti (1999). "Material properties assignment to finite element models of bone structures: a new method". In: *Med. Eng. Phys.* 20.10, pp. 735–740.

Zhang, Q., L.L. Shi, K.C. Ravella, J.L. Koh, S. Wang, and C. Liu (2016). "Distinct Proximal Humeral Geometry in Chinese Population and Clinical Relevance." In: *J. Bone Joint Surg. Am.* 98.24, pp. 2071–2081.

Zimmer-Biomet (2015). *Comprehensive Reverse Shoulder System: Surgical Technique*. Zimmer-Biomet.

Appendix A

Shoulder anatomy and function

The shoulder (Figure A.1) consists of the clavicle, scapula and humerus bones; which are connected via a series of joints that enable movement of the upper arm. The shoulder joints are the sternoclavicular, acromioclavicular, scapulothoracic and glenohumeral joints. Muscles and ligaments surround these bones and assist in articulation of the upper arm. The subsequent sections will summarise the key anatomical features of the shoulder and its functional characteristics (Neumann 2002; Morton et al. 2011; Schuenke et al. 2012). In addition, a brief summary of the elbow joint is provided.

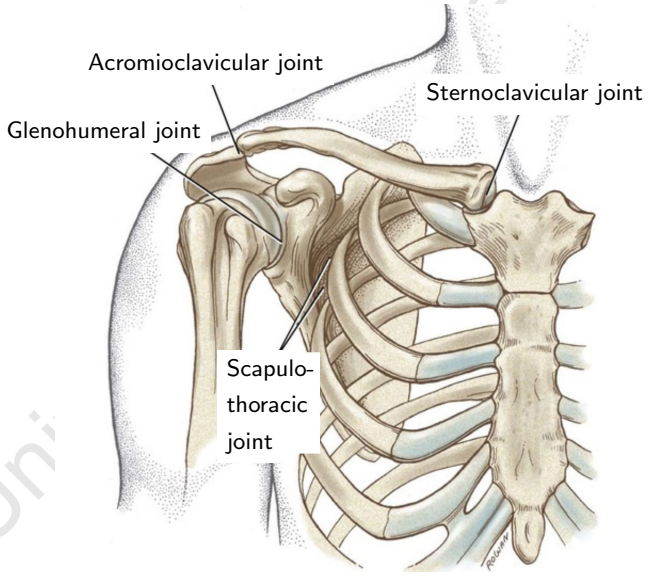

Figure A.1 The shoulder (adapted from Neumann (2002))

Bones

Sternum

The sternum is a flat, blade-like bone that forms a part of the anterior thoracic wall and consists of the manubrium, body and xiphoid process (Figure A.2). It articulates with the first to seventh rib at the costal notches along both of its lateral edges and with the clavicle at the clavicular notch on the manubrium.

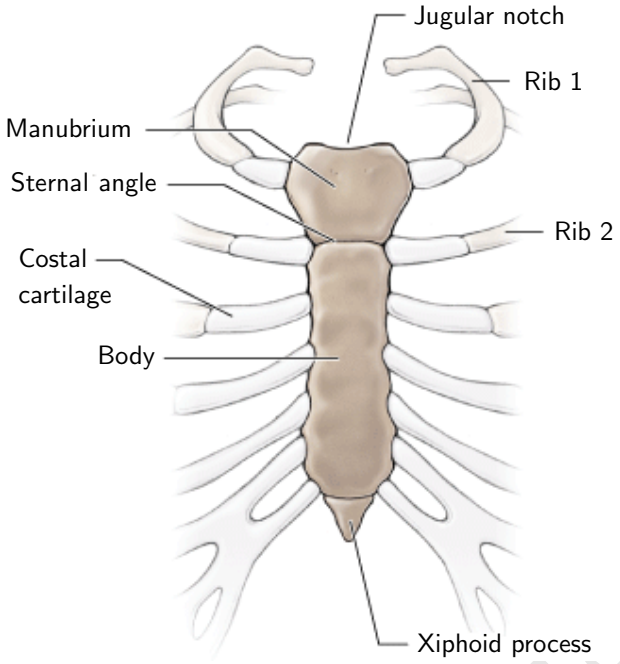

Figure A.2 The sternum (adapted from Morton et al. (2011))

Clavicle

The clavicle is an S-shaped bone that is located on top of the thorax (Figure A.3). It articulates with the sternum at the sternal end of the bone and with the acromion at the acromial end of the bone. The clavicle acts as the only bony connection between the upper limb and the trunk. It has a flat and smooth superior surface and a rough inferior surface that acts as attachment sites for muscles and ligaments.

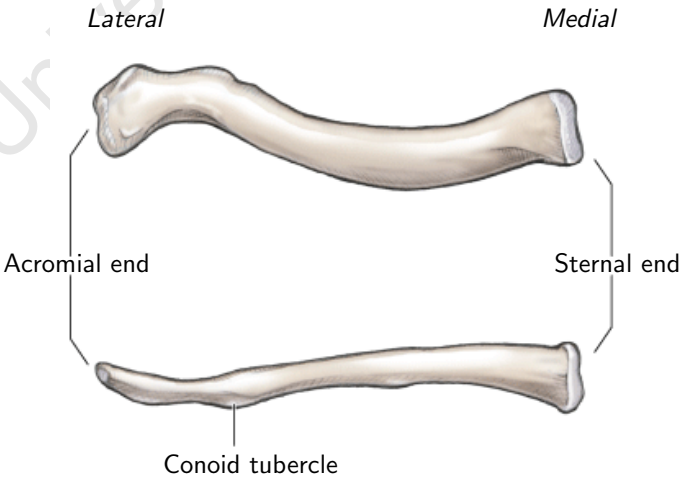

Figure A.3 The clavicle (adapted from Morton et al. (2011))

Scapula

The scapula is a triangular bone, defined by lateral, medial and superior borders, that rests above the posterior portions of the second to seventh rib (Figure A.4). It articulates with the clavicle at the acromion, with the humerus at the pear-shaped glenoid fossa and with the thorax by gliding over the ribs. It is highly contoured bone and has several processes and fossae that act as attachment sites for muscles and ligaments.

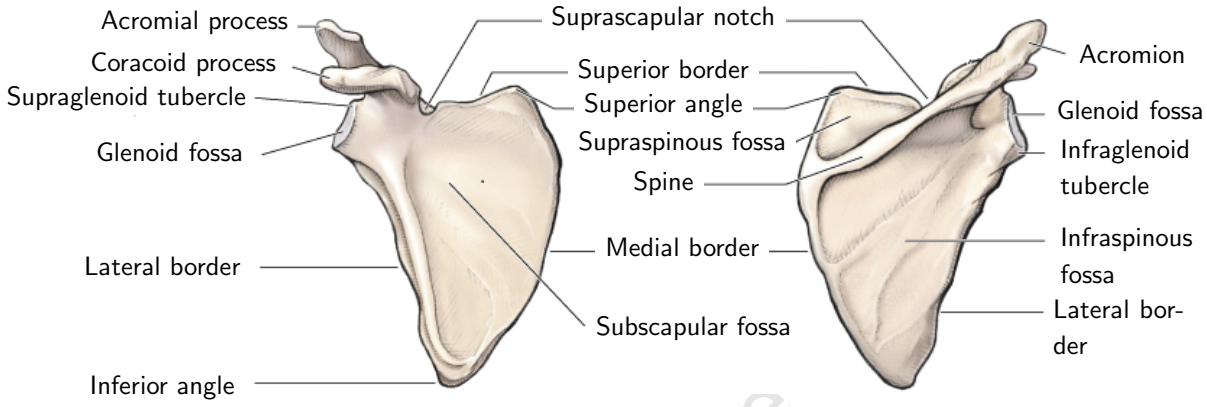

Figure A.4 The scapula (adapted from Morton et al. (2011))

Humerus

The humerus is a long bone that has a rounded proximal end, a cylindrical shaft and distal end comprised of epicondyles (Figure A.5). The spherical humeral head (which meets the shaft at an oblique and slightly retroverted angle) articulates with the scapula, the rounded capitellum articulates with the radius head and the bearing-like trochlea articulates with the ulna. Muscles attach to the humerus via the tuberosities and along the shaft.

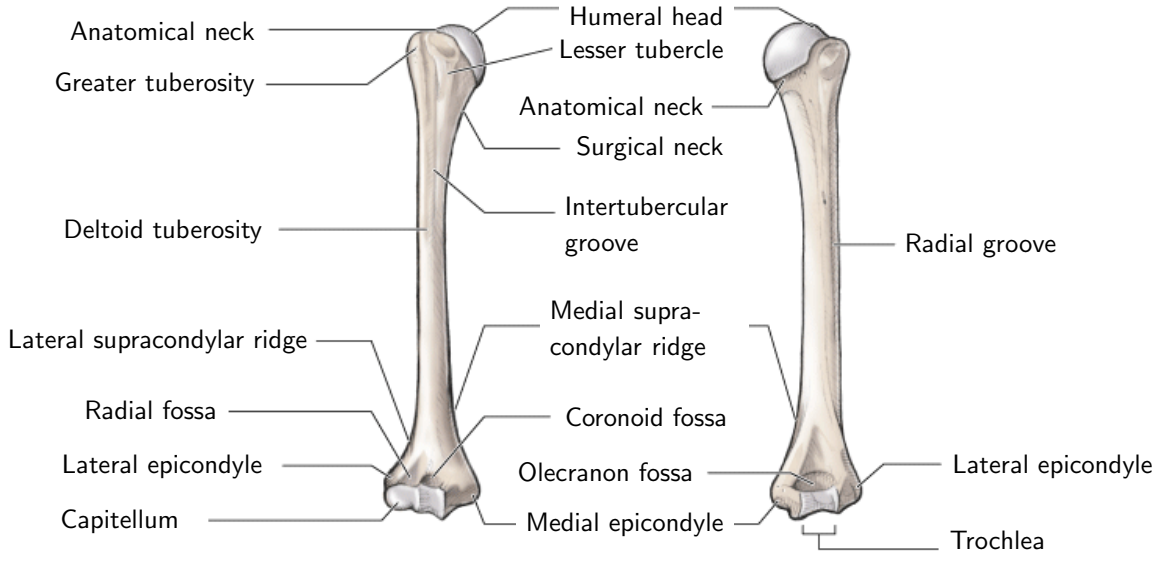

Figure A.5 The humerus (adapted from Morton et al. (2011))

Radius and ulna

The radius and ulna are both long bones that form the forearm (Figure A.6). The radius has a rounded proximal end and a broad distal end; whereas, the ulna has a broad proximal end and a narrowed distal end. In the anatomical position the radius is located lateral to the ulna. The elbow joint is formed by the articulation of the humerus with the radius and ulna at the articular fovea and trochlear notch, respectively. Additionally, the radius and ulna articulate with one another using the radial notch and ulnar head, and these articulations enable pronation and supination of the forearm.

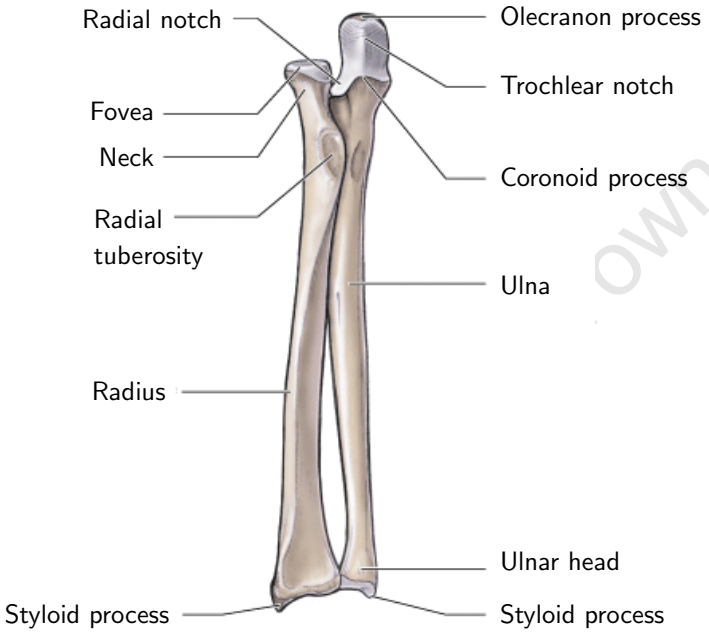

Figure A.6 The radius and ulna (adapted from Morton et al. (2011))

Joints and ligaments

Sternoclavicular joint

The sternoclavicular (SC) joint connects the sternal end of the clavicle to the manubrium of the sternum. The joint has three degrees of freedom (DOF) that allow for protraction-retraction, depression-elevation and axial rotation of the clavicle. It is surrounded by a capsule that is attached to the interclavicular ligament and the anterior and posterior sternoclavicular ligaments. The costoclavicular ligament extends from the superior aspect of the junction between the manubrium and the first rib to the inferior aspect of the medial clavicle and aids in joint stabilisation.

Acromioclavicular joint

The acromioclavicular (AC) joint connects the convex acromial end of the clavicle to the concave acromial process of the scapula (Figure A.7). The joint has three degrees of freedom that allows for protraction-retraction, medial-lateral rotation and anterior-posterior tilt of the scapula. It is contained within a capsule that is stabilised by the acromioclavicular ligament. The clavicle is further constrained with respect to the scapula by the coracoclavicular ligament. It extends from the coracoid to the inferior portion aspect of the lateral clavicle and has two components. The first is the lateral trapezoid that extends from the anterior aspect of the coracoid and the second is the medial conoid ligament that extends from the posterior aspect of the coracoid and attaches to the clavicle at the conoid tubercle.

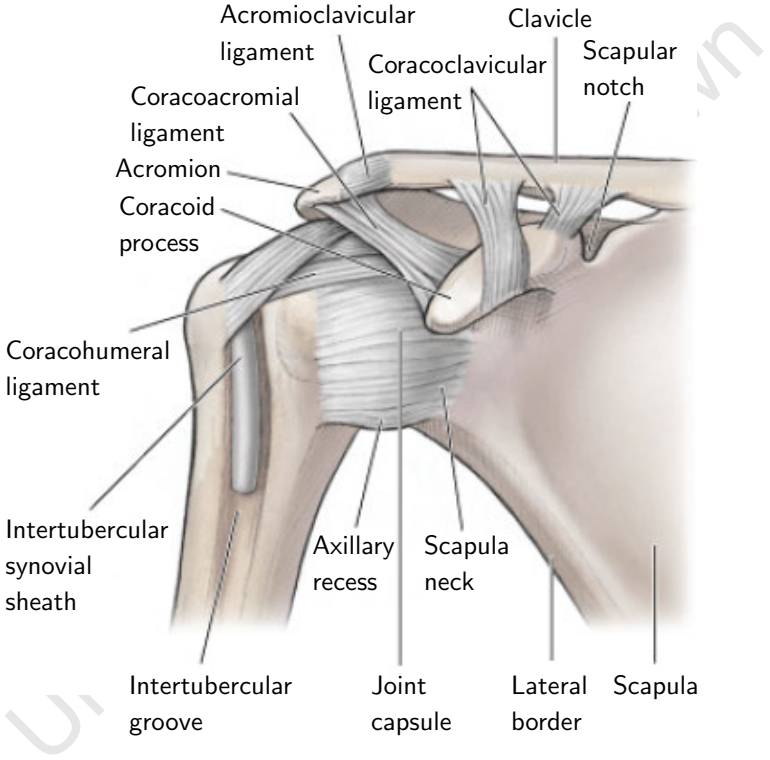

Figure A.7 The acromioclavicular and glenohumeral joints (adapted from Morton et al. (2011))

Scapulothoracic joint

The scapulothoracic joint (Figure A.8) is a non-standard joint in that it does not have any of the typical characteristics, such as containment within a capsule. The joint allows for articulation between the scapula and the posterior portion of thorax. This articulation is described as the gliding of the scapula on loose connective tissue between the serratus anterior and subscapularis muscles and occurs in response to articulation of the SC and AC joints.

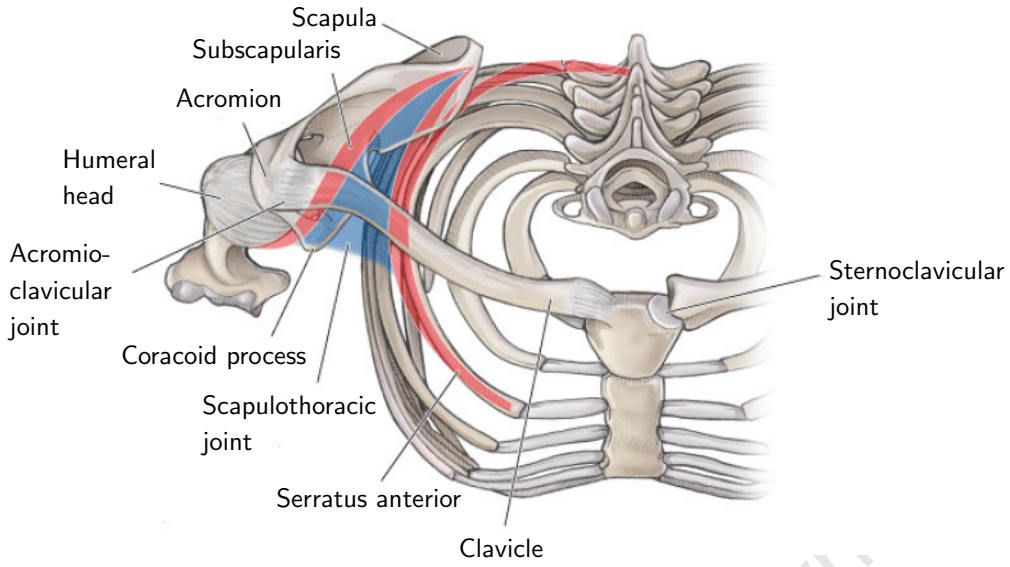

Figure A.8 The scapulothoracic joint (adapted from Morton et al. (2011))

Glenohumeral joint

The glenohumeral (GH) joint connects the convex humeral head to the concave glenoid fossa of the scapula (Figure A.7). It is a ball-and-socket type joint that has three rotational degrees of freedom that can produce abduction-adduction, flexion-extension and internal-external rotation (see Section A for further details). Due to the shallow, pear-shaped glenoid fossa and large humeral head, the GH joint is the most mobile (and consequently, least stable) joint in the human body that can migrate during upper arm motion. A fibrocartilaginous labrum covers the glenoid fossa and slightly deepens the socket. The joint and labrum are surrounded by a capsule that extends from the scapula to the anatomical neck of the humerus and which is supported by the glenohumeral ligament. The coracoacromial ligament, in conjunction with the acromial and coracoid processes, form an arch that restricts superior migration of the humeral head.

The muscles that cross the GH joint play a crucial role in not only mobility, but also stability (even more so than the capsule and ligaments). The rotator cuff muscles, which are discussed in further detail in Section A, are primary actuators and stabilisers of the joint. Finally, like the other joints in the body, bursae can be found between the capsule and muscles to help reduce friction during movement. These include the subacromial, subcoracoid, subscapular and subdeltoid bursae.

Muscles

Thoracic muscle group

The thoracic muscle group refers to the muscles that originate on the thorax and insert somewhere along the clavicle or scapula (Figure A.9). These include the trapezius, levator scapulae, rhomboid,

serratus anterior, subclavius and pectoralis minor muscles. The rhomboid, subclavius and pectoralis minor are entirely deep muscles, with the latter two not shown in Figure A.9.

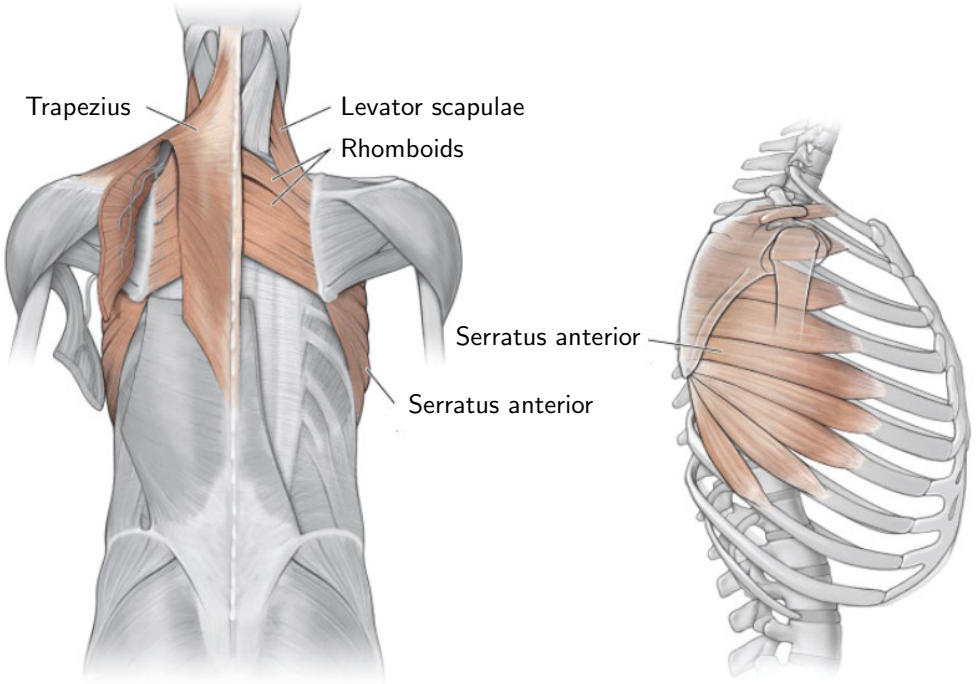

Figure A.9 The thoracic muscle group (adapted from Morton et al. (2011))

The trapezius is a broad muscle that inserts on the superior aspect of both the scapula and clavicle. Depending on where the muscle contracts it can either draw the scapula upward and superiorly rotates the glenoid fossa or draw the scapula medially. The levator scapulae inserts on the superior aspect of the scapula and elevates the scapula when it contracts. The rhomboid muscle inserts along the medial border of the scapula, helps to stabilise the scapula and can draw the scapula medially upward when contracted. The serratus anterior is a fan-like muscle that originates along the lateral aspect of the first to ninth rib and inserts along the anterior aspect of medial border. The entire muscle draws the scapula laterally forward, and the superior portion can assist in lowering the raised arm; whereas, the inferior portion can assist in scapula protraction. The subclavius and pectoralis minor muscles insert on the inferior aspect of the clavicle and coracoid process respectively. These muscles can both depress and protract the acromial end of the clavicle when contracted.

Glenohumeral muscle group

The muscles in the glenohumeral muscle group have broad origins, cross over the glenohumeral joint and taper to insert on the humerus (Figure A.10). These include the deltoid, pectoralis major and latissimus dorsi muscles. The deltoid originates along the anterior aspect of the acromial-end of the clavicle and along the acromion and scapular spine of the scapula. It inserts on the humerus at the deltoid tuberosity and is commonly subdivided into three parts: anterior, middle and posterior. The

anterior part can flex and internally rotate the humerus, the middle can abduct the humerus, and the posterior can extend and externally rotate the humerus. The pectoralis major originates along the anterior thoracic wall and the medial half of the clavicle and inserts at the crest of the greater tuberosity. The thoracic component of the muscle helps to adduct and internally rotate the humerus; whereas, the clavicular component plays a role in flexion. The latissimus dorsi originates from the spinous processes of the T7 to T12 vertebrae and inserts at the floor of the intertubercular groove of the humerus and assists during extension, adduction and internal rotation.

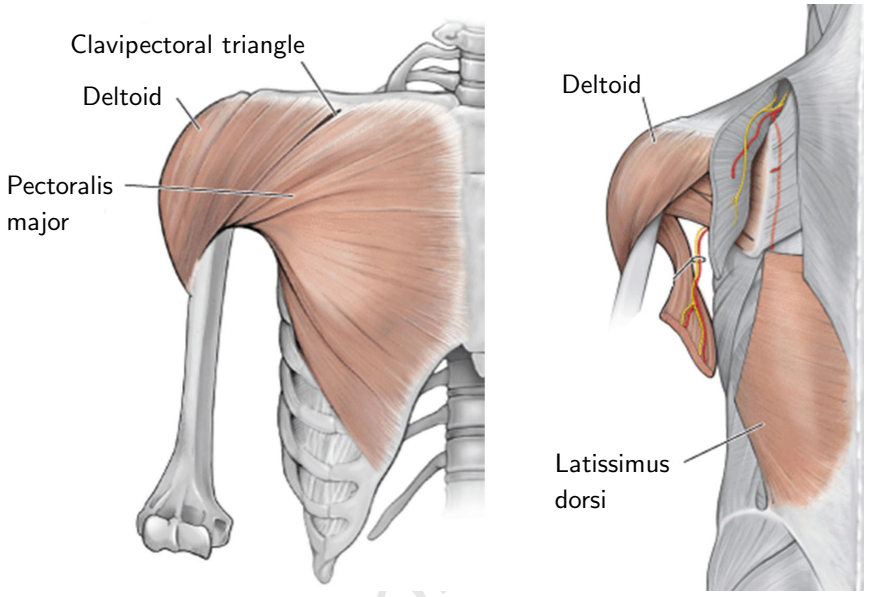

Figure A.10 The glenohumeral muscle group (adapted from Morton et al. (2011)). Anterior view (left) and posterior view (right)

Brachial muscle group

The brachial muscle group refers to the muscles that insert somewhere along the humerus or proximal forearm (Figure A.11). The rotator cuff, as mentioned previously, consists of the supraspinatus, infraspinatus, subscapularis and teres minor muscles. These originate at the scapula and encase the anterior, superior and posterior aspects of the humeral head. The supraspinatus plays a large role during abduction, the infraspinatus and teres minor aid in external rotation and the subscapularis aids in internal rotation. The teres major originates near the inferior angle and inserts at the crest of the lesser tuberosity. The muscle is active during internal rotation, adduction and extension. The coracobrachialis originates at the coracoid process and inserts in line with the crest of the lesser tuberosity; it aids in flexion, adduction and internal rotation.

The biceps brachii has a long head and a short head; the origin of the long head is the supraglenoid tubercle and the origin of the short head is the coracoid process. Both heads come together to insert at the radial tuberosity. With regards to the elbow joint, they are responsible for flexion and supination and with regards to the shoulder joint, they assist in abduction and internal rotation, and help to stabilise the joint during deltoid contraction. The triceps brachii has a long, medial and

lateral head. The origin of the long head is the infraglenoid tubercle and the origin of the medial and lateral head is the posterior humerus. These muscles come together to insert at the olecranon. With regards to the elbow joint, they are responsible for extension and, with regards to the shoulder joint, they assist in extension and adduction. Finally, the brachialis originates at the distal portion of the humerus, inserts at the ulnar tuberosity and helps flex the elbow joint.

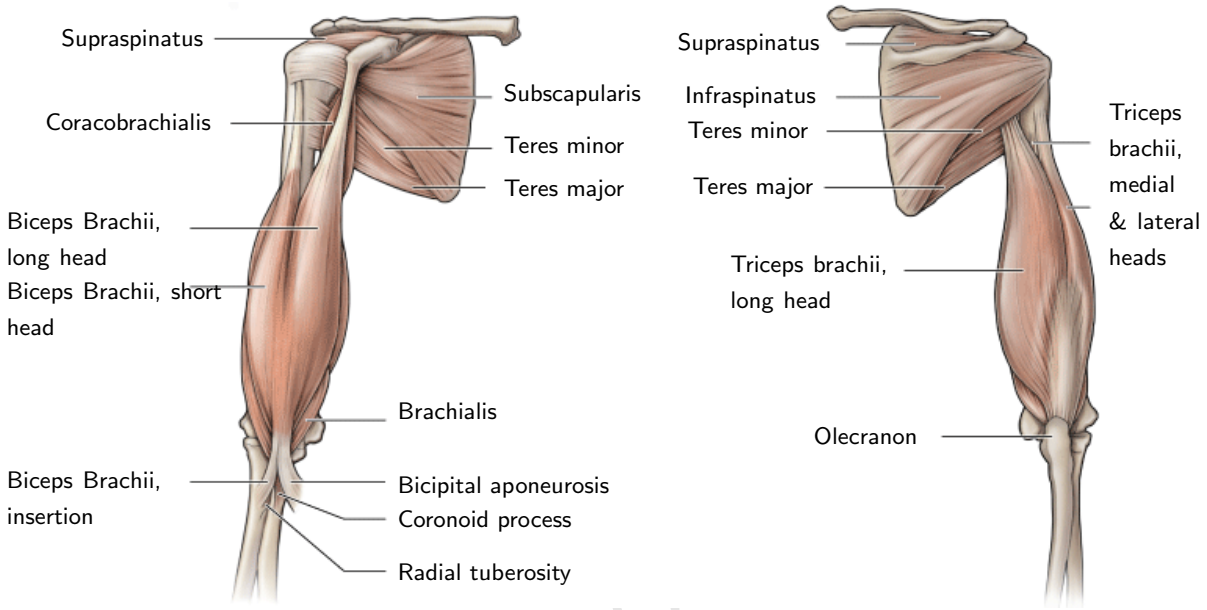

Figure A.11 The brachial muscle group (adapted from Morton et al. (2011)). Anterior view (left) and posterior view (right)

Function

The standardised motions of the humerus are shown in Figure A.12:

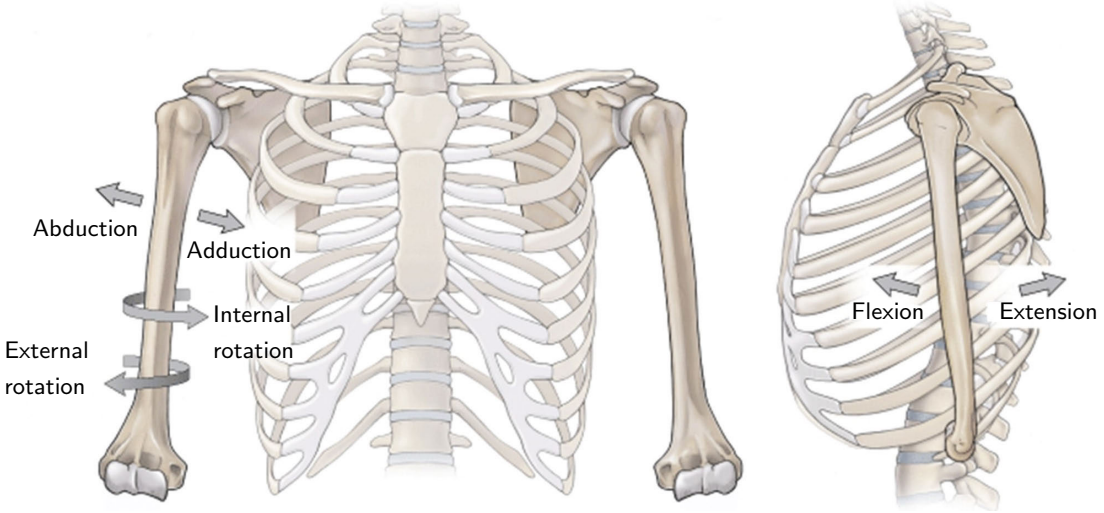

Figure A.12 Standardised humeral motions (adapted from Morton et al. (2011))

Gross movements of the shoulder are driven by the glenohumeral joint. As mentioned previously, it has 3 degrees of freedom joint that can produce abduction-adduction, flexion-extension and internal-external rotation. Abduction-adduction occurs in the coronal plane, where abduction refers to movement away from the body and adduction refers to a movement towards the body. Flexion-extension is a similar type of motion that occurs in the sagittal plane, where flexion refers to an anterior movement away from the body and extension refers to a posterior movement away from the body. Internal-external rotation occurs about the long axis of the humeral stem, where internal rotation refers to a twisting of arm in to the body and external rotation refers to a twisting of arm away from the body.

The elbow joint also performs two standardised motions, flexion-extension and pronation-supination (Figure A.13). Flexion refers to movement of the forearm towards the upper arm and extension refers to the opposite, except, in this instance, extension is limited by the olecranon fossa and process. Pronation refers to a twisting motion that directs the palm downwards and supination refers to a twisting motion that directs the palm upwards.

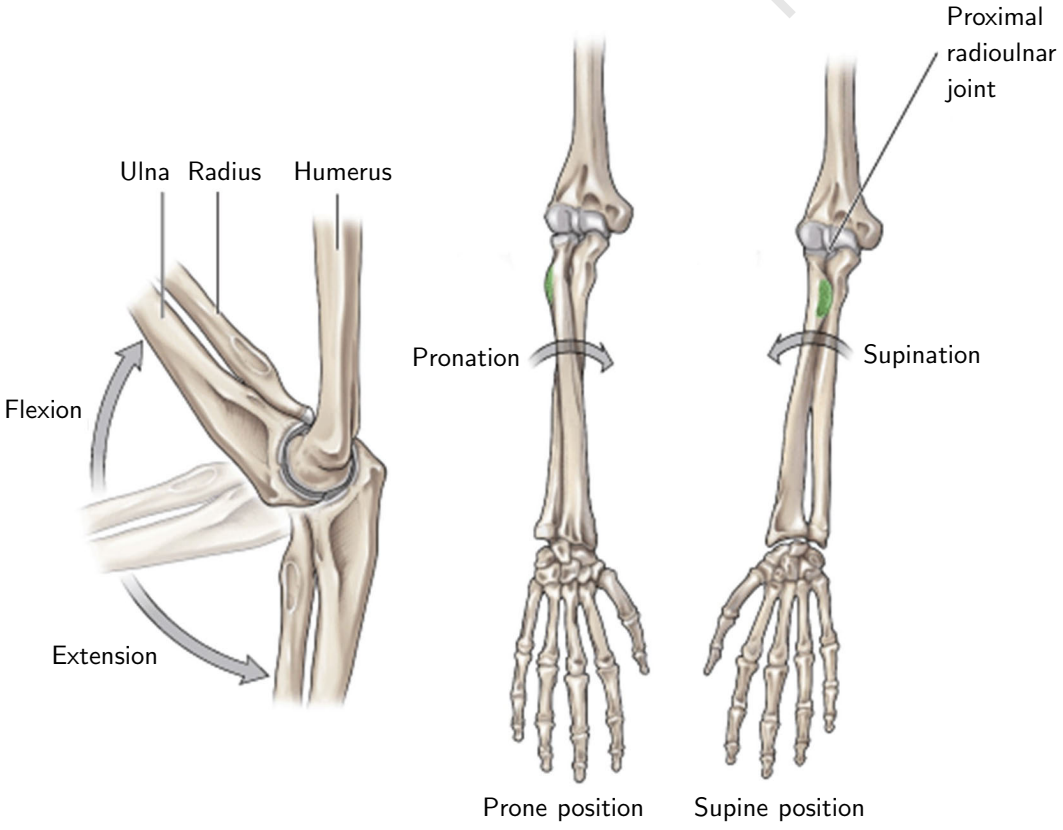

Figure A.13 Standard elbow motions (adapted from Morton et al. (2011))

Appendix B

Clinical Biomechanics manuscript

Preface

The observations of this manuscript are based upon the usage of the Biomet Comprehensive Reverse Shoulder System (Biomet, IN, USA), as opposed to the Delta XTEND Reverse Shoulder System (DePuy Synthes, IN, USA), which was used in the thesis. Consequently, the numerical results differ between the thesis and this manuscript. However, the antagonistic relationship between outcome measures was identified in both studies, and the overall effect of humeral tray placement on deltoid moment arms and impingement-free range of motion was consistent for both prosthesis designs. Therefore, the observations of this manuscript are complementary to those of Chapter 4.

Status

Under review (at time of thesis submission).

Title

Effect of humeral tray placement on impingement-free range of motion and muscle moment arms in reverse shoulder arthroplasty.

Authors

Jonathan Glenday[1], Andreas Kontaxis[2], Stephen Roche[3], Sudesh Sivarasu[1]

1. Department of Human Biology, University of Cape Town, South Africa
2. Leon Root Motion Analysis Laboratory, Rehabilitation Department, Hospital for Special Surgery, New York, NY, USA
3. Department of Orthopaedic Surgery, Groote Schuur Hospital, Cape Town, South Africa

Abstract

Background

It has been suggested that onlay humeral tray placement in reverse shoulder arthroplasty can affect impingement and muscle functionality. This study investigates biomechanical changes to the reversed shoulder using a variety of tray positional configurations.

Methods

The reconstructed scapula and humerus from 12 CT scans were used to customise a 3D biomechanical model of the shoulder. Each model underwent virtual RSA surgery using a commercially available prosthesis that was reconstructed from an explant. 17 tray positions were tested: the default location with no offset and 16 offset locations (2.5 and 5 mm radial offsets over 45° circumferential intervals). Impingement and muscle moment arms were measured during three standardised activities, and impingement was measured during an activity of daily living.

Findings

Offset direction was found to have an effect ($P < 0.05$) on impingement and muscle moment arms for all activities; whereas, offset distance did not ($P > 0.05$). Overall, impingement-free range of motion was maximised using a posterolateral tray offset and muscle moment arms were maximised using a medial tray offset. An antagonistic relationship between changes to impingement and muscle moment arms due to tray placement was identified and, consequently, the simultaneous maximisation of both outcome measures was not possible

Interpretation

The functional outcomes of reverse shoulder arthroplasty can be improved by altering onlay humeral tray placement. Due to the antagonistic relationship between the impingement and muscle moment arms, placement of the tray should be guided by patient-specific characteristics.

Introduction

Reverse shoulder arthroplasty (RSA) has become an established solution for alleviating pain and restoring shoulder functionality to patients with massive rotator cuff tears or rotator cuff arthropathies (Grammont and Baulot 1993; Sirveaux et al. 2004; Frankle et al. 2005; Boileau et al. 2006). The prosthesis medialises the glenohumeral joint's centre of rotation and distalises the humerus (Boileau et al. 2005). These modifications change the biomechanics of the glenohumeral joint by reversing the envelope of contact forces providing stability (Kontaxis and Johnson 2009). One of the main effects of RSA is that it increases the deltoid muscle moment arm, allowing it to compensate for the absent rotator cuff during movements that require abduction or flexion (Boileau et al. 2005; Kontaxis and Johnson 2009; Ackland et al. 2010).

However, many clinical studies have reported several complications after long term use of RSA (Frankle et al. 2005; Guery et al. 2006; Wall et al. 2007; Gallo et al. 2011). Two such drawbacks are scapular notching and limited internal/external rotation range of motion. It is suggested that scapular notching could be a result of the impingement of the polyethylene cup with the scapula, described as intra-articular impingement (Sirveaux et al. 2004; Nyffeler et al. 2005; Simovitch et al. 2007). Recent studies have shown that impingement can also occur between the tuberosity and the acromion or coracoid process (described as extra-articular impingement) when the humerus is abducted (Kontaxis et al. 2017). In general, impingement reduces range of motion and has been shown to cause polyethylene wear, joint inflammation and potential implant loosening (Nicholson et al. 2011).

Previous studies have investigated the effect of altering glenoid parameters, such as, glenosphere lateralisation and glenoid baseplate placement (Gutiérrez et al. 2008b; Chou et al. 2009; De Wilde et al. 2010; Henninger et al. 2012b; Berhouet et al. 2014b; Clouthier et al. 2013; Costantini et al. 2015; Langohr et al. 2015). However, these design alterations focused primarily on the glenoid site, neglecting the humerus. Recently, it has been shown that humeral parameters such as neck-shaft angle, cup size and onlay versus inlay placement can affect impingement and internal-external rotation range of motion (Gulotta et al. 2012; Berhouet et al. 2014b; Berhouet et al. 2014a; Kontaxis et al. 2017). In addition, the inlay humeral tray found in the original Grammont-style prosthesis has been replaced by an onlay humeral tray in recent designs to accommodate for the potential conversion from a total shoulder arthroplasty to a reverse shoulder arthroplasty.

A biomechanical study by Berhouet et al. (2014a) investigated the effect of onlay humeral tray placement on RSA impingement and the moment arms of the deltoid and rotator cuff muscles. However, this study used a limited number of tray positional setups and was unable to account for anatomical variability as it utilised only one subject. The aim of this biomechanical study is to enhance our understanding of the effect of onlay humeral tray placement on impingement and the muscle moment arms of the deltoid and rotator cuff using a cohort of specimens and a variety of tray positional configurations.

Methods

Shoulder CT Data

Computed tomography (CT) scans of 12 shoulders (2 left, 10 right) were acquired from 4 female and 8 male subjects (average age 59.1 $\pm$ 14.0 years old and BMI 23.6 $\pm$ 4.4). Seven of the subjects were healthy and 5 were diagnosed with primary osteoarthritis (OA) by an orthopaedic surgeon. The raw CT data were imported into the Mimics software (Materalise, Leuven, Belgium) and 3D bony geometries were reconstructed.

During the data collection process, the native version and tilt of the glenoid of each subject were determined. Version was calculated from bony landmarks found in the plane defined by the centre of the glenoid fossa, medial border of the scapular spine and the inferior angle (Friedman et al. 1992). Similarly, tilt was calculated from bony landmarks found in a plane defined by the angle formed by the intersection of the line between the centre of the glenoid fossa to the medial border and the line between the points defining the inferior and superior glenoid rim.

Biomechanical computer model

A 3-dimensional (3D) biomechanical model, the Newcastle Shoulder Model (NSM), was used in this study (Charlton and Johnson, 2006). In its original state, the model represents a normal shoulder that consists of six rigid bony segments (thorax, clavicle, scapula, humerus, radius and ulna) and includes 31 muscles and 3 ligaments that are divided into 90 lines of action (Johnson et al. 1996; van der Helm 1996). The model can simulate scapula-thoracic and clavicle kinematics based on regression equations that were derived from measurements of healthy subjects (Barnett et al. 1999; Marchese and Johnson 2000).

The shoulder CT data were used to customise the glenohumeral joint of the NSM. The model's original humerus and scapula were replaced with the corresponding bony geometries of each subject. The origin and insertion sites of the muscles were also modified to reflect the specific bony landmarks of each specimen. The OpenSim software (Stanford University, Stanford, CA, USA) was used to visualise the 12 individual models and to calculate muscle moment arms over a predefined motion using the tendon-excursion method (Delp et al. 2007; Sherman et al. 2013).

RSA shoulder model - virtual surgery

Following previous methodology of adapting the NSM to describe RSA geometry (Costantini et al. 2015), virtual surgery was performed on all 12 customise models using a commercial RSA design (Comprehensive Reverse Shoulder System. Biomet, Inc., Warsaw, IN, USA). The 3D model of the prosthesis was created from a retrieved implant that had been laser scanned (NextEngine 3D Laser Scanner; NextEngine, Santa Monica, CA, USA).

The surgery and placement of the RSA components were performed in Mimics and, to replicate surgical best practice, any osteophytes present on the glenoid rim and the humeral head were resected prior to prosthesis implantation. As per the recommendations of (Kelly et al. 2008) the glenoid baseplate was implanted 12 mm superior to the inferior glenoid rim. To ensure that the glenoid baseplate was implanted with in a neutral (0°) orientation, the native glenoid version and tilt were corrected. The baseplate was placed in neutral (0°) version and tilt. Following the manufacturers guidelines, the humeral head was resected at the anatomical neck using a neck-shaft angle of 135°, and the stem was inserted at 20° of retroversion (Fig. B.1(a), Gulotta et al. (2012)).

The subscapularis and infraspinatus muscles were modelled with three lines of action representing the superior, middle and inferior bands of the muscles respectively. The superior and middle bands of both muscles, along with the supraspinatus, were excluded from the models to replicate typical post-surgical status of the rotator cuff (Fig. B.1(b)).

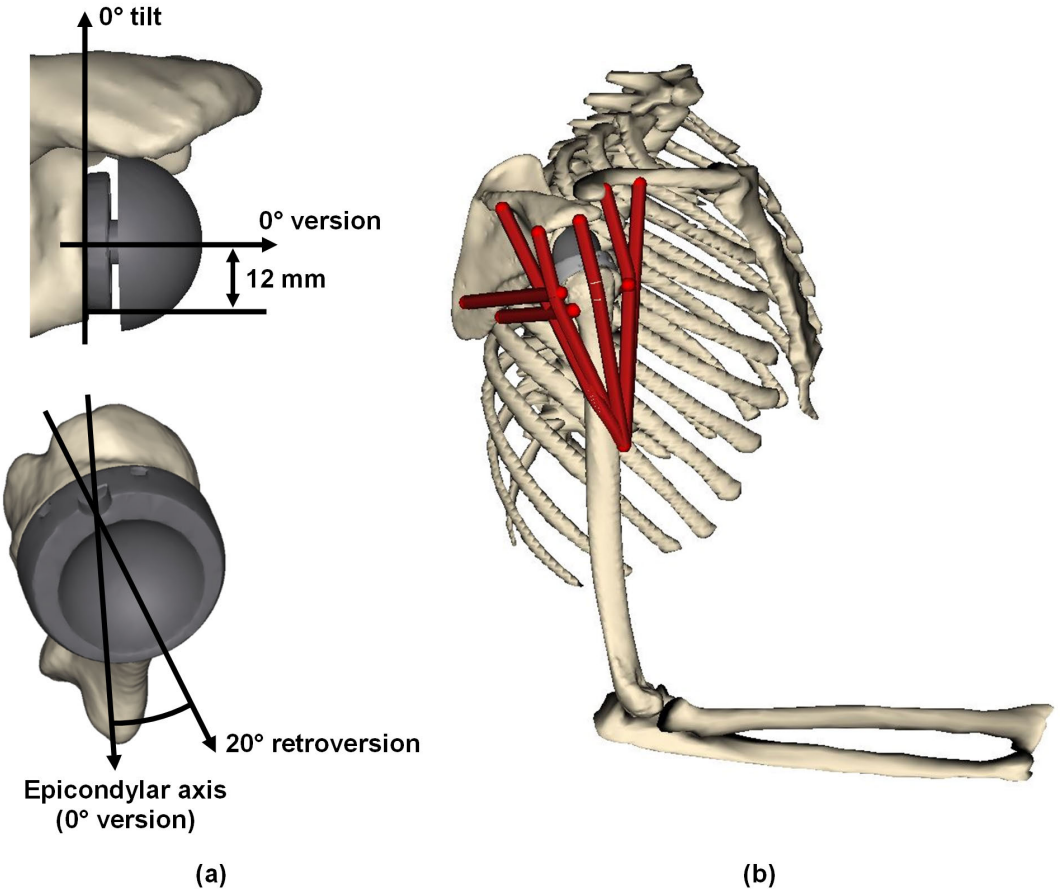

Figure B.1 (a) The placement of the Biomet Comprehensive Reverse Shoulder System after virtual surgery. **(b)** Post-surgical status of the rotator cuff and deltoid muscles

Humeral tray placement

Seventeen humeral tray placements for each model were simulated: one default location and 16 offset locations. Eight offset directions, equally distributed along the circumference of 2 circles (with 2.5 and 5 mm radii), were used to establish the 16 modified locations (Fig B.2(a)). The offset directions included: lateral (L), posterolateral (PL), posterior (P), posteromedial (PM), medial (M), anteromedial (AM), anterior (A) and anterolateral (AL). Fig. B.2(b) uses a 5 mm anteromedial offset to demonstrate the effect of tray offset. The placement of the stem was not affected by tray offset.

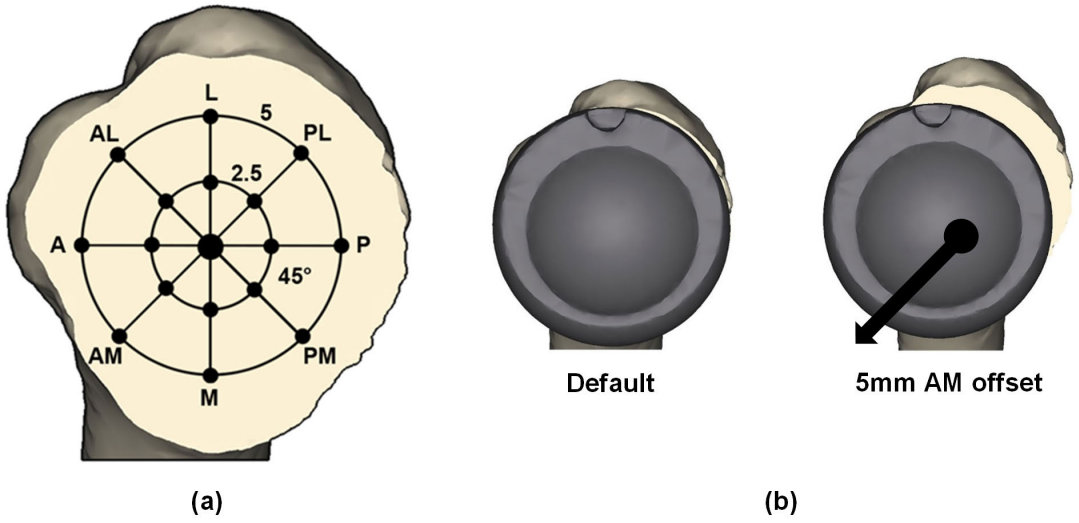

Figure B.2 (a) Humeral tray offset locations projected on to a resected humeral head. The central dot represents the default location of the stem-bearing interface and acts as a reference point for the offset locations. **(b)** A comparison between the default location and the 5 mm anteromedial offset location. The black dot represents the location of the stem-bearing interface and the arrow indicates the offset direction

Motions assessed

Four motions, each with a 1° resolution, were assessed in this study; three standardised motions and one activity of daily living (ADL):

1. Abduction - humeral elevation from 0° to 150° in the frontal plane
2. Forward flexion - humeral elevation from 0° to 150° in the sagittal plane
3. Humeral rotation with the humerus at 90° of abduction:
   (a) Internal rotation from 0° to 60°
   (b) External rotation from 0° to -90°. As per the International Society of Biomechanics recommendations,, external rotation is negative and internal rotation positive (Wu et al. 2005).

4. ADL - reaching for an object at head height. The kinematic data of this motion were retrieved from a previous study in which healthy subjects were recorded performing ADLs with a motion capture system (Murray and Johnson 2004)

Outcome measures

Two outcomes were measured during the study: (1) impingement-free range of motion (IFROM) and (2) moment arms of the deltoid, teres minor and intact infraspinatus and supraspinatus.

Impingement-free range of motion

A custom-made MATLAB (MathWorks, Natick, MA, USA) algorithm was used to detect any graphical overlaps between the scapula and the humeral cup or humerus. These graphical overlaps are representative of locations of impingement during a given motion and the algorithm does not influence the kinematic profiles of the assessed motions. IFROM was calculated as the amount of motion unobstructed by both intra- and extra-articular impingement.

Muscle moment arms

The muscle moment arms of the deltoid and intact rotator cuff were calculated using OpenSim's tendon-excursion method. The abductive moment arm of the deltoid was measured during abduction and forward flexion. The internal rotation moment arm of the subscapularis was measured during internal rotation, and the external rotation moment arm of infraspinatus and teres minor were measured during external rotation.

Data analysis

IFROM data were assessed by calculating the subject-averaged change in IFROM for each motion at each of the 16 offset locations (2.5 and 5 mm offset distances and the eight offset directions: L, PL, P, PM, M, AM, A and AL). Similarly, the moment arm data of each muscle were assessed by calculating the subject-averaged mean change between each offset and the default configuration.

The effect of offset distance and offset direction on IFROM and muscle moment arms were measured using two one-way analysis of variance (ANOVA) tests, with Bonferroni pair-wise comparison. The offset distance ANOVA test, for a given outcome measure, used all the data at a given distance. Whereas, the offset direction ANOVA test used all the data in each direction. A difference was considered significant when $P < 0.05$.

To concisely represent the data collected, IFROM and moment arm heat maps were generated. These used the subject-averaged data ate each offset distance and offset direction to interpolate all possible changes within the 5 mm circular region of interest.

Results

Impingement-free range of motion

The occurrence of intra-articular impingement was not affected by humeral tray offset for the assessed motions. However, the occurrence of extra-articular impingement was affected by humeral tray offset and was dependent on the motion assessed. For example, during abduction, the average IFROM (across all subjects) increased by 4.0 % $\pm$ 1.5 % and 6.7 % $\pm$ 3.2 % when the 2.5 and 5 mm lateral tray offsets were implemented respectively. Whereas, during forward flexion, the average IFROM increased by 2.4 % $\pm$ 3.2 % and 4.3 % $\pm$ 6.1 % when the same tray offsets were implemented. A summary of the IFROM percentage changes for each motion is shown in Fig. B.3.

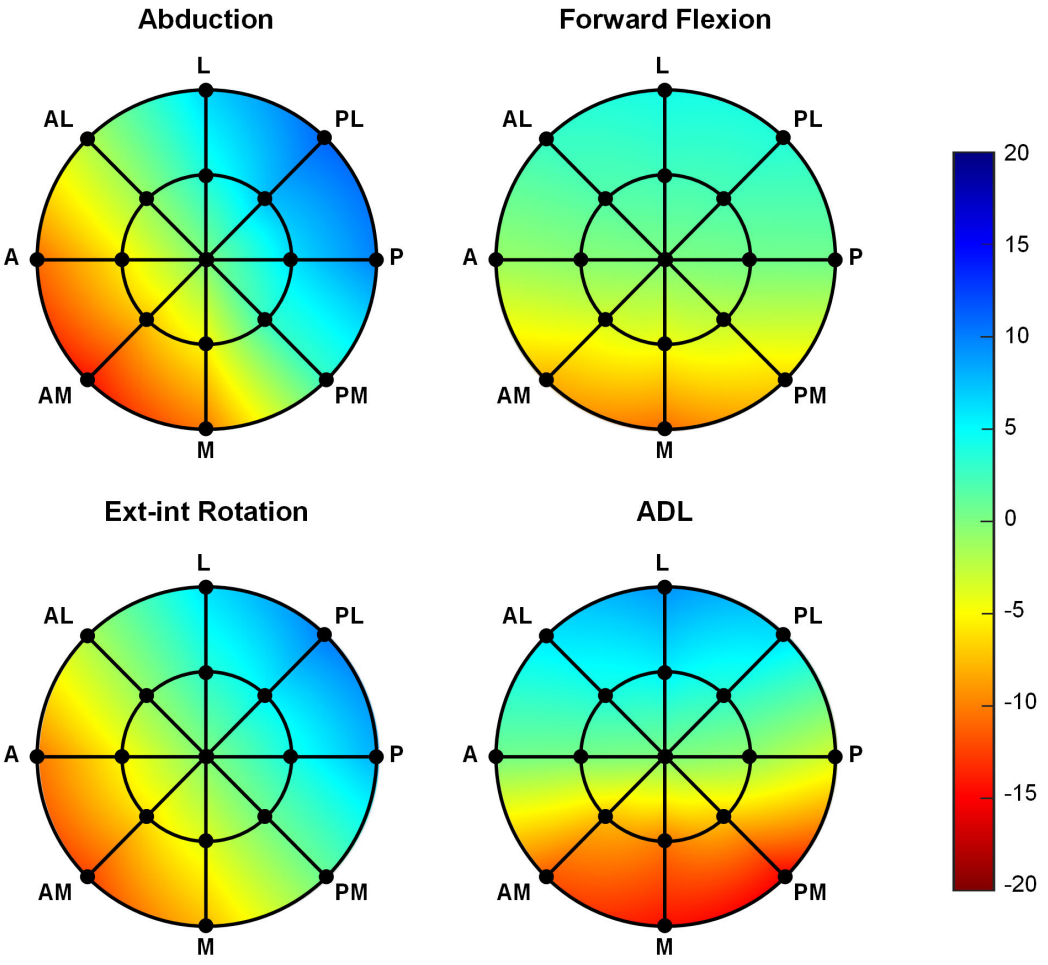

Figure B.3 Percentage change in impingement-free range of motion relative to the default configuration

The offset distance (2.5 and 5 mm) did not show significant differences ($P > 0.05$) for all motions, whereas, the offset direction was found to affect the IFROM results significantly ($P < 0.05$) for all motions. The highest increases in IFROM at the 2.5 mm offset were: 7.6 % ± 5.9 % for abduction (posterolateral offset), 2.4 % ± 3.2 % for forward flexion (lateral offset), 5.5 % ± 2.6 % for rotation (posterior offset) and 5.5 % ± 9.5 % for the ADL (lateral offset). Decreases in IFROM due to humeral tray offset were observed in diametrically opposite locations to those that increased IFROM (Fig. B.3).

Muscle moment arms

Muscle moment arms were affected by humeral tray offset. This effect was dependent on the muscle and motion assessed. For example, during internal rotation, the mean subscapularis moment arm (across all subjects) increased by 5.8 % ± 0.8 % and 11.4 % ± 1.6 % when the 2.5 mm and 5 mm posteromedial tray offsets were implemented respectively. Whereas, during external rotation, the mean teres minor moment arm decreased by 2.0 % ± 1.7 % and 4.0 % ± 2.8 % when the same tray offsets were implemented. The summarised muscle moment arm percentage changes for each motion are shown in Fig. B.4.

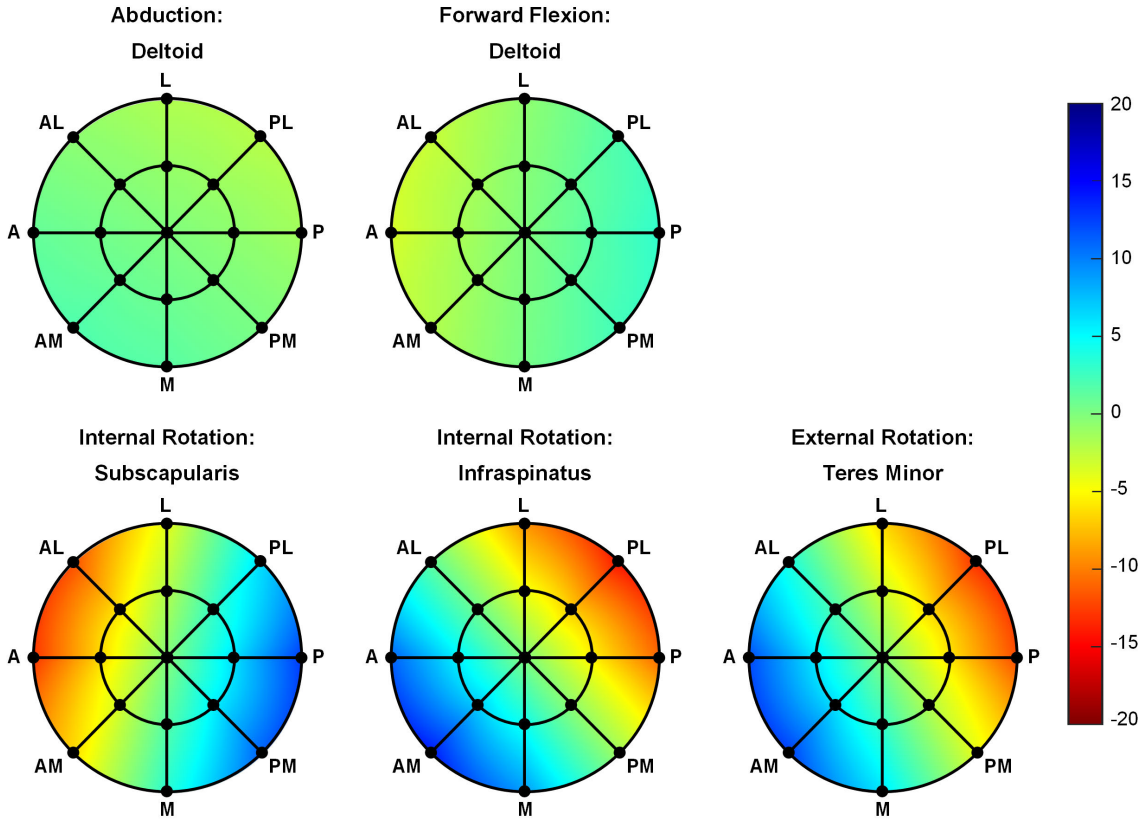

Figure B.4 Percentage change in mean muscle moment arms during the assessed motion relative to the default configuration

The choice of offset distance was found to not affect the muscle moment arms significantly ($P > 0.05$) for all motions, whereas, the choice of offset direction showed significant differences ($P < 0.05$) for all motions. The highest mean increase in middle deltoid moment arm during abduction and forward flexion, at the 2.5 mm offset, was found to be 1.0 % $\pm$ 0.4 % (anteromedial offset) and 1.6 % $\pm$ 0.4 % (posterior offset) respectively. In contrast, the highest mean increases in moment arm for the rotator cuff muscles at the 2.5 mm offset were 6.4 % $\pm$ 0.6 % for the subscapularis (posterior offset), 7.1 % $\pm$ 0.7 % for the infraspinatus (anteromedial offset) and 6.4 % $\pm$ 0.7 % for the teres minor (anteromedial offset). As with IFROM, decreases in the moment arms due to humeral tray offset were observed in diametrically opposite locations to those that increased the moment arms (Fig. B.4).

Task-averaged outcome measures

The task-averaged IFROM and muscle moment arm results are shown in Fig. B.5. At the 2.5 mm offset distance, the posterolateral offset had the greatest beneficial effect on IFROM (4.6 % $\pm$ 2.5 % increase). This offset simultaneously decreased muscle moment arms by 2.1 % $\pm$ 4.6 %. At the same offset distance, the medial offset had the greatest beneficial effect on muscle moment arms (2.1 % $\pm$ 1.7 %), whilst also decreasing IFROM by 5.9 % $\pm$ 2.9 %.

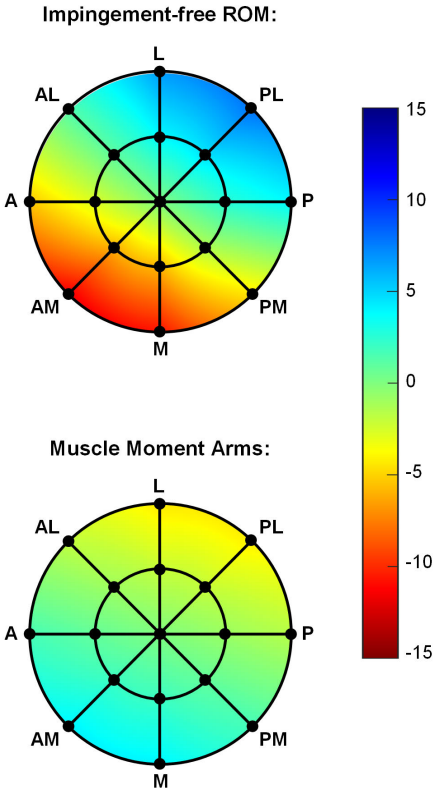

Figure B.5 Task-averaged percentage change in impingement-free range of motion (top) and muscle moment arms (bottom)

Discussion

The results of our study have shown that altering the position of the onlay humeral tray influenced both impingement and muscle moment arms of the reversed shoulder. These changes were specific to the motion assessed and the direction of the tray offset. Changes were also found not to be affected by the tray offset distance (2.5 and 5 mm). A smaller offset distance can reduce humeral tray overhang, which can cause soft tissue impingement (Berhouet et al. 2014a).

Tray location alters the position of the humerus relative to the tray. Despite the change, intra-articular impingement was not affected by tray offset as the position of the cup did not change relative to the glenosphere or to the inferior scapular neck, which is the most frequent site of intra-articular impingement (Sirveaux et al. 2004; Nyffeler et al. 2005; Simovitch et al. 2007). In contrast, extra-articular impingement was affected by tray offset, as the modification altered humeral position. Depending on the offset position utilised, the humerus was either moved away from or towards the acromion or coracoid process when the arm is elevated (Fig. B.6).

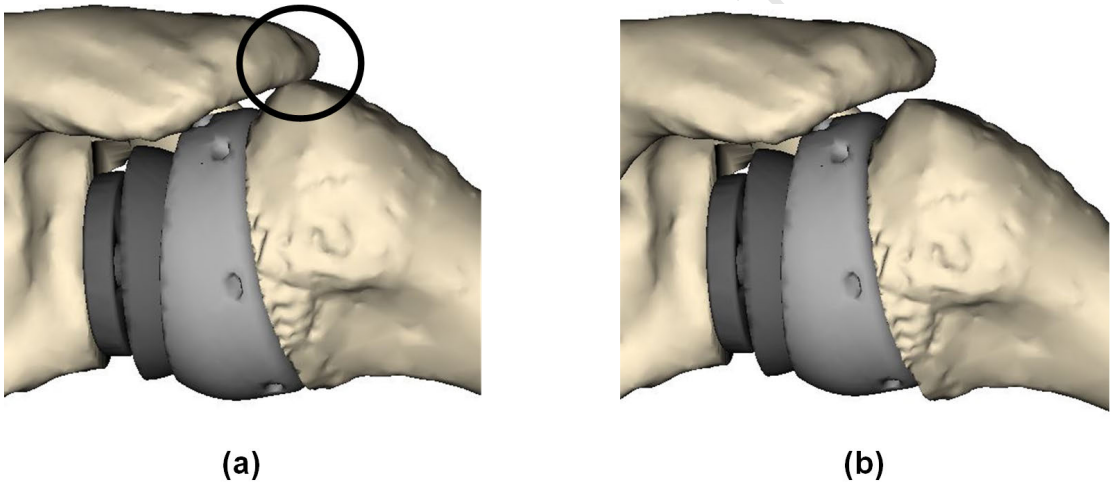

Figure B.6 Humeral position during abduction with **(a)** the default humeral tray placement and **(b)** a 2.5 mm laterally offset humeral tray. Note that in **(b)** contact between the humerus and acromion has not yet been made for the same elevation angle

Altering the position of the humerus also influenced muscle moment arms as it changed the muscle path. Rotator cuff muscles insert closer to the centre of rotation of the humeral head than the deltoid. Consequently, rotator cuff moment arms were more sensitive to small changes in tray offsets than deltoid moment arms (Fig. B.5).

The results of this study agree with previously published data from Berhouet et al. (2014a). They also acknowledged the conflicting nature of impingement and muscle moment arms. They concluded that, while a lateral offset would have the greatest effect on impingement, a posterior offset would have the greatest effect on muscle moment arms. Their work, however, was limited as only a single subject was used and four offset directions (lateral, posterior, medial and anterior) placed along a single offset distance (5 mm) were assessed. Therefore, they were unable to account

for anatomic variability, offset distance or intermediate offset directions (e.g. a posteromedial offset), all of which included in this study.

This study has limitations that need to be taken into consideration when interpreting the results. A combination of healthy and OA cohorts was used. The limited number of the two cohorts makes it difficult to identify whether OA and glenoid erosion influenced the results. In general, subjects with OA required more reaming to achieve neutral version and were inserted with glenoid baseplates that were more medialised than the healthy subjects, but it is unclear whether tray placement affected the healthy or OA subjects differently. The kinematic data used on this investigation were taken from a study that recorded a healthy population (Barnett et al. 1999; Marchese and Johnson 2000) but RSA subjects are known to have altered joint kinematics, for example, altered scapula-thoracic motion (Kontaxis and Johnson 2008; Kwon et al. 2012). Future investigations should look to incorporate abnormal joint kinematics into the analysis.

One of the limitations of this study was that a single retroversion angle of 20° was used during the humeral resection. This humeral retroversion has been suggested to be a compromise between range of motion and muscle moment arms (Gulotta et al. 2012; Berton et al. 2015). Additionally, only one activity of daily living was assessed during this study. It has been shown that maximising IFROM in standardised activities (such as abduction or forward flexion) does not minimise impingement in ADLs (Kontaxis et al. 2017). Therefore, it is important that future studies of tray placement include a variety of ADLs to provide a more comprehensive understanding of the effect humeral tray placement.

The task-averaged results highlighted the locations that had net improvements for impingement and moment arms. Decreases in impingement were observed in offsets that had a medialising effect on the humerus (lateral, posterolateral and posterior tray offsets) and, thereby, shifted the humerus away from the acromion or coracoid process. Whereas, increases in muscle moment arms were observed in offsets that had a lateralising effect on the humerus (medial, anteromedial and anterior offsets). From this observation (Fig. B.6) it is evident that improvements of impingement-free range of motion and muscle moment arms due to tray placement are antagonistic. This antagonistic relationship should be taken into consideration during the selection process of onlay humeral tray placement. If a patient has a partially intact rotator cuff, a surgeon may opt for a reduction in muscle moment arms to maximise IFROM. Whereas, if a patient has a massive rotator cuff tear, a surgeon may opt for a reduction in IFROM to maximise the moment arms of any remaining cuff muscles.

Conclusion

This study has highlighted that onlay humeral tray offsets can improve either impingement-free range of motion or muscle moment arms and that intermediate tray offsets have the potential to maximise this effect. Due to the antagonistic relationship between these two measures, the maximisation of both properties simultaneously is not possible. Therefore, this may necessitate an approach to the implementation of onlay tray placement modifications that is driven by patient-specific characteristics.

Appendix C

Additional muscle forces evaluated during the assessment of muscle fatigue

The additional muscle forces evaluated during the assessment of muscle fatigue are shown in Figures C.1 to C.9. These figures follow the same style convention used for the muscle force plots in Chapter 6. The black lines indicate the default configuration, the red lines indicate the optimised configuration, solid lines indicate the fatigable muscles and dotted lines indicate the non-fatigable muscles. Each figure represents the muscle forces generated for one of the motions (ABD, FF and SPE) held at a humeral elevation angle (30°, 60° and 90°). The muscle forces of the clavicular trapezius (Clav. Trap), scapular trapezius (Scap. Trap.), serratus anterior (Serr. Ant.), latissimus dorsi (Lat. Dorsi), clavicular pectoralis major (C. Pec. Maj), thoracic pectoralis major (T. Pec. Maj), teres minor (T. Min), teres major (T. Maj), coracobrachialis (Cbrac.), biceps short head (Bic. Short) and triceps.

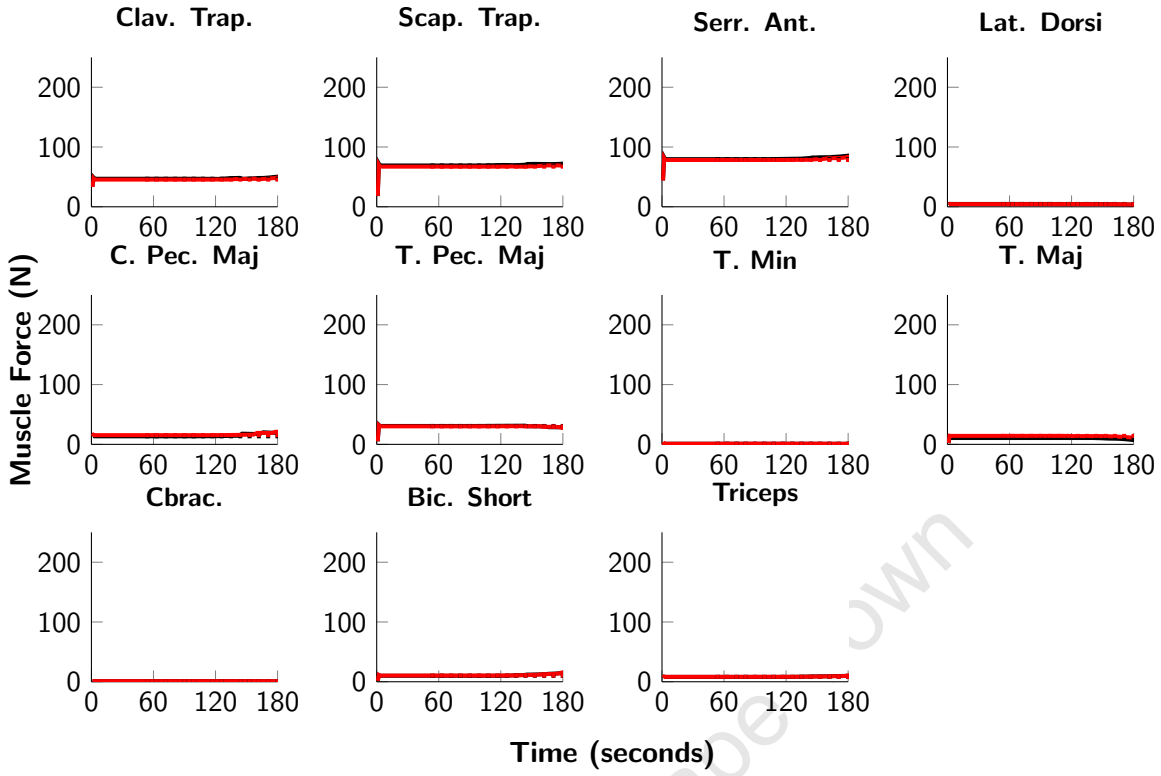

Figure C.1 Subject-averaged muscle forces during ABDh at 30° of humeral elevation

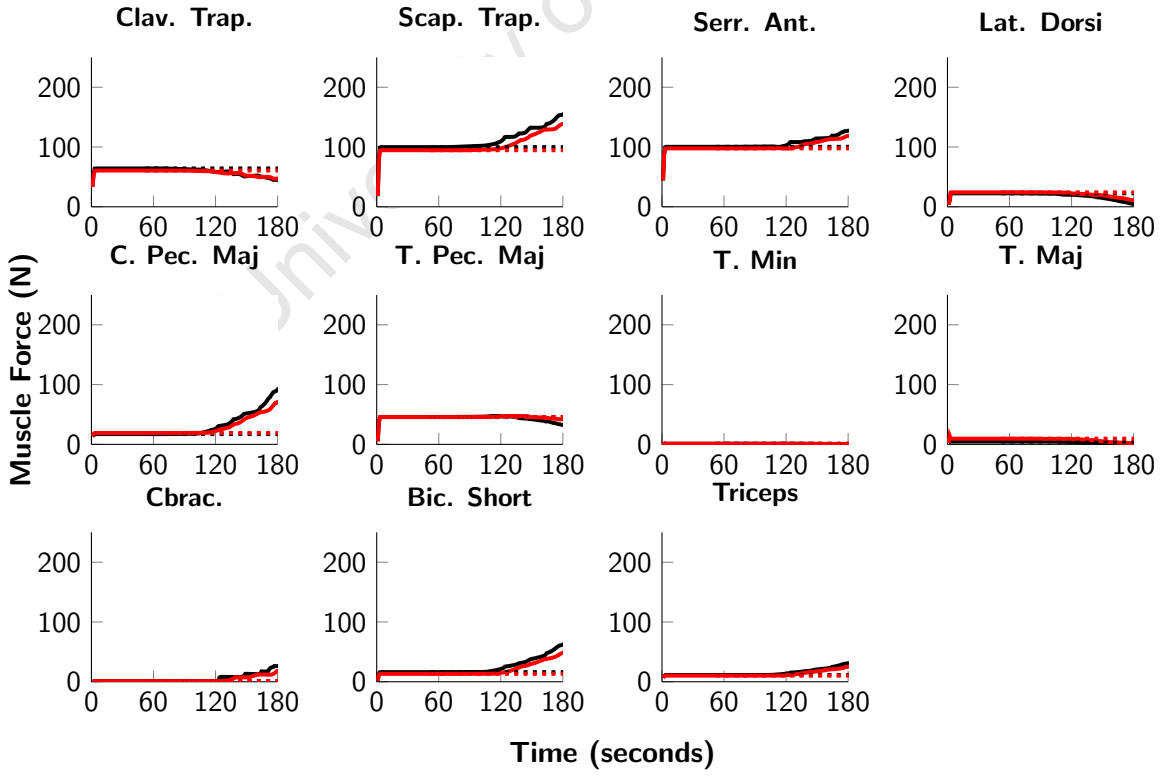

Figure C.2 Subject-averaged muscle forces for ABDh at 60° of humeral elevation

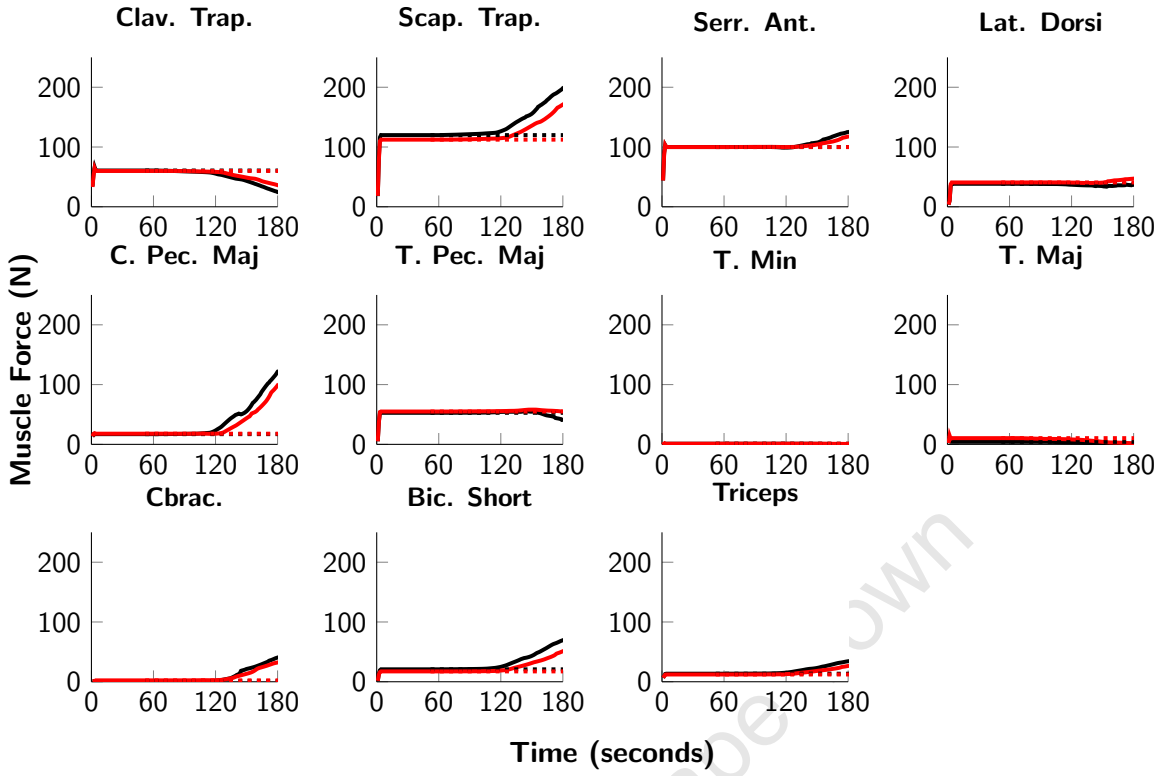

Figure C.3 Subject-averaged muscle forces for ABDh at 90° of humeral elevation

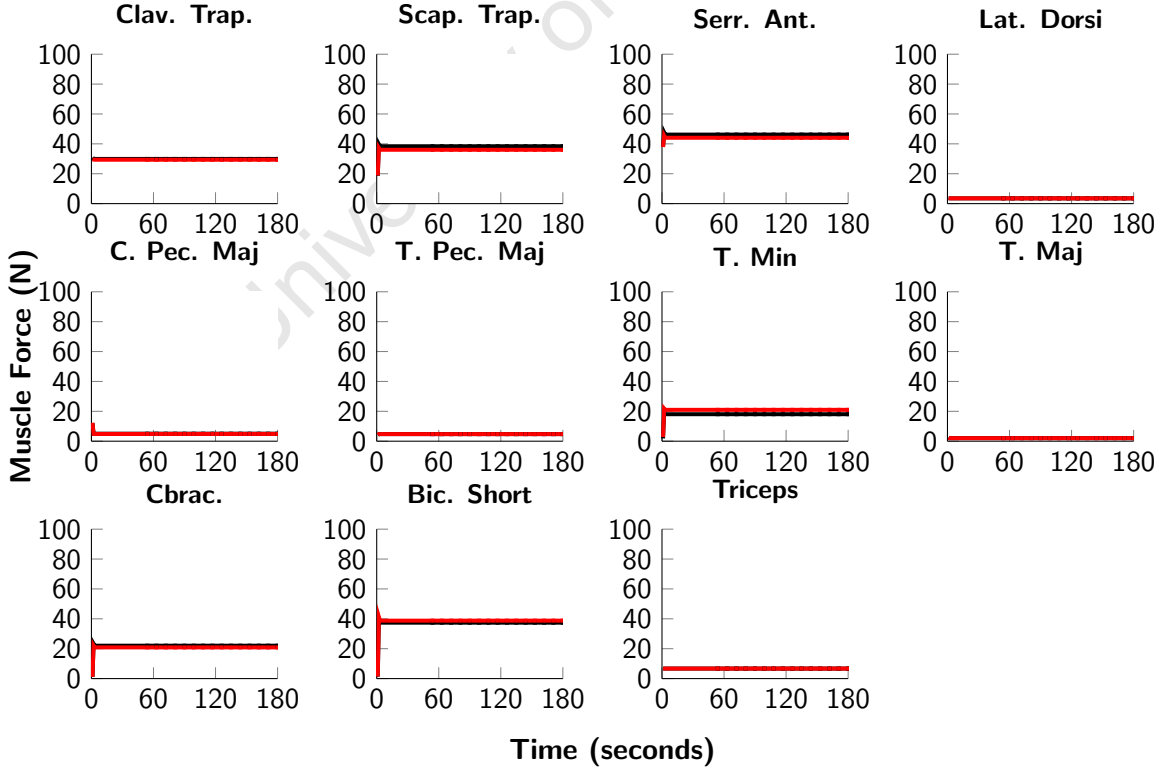

Figure C.4 Subject-averaged muscle forces for FFh at 30° of humeral elevation

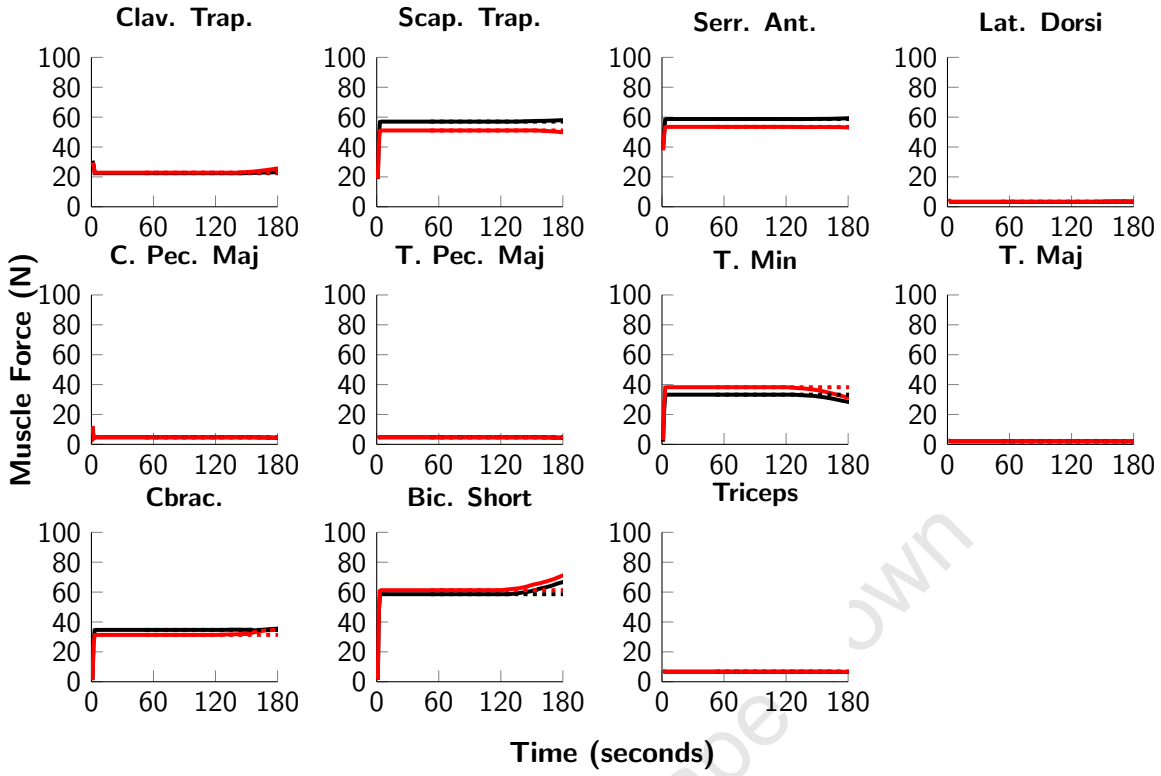

Figure C.5 Subject-averaged muscle forces for FFh at 60° of humeral elevation

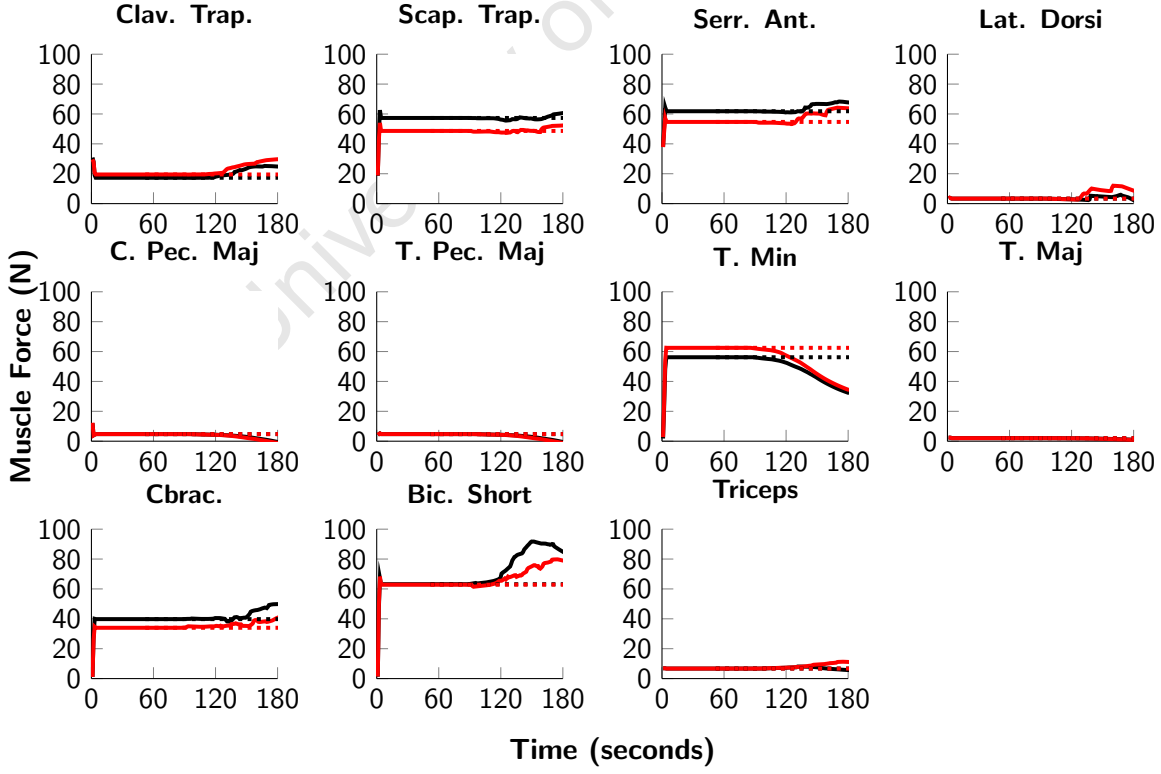

Figure C.6 Subject-averaged muscle forces for FFh at 90° of humeral elevation

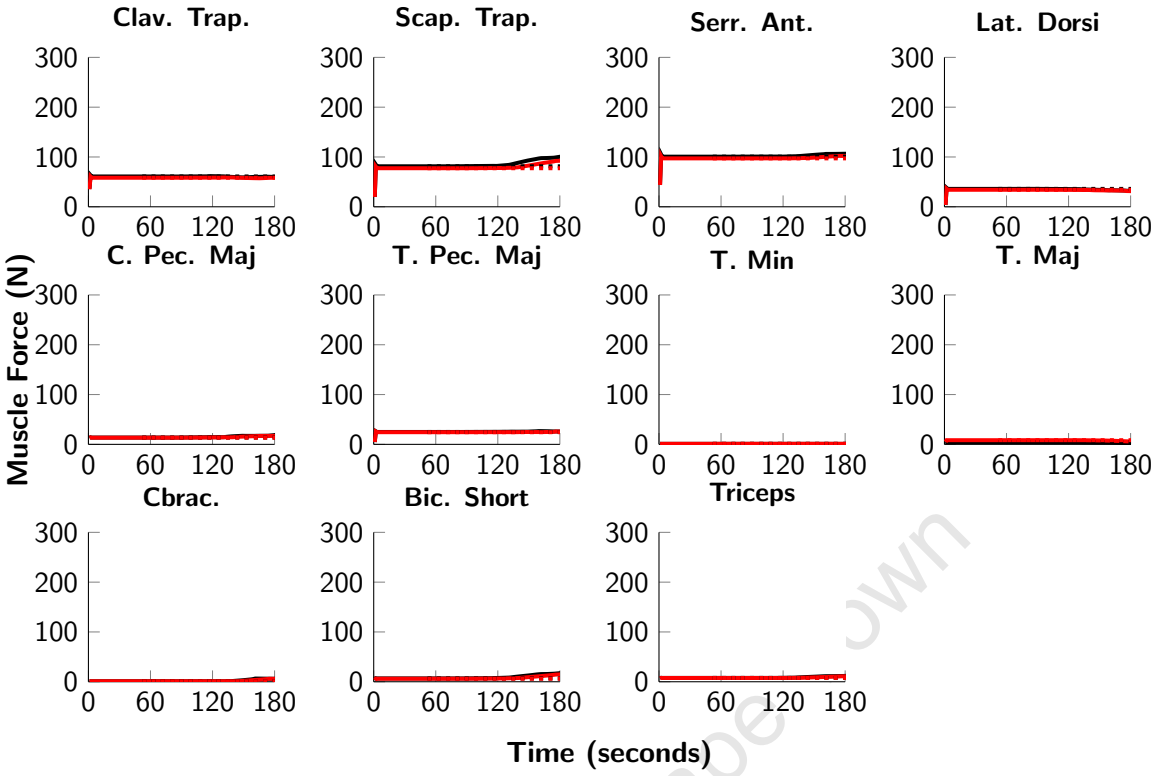

Figure C.7 Subject-averaged muscle forces for SPEh at 30° of humeral elevation

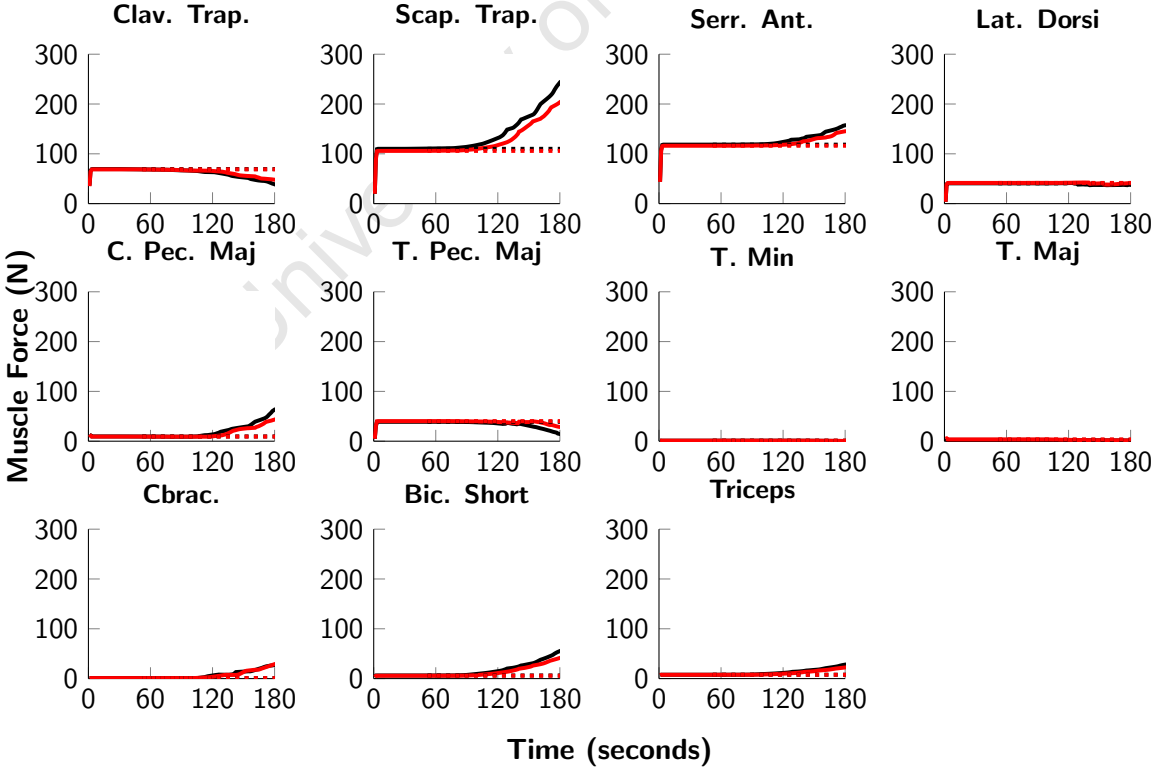

Figure C.8 Subject-averaged muscle forces for SPEh at 60° of humeral elevation

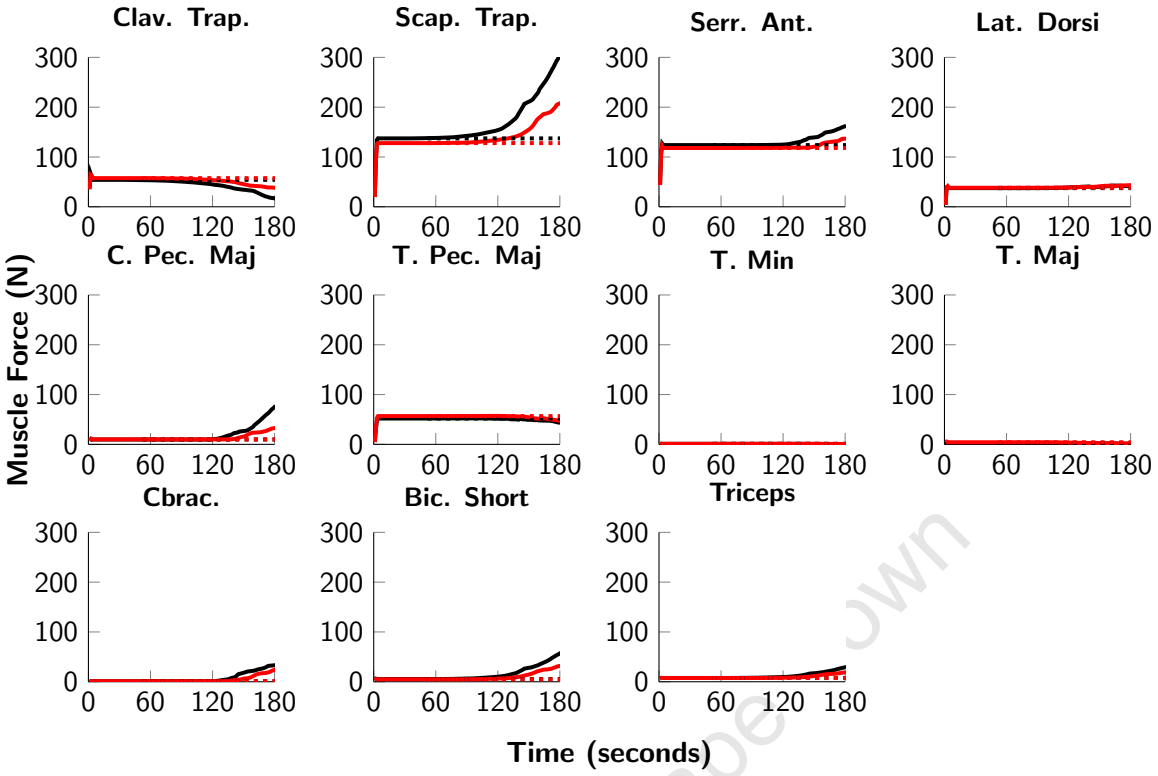

Figure C.9 Subject-averaged muscle forces for SPEh at 90° of humeral elevation

Appendix D

Selection process for the finite element model-set

The subset of subjects from the reverse shoulder model-set used to create the finite element model-set were selected based on the subject-specific joint contact forces in the glenosphere reference frame. The resultant joint contact force of each subject for ABD, FF and SPE is shown in Figure D.1. The subjects were selected based on their representative distribution, with the five subjects producing low, average and high resultant joint contact forces relative to the overall distribution.

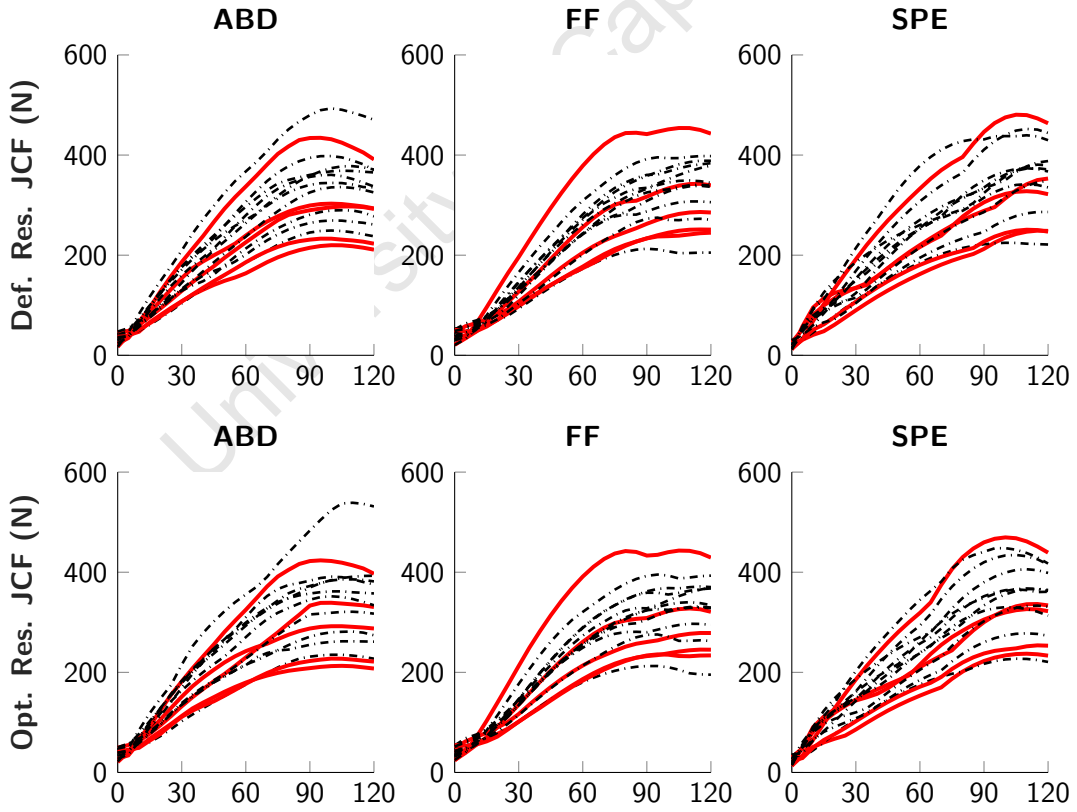

Figure D.1 Subject-specific resultant joint contact forces for the default and optimised configurations (top and bottom rows, respectively). Red lines represent the subjects selected for the FE model-set. Dotted black lines represent the other subjects in the reverse shoulder model-set that were not selected